Abstract

Title of Dissertation: MAGNETIC FIELD EFFECTS ON
THE MOTION OF CIRCUMPLANETARY DUST

Daniel Simon Jontof-Hutter, Doctor of Philosophy, 2012

Dissertation directed by: Professor Douglas P. Hamilton
Department of Astronomy

Hypervelocity impacts on satellites or ring particles replenish circumplanetary dusty rings with grains of all sizes. Due to interactions with the plasma environment and sunlight, these grains become electrically charged. We study the motion of charged dust grains launched at the Kepler orbital speed, under the combined effects of gravity and the electromagnetic force.

We conduct numerical simulations of dust grain trajectories, covering a broad range of launch distances from the planetary surface to beyond synchronous orbit, and the full range of charge-to-mass ratios from ions to rocks, with both positive and negative electric potentials. Initially, we assume that dust grains have a constant electric potential, and, treating the spinning planetary magnetic field as an aligned and centered dipole, we map regions of radial instability (positive grains only), where dust grains are driven to escape or collide with the planet at high speed, and vertical instability (both positive and negative charges) whereby grains launched near the equatorial plane and are forced up magnetic field lines to high latitudes, where they may collide with the planet.

We derive analytical criteria for local stability in the equatorial plane, and solve for the boundaries between all unstable and stable outcomes. Comparing our analytical solutions to our numerical simulations, we develop an extensive model for the radial, vertical and azimuthal motions of dust grains of arbitrary size and launch location. We test these

solutions at Jupiter and Saturn, both of whose magnetic fields are reasonably well represented by aligned dipoles, as well as at the Earth, whose magnetic field is close to an anti-aligned dipole.

We then evaluate the robustness of our stability boundaries to more general conditions. Firstly, we examine the effects of non-zero launch speeds, of up to 0.5 km s^{-1}, in the frame of the parent body. Although these only weakly affect stability boundaries, we find that the influence of a launch impulse on stability boundaries strongly depends on its direction.

Secondly, we focus on the effects of higher-order magnetic field components on orbital stability. We find that vertical stability boundaries are particularly sensitive to a moderate vertical offset in an aligned dipolar magnetic field. This configuration suffices as a model for Saturn's full magnetic field. The vertical instability also expands to cover a wider range of launch distances in slightly tilted magnetic dipoles, like the magnetic field configurations for Earth and Jupiter. By contrast, our radial stability criteria remain largely unaffected by both dipolar tilts and vertical offsets.

Nevertheless, a tilted dipole magnetic field model introduces non-axisymmetric forces on orbiting dust grains, which are exacerbated by the inclusion of other higher-order magnetic field components, including the quadrupolar and octupolar terms. Dust grains whose orbital periods are commensurate with the spatial periodicities of a rotating non-axisymmetric magnetic field experience destabilizing Lorentz resonances. These have been studied by other authors for the largest dust grains moving on perturbed Keplerian ellipses. With Jupiter's full magnetic field as our model, we extend the concept of Lorentz resonances to smaller dust grains and find that these can destabilize trajectories on surprisingly short timescales, and even cause negatively-charged dust grains to escape within weeks. We provide detailed numerically-derived stability maps highlighting the destabilizing effects of specific higher-order terms in Jupiter's magnetic field, and we develop

analytical solutions for the radial locations of these resonances for all charge-to-mass ratios.

We include stability maps for the full magnetic field configurations of Jupiter, Saturn, and Earth, to compare with our analytics. We further provide numerically-derived stability maps for the tortured magnetic fields of Uranus and Neptune.

Relaxing the assumption of constant electric charges on dust, we test the effects of time-variable grain charging on dust grain motion in two distinct environments. Firstly, we examine orbital stability in the tenuous plasma of Jupiter's main ring and gossamer ring where sunlight, the dominant source of grain charging, is periodically interrupted by transit through the planetary shadow. This dramatically expands dynamical instabilities to cover a large range of grain sizes. Secondly, we study the motion of dust grain orbits in the dense plasma environment of the Io torus. Here dust grain charges deviate little from equilibrium, and our stability map conforms closely to that of constant, negatively-charged dust grains.

Finally, we focus on the poorly understood spokes in Saturn's B ring, highlighting the observational constraints on spokes, and present our hypothesis for spoke formation.

MAGNETIC FIELD EFFECTS ON THE MOTION OF CIRCUMPLANETARY DUST

by

Daniel Simon Jontof-Hutter

Dissertation submitted to the Faculty of the Graduate School of the
University of Maryland at College Park in partial fulfillment
of the requirements for the degree of
Doctor of Philosophy
2012

Advisory Committee:

Professor Douglas P. Hamilton, chair
Professor Michael A'Hearn
Professor Douglas C. Hamilton
Professor Matthew Hedman
Professor Christopher Reynolds
Professor Derek C. Richardson

© Daniel Simon Jontof-Hutter 2012

Acknowledgements

My path to Ph.D. has been an interesting journey, and I would not have made it were it not for the generous help I have received along the way from many people. Firstly, I would like to thank my mentor and advisor, Doug Hamilton. Doug has not just been an excellent teacher to me in planetary sciences and dynamics, he has also helped improve my coding and scripting, writing, editing and public speaking. Beyond these skills that I carry with me and will continue to build on, Doug has also offered me invaluable advice on research strategy and planning my own career. Ultimately though, most of what I have learned from Doug is from seeing his example. Doug's quiet determination to solve big problems methodically is balanced by his infectious interest in all topics, and observing him has made me a better scientist. Thank you very much Doug for your patience and hard work in teaching me.

I also want to thank all my other colleagues and teachers who have made this Ph.D. possible, including my professors in grad school: Massimo Ricotti, Stuart Vogel, Patrick Harrington, Mike A'Hearn, Richard Walker, Andy Harris, Eve Ostriker, Cole Miller and Derek Richardson. I am sure there is a

more nuanced word than ‘nostalgia’ to describe how I feel now about working on those assignments and studying for exams, but for now, let me simply take this chance to thank you all for the fine education that I have received.

Derek Richardson and Mike A’Hearn have also served on my research committees throughout grad school, alongside Chris Reynolds. Thank you all for your interest in my research over these last few years. I am honored and delighted to have Matt Hedman from Cornell University, join them on my committee, as well as Douglas C. Hamilton from the physics department, who is representing the dean. I thank all of you for taking the time to read my work and offer feedback.

I am also indebted to the many planetary scientists who have taken an interest in my work at and between conferences, including Joe Burns, Mihály Horányi, Amara Graps, Colin Mitchell, and Joe Hahn. A special thank you for Les Schaffer; your ideas and feedback have helped me immeasurably in writing papers and this thesis.

My years in grad school would have never have passed so quickly without the friendship and camaraderie of my classmates, especially Megan Decesar, Mike Koss, Steve Schwartz, Bo Li, Sid Kumar, Hao Gong, Edmund Hodges-Kluck, Dheeraj Pasham and Mark Avara. You were all great company seeking food, throwing frisbees, kicking soccer balls, hitting racquetballs, and even working in the library or the computer lab.

I owe a big thank you for the love and support of my family, both abroad and locally. My Dad encouraged me to subscribe for my first public library card when I was nine, and I finished the whole astronomy section in a few short weeks. Little did I know then, that you can never really exhaust the

astronomy literature, but nevertheless, you should try. Thank you for the support of my sister Sasha, and my brother Shaul and his family, who helped me immeasurably before I turned my attention to seeking a PhD in the United States.

I especially want to thank my dear wife Laura for years of companionship and support, encouraging me and motivating me whenever obstacles have arisen. Her family has also been especially helpful and supportive over these years. Finally, I owe an enormous debt of gratitude to little Eitan, who in his first few weeks of life has shown remarkable calmness and patience. This has made writing my dissertation a fairly smooth ride after a long journey.

Contents

List of Tables viii

List of Figures ix

1 Introduction 1
- 1.1 A Renaissance in Dynamics . . . 1
- 1.2 The Electromagnetic Force on Dust . . . 2
- 1.3 Outline of Chapters . . . 4

2 Planetary Magnetic Fields 6
- 2.1 The Magnetic Dipole . . . 7
  - 2.1.1 Gyromotion . . . 8
  - 2.1.2 Mirror Motion . . . 9
  - 2.1.3 Azimuthal Drift . . . 14

3 The Dynamics of Charged Dust Grains in Aligned Dipolar Magnetic Fields 16
- 3.1 Introduction . . . 16
  - 3.1.1 Motion in the Kepler and Lorentz Limits . . . 17
  - 3.1.2 Dust Affected by both Gravity and Electromagnetism . . . 18
  - 3.1.3 Research Goals . . . 21
- 3.2 Numerical Simulations . . . 22
- 3.3 Local Radial Stability Analysis . . . 29
  - 3.3.1 Radius of Gyration . . . 33
- 3.4 Global Radial Stability Analysis . . . 34
  - 3.4.1 Escaping Grains . . . 36
  - 3.4.2 Grains that Strike the Planet . . . 38
- 3.5 Local Vertical Stability Analysis . . . 40
  - 3.5.1 Vertical Instability in the Lorentz Limit . . . 42
  - 3.5.2 Vertical instability for all charge-to-mass ratios . . . 44
- 3.6 Azimuthal Motion . . . 47
- 3.7 Saturn and Earth . . . 50
- 3.8 Conclusion . . . 54

4 The Dynamics of Dust in Multipolar Magnetic Fields **58**
4.1 Introduction . . . 58
4.2 Motion in an Aligned Dipolar Magnetic Field . . . 60
4.3 Jupiter . . . 63
4.3.1 Varied Launch Speed . . . 65
4.3.2 Vertically Offset Dipole . . . 69
4.3.3 Tilted Dipole . . . 71
4.3.4 Resonant Effects in a Tilted Dipole Field . . . 76
4.3.5 Quadrupole Terms . . . 82
4.3.6 Realistic Full Magnetic Field Models . . . 86
4.4 Other planets . . . 90
4.4.1 Saturn . . . 91
4.4.2 Earth . . . 96
4.4.3 Uranus . . . 98
4.4.4 Neptune . . . 102
4.5 Discussion . . . 103

5 Time Variable Grain Charging **106**
5.1 Introduction . . . 106
5.2 Spherical Dust Grain Model . . . 107
5.3 Plasma Effects . . . 108
5.3.1 Direct Capture of Electrons and Ions . . . 108
5.3.2 Secondary Electron Emission . . . 113
5.4 Insolation . . . 115
5.4.1 Charging Timescale . . . 116
5.5 The Shadow Resonance in the Main and Gossamer Rings . . . 116
5.6 The Io Plasma Torus and Jovian Dust Stream . . . 124
5.7 Discussion . . . 134

6 Saturn's Spokes **136**
6.1 Introduction . . . 136
6.2 The Radial Spokes in Saturn's B-ring . . . 138
6.2.1 Spoke Particles are Dust . . . 138
6.2.2 Morphology and Formation . . . 140
6.3 Spoke Formation Theories . . . 142
6.3.1 Grain Orientation Models . . . 143
6.3.2 Grain Levitation Models . . . 146
6.3.3 Other Theories for Spoke Formation . . . 151
6.3.4 Comments on Spoke Seasonality . . . 151
6.4 Collisional Cascade Model . . . 152
6.5 Strategy . . . 154

6.5.1 Measuring Impact Energies Numerically 154
6.6 A Simple Cascade 159
6.6.1 Leaping Across the B Ring 160
6.6.2 Tip-toeing Across the B Ring 164
6.7 Discussion and Prospects 166
6.8 Conclusion 171

Bibliography **172**

List of Tables

4.1 Determining L_* 60
4.2 Jovian Magnetic Field Coefficients 71
4.3 Lorentz Resonances at Jupiter 79
4.4 Saturnian Magnetic Field Coefficients 91
4.5 Geomagnetic Field Coefficients 96
4.6 Uranian Magnetic Field Coefficients 100
4.7 Neptunian Magnetic Field Coefficients 102

List of Figures

2.1 Geometry of a dipole magnetic field in cylindrical coordinates 11
2.2 The bounce period in a slowly rotating magnetic dipole 12
2.3 The tilt of a gyroloop 13

3.1 Stability maps with prior analytical boundaries at Jupiter 24
3.2 The trajectory of a vertically unstable grain 26
3.3 A stable orbit between two different instabilities 27
3.4 A grain with coupled vertical and radial motions 28
3.5 Confinement in a large volume 29
3.6 The radial ranges of negative and positive grains 35
3.7 Potential wells near the escape threshold for highly charged grains 37
3.8 Potential wells for moderately charged grains on the threshold of striking the planet 39
3.9 Analytical solutions for the boundaries in stability maps 41
3.10 Vertical motion in the Lorentz limit 43
3.11 Radial, vertical and azimuthal periods 48
3.12 Azimuthal drift rates in the Lorentz regime 49
3.13 Stability maps in an aligned dipolar magnetic field for Saturn 51
3.14 Stability maps in an anti-aligned dipolar magnetic field configuration for Earth 53
3.15 Coupled radial and vertical motions at Earth 54
3.16 Non-linear stable oscillations at Earth 55
3.17 Local and global stability criteria summarized 56

4.1 Stability boundaries in a centered and aligned dipolar magnetic field summarized 64
4.2 Radial range of motion with launch impulses 66
4.3 Stability of orbits with launch impulses 68
4.4 Stability in a vertically offset dipolar magnetic field 70
4.5 Stability of negative grain orbits in a tilted magnetic dipole 72
4.6 Stability of positive grain orbits in a tilted magnetic dipole 74
4.7 Destabilizing resonances in a tilted dipole magnetic field 77

4.8 Theoretical Lorentz resonances for highly-charged dust grains 81
4.9 Lorentz resonances due to quadrupolar magnetic field terms 83
4.10 Lorentz resonances with quadrupolar and octupolar magnetic field terms . 87
4.11 Theoretical resonance curves in Jupiter's full magnetic field 89
4.12 Stability of charged grains in Saturn's full magnetic field 93
4.13 Vertical Equilibrium Point in an Offset Dipolar Magnetic Field 95
4.14 Stability of charged grains in Earth's full magnetic field 99
4.15 Stability of charged grains in Uranus' full magnetic field 101
4.16 Stability of charged grains in Neptune's full magnetic field 104

5.1 Charging Currents on a Dust Grain in Tenuous Plasma 118
5.2 Variable Charging due to the Planetary Shadow 119
5.3 The Effect of the Planetary Shadow on the Stability of Orbits 121
5.4 High speed dust stream trajectories and detectability 126
5.5 Charging potential on a 10-nm dust grain in the Io plasma torus 129
5.6 Stability map for the Io plasma torus 131
5.7 Precession and the shadow resonance 133
5.8 Trajectory of a 10-nm grain launched in the Io plasma torus 134

6.1 Voyager 2 spokes image 139
6.2 The location of grain impacts in the B ring 157
6.3 Impact kinetic energy 158
6.4 The radial progression of a simple cascade with large epicycles 161
6.5 The specific kinetic energy in cascade collisions 162
6.6 The azimuthal spread of a simple cascade with large epicycles 163
6.7 Tracing the path of a cascade chain leaping across the B ring 164
6.8 The radial progression of a simple cascade with compact epicycles 165
6.9 The azimuthal spread of a simple cascade with compact epicycles 166
6.10 Tracing the path of a cascade chain tip-toeing across the B ring 167

Chapter 1

Introduction

1.1 A Renaissance in Dynamics

In recent decades, a plethora of non-gravitational effects on orbital mechanics has expanded the study of how small bodies move. Rotating asteroids with temperature differences on the surface experience the gentle thermal radiative thrust of the Yarkovsky effect. Comets sojourning the inner solar system develop surface jets that provide significant orbital impulses. The dust grains sprinkled throughout the solar system by these bodies are sensitive to radiation pressure, Poynting-Robertson drag, and corpuscular drag in the Solar wind. Around other stars, gas drag can be a significant force on the dust that we see in circumstellar debris disks. Near planets, drag from the upper atmosphere becomes the dominant cause of orbital decay, and in optically thick ring systems, collisions and contact forces are crucial to understanding the motions and lifetimes of ring particles. Each of these processes work on individual particles or planetesimals in addition to gravity, depending on the environment around the particle as well as its own properties, particularly its mass. Although dust grains are modest in mass, their presence in great numbers makes them of particular importance in astronomy. Dusty debris disks around

other stars are frequently the only observable clues we have about unseen planets. This makes the dynamics of dust crucial to interpreting images of systems where planets are forming. Understanding the motion of dust released by comets or the collisional grinding of asteroids can help us trace the origins of meteoroids that make their way to the Earth from elsewhere in the Solar System, or even from other stars. In the dusty ring systems, the fate of dust grains may determine the lifetime of the rings themselves, or elucidate the rate of dust replenishment.

1.2 The Electromagnetic Force on Dust

For the dust grains generated in the planetary ring systems, the most important forces are gravity and the Lorentz force. Dust in space acquires electric charges in several ways. Moving through the plasma environment produces a negative charge on a grain, since the plasma electrons are much lighter and swifter than ions and hence are captured more frequently by orbiting dust grains (Goertz 1989). On the other hand, sunlight ejects photo-electrons from the surface of a grain, leaving positive charges (Horányi et al. 1988). Electron or ion impacts will also produce secondary electron emission, which also favors a net positive equilibrium charge on the grain (Whipple 1981). These currents interact in complicated ways; the charging of a dust grain depends on the physical properties of the grain itself and also on its charge history (Meyer-Vernet 1982). Graps et al. (2008) provide an excellent review of these processes.

Combined with gravity, EM effects determine the morphology of dusty rings, particularly those of Jupiter and Saturn. At Jupiter, resonant perturbations by the rotating planetary magnetic field on orbiting dust grains excite their inclinations forming a faint extended halo that envelops the main ring north and south of the equator plane (Burns et al. 1985). Furthermore, time resonant charge-variation acting on dust grains in the

Thebe ring increases their orbital eccentricities, extending the dusty ring well beyond the orbit of Thebe (Hamilton and Krüger 2008). Streams of tiny dust grains are expelled at high speed from both the Jupiter system (Hamilton and Burns 1993a; Horányi et al. 1993a) as well as Saturn (Kempf et al. 2005). These effects are all determined by the motions of grains dominated by the Lorentz force and gravity. Even in Saturn's B ring, an optically thick belt of boulder sized particles, EM effects are at the heart of the mysterious spokes of dust. It is to explain these diverse phenomena that motivates this thesis on the dynamics of charged dust.

In our Solar System, the planetary magnetic field configurations are as diverse as the planets themselves. Saturn has the simplest magnetic field, well modelled by a simple axisymmetric dipolar field slightly offset northwards from the center of the planet. Jupiter, with by far strongest planetary magnetic field, has a more general configuration, but one that is dominated by an offset and moderately tilted magnetic dipole. A similar configuration exists at Earth, however, at the current epoch, the Earth is unique in the Solar System for having its dipolar magnetic field component anti-aligned with the planetary rotation. Hence, at the Earth, the magnetic north pole is very close to the geographic south pole. Voyager 2 measured the magnetic fields of both Uranus and Neptune, and in both cases found complex configurations that conform poorly to a tilted or offset dipole model.

Our goal is to develop an understanding of how dust grains of all sizes in the circumplanetary environment, move under the forces of planetary gravity and the Lorentz force. To isolate the important physics in this problem, we shall first look at the motion of EM-dominated grains in the simplest magnetic field configuration possible, a dipole. We shall then extend our analysis to cover the entire spectrum of dust grain sizes, from ions dominated by EM forces to rocks controlled by gravity. The next step is to examine the effects of general magnetic field configurations on the dynamics of charged dust. Beyond these effects, we study time variable grain charging and its influence on orbital

stability. And finally, we will have the tools and insights necessary to understand such diverse phenomena in the rings the Jovian dust stream and Saturn's spokes.

1.3 Outline of Chapters

The Lorentz force applies only where particles carry electric charges and move relative to a magnetic field. In Chapter 2 we introduce the motion of charges in a simple dipolar magnetic field with the Lorentz force acting in isolation. This will serve not only to review an important limiting case for our problem, to which we shall add complexity in later chapters, but we shall obtain results in this regime that do not appear in the literature.

In Chapter 3, we explore the stability of Kepler-launched grains for all charge-to-mass ratios and for all launch distances in a centered and aligned dipolar magnetic field model for Jupiter. We consider the motion of grains launched from ring particles or from satellites in a collisionless environment, and assume that dust grains maintain a constant charge-to-mass ratio. This study determines the boundaries between launch conditions that permit stable orbits from those that result in trajectories that where dust grains are either expelled from planet or coerced to crash into the planet immediately after launch. For the stable grains, our analysis includes solutions to the fundamental orbital frequencies in the epicyclic model of dust grain motions. Chapter 3 is based largely on the paper Jontof-Hutter and Hamilton (2012a), and the solutions are applicable wherever an aligned dipole approximation can be defended.

In chapter 4, we test the stability boundaries of Chapter 3 to non-zero launch impulses in the frame of the parent particle. These launch conditions are appropriate for material released from parent bodies by high speed impacts. We then consider the effects of higher-order magnetic field terms on the fate of grains. We isolate the effects of Jupiter's offset and tilted dipolar magnetic field terms, then we explore the higher-order field components,

and study the destabilizing effect of Lorentz resonances over all charge-to-mass ratios. Finally, we compile stability maps for dust grains in the general magnetic fields of Jupiter, Saturn, Uranus, Neptune and Earth.

In chapter 5, we relax our assumption of constant charge-to-mass ratio on a dust grain. Here we review the grain charging equations and discuss the assumptions adopted in our numerical models. We then explore the effects of time-varying electric charges on dust grains due to transit through planetary shadows, in two distinct charging environments: the tenuous plasma of Jupiter's main and gossamer rings, and the dense plasma in the Io torus. The latter motivates our discussion of the origin and dynamics of the Jovian high speed dust stream.

In chapter 6, we investigate the spokes in Saturn's B ring, summarizing the observational constraints and existing theoretical challenges presented by these ghostly apparitions. We then develop a hypothesis for the spokes using the results of chapters 3, 4 and 5 to highlight the relevant dynamics in our collisional cascade model for spoke formation.

Chapter 2

Planetary Magnetic Fields

Motivated by the aurora borealis, the Norwegian physicist Carl Störmer pioneered studies of the motion of charged particles in the Earth's magnetosphere in the early twentieth century. His development of analytical and numerical techniques to model the trajectories of charges in the geomagnetosphere were an intellectual achievement matched by his practical creativity. Using cameras deployed around Norway linked by early telephone communications, Störmer was the first to measure the latitudes and altitudes of aurorae in 1910. His work made him the world's leading authority on aurorae, and he also made major contributions in the study of cosmic rays.

It was not long before the technology to lift scientific instruments high above the ground permitted direct experiments in space, with the mysterious cosmic rays being one of the first targets. On the eve of the Space Age, James Van Allen led experiments using balloons, rockets and ultimately balloon-launched rockets to observe cosmic rays in the upper atmosphere. His results led him to predict the existence of high energy plasma trapped in the Earth's magnetic field.

Following the launch of Sputnik by the Soviet Union, Van Allen argued to include a Geiger Counter aboard the first artificial satellite launched by the United States, Explorer 1. This enabled the discovery of the radiation belts that bear his name. It also

heralded the age of interplanetary exploration. Within just 30 years, the Pioneer and Voyager missions had revealed the magnetospheres of all four of the giant planets. In the ring systems of these distant worlds, charged dust grains are significantly perturbed by electromagnetic forces, arising from rotating magnetic fields. Our aim is to study the motion of such grains. We assume that dust grains are launched from parent particles in planetary rings at the Kepler orbital speed, and we seek to understand their orbital motions for all sizes and launch distances.

The results of Störmer (1955) and Thomsen and van Allen (1980) implicitly assume that all other perturbations are negligible, an excellent assumption in the regime of high energy plasma in radiation belts or aurora, or equivalently, since the particles we are interested in are launched at the local Kepler orbital speed, that the rotation rate of the planetary magnetic field is much less than the Kepler frequency. We begin here by considering the motion of highly charged particles in the simplest magnetic field configuration possible, the magnetic dipole. In chapter 3, we will test to what extent the equations in this chapter apply to orbiting dust grains.

2.1 The Magnetic Dipole

For an aligned magnetic dipole in a spherical coordinate system (r, λ, ϕ), where λ, the latitude, is the angle from the dipolar equator;

$$\vec{B} = \frac{3(\vec{m_B} \cdot \hat{r})\hat{r} - \vec{m_B}}{r^3}. \tag{2.1}$$

Here $m_B = g_{10} R_p^3$ is the scalar strength of the dipole moment at the planetary equator, R_p is the planetary radius, and g_{10} is the equatorial magnetic field strength in Gauss. To express the field strength as a scalar $B(m_B, r, \lambda)$, we take the dot product of equation 2.1 with itself and find

$$B(m_B, r, \lambda) = \frac{m_B}{r^3}(1 + 3\sin^2\lambda)^{1/2}. \tag{2.2}$$

Note that due to axial symmetry there is no dependence on the azimuthal angle ϕ, and it is a simple matter to consider the same geometry in cylindrical coordinates (ρ, z), where $\rho = r\cos(\lambda)$, and $z = r\sin(\lambda)$. For a particular point in this system, it is conventional to keep track of the radial distance r_0 at which a local field line crosses the equatorial plane. Each field line is given by the equation

$$r = r_0 \cos^2 \lambda \tag{2.3}$$

(Lew 1961). Thus the magnetic field strength at latitude λ on a field line crossing the equatorial plane at a distance r_0 becomes

$$B = \frac{m_B}{r_0^3} \frac{(1+3\sin^2\lambda)^{1/2}}{\cos^6 \lambda} \tag{2.4}$$

(Lew 1961). The magnetic field is weakest at the equator and increases rapidly towards the poles. For $\lambda = 30^\circ$, the field is already more than three times its strength at the equator. Motion in an aligned dipole occurs on three timescales; rapid gyromotion around magnetic field lines, slower bounce motion up and down field lines, and still slower azimuthal drift.

2.1.1 Gyromotion

The Lorentz force acting on a charge q moving at velocity $\vec{v}$ through a magnetic field is given by

$$\vec{F_B} = \frac{q}{c}\vec{v} \times \vec{B} \tag{2.5}$$

where c is the speed of light. Note that we use CGS units here and throughout. Only the velocity component perpendicular to the magnetic field $v_\perp$ contributes to the Lorentz force, and the force itself is perpendicular to both $\vec{v}_\perp$ and $\vec{B}$. The grain rapidly spirals about the field lines with gyroradius r_g. Equating the electromagnetic force with the centrifugal force $\frac{mv_\perp^2}{r_g}$, then in the frame of the guiding center a gyrating particle of mass

m, experiences gyrations at frequency:

$$\Omega_g = \frac{v}{r_g} = \frac{qB}{mc}. \tag{2.6}$$

2.1.2 Mirror Motion

Consider a charged particle rapidly gyrating due to the Lorentz force. The particle is free to drift parallel to the magnetic field lines. Following Eq. 2.4, the magnetic field strength increases rapidly along a field line moving away from the magnetic equator.

Any force oriented at right angles to a particle's motion can do no work on that particle. Thus, in the frame rotating with the guiding center, the Lorentz force does no work and a dust grain's speed v remains constant:

$$v^2 = v_\perp^2 + v_\parallel^2 = \text{constant}, \tag{2.7}$$

where $v_\perp$ and $v_\parallel$ are the speeds perpendicular and parallel to the magnetic field lines, respectively. The $v_\perp$ component determines the radius of the gyrocycle, while the $v_\parallel$ component moves the center of gyration to regions of differing magnetic field strength. If changes to a non-rotating magnetic field $\vec{B}$ are small over the size and time scales of gyromotion, the ratio

$$\frac{v_\perp^2}{B} = \text{constant}, \tag{2.8}$$

is an adiabatic invariant (de Pater and Lissauer 2010). These two conditions provide an important constraint on the grain's motion parallel to the field lines. As a grain with a vertical velocity component climbs up a magnetic field line away from the equatorial plane, the field strength B increases in accordance with Eq. 2.4, and the adiabatic invariant (Eq. 2.8) implies that $v_\perp$ also increases. Hence, by conservation of energy (Eq. 2.7), $v_\parallel$ must decrease. There is thus a restoring force directed towards the equatorial plane where the magnetic field strength is a local minimum, and the motion parallel to the field lines

takes the form of bounce oscillations between mirror points north and south of the equator (Störmer 1955).

To calculate the bounce period in this regime, we evaluate the integral

$$T_B = \int \frac{ds}{v_{||}} = 4\int_0^{\lambda_m} \frac{ds}{v_{||}} \tag{2.9}$$

where ds is an increment in the path of the grain as it climbs a magnetic line, at velocity $v_{||}$ (Thomsen and van Allen 1980), and λ_m is the latitude at the mirror point. Equations 2.7 and 2.8 allow us to isolate $v_{||}$.

$$v_{||}^2 = v^2\left(1 - \frac{B}{B_m}\right), \tag{2.10}$$

where B_m is the magnetic field strength at the mirror point (Lew 1961).

Figure 2.1 illustrates the path along a dipolar field line that crosses the magnetic equator at r_0. An increment along this path, ds, satisfies the following equation:

$$ds^2 = (rd\lambda)^2 + dr^2. \tag{2.11}$$

Differentiating equation 2.3 to put dr in terms of $d\lambda$, we find

$$ds = r_0 \cos\lambda (1 + 3\sin^2\lambda)^{1/2} d\lambda, \tag{2.12}$$

and finally, substituting equations 2.12 and 2.10 into Eq. 2.9, and assuming small vertical oscillations from the magnetic equator ($\lambda_m << 1$), we expand Eq. 2.4 to order λ^4, and evaluate the integral to find

$$T_B = \frac{2\sqrt{2}\pi}{3}\frac{r_0}{v}\left(1 + \frac{23}{16}\lambda_m^2 + \frac{5165}{3072}\lambda_m^4 + O(\lambda_m^6)\right). \tag{2.13}$$

The latitudinal range of the mirror motion depends on the pitch angle of motion α_0 at the magnetic equator, defined as the angle between $\vec{v}$ and $\vec{B}$. The pitch angle directly determines the mirror point via the following relation:

$$\sin^2(\alpha_0) = \frac{\cos^6\lambda_m}{\sqrt{1 + 3\sin^2\lambda_m}}. \tag{2.14}$$

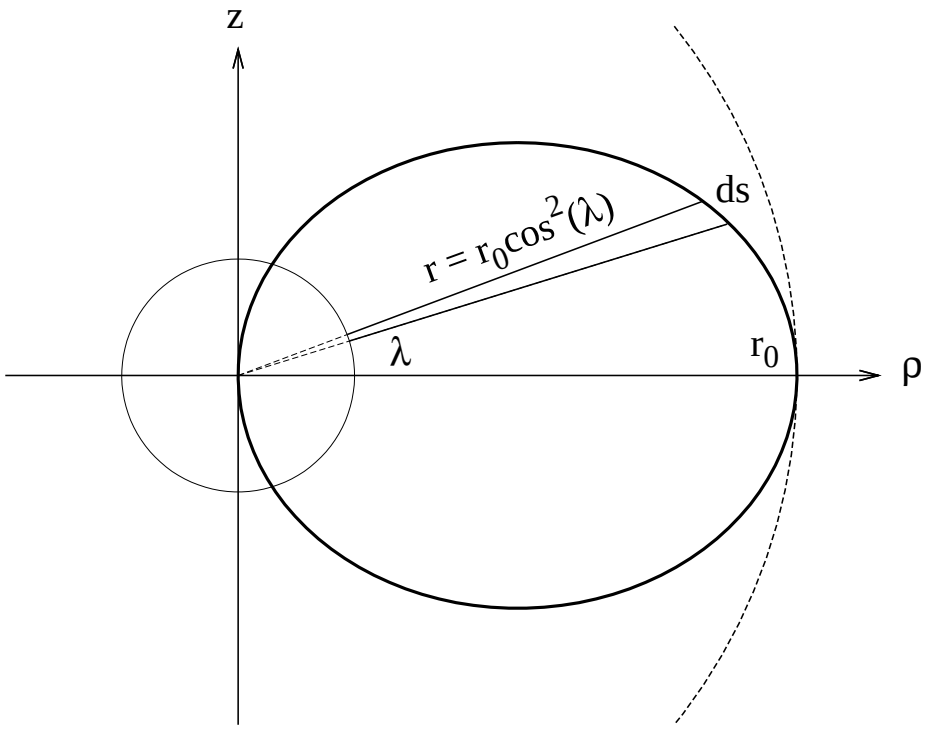

Figure 2.1: Geometry of a dipole magnetic field. The circle centered at the origin represents the planet, and the solid curve permeating the planetary surface denotes a magnetic field line. The dotted curve marks a circular arc at the distance that the field line crosses the equator. A small increment along the length of the field line *ds* is illustrated, defined by equation Eq. 2.11.

To test the accuracy of Eq. 2.13, we modeled the bounce period in hours, for grains dominated by Lorentz forces in a slowly rotating magnetic dipole field. Figure 2.2 compares the bounce period of Eq. 2.13 with an empirical model of Thomsen and van Allen (1980) based on the work of Lenchek et al. (1961). Alongside these solutions we plot numerical results for grains launched at the Kepler speed at Saturn.

As the vertical oscillations increase in amplitude and become non-linear, the bounce period increases. Figure 2.2 also shows that for small vertical oscillations, where $\alpha \approx 90^\circ$, the bounce period is fairly constant over a range of amplitudes, and all three models are in close agreement with our simulations. For higher bounce amplitudes, however, our second and fourth-order approximations do not match the data as well as the Lenchek

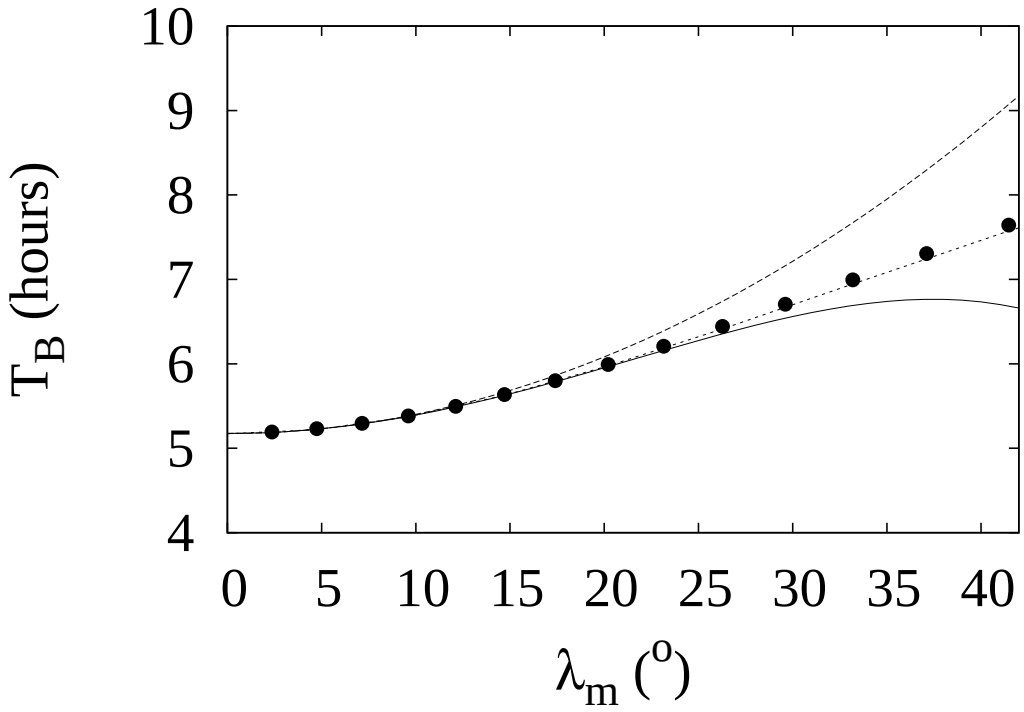

Figure 2.2: The bounce period T_B between mirror point latitudes λ_m in a slowly rotating magnetic dipole. The points are numerical data for a planet, identical to Saturn in mass and size but with a leisurely 10,000 hour rotation period. The grains, launched at $1.9R_p$ at the Kepler speed, collide with the planet if $\lambda_m \geq 42^\circ$. The dotted curve is an empirical solution following Thomsen and van Allen (1980), and the lower solid curve marks the fourth order approximation of Eq. 2.13. The upper dashed curve denotes just the second order terms in Eq. 2.13.

et al. (1961) empirical model.

As a gyrating particle climbs up a magnetic field line, the curvature of the field line also determines the tilt of the gyroloop. Figure 2.3 illustrates the attitude of a gyroloop at its maximum latitude λ_m, with tilt angle ψ at right angles to the field line at the mirror point. Along a magnetic field line described by Eq. 2.3, and near the magnetic equator where λ_m is small;

$$\rho = r_0 \cos^3(\lambda) \approx r_0 \left(1 - \frac{3\lambda^2}{2}\right) \tag{2.15}$$

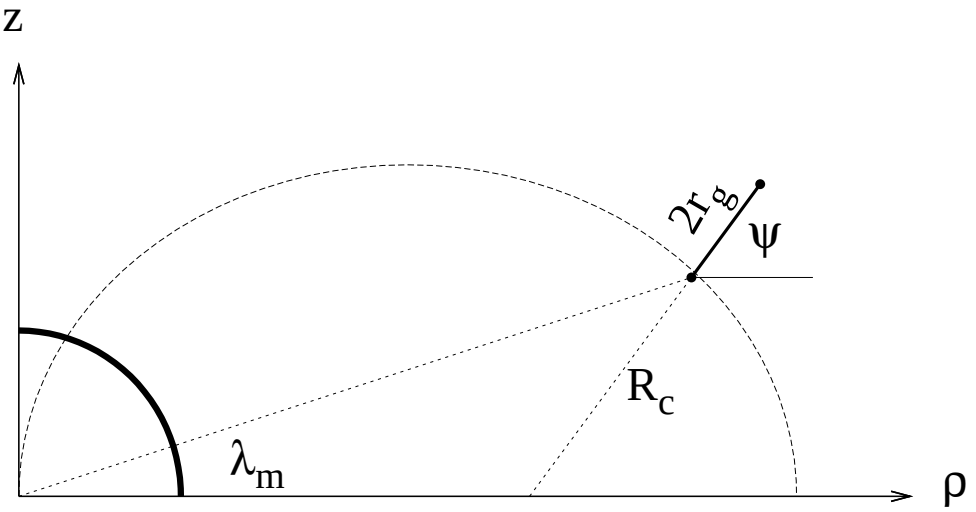

Figure 2.3: The tilt of a gyroloop at a mirror point λ_m, seen as a line of length $2r_g$ from the side. Here the size of the gyroloop is exaggerated for illustrative purposes. For small latitudes, the tilt angle $\Psi \approx 3\lambda$.

and

$$z = r_0 \cos^2(\lambda) \sin(\lambda) \approx r_0 \lambda. \tag{2.16}$$

Evaluating $\frac{\partial z}{\partial \rho} = \frac{dz}{d\lambda} / \frac{d\rho}{d\lambda}$, and ignoring terms of order λ^2,

$$\psi \approx -\left(\frac{\partial z}{\partial \rho}\right)^{-1} \approx 3\lambda_m. \tag{2.17}$$

Thus, for small bounce oscillations, the tilt of the gyroorbit is three times its instantaneous latitude at the mirror point.

2.1.3 Azimuthal Drift

Even the most highly charged dust grains are not tied to magnetic field lines, but rather drift azimuthally due to other perturbative forces or a non-uniform magnetic field. For a complete survey of all such effects, we recommend Nicholson (1983) or de Pater and Lissauer (2010). Here we focus on the drifts that are relevant for particles launched near the magnetic equator.

Consider an arbitrary force acting on a charged particle in addition to the Lorentz force. The component parallel to the magnetic field will cause unchecked acceleration along the field, but the part perpendicular to the field will cause a drift at speed

$$\vec{v}_f = \frac{c}{q}\frac{\vec{F}_\perp \times \vec{B}}{B^2}, \tag{2.18}$$

relative to the magnetic field lines.

If $F_\perp$ is an electric field, the drift rate is

$$\vec{v}_E = \frac{c\vec{E} \times \vec{B}}{B^2}. \tag{2.19}$$

Electric fields can arise near the ionosphere at the Earth, but more relevantly for our purposes, a spinning magnetic field can be treated as a stationary magnetic field plus an electric field with magnitude

$$\vec{E} = -\frac{(\vec{\Omega}_p \times \vec{r}) \times \vec{B}}{c}, \tag{2.20}$$

where Ω_p is the rotation rate of the planet on its axis. This electric field causes charged grains to accelerate radially across magnetic field lines and adds a contribution to the azimuthal drift. Since the electric field is independent of the charge on the grain, the drift is in the same direction for both positive and negative charges. The effect in the high q/m limit is that charged particles are nearly tied to magnetic field lines in the rotating frame, or alternatively, drift at speed $\Omega_p r$, the rotation speed of the magnetic field in the inertial frame.

Near the magnetic equator, the force of gravity is always perpendicular to the magnetic field. Hence, the gravitational drift

$$\vec{v}_g = \frac{mc\vec{g} \times \vec{B}}{qB^2}, \tag{2.21}$$

has a similar form to Eq. 2.19. With gravity acting alone, the drift on a positive ion is retrograde, or clockwise as viewed from the north. Negative grains go the opposite way.

The radial gradient in a dipolar magnetic field also causes an azimuthal drift:

$$\vec{v}_\nabla = \frac{1}{2B^2}\frac{v^2}{\Omega_g}(\vec{B} \times \vec{\nabla} B). \tag{2.22}$$

Note that the gyrofrequency Ω_g from Eq. 2.6 is a signed quantity, hence electrons and again, ions drift in opposite directions.

The vertical motion along the magnetic field lines causes a centrifugal force

$$F_{cent} = \frac{mv_{||}^2}{R_c}, \tag{2.23}$$

where R_c is the radius of curvature of the field line (Fig. 2.3). For small vertical excursions, the radius of curvature of a field line is simply $R_c = \frac{r_0}{3}$. Substituting this force into Eq. 2.18 yields

$$\vec{v}_{curv} = \frac{v_{||}^2}{\Omega_g R_c}(\hat{R}_c \times \hat{B}). \tag{2.24}$$

The curvature drift is the weakest contribution of the drift rates we consider here, since we are assuming only small vertical excursions from the magnetic equator.

These drift rates are strictly valid only in the electromagnetically-dominated regime. Furthermore, the equations implicitly assume that the rotation speed of the planetary magnetic field is negligible compared to the motion of individual charges. We shall return to consider how these drift rates are affected with both gravity and planetary rotation on Kepler-launched grains in the following chapter.

Chapter 3

The Dynamics of Charged Dust Grains in Aligned Dipolar Magnetic Fields

3.1 Introduction

[1] The discoveries of the faint dusty ring systems of the giant planets beginning in the late 1970s greatly changed our understanding of planetary rings. Unlike Saturn's classical rings, which are most likely ancient (Canup 2010), dusty rings are young and are continually replenished from source satellites. Individual ring particles have short lifetimes against drag forces and other loss mechanisms, and because dusty rings are so diffuse, they are essentially collisionless. Furthermore, dusty rings are affected by a host of non-gravitational forces including solar radiation pressure and electromagnetism, which can sculpt them in interesting ways.

Since the giant planets are far from the Sun and dusty rings are normally near their primary, radiation pressure is usually a weak perturbation to the planet's gravity. The electromagnetic force arising from the motion of charged dust grains relative to the planetary

[1] This chapter is based on published work of Jontof-Hutter and Hamilton (2012a).

magnetic field, however, can be quite strong. In particular, with nominal electric charges, dust grains smaller than a fraction of a micron in radius are more strongly affected by electromagnetism than gravity.

Many authors have investigated detailed aspects of the motion of charged grains in planetary magnetic fields, but no study has yet determined the orbital stability of grains for all charge-to-mass ratios launched at all distances in a systematic way. In this chapter, we explore the local and global stability of both positive and negative dust grains launched from ring particle parent bodies which themselves orbit at the local Kepler speed.

3.1.1 Motion in the Kepler and Lorentz Limits

As grains with radii greater than several microns have small charge-to-mass ratios, electromagnetic effects are weak, and the grains orbit the planet along nearly Keplerian ellipses. In the frame rotating with the mean motion of the dust particle, the orbits appear as retrograde elliptical epicycles with a 2:1 aspect ratio (Mendis et al. 1982). When gravity acts alone, the vertical, radial and azimuthal motions all have precisely the same frequency. Equations governing the slow changes to the ellipse's orbital elements due to weak electromagnetic perturbations from a rotating aligned dipole magnetic field are given by Hamilton (1993a). These equations show that the three frequencies diverge slightly and are functions of the sign and magnitude of the charge as well as the distance from the planet and from synchronous orbit.

Conversely, the very smallest dust grains approach the Lorentz limit, discussed in Chapter 2, where the electromagnetic force dominates over gravity. In this regime, the frequencies of radial, vertical and azimuthal motions differ significantly. The radial oscillation is fastest and, as the electromagnetic force is perpendicular to the rotating magnetic field, particles gyrate about local field lines on typical timescales of seconds for dust, and microseconds for ions. Vertical motions are slower and azimuthal drift rates are the

slowest of all as discussed in Chapter 2.

3.1.2 Dust Affected by both Gravity and Electromagnetism

For a broad range of grain sizes from nanometers to microns, both gravity and the Lorentz force are significant, and their combined effect causes a number of dynamical phenomena that are distinct from either limiting case. As dust in this size range predominates in many planetary rings (Burns et al. 1999; de Pater et al. 1999; Krüger et al. 2009; Showalter et al. 2008), their dynamics have attracted much attention.

Schaffer and Burns (1994) provide a general framework for the motion of dust started on initially Keplerian orbits. Since the radial forces on a dust grain at launch are not balanced as they are for a large parent body on a circular orbit, these dust grains necessarily have non-zero amplitude epicyclic motion. For the magnetic field configurations of the giant planets, a negatively-charged dust grain gyrates towards synchronous orbit while positively-charged dust initially moves away from this location. In fact, some positively-charged grains are radially unstable and either crash into the planet if launched inside synchronous orbit, or are expelled outwards if launched from beyond this distance. The latter have been detected as high-speed dust streams near Jupiter (Grün et al. 1998, 1993) and Saturn (Kempf et al. 2005). Theoretical explanations for the electromagnetic acceleration process have been given by Horányi et al. (1993a,b), Hamilton and Burns (1993b) and Graps et al. (2000).

Mendis et al. (1982) explored the shape and frequency of epicycles for negatively-charged grains in the transitional regime, where both EM effects and gravity are comparable. The epicycles make a smooth transition from perfectly circular clockwise (retrograde) gyromotion in the Lorentz limit, to 2:1 retrograde elliptical epicycles in the Kepler limit. Mitchell et al. (2003) studied the shapes of epicyclic motion for positive grains and found that there is not a similarly smooth transition from prograde gyromotion to

retrograde Kepler epicycles, and that the epicyclic motions of intermediately-sized grains cannot be represented as ellipses. The effects of gravity and electromagnetism compete for intermediate charge-to-mass values and the resulting motion can be primarily radial, leading to escape or collision (Hamilton and Burns 1993b; Horányi et al. 1993b).

Northrop and Hill (1982, 1983a) and Northrop and Connerney (1987) studied the vertical motion of negatively-charged dust grains on circular uninclined orbits in a centered and aligned dipole field, a configuration most closely realized by Saturn. They found that some small grains on initially centrifugally-balanced circular trajectories inside the synchronous orbital distance are locally unstable to vertical perturbations, climbing magnetic field lines to crash into the planet at high latitudes. Some motions at high latitude, however, are stable: Howard et al. (2000, 1999) identified non-equatorial equilibrium points for charged dust grains, and showed that dust grains can orbit them stably. They characterized these "halo" orbits for positive and negative charged grains on both prograde and retrograde trajectories. Howard and Horányi (2001) used these analytical results to argue for a stable population of positively-charged grains in retrograde orbits and developed numerical models of such halo dust populations at Saturn. Grains that may populate these halos, however, are unlikely to originate from the equatorial parent bodies considered here.

If one of the dust grain's natural frequencies matches a characteristic spatial frequency of the rotating multipolar magnetic field, the particle experiences a Lorentz resonance (Burns et al. 1985; Hamilton 1994; Hamilton and Burns 1993a; Schaffer and Burns 1987, 1992). Lorentz resonances behave similarly to their gravitational counterparts and can have a dramatic effect on a dust grain's orbit, exciting large radial and/or vertical motions. These resonances have been primarily studied in the Kepler limit appropriate for the micron-sized particles seen in the dusty rings of Jupiter. In the idealized problem that we address in this chapter, with an axisymmetric magnetic dipole, Lorentz resonances

cannot occur.

Variations in a dust grain's charge can also alter its trajectory over surprisingly rapid timescales. Gradients in the plasma properties, including density, temperature and even composition affect the equilibrium potential of a grain by altering the direct electron and ion currents. This can result in resonant charge variation with gyrophase, causing radial drift. Working in the Lorentz limit, Northrop and Hill (1983a) noted that with large radial excursions, the grain's speed through the plasma can vary significantly with gyrophase, leading to enhanced charging at one extremity. A similar effect occurs in the Kepler limit where resonant charge variation can cause a dramatic evolution in the orbital elements of a dust grain (Burns and Schaffer 1989). Northrop et al. (1989) found that the varying charge has a time lag that depends on the plasma density and grain capacitance. These time lags can cause grains to drift towards or away from synchronous orbit depending on the grain speed, and on any radial temperature or density gradients in the plasma. Schaffer and Burns (1995) explored the effects of stochastic charging on extremely small grains, where the discrete nature of charge cannot be ignored. They found that Lorentz resonances are robust enough to survive even for small dust grains with only a few electric charges.

The dynamics of time-variable charging may play an important role in determining the structure of Saturn's E ring (Juhász and Horányi 2004) and Jupiter's main ring and halo (Horányi and Juhász 2010). Another example of charge variation occurs when the insolation of a dust grain is interrupted during transit through the planetary shadow. This induces a variation in charge that resonates with the grain's orbital frequency (Horányi and Burns 1991). Hamilton and Krüger (2008) found that this shadow resonance excites radial motions while normally leaving vertical structure unaltered. This effect can explain the appearance of the faint outward extension of Jupiter's Thebe ring, and the properties of its dust population sampled by the Galileo dust detector (Krüger et al. 2009).

3.1.3 Research Goals

In this chapter, we consider the orbits of charged grains launched in planetary ring systems. Our aim is to explore the boundaries between stable and unstable orbits in aligned and centered dipolar magnetic fields. Dipolar fields have the advantage of being analytically tractable while still capturing most of the important physics. Under what conditions are grains unstable to vertical perturbations? Which grains escape the planet as high speed dust streams? And which grains will strike the planet after launch? All of these instabilities depend on the launch distance of the grain and its charge-to-mass ratio. We first explore grain trajectories numerically and then derive analytical solutions for the stability boundaries that we find.

There are several standard choices for expressing the ratio of the Lorentz and gravitational forces. The charge-to-mass ratio q/m in C/kg (Northrop and Hill 1982) or in stat-Coulomb/g (Mitchell et al. 2003) may be the most straightforward, but it is cumbersome. For this reason, converting to the grain potential measured in Volts, which is constant for different-sized dust grains, is a common choice (Howard et al. 2000; Mendis et al. 1982; Mitchell et al. 2003; Schaffer and Burns 1994). Yet another option is to express the charge-to-mass ratio in terms of frequencies associated with the primary motions of the grain, such as the gyrofrequency, orbital frequency and the spin frequency of the planet (*eg*. Mendis et al. 1982; Mitchell et al. 2003).

We choose a related path, namely to fold q/m and key planetary parameters into a single dimensionless parameter L_* following Hamilton (1993a). Consider the Lorentz force in a rotating magnetic field:

$$\vec{F_B} = \frac{q}{c}(\vec{v} - \vec{\Omega}_p \times \vec{r}) \times \vec{B}, \tag{3.1}$$

where c is the speed of light, $\vec{r}$ and $\vec{v}$ are the grain's position and velocity in the inertial frame, $\vec{\Omega}_p$ is the spin vector of the planet, and $\vec{B}$ is the magnetic field rotating

with the planet. Note that Eq. 3.1 differs from Eq. 2.5 by introducing the motion of the magnetic field itself in inertial space. The second component of Eq. 3.1 is $q\vec{E}$, where $\vec{E} = -\frac{1}{c}(\vec{\Omega_p} \times \vec{r}) \times \vec{B}$ is the so-called co-rotational electric field. In Chapter 2, we saw that a rotating magnetic field is equivalent to a stationary magnetic field in the rotating frame with a radial electric field, which acts to accelerate charged grains across magnetic field lines. Since a dipolar magnetic field obeys $\vec{B} = -g_{10}R_p^3/r^3\hat{z}$ in the midplane (with g_{10} the magnetic field strength at the planet's equator), $\vec{E}$, like gravity, is proportional to $1/r^2$ there (Hamilton 1993a). Thus the ratio of the electric force to gravity is both independent of distance and dimensionless:

$$L_* = \frac{qg_{10}R_p^3\Omega_p}{GM_pmc}. \tag{3.2}$$

Here, M_p is the planetary mass, m is the dust grain mass and G is the gravitational constant. Note that the sign of L_* depends on the product of two signed quantities, q and g_{10}. For all of the giant planets, the magnetic north pole is in the northern hemisphere, and $g_{10} > 0$. However, for the Earth at the current epoch, $g_{10} < 0$ and the magnetic and geographic poles are in opposite hemispheres.

We have made a slight notational change $L \rightarrow L_*$ from Hamilton (1993a), Hamilton (1993b), to avoid confusion with the L-shell of magnetospheric physics. Choosing L_* as an independent variable takes the place of assuming a particular electric potential, grain size and grain density. We focus our study primarily on Jupiter, the planet with by far the strongest magnetic field, but also apply our results to Saturn and to the Earth.

3.2 Numerical Simulations

Approximating Jupiter's magnetic field as an aligned dipole by including just $g_{10} = 4.218$ Gauss (Dessler 1983), we have tested the stability of dust grain orbits over a range of grain sizes and launch distances both inside and outside synchronous orbit. We used a

Runge-Kutta fourth-order integrator with a step-size chosen to satisfy a minimum accuracy threshold, set at one part in 10^{10}. We launched grains at the local Kepler speed with a small initial latitude of $\lambda = 0.01^\circ$. This tiny nominal value ensures a launch close to the midplane, whilst avoiding any potential numerical problems from launching a grain precisely at $\lambda = 0$. Non-zero launch speeds from the parent particle do have a small effect on the stability boundaries, one that we will explore in more depth in a Chapter 4.

Our models treat the grain charge as constant and neglect the gravitational effect of Jupiter's oblateness (the J_2 term) and other higher-order components of the gravitational field, and radiation pressure. For both negative and positive grains, we ran simulations for a grid of 80 values of L_* and 100 launch distances (r_L). The charge-to-mass ratio spans four decades from the Lorentz regime where EM dominates ($|L_*| >> 1$), to the Kepler regime where gravity reigns ($|L_*| << 1$). The range of launch distances extends from the planetary surface to well beyond the synchronous orbital distance (R_{syn}), and trajectories were followed for up to 0.1 years. With some experimentation, we determined that all relevant dynamical timescales are < 0.1 years and that for longer integration times, the appearance of our stability plots does not change significantly.

In Fig. 3.1 we plot the fate of 8000 negative and 8000 positive dust grains and find complex regions of instability. The negatively-charged dust grains in Fig. 3.1a display only vertical instability at moderate to high L_* and inside R_{syn}. Some are bound by high latitude restoring forces (locally unstable, light grey) whilst others crash into the planet at high latitude (both locally and globally unstable, darker grey). To separate these globally stable grains from locally stable ones, we choose a latitude threshold at $\lambda_m = 5^\circ$. Although 5° is a small latitude, it is far greater than the launch latitude of 0.01°; any grains excited beyond λ_m are clearly locally unstable, and we determined that our results were fairly insensitive to actual value of λ_m.

Northrop and Hill (1982) derived a boundary for the threshold between locally sta-

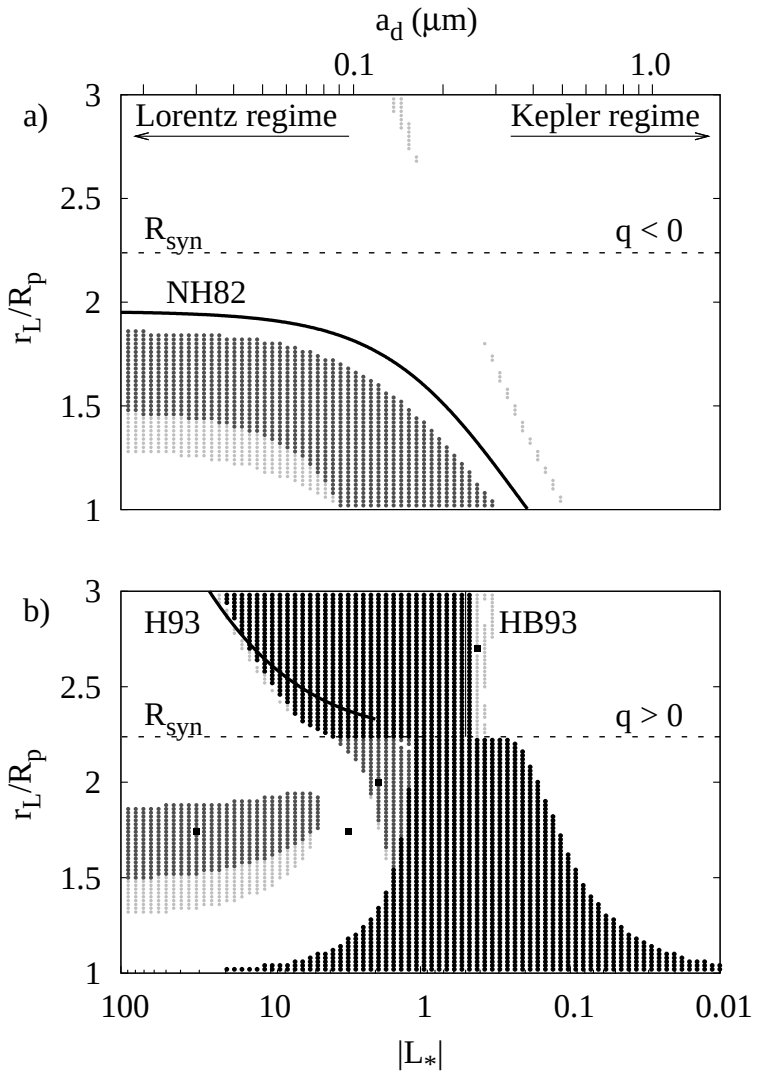

Figure 3.1: Stability of Kepler-launched **a)** (negative) and **b)** (positive) dust grains at Jupiter. We model the planet with a spherically-symmetric gravitational field, and a centered and aligned dipolar magnetic field. All grains were launched with an initial latitude of $\lambda = 0.01^\circ$ and followed for 0.1 years. The horizontal dashed line in both panels denotes the synchronous orbital distance at $R_{syn} = 2.24R_p$. The grain radii (a_d) in microns along the upper axis are calculated assuming a density of 1 g cm^3 and an electric potential of ± 5 V so that $|L_*| = 0.0284/a_d^2$. Dust grains in the white regions and lightest grey areas survive the full 0.1 years, with the latter reaching latitudes λ in excess of 5°. Grains in the moderately-grey areas are vertically unstable and strike the planet, also at high latitudes ($\lambda > 5^\circ$). The darkest regions, seen only in panel **b**, are radially unstable grains that crash into the planet (those with launch radius $r_L < R_{syn}$), or escape to beyond $r_{esc} = 30R_p$ (from $r_L > R_{syn}$) at latitudes less than 5°. We overplot three analytically-derived stability boundaries, obtained by Northrop and Hill (1982) for negative grains, by Horányi et al. (1993b) for small positive grains, and by Hamilton and Burns (1993b) for large positive grains. Each point on the plot is a trajectory, four of which (marked by filled squares), are illustrated in detail in Figs. 3.2 to 3.5.

ble and unstable trajectories for negatively-charged dust and found that grains launched within a certain distance should leave the equatorial plane (NH82 curve in Fig. 3.1a). In the Lorentz limit, the vertical instability allows grains to climb up local magnetic field lines into regions of stronger magnetic field, while for smaller L_* the path taken by these grains follows the lines of a pseudo-magnetic field, which includes the effects of planetary rotation (Northrop and Hill 1982). The Northrop curve however, is not a good match to our data, which reveal additional stable orbits (white areas) immediately inside this boundary and also close to the planetary surface. These differences arise from the fact that Northrop and Hill (1982) assumed that grains are launched at their equilibrium circular speeds, which differ from the circular speeds of parent bodies when $L_* \neq 0$. Conversely, we launch our grains at $v = \sqrt{GM_p/r}$, the circular speed of the parent body, which is appropriate for debris produced by cratering impacts into these objects. In section 3.5, we develop a vertical stability criterion appropriate for our launch conditions. (In Chapter 4, we shall relax our assumption on launch conditions and test non-zero launch speeds from parent bodies for impact ejecta.)

The situation for positive grains is quite different. Figure 3.1b shows a less extensive region of vertical instability than Fig. 3.1a, and one that is not active close to Jupiter. More dramatic, however, are the two regions of radial instability (darkest grey areas), separated by the synchronous orbital distance. Grains inside R_{syn} are driven to strike Jupiter, while those outside escape the planet. If grains move beyond $r_{esc} = 30R_p$, the inner magnetosphere, we consider them to have escaped. As with λ_m, our numerical results are fairly insensitive to the exact value chosen for r_{esc}, so long as it is large.

To characterize the individual trajectories that make up Fig. 3.1, we explore a few examples in detail, focusing on the positively-charged dust grains and proceeding from smaller to larger grains. Figure 3.2 shows the trajectory of a dust grain that becomes vertically unstable and crashes into the planet at high latitude. These smallest grains

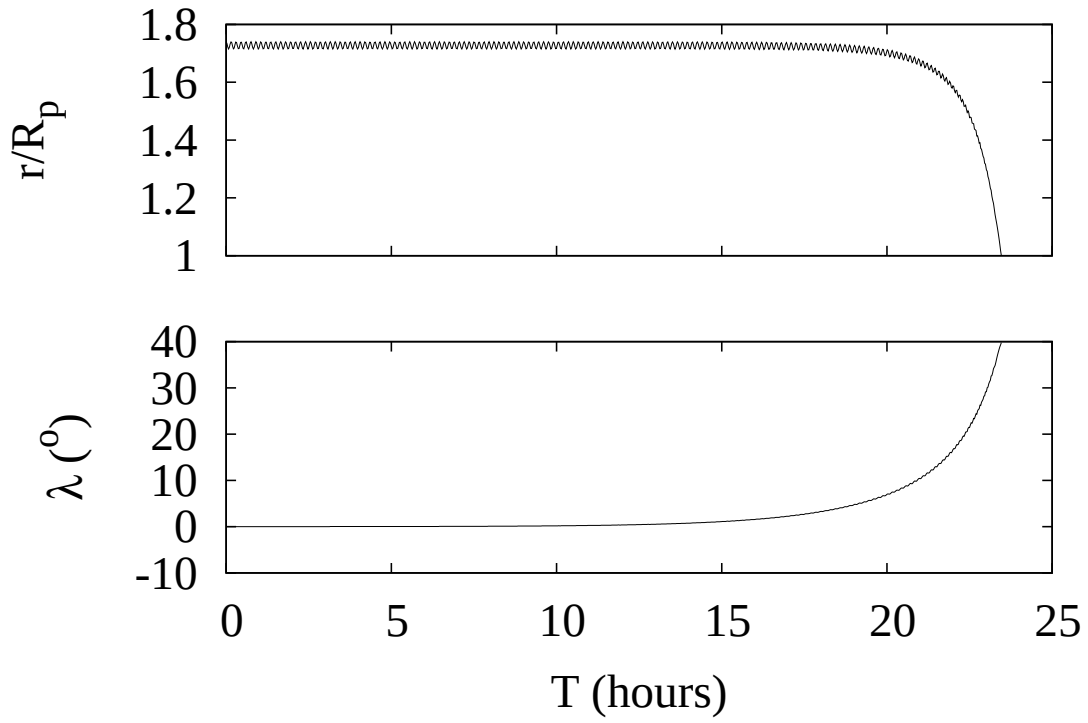

Figure 3.2: The trajectory of a positively-charged grain orbiting Jupiter after launch at $r_L = 1.74R_p$, with $L_* = 31.31$ ($a_d = 0.03\,\mu$m). We plot the scaled distance and latitude of the dust grain against time. The small, rapid radial gyrations are just visible in the upper plot. The dust grain is vertically unstable on a much longer timescale and ultimately crashes into the planet. This trajectory is represented by the left-most filled square in Fig. 3.1b.

spiral up magnetic field lines, which for a dipole are given by $r/\cos^2\lambda = r_L$ (Eq. 2.3); collision with the planet or reflection from a high latitude mirror point typically occurs within a few tens of hours. By contrast, Fig. 3.3 shows an electromagnetically-dominated grain that remains stable at low latitude.

A more subtle interplay between radial and vertical motions is illustrated in Fig. 3.4. This grain is outside the radial instability region in which grains collide with the planet at low latitude (darkest grey). Instead, large radial motions lead to instability in the vertical direction, and ultimately, the grain strikes the planet at high latitude. Notice the two white dots near ($L_* = 1.34$, $r_L/R_p = 2.2$) in Fig. 3.1b, signifying grains that survive the full 0.1

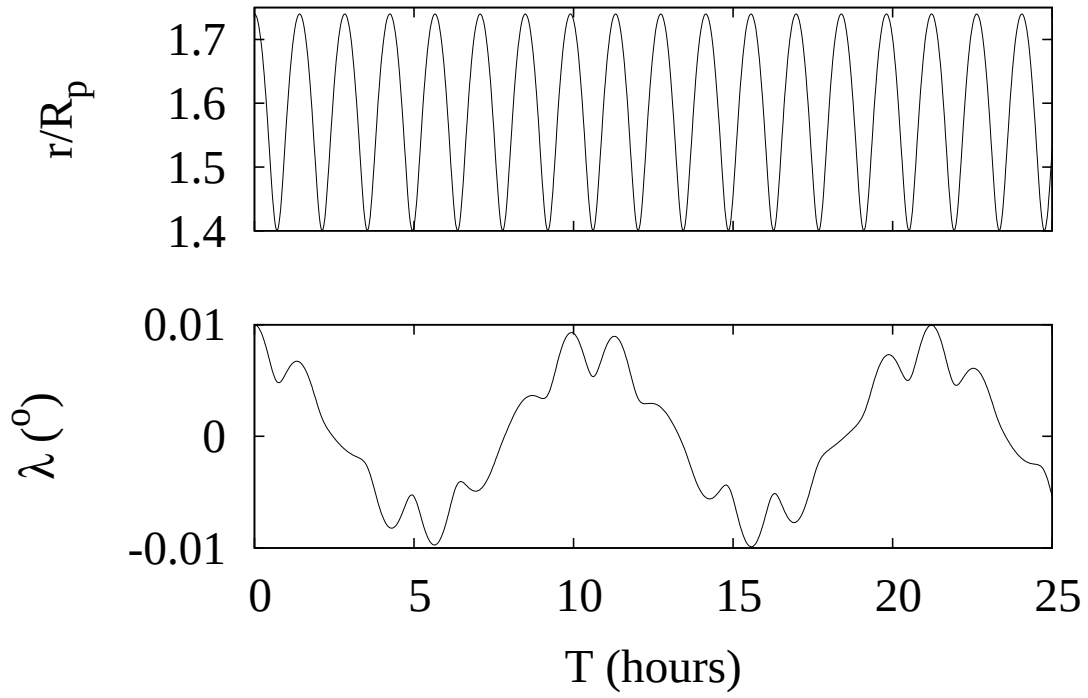

Figure 3.3: The trajectory of a stable positively-charged grain orbiting Jupiter after launch at $r_L = 1.74R_p$, with $L_* = 3.04$ ($a_d = 0.097$ μm). The grain undergoes radial oscillations much larger than in Fig. 3.2 but its latitude remains low. Here the bounce period is ~ 7 times longer than the gyroperiod.

year integration. These trajectories are indeed stable (for at least 100 years) and, as the effect is much more prominent for the Earth, we discuss it in more detail in section 6.

Finally, Fig. 3.5 shows a dust grain just inside the Hamilton and Burns (1993b) $L_* = \frac{1}{2}$ stability limit. Although the dust grain does not escape, the non-linearity of its radial oscillation is large enough to excite substantial vertical motions.

A glance at Fig. 3.1 shows that most stability boundaries are unexplained. The Northrop and Hill (1982) vertical stability boundary does not match the numerical data especially well, and only applies to negative grains. For positive grains, Horányi et al. (1993a) provided an approximate criterion for radial escape, which they applied far from synchronous orbit near Io. Their criterion is based on a comparison between the radius of gyromotion

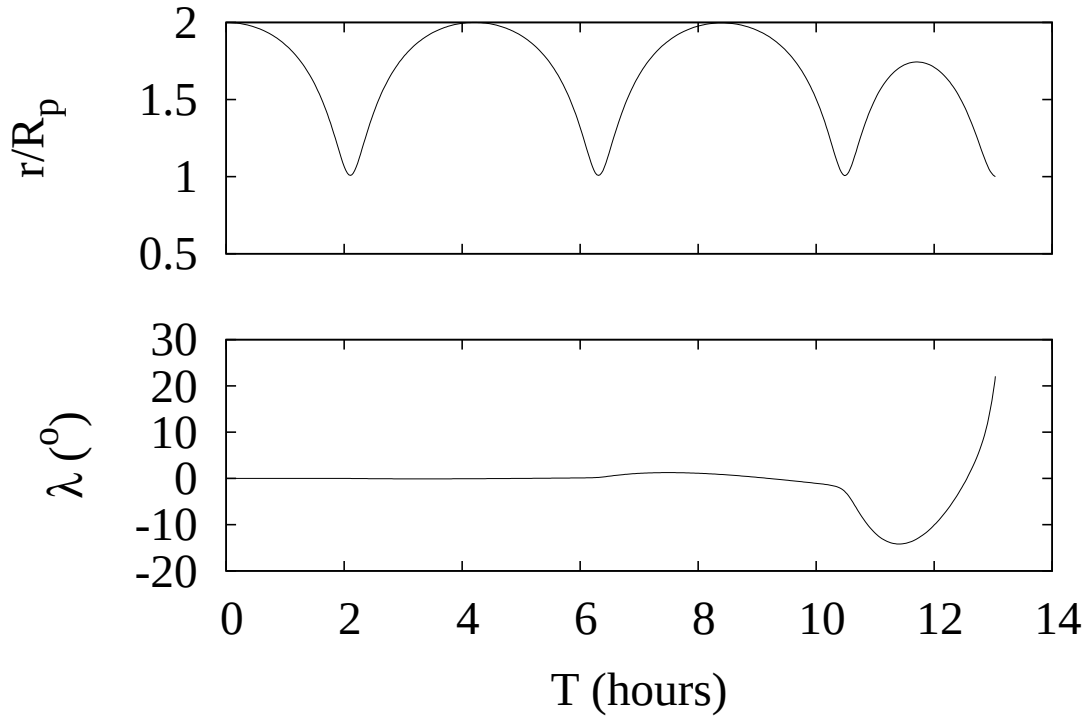

Figure 3.4: The trajectory of a positive grain inside R_{syn} ($r_L = 2.0R_p, L_* = 1.908$, $a_d = 0.122\ \mu$m). Here, unlike Fig. 3.3, large radial motions ultimately excite vertical motions, forcing the trajectory to end with a collision at the planetary surface after just a few orbits.

r_g, and the length scale over which the magnetic field changes substantially, namely where $|B/(r_g \nabla B)| \approx 10$, with the gyroradius calculated in the Lorentz limit. Although not intended for use near synchronous orbit where $r_g \to 0$, we nevertheless plot it on the left side of Fig. 3.1b. Finally, the Hamilton and Burns (1993b) $L_* = \frac{1}{2}$ limit, derived from an energy argument, is a good match to the largest escaping grains. There is however, no analytical model for the broad class of grains that strike the planet. Accordingly, we seek to develop a unified theory that can cleanly determine all of these boundaries. We take up this task first for radial and then for vertical motions.

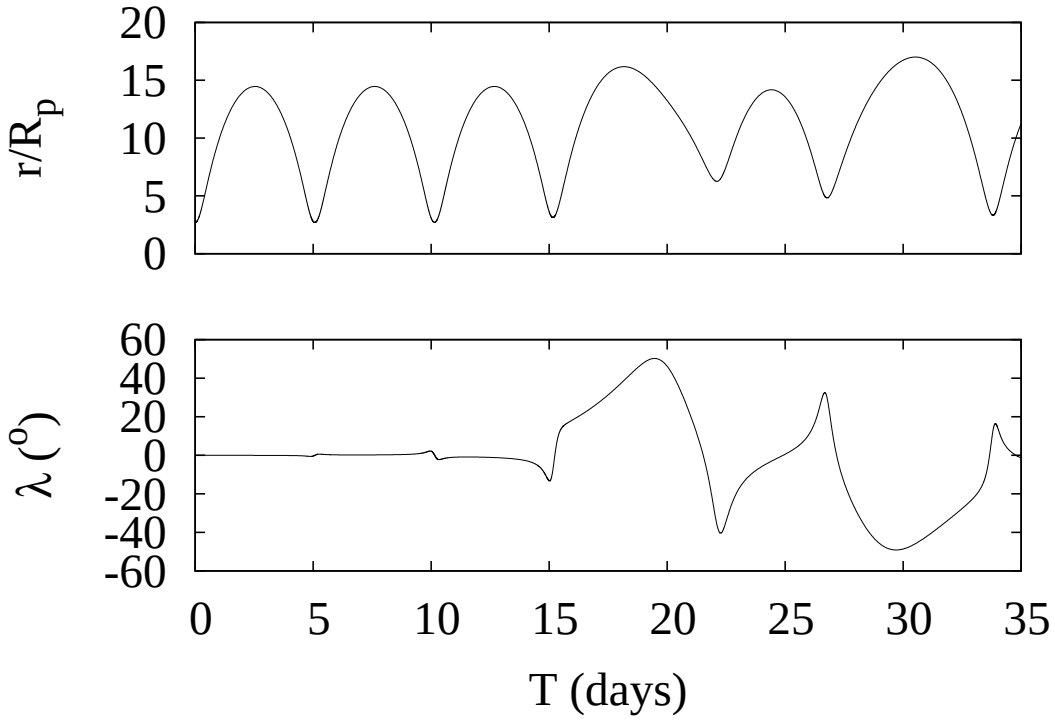

Figure 3.5: The trajectory of a positive grain outside R_{syn} ($r_L = 2.7R_p, L_* = 0.419$, $a_d = 0.26$ μm). As in Fig. 3.4, large radial oscillations eventually excite large vertical oscillations. Since the dust grain has $L_* < \frac{1}{2}$, it is energetically required to remain bound (Hamilton and Burns 1993b). Here T is measured in Earth days.

3.3 Local Radial Stability Analysis

Consider a centered magnetic dipole field that rotates with frequency Ω_p around a vertical axis aligned in the z-direction. Northrop and Hill (1982) derived the Hamiltonian for a charged dust grain in the rotating frame in cylindrical coordinates:

$$H = U(\rho, z) + \frac{\dot{\rho}^2 + \dot{z}^2}{2} \tag{3.3}$$

where $\dot{\rho}$ and $\dot{z}$ are the radial and vertical velocity components. The potential is given by

$$U(\rho, z) = \frac{1}{2\rho^2}\left(\frac{p_\phi}{m} - \frac{GM_p\rho^2 L_*}{\Omega_p r^3}\right)^2 + \frac{GM_p}{r}\left(\frac{L_*\rho^2}{r^2} - 1\right) \tag{3.4}$$

where the spherical radius r satisfies $r^2 = \rho^2 + z^2$ (Howard et al. 2000; Mitchell et al. 2003; Northrop and Hill 1982; Schaffer and Burns 1994). Equation 3.4 is the sum of two

energetic components: first the azimuthal specific kinetic energy, which can be expressed as a function of r using the conservation of angular momentum, and then the potential associated with both the corotational electric field and gravity. Note that we have chosen the zero of our potential to be approached as $\rho \to \infty$. Because $U(\rho, z)$ is independent of ϕ, the azimuthal coordinate, the canonical conjugate momentum p_ϕ is a constant of the motion. For our launch condition from a large parent body on a circular orbit at $r = r_L$:

$$\frac{p_\phi}{m} = r_L^2(n_L + \Omega_{gL}) \tag{3.5}$$

(Schaffer and Burns 1994), where n_L and Ω_{gL} are the Kepler frequency and gyrofrequency evaluated at the launch distance r_L:

$$n_L = \sqrt{\frac{GM}{r_L^3}}, \tag{3.6}$$

and

$$\Omega_{gL} = \frac{qB}{mc} = \frac{n_L^2 L_*}{\Omega_p}. \tag{3.7}$$

Notice that in the gravity limit ($L_* \to 0$), Eq. 3.5 reduces to $r_L^2 n_L$, the specific angular momentum about the planet, while in the Lorentz limit ($L_* \to \pm\infty$), it is $r_L^2 \Omega_{gL}$, the specific angular momentum about the center of gyromotion that moves with the magnetic field.

If the motion of the particle is radially stable, it exhibits epicyclic motion about an equilibrium point determined from Eq. 3.4. The existence of equilibrium points requires that $\frac{\partial U}{\partial \rho} = \frac{\partial U}{\partial z} = 0$, both in the equatorial plane (Northrop and Hill 1982) and at high latitudes (Howard et al. 2000, 1999). The local stability of the equilibrium points, defined as whether oscillations about these points remain small, is then determined by considering the second derivatives of the potential. Given our launch condition, we focus on the equatorial equilibrium points which are of greatest interest. For these, $\left.\frac{\partial^2 U}{\partial \rho \partial z}\right|_{\rho=\rho_c, z=0} = 0$, $r \to \rho$, and radial and vertical motions are initially decoupled and may be considered separately (Mitchell et al. 2003; Northrop and Hill 1982).

The equilibrium point is the guiding center of epicyclic motion. Grains launched at the guiding center have canonical conjugate momenta that are different from our Kepler-launched grains: namely, $\frac{p_\phi}{m} = \rho_c^2(\omega_c + \Omega_{gc})$, where ω_c is the orbital frequency of a grain at the guiding center, Ω_{gc} is the gyrofrequency at the guiding center, and ρ_c is the guiding center distance in the equatorial plane. A local radial stability analysis is most relevant for our Kepler-launched grains if an equilibrium point is not too distant. Accordingly, it is important to distinguish between quantities evaluated at the Kepler launch position and those determined at the guiding center. Here and throughout, we use the subscript c for the guiding center and the subscript L for the launch position. At the equilibrium point, $\frac{\partial U}{\partial \rho}\Big|_{\rho=\rho_c, z=0} = 0$, which evaluates to:

$$\omega_c^2 \rho_c + \frac{GM_p L_*}{\rho_c^2}\left(1 - \frac{\omega_c}{\Omega_p}\right) - \frac{GM_p}{\rho_c^2} = 0. \tag{3.8}$$

Physically, Eq. 3.8 just implies a balance of forces in the rotating frame, whereby the centrifugal force, the Lorentz force and gravity sum to zero. We solve Eq. 3.8 for the angular speed of the guiding center ω_c, and find two real roots for $L_* < 1$, which includes all negative charges. For $L_* > 1$ conversely, two equilibrium points exist only if

$$\frac{\rho_c^3}{R_{syn}^3} \leq \frac{L_*^2}{4(L_* - 1)}. \tag{3.9}$$

Two equilibria always exist inside R_{syn} and everywhere for $L_* >> 1$ and $L_* << 1$. There are no equilibrium points in a region starting at ($L_* = 2$, $\rho_c = R_{syn}$) in Fig. 3.1b, and opening upward to include an increasing range of L_* values for increasing distance ρ_c. In this region, with no equilibrium, grains are guaranteed to escape. Not surprisingly, this region is fully contained within the unstable portion of Fig. 3.1b (darkest grey region outside R_{syn}). The existence of an equilibrium point, therefore, is a necessary prerequisite for stability.

Additional instability in Fig. 3.1b comes from two sources: i) the intrinsic instability of the equilibrium point, if it exists, and ii) large amplitude motions about a locally stable

equilibrium point. Large oscillations are beyond the scope of a local stability analysis and so we focus on small amplitude radial motion near an equilibrium point, which takes the form

$$\ddot{\rho} + \frac{\partial^2 U}{\partial \rho^2}\rho = 0. \tag{3.10}$$

Small radial motions are stable when $\frac{\partial^2 U}{\partial \rho^2}\Big|_{\rho=\rho_c, z=0} = \kappa_c^2 > 0$, which, from Eq. 3.4 can be written as:

$$\kappa_c^2 = \omega_c^2 - 4\omega_c\Omega_{gc} + \Omega_{gc}^2 \tag{3.11}$$

(Mendis et al. 1982; Northrop and Hill 1982; Mitchell *et al.* 2003). Note here that the gyrofrequency Ω_{gc} is evaluated at the guiding center, and is given by Eq. 3.7 with the subscript change: $L \rightarrow c$. The epicyclic frequency κ_c reduces to the Kepler orbital frequency n_c at the guiding center r_c in the gravity limit, and to the gyrofrequency Ω_{gc} in the Lorentz limit. Radial excursions in both of these cases are small and, since $\kappa_c^2 > 0$, are guaranteed to be stable.

Radial motions are also initially small near synchronous orbit where electromagnetic forces are very weak (Eq. 3.1), and so a local stability analysis is also applicable. At synchronous orbit, $\omega_c = n_c = \Omega_p$ and Eq. 3.11 reduces to $\kappa_c^2 = \Omega_p^2(1 - 4L_* + L_*^2)$, which is positive for small or large L_*. For $2 - \sqrt{3} < L_* < 2 + \sqrt{3}$, however, Eq. 3.10 shows that radial motions near synchronous orbit are locally unstable. Comparing this analysis with Fig. 3.1b, we see that all orbits with $r_L \sim R_{syn}$ that are locally stable are, not surprisingly, also globally stable. The converse, however, does not hold: although most of the locally unstable orbits are also globally unstable, some are in fact globally stable (*e.g.* $L_* < \frac{1}{2}$ just outside R_{syn} in Fig. 3.1b). In conclusion, the local analysis is consistent with our numerical experiments but cannot fully account for our stability boundaries. Accordingly, we turn to a global analysis, pausing first to put the potential of Eq. 3.4 into a more useful form and to derive the radius of gyration, r_g.

3.3.1 Radius of Gyration

With our launch condition, grains are often far enough from an equilibrium point that the small oscillation approximation of Eq. 3.10 is invalid. This is particularly true far from R_{syn} and for $L_* \approx 1$. Returning to the effective potential of Eq. 3.4 with the canonical conjugate momentum determined by launching the grain at the Kepler speed (Eq. 3.5), and limiting our attention to planar orbits for which $z = 0$ and $r = \rho$, we express the potential as a quartic polynomial function of distance and a quadratic function of L_*:

$$U(r, L_*) = \frac{GM_p}{r_L}\left(A\frac{r_L^4}{r^4} + B\frac{r_L^3}{r^3} + C\frac{r_L^2}{r^2} + D\frac{r_L}{r}\right), \tag{3.12}$$

with dimensionless coefficients

$$\begin{aligned} A &= \frac{n_L^2 L_*^2}{2\Omega_p^2} \\ B &= -\frac{n_L L_*}{\Omega_p}\left(\frac{n_L L_*}{\Omega_p} + 1\right) \\ C &= \frac{1}{2}\left(\frac{n_L L_*}{\Omega_p} + 1\right)^2 \\ D &= L_* - 1. \end{aligned}$$

To determine the radius of the epicycles (r_g) induced by a Kepler launch, we follow the procedure of Schaffer and Burns (1994), and solve for the distance to the potential minimum where $\left.\frac{\partial U}{\partial r}\right|_{\rho=\rho_c, z=0} = 0$. Note that this is only valid to first order in small quantities, since we are effectively assuming that the potential is symmetric about the equilibrium point. Evaluating the derivative, multiplying by r^5, setting $r = r_L + r_g$, and assuming $r_g << r_L$, we obtain the epicycle radius for a grain launched at r_L in terms of parameters known at launch:

$$r_g = \frac{r_L(\Omega_p - n_L)\Omega_{gL}}{\Omega_{gL}^2 - \Omega_{gL}(3\Omega_p + n_L) + n_L^2}. \tag{3.13}$$

In this limit, the radial range of motion of a dust grain is simply $2|r_g|$, and the grain reaches a turning point at $r_t = r_L + 2r_g$. Note the sign conventions used here; r_g and Ω_{gL}

may be either positive or negative. Equation 3.13 corrects a sign error in Schaffer and Burns (1994) which led to an artificial disagreement between the numerical and analytical model in their Fig. 6. Equation 3.13, by contrast, shows excellent agreement with our numerical data for negative grains (Fig. 3.6a). The peak in Fig. 3.6a, for oscillations towards synchronous orbit, occurs at

$$r_g = \frac{r_L}{3}\left(\frac{n_L - \Omega_p}{n_L + \Omega_p}\right),\ L_* = -\frac{\Omega_p}{n_L}. \tag{3.14}$$

Equation 3.14 predicts that grains with $L_* = -\frac{\Omega_p}{n_L}$ launched near R_{syn} reach about halfway to the synchronous orbital distance, in agreement with Fig. 3.6a.

For the positive grains, Eq. 3.13 gives the proper radial range about stable local minima in both the Lorentz limit and in the Kepler limit (Fig. 3.6b). At critical values of L_*, however, $|r_g| \to \infty$ and the assumptions under which Eq. 3.13 was derived are violated. This is readily apparent in the decreasing quality of the match between the theory and the data for intermediate-sized grains in Fig. 3.6b. Note that this is the same region where Mitchell et al. (2003) find large non-elliptical gyrations. Nevertheless, the relatively close agreement between theory and numerical data in Fig. 3.6 confirms that the epicyclic model is usually a good assumption in planetary magnetospheres.

3.4 Global Radial Stability Analysis

Our local radial stability analysis makes a number of successful predictions, but cannot fully account for the boundaries in Fig. 3.1b, primarily because of the large radial excursions experienced by the positive grains. Nevertheless, the quartic potential within the equatorial plane given by Eq. 3.12 contains all the information necessary to determine which grains strike the planet and which escape into interplanetary space.

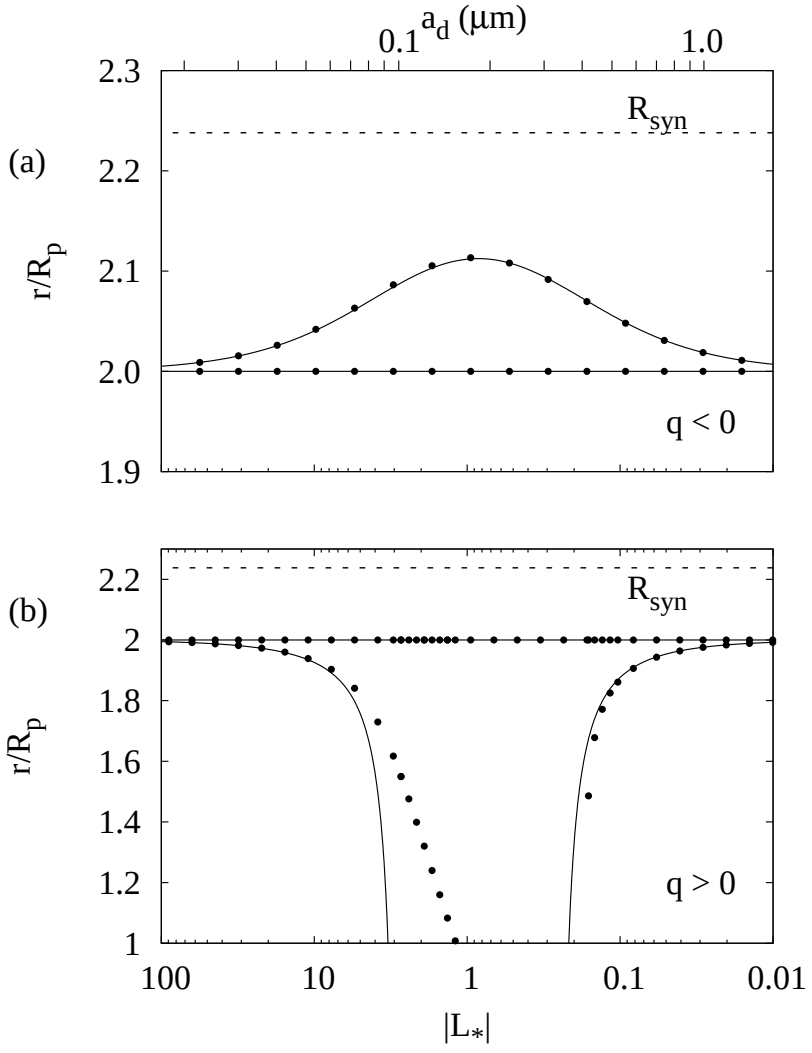

Figure 3.6: The radial range of **(a)** negative and **(b)** positive grains launched azimuthally with the Kepler speed $v = \sqrt{GM/r_L}$ at $2.0R_p$. Both numerical data (points) and the analytical results (curves from Eq. 3.13) are included. The total radial excursion is twice the epicyclic radius r_g.

3.4.1 Escaping Grains

Close to the planet, the A/r^4 term of Eq. 3.12 dominates the potential, and $U(r \to 0, L_*) \to +\infty$, while for the distant particles we have $U(r \to \infty, L_*) \to 0$. Accordingly, the quartic potential can have at most three stationary points (one local maximum and two local minima). Setting $r = r_L$ in Eq. 3.12 gives a simple form for the launch potential

$$U(r_L, L_*) = \frac{GM_p}{r_L}\left(L_* - \frac{1}{2}\right). \tag{3.15}$$

Energetically, a particle is able to escape if $U(r_L, L_*) > U(r \to \infty, L_*) = 0$ and we immediately recover the $L_* < 1/2$ stability criterion of Hamilton and Burns (1993b). Note that only positive grains can escape from a dipolar magnetic field with $g_{10} > 0$ and that, in principle, grains with $L_* > \frac{1}{2}$ at all launch distances, both inside and outside R_{syn} are energetically able to escape. Whether or not they do so depends on the form of $U(r, L_*)$, in particular, on the possible existence of an exterior potential maximum with $U(r_{peak}, L_*) > U(r_L, L_*)$.

Analysis of Eq. 3.12 shows that the potential prevents all grains launched with Kepler initial conditions from crossing R_{syn}. Positive grains gyrate away from R_{syn}, while negative grains cannot reach R_{syn} (Eq. 3.13, Fig. 3.6).

Outside R_{syn}, for all moderately charged grains $U(r, L_*)$ decreases monotonically for $L_* \gtrsim \frac{1}{2}$. Thus $L_* = \frac{1}{2}$ is a global stability boundary and it matches Fig. 3.1b very well. For larger L_* (smaller grains), the topography of the potential includes local extrema, as illustrated in Fig. 3.7. For these trajectories, stability is determined by the height of the distant peak in the potential. For $L_* \sim 1$ no such peak exists. For larger L_*, however, the radial potential decreases with distance from r_L, then increases to the distant peak, and finally declines to zero as $r \to \infty$.

Consider the quartic equation $U(r, L_*) - U(r_L, L_*) = 0$, which by construction, has one root at $r = r_L$, and one root at a more distant turning point $r = r_t$. The critical quartic,

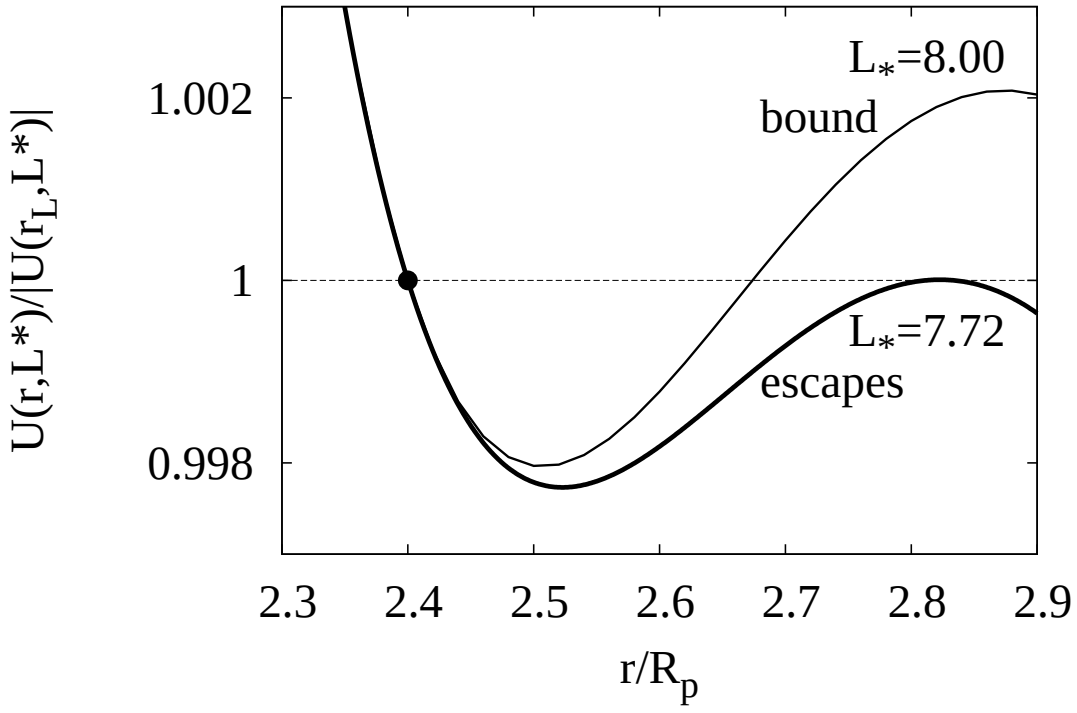

Figure 3.7: Potential wells for positive grains launched just outside Jupiter's synchronous orbit, at $r_L = 2.4R_p$, marked with a solid point. For $L_* = 8.00$ ($a_d = 0.0596\,\mu$m), a distant local maximum bounds the motions. If $L_* = 7.72$ ($a_d = 0.0607\,\mu$m) the distant peak in the potential is at the radial turning point, and the potential is equal to the launch potential; this is the stability threshold. For smaller L_*, the peak is lower and escape occurs.

where the turning point is also a local maximum (as in Fig. 3.7) has a double root at $r = r_t$. By factoring out $(r - r_L)$, and then differentiating with respect to r, we find a quadratic equation for the location of the turning point; r_t varies smoothly from $r_t = r_L$ at synchronous orbit to $r_t = \frac{3}{2} r_L$ for $r_L >> R_{syn}$. The stability boundary, $r_L(L_*)$ starts at $(r = R_{syn}, L_* = 2 + \sqrt{3})$ and asymptotes to

$$\frac{r_L}{R_{syn}} = \left(\frac{2L_*}{27}\right)^{\frac{1}{3}} \tag{3.16}$$

for $r_L >> R_{syn}$. Equation 3.16 for $r >> R_{syn}$ is a useful approximation for the boundary far from R_{syn}, which nicely compliments the exact value we have found at the synchronous orbital distance. The full solution for the boundary $r_L(L_*)$ is given by a rather messy

cubic equation and so we resort to numerical methods for its solution, which we plot on Fig. 3.9b.

3.4.2 Grains that Strike the Planet

Inside R_{syn}, the surface of the planet presents a physical boundary to radial motion. Particles that strike the atmosphere are slowed and removed from orbit. The potential at the planet's surface $U(\rho, z)$ varies with latitude, and so for simplicity, we restrict our attention to planar motions where Eq. 3.12 applies. Since, for positive grains in the equatorial plane, the potential declines as the grain moves inwards from its launch distance r_L, it can have at most one local maximum within r_L. There are thus two ways in which a grain can be prevented from striking the planet: i) the potential U at the surface is greater than the launch potential, or ii) a potential peak exists between the surface and the launch position and its value is greater than or equal to the launch potential. These two scenarios are illustrated in Fig. 3.8. For case i), the stability criterion is where $U(R_p, L_*) = U(r_L, L_*)$. Using Eq. 3.12, we find a quadratic expression in L_* that implies two boundaries:

$$\frac{n_L^2 r_L^2}{2\Omega_p^2 R_p^2}\left(\frac{r_L}{R_p} - 1\right) L_*^2 + \left(1 - \frac{n_L r_L^2}{\Omega_p R_p^2}\right) L_* + \frac{1}{2}\left(\frac{r_L}{R_p} - 1\right) = 0. \tag{3.17}$$

The two quadratic roots of Eq. 3.17, L_1 and L_2, may be obtained analytically and are plotted on Fig. 3.9b. The roots obey the simple expression

$$L_1 L_2 = \frac{r_L R_p^2}{R_{syn}^3} < 1. \tag{3.18}$$

Equation 3.18 conveniently highlights several features of the lower curves in Fig. 3.9b: The two curves marking the grains on the threshold of collision with the planet are centered on $L_* < 1$, as required by Eq. 3.18. In addition, for smaller r_L, the center of the instability shifts to smaller L_*, hence the left-most curve is steeper than the right-most. Finally, a planet with a larger R_{syn} (eg. the Earth) will have roots that shift to very low L_* near the planet.

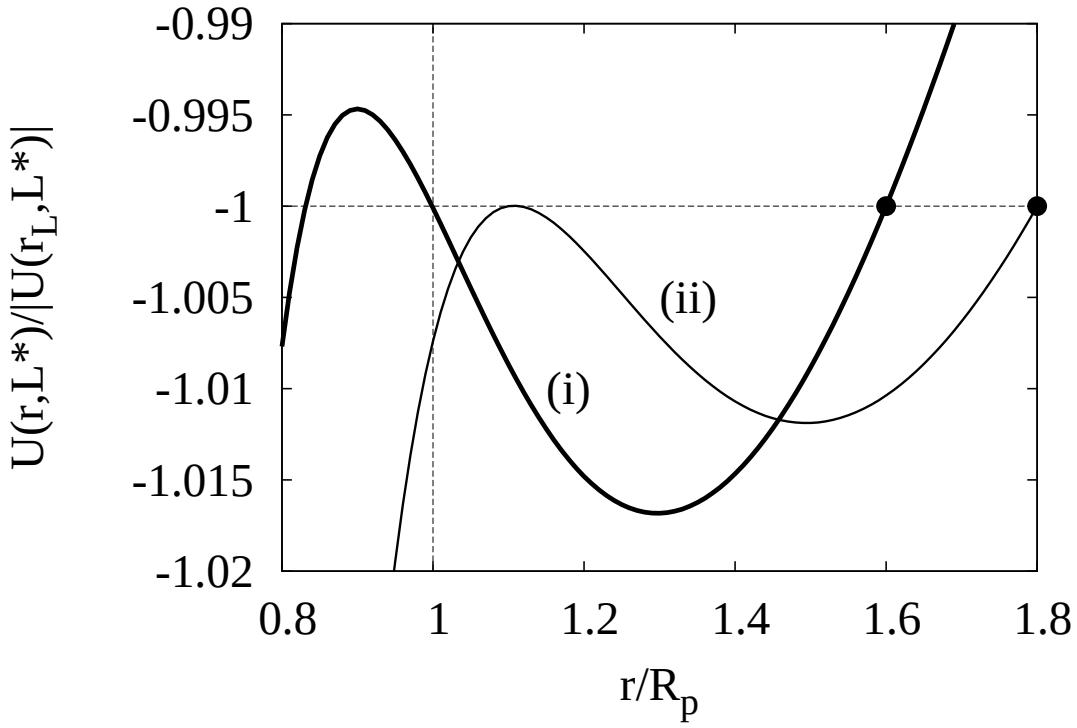

Figure 3.8: Potential wells for two planar trajectories launched from the solid points, which are inside Jupiter's synchronous orbit. Distances are in planetary radii, and the potential is scaled to the launch value. Curve (i) ($r_L = 1.6R_p, L_* = 0.0991$, $a_d = 0.53\mu$m) has a potential peak higher than the launch potential inside the planetary surface. Equating $U(r_L) = U(R_p)$ gives an analytic solution (Eq. 3.17) for the stability boundary in Fig. 3.9b. Curve (ii) ($r_L = 1.8R_p, L_* = 0.1277$, $a_d = 0.48\mu$m) has a potential peak outside the planetary surface. In this case, the stability boundary is best obtained numerically. Both grains depicted here are poised on the stability threshold.

The curves determined by Eq. 3.17 match our numerical data cleanly with two important exceptions. Firstly, because our method is only valid for grains that collide with the planet in the equatorial plane (recall our assumption $z = 0$), it misses the high latitude collisions near ($r_L = 2R_p$, $L_* = 2$) in Fig. 3.9b. All collisions exterior to the boundaries given by Eq. 3.17 necessarily involve substantial vertical motions, and the greyscale shading of Fig 3.9b shows that they do. Secondly, our criterion predicts instability for a small region near ($r_L = R_{syn}$, $L_* = 0.2$) that our numerical data show, in fact, are stable. These grains encounter a high peak, similar to curve (ii) in Fig. 3.8, that prevents them from

reaching the planetary surface. Thus $U(r_L, L_*) > U(R_p, L_*)$ is a necessary condition for radial instability in the equator plane, but it is not sufficient.

The additional requirement for instability is that $U(r_L, L_*) > U(r_{peak}, L_*)$, where r_{peak} is the location of an interior maximum. Just as for the escaping grains exterior to synchronous orbit, evaluation of this condition necessarily involves a cubic and a semi-analytic method. We find that no corrections to Eq. 3.18 are needed for the high L_* radial boundary and for all grains near the planet. Only for the right-most curve near R_{syn} is there a discrepancy. Our new curve is plotted in Fig 3.9b and it perfectly matches the numerical instability boundary. Although the stability curve in this region can only be obtained semi-analytically, the point at which it becomes necessary occurs when the potential maximum is located at the planetary surface; $\frac{\partial U}{\partial r}\Big|_{r=R_p} = 0$ and $U(r_L, L_*) = U(R_p, L_*)$. Evaluating these conditions, we find

$$L_* = \frac{(\frac{r_L}{R_p} - 1)^2}{\frac{R_{syn}^{3/2} r_L^{3/2}}{R_p^3} + 2 - \frac{3 r_L}{R_p}}. \tag{3.19}$$

For Jupiter, the critical point that satisfies both Eqs. 3.17 and 3.19 is at $L_* = 0.112, r_L = 1.694 R_p$ (solid point in Fig 3.9b). The stability curve meets $r_L = R_{syn}$ at $L_* = 2 - \sqrt{3}$, a result suggested by our local stability analysis of section 3.3. Note that our energy arguments yield analytic expressions both inside and outside R_{syn}. Arguments involving the location of potential maxima, conversely, require semi-analytic methods.

3.5 Local Vertical Stability Analysis

The stability of grains against vertical perturbations was first explored by Northrop and Hill (1982). In their model, a grain is launched on a circular orbit at the equilibrium orbital frequency ω_c in the potential of Eq. 3.4 so that there is no gyromotion around magnetic field lines. If the grain orbit at the equilibrium point is stable to vertical perturbations, the

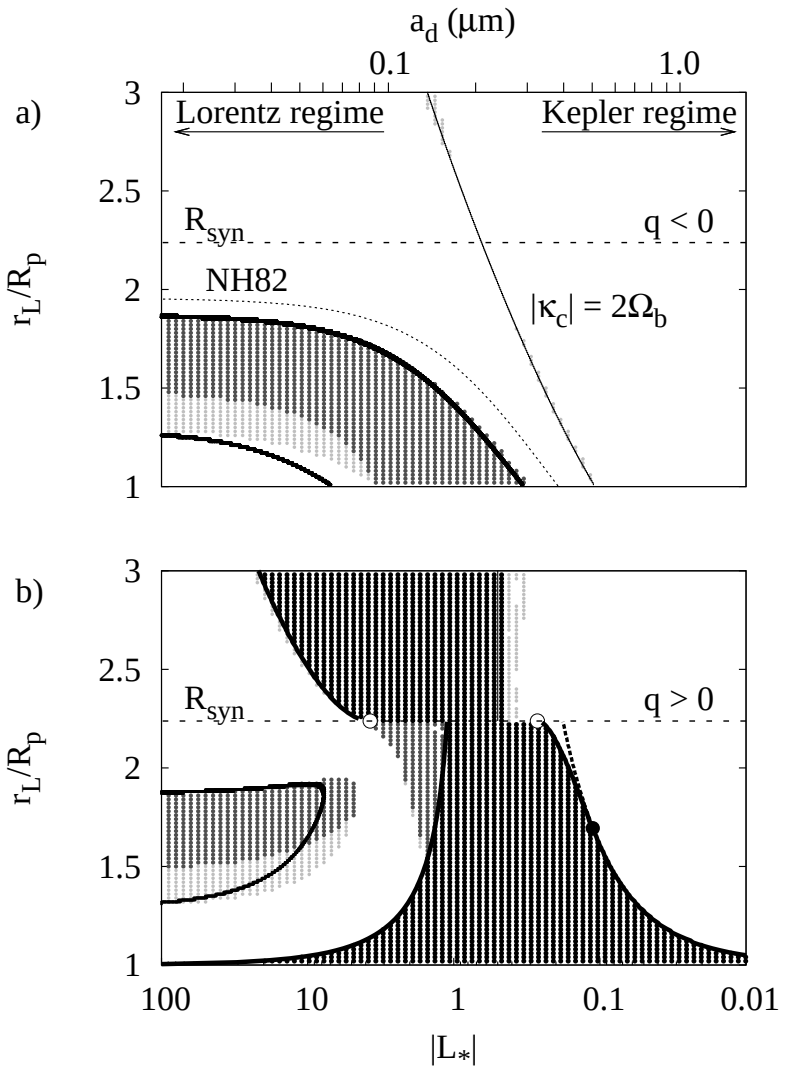

Figure 3.9: Our new analytic results (heavy solid lines) are plotted over the numerical data from Fig. 3.1. **a)** Northrop's solution (dotted line) is superseded by our two semianalytic boundaries where $\Omega_b^2 = 0$ from Eq. 3.29. The new boundaries are a significantly better fit to the data and indicate an inner stability zone. The $|\kappa_c| = 2\Omega_b$ curve indicates the 2:1 resonance between the epicyclic and the vertical bounce frequencies; it matches the data points well. **b)** We extend our vertical stability boundary to positive grains. The radial stability boundaries for grains that escape or crash into the planet are discussed in the text (section 4). Between the open circles at $r_L = R_{syn}$ and $L_* = 2 \pm \sqrt{3}$, orbits are locally, radially unstable. The solid circle is the critical point defined by Eqs. 3.17 and 3.19.

square of the bounce frequency Ω_b, given by

$$\Omega_b^2 = \frac{\partial^2 U}{\partial z^2}\Big|_{\rho=\rho_c,z=0} = \frac{GM_p}{\rho_c^3}\left(\frac{3L_*\dot{\phi}_c}{\Omega_p}+1\right) = 3\omega_c^2 - 2n_c^2 \tag{3.20}$$

(Northrop and Hill 1982) is positive. Here $\dot{\phi}_c = \omega_c - \Omega_p$ is the dust grain's azimuthal frequency in the frame rotating with the magnetic field. When multiplied by z, Eq. 3.20 gives the centrifugal (first term), and gravitational (last term) accelerations along a magnetic field line.

For $\Omega_b^2 < 0$, the vertical motion is unstable. Note that the gravitational acceleration is negative and thus destabilizing. This follows from the fact that the dipolar magnetic field curves toward the planet (see Fig. 2.1) and so a grain leaving the equatorial along a field line plane moves downhill in the gravitational potential. The Northrop and Hill (1982) solution for the boundary where $\Omega_b = 0$ is plotted in Figs. 3.1a and 3.9a. At distances closer to the planet than a critical distance ρ_{crit}, the Northrop solution predicts that gravity will force grains to leave the equatorial plane.

3.5.1 Vertical Instability in the Lorentz Limit

In the limit of high charge-to-mass ratio, Eq. 3.20 can be solved exactly:

$$\frac{\rho_{crit}}{R_{syn}} = (2/3)^{\frac{1}{3}} \approx 0.87. \tag{3.21}$$

The effect of our initial condition, launching grains at the Kepler speed, however, necessarily causes epicyclic gyromotion as the grain orbits the planet. This leads to a stabilizing magnetic mirror force, in which the grain resists moving out of the equatorial plane to regions of higher magnetic field strength as discussed in section 1.1. Following the procedure of Lew (1961) and Thomsen and van Allen (1980), the magnetic mirror force for equatorial pitch angles near 90° adds a component of strength $9r_g^2\Omega_{gc}^2/2\rho_c^2$ to Eq. 3.20. In the Lorentz limit, Eq. 3.13 simplifies to $r_g\Omega_{gc} = \rho_c(\Omega_p - n_c)$, and the bounce frequency

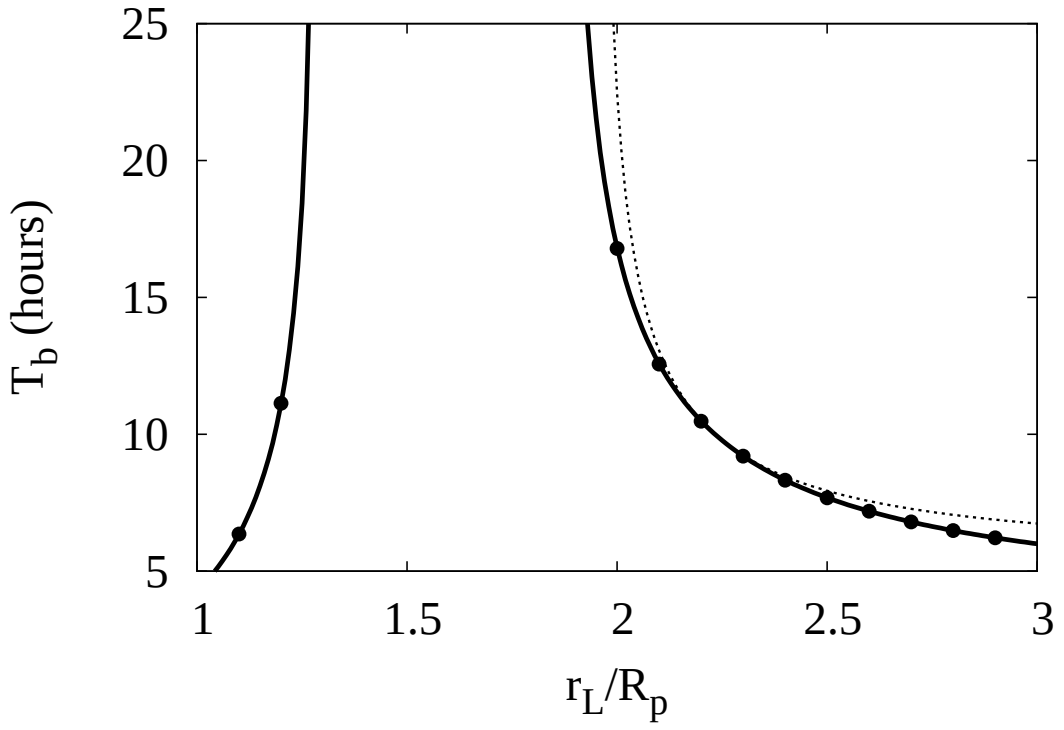

Figure 3.10: The bounce period for $L_* = -10^4$ grains at Jupiter over a range of launch distances. Northrop's solution (Eq. 3.20, dotted line) and our solution (Eq. 3.29, solid lines) with $T_b = 2\pi/\Omega_b$, are plotted alongside numerical data (points). Note that in our solution T_b is smaller than in Northrop's solution everywhere except at $R_{syn} = 2.24R_p$. In the limit where $r_c << R_{syn}$, Eq. 3.22 shows that grains satisfy $\Omega_b \rightarrow \sqrt{\frac{5}{2}}n_c$, while for $r_c >> R_{syn}$, $\Omega_b \rightarrow \sqrt{\frac{15}{2}}\Omega_p$ and $T_b \rightarrow 3.62$ hours.

can be found from:

$$\Omega_b^2 = 3\Omega_p^2 - 2n_c^2 + \frac{9}{2}(n_c - \Omega_p)^2. \tag{3.22}$$

As above, the first two terms are due to the centrifugal and gravitational forces on a grain tied to a nearly vertical magnetic field line. The third term of Eq. 3.22 is the magnetic mirror term, generalized to account for a rotating magnetic field. The three vertical accelerations add linearly, and are valid in the limit that $L_* \rightarrow \pm\infty$ and $r_g \rightarrow 0$.

Fig. 3.10 compares the Northrop and Hill (1982) bounce period (Eq. 3.20) with our Eq. 3.22 which accounts for epicyclic motion for small dust grains at Jupiter. The Northrop formalism erroneously predicts bounce periods that are too long both inside and outside

synchronous orbit and, more seriously, misses the second solution near the planet.

The third term in Eq. 3.22 is positive everywhere inside the Northrop boundary and thus leads to enhanced vertical stability. The stability boundaries in the high $|L_*|$ limit are determined by Eq. 3.22; setting $\Omega_b = 0$, we find:

$$\frac{r_L}{R_{syn}} = \left(\frac{5}{9 \pm \sqrt{6}}\right)^{2/3} \approx 0.58, 0.84. \tag{3.23}$$

These limits are valid for both positive and negative grains with $|L_*| \to \infty$. Between these limits, $\Omega_b^2 < 0$ and grain orbits are locally unstable; the enhanced stability from the mirroring force moves the vertical stability boundary inwards from Northrop's $0.87R_{syn}$ to $0.84R_{syn}$. A more important change, regained stability inside $0.58R_{syn}$, is due to the higher launch speeds relative to the field lines, larger gyroradii, and a stronger magnetic mirror force. For Jupiter these distances are at $1.29R_p$ and $1.87R_p$ respectively (see Fig. 3.9). Hints of this inner stability zone were seen numerically by Northrop and Hill (1983a) and by Northrop and Connerney (1987); here we have derived analytical solutions for vertical stability in the Lorentz limit.

3.5.2 Vertical instability for all charge-to-mass ratios

To extend our model for bounce motion over all charge-to-mass ratios we must, in principle, account for the variation in the strengths of the vertical gravitational, centrifugal and electromagnetic accelerations over one gyrocycle. Extending the electromagnetic mirror acceleration requires breaking the assumption of perfectly circular gyrocycles, and is beyond the scope of this work. The remaining two accelerations, however, can be extended to second order in r_g/ρ_c while retaining circular gyrations. We begin by writing the vertical acceleration as a function of the epicyclic phase θ (see Eq. 3.20):

$$\frac{\partial^2 U}{\partial z^2} z = \frac{GM_p z(\theta)}{\rho^3(\theta)} \left(\frac{3L_* \dot{\phi}(\theta)}{\Omega} + 1\right). \tag{3.24}$$

To first order in r_g, the epicycles are circles in the guiding center frame. Setting $\theta = 0$ at the closest point to the planet, we find

$$\rho(\theta) = \rho_c - |r_g| \cos\theta, \tag{3.25}$$

and

$$\dot{\phi}(\theta) = \dot{\phi}_c - \kappa_c \frac{|r_g|}{\rho_c} \cos\theta. \tag{3.26}$$

Due to the geometry of a dipole near its equator, an epicycle is tilted by an angle $\approx 3\lambda$, where λ is the latitude (Eq. 2.17). Hence the vertical offset is given by:

$$z(\theta) = z_c - \frac{3|r_g|}{\rho_c} \cos\theta, \tag{3.27}$$

To calculate the bounce frequency, we average the restoring acceleration over an epicycle, a procedure that is valid as long as $\kappa_c >> \Omega_b$:

$$\Omega_b^2 = \frac{\left\langle z \frac{\partial^2 U}{\partial z^2} \right\rangle}{\langle z \rangle} = \frac{1}{2\pi z_c} \int_0^{2\pi} \frac{\partial^2 U}{\partial z^2} z(\theta) d\theta. \tag{3.28}$$

Using Eqs. 3.25 and 3.26 to eliminate $\rho(\theta)$ and $\dot{\phi}(\theta)$ in Eq. 3.24, we expand to $O(r_g^2)$, integrate Eq. 3.28, and add in the magnetic mirroring term from Eq. 3.22 to obtain:

$$\Omega_b^2 = 3\omega_c^2 - 2n_c^2 + \frac{9}{2}(n_c - \Omega_p)^2 - \frac{r_g^2}{\rho_c^2} \left(\frac{9}{2} \Omega_{gc} \dot{\phi}_c + \frac{3}{2} n_c^2 \right). \tag{3.29}$$

The frequencies in Eq. 3.29, ω_c (Eq. 3.8), n_c (Eq. 3.6), Ω_{gc} (Eq. 3.7), and $\dot{\phi}_c = \omega_c - \Omega_p$, are all evaluated at the guiding center of motion $\rho_c = r_L + r_g$, which is determined by Eq. 3.13. Our calculation adds two additional destabilizing terms that are strongest for intermediate values of L_*, where gyroradii are largest (Fig. 3.6).

How does our solution compare to numerical data? In Fig. 3.9, we plot our theoretical curves against the numerical data for both negative and positive grains launched at the Kepler rate in an aligned dipole field for Jupiter. We find the curves tracing the unstable zone semi-analytically by setting $\Omega_b = 0$ in Eq. 3.29. Within the regions bordered by

the curves, trajectories are locally unstable but may remain globally bound due to high-latitude restoring forces.

Our model closely matches the outer stability boundary for negative grains but is less successful for the inner boundary, especially for moderate L_*. This is precisely where our derivation is weakest; recall that we have not accounted for higher-order corrections for the magnetic mirror force which are strongest closest to the planet and for $|L_*| \sim 1$. Near $|L_*| = 1$ epicycles become large and distorted for negative grains and even more so for positive grains (Mendis et al. 1982; Mitchell et al. 2003). Figure 3.6b shows that the epicyclic model matches the radial range of positively-charged grains well for values $L_* > 10$. This is exactly where the numerical data depart from the theory in Fig. 3.9b. Apparently, large gyroradii and interference from the proximate radial instability strip lead to unmodeled effects and excess vertical instability.

The curvature of the outer boundary in Fig. 3.9a is similar to that for the Northrop curve, albeit displaced to locations closer to the planet. Notice that, with decreasing $|L_*|$, the instability region curves towards the planet for negative grains, and away from it for positive grains (Fig. 3.9). This is primarily due to the $3\omega_c^2 - 2n_c^2$ term that determines the Northrop boundary. For negative grains inside synchronous orbit, $n_c > \omega_c$, and ω_c increases with decreasing $|L_*|$ due to a weakening outwardly-directed electromagnetic force. It thus takes a greater value of n_c to make $3\omega_c^2 - 2n_c^2$ change sign and destabilize the vertical motion. Hence, the boundary curves move to lower launch distances in Fig. 3.9a. For the positive grains in the Lorentz limit, by contrast, ω_c decreases as L_* decreases, and a smaller n_c will destabilize the grain. Thus with decreasing L_* this boundary in Fig. 3.9b curves up to higher launch radii.

Finally, notice the band of locally unstable but globally stable points that stretches from $|L_*| \approx 0.1$ at the surface of the planet to $|L_*| \approx 1$ at large distances in Figs. 3.1a and 3.9a. These grains are affected by a $|\kappa_c| = 2\Omega_b$ resonance that couples their radial and

vertical motions. Energy is transferred from the radial oscillation to a vertical oscillation and back again. Near synchronous orbit, gyroradii are initially small and therefore there is not as much radial motion to transform into vertical motion; these grains do not reach our $\lambda_m = 5^\circ$ threshold and appear as white space in Fig. 3.9a.

The existence of stable trajectories within the Northrop boundary is an important result, particularly for small slowly-rotating planets with distant synchronous orbits like Earth. Small dust grains generated by the collisional grinding of parent bodies on Keplerian orbits can remain in orbits near the planetary surface. High energy plasma, like that found in Earth's Van Allen radiation belts, is more stable than we have calculated here by virtue of exceedingly rapid gyrations and a greatly enhanced mirroring force.

3.6 Azimuthal Motion

For completeness, we return to the azimuthal motion of highly charged dust-grains. In Chapter 2 we explored azimuthal drift rates non-rotating magnetic field due to additional forces beyond the Lorentz force. Here, we have a rotating magnetic dipole and gravity.

In the epicyclic approximation, we now have accurate expressions for the radial, vertical and azimuthal motions in the inertial frame. In the Kepler regime, these three frequencies all converge to the Kepler orbital frequency. In Fig. 3.11, we highlight the divergence of these three timescales as $|L_*|$ increases.

Here we test these equations in the Lorentz limit for Kepler launched grains. Fig. 3.12 compares drift rates numerically and analytically with Jupiter's gravity and rotation initially switched off. We find that the azimuthal drifts of Chapter 2 are in the opposite direction if Jupiter's gravity and rotation are accounted for.

Our analysis to this point is completely general and, although we have focused on Jupiter, can be easily applied to other planets. Saturn and Earth are logical choices, as their

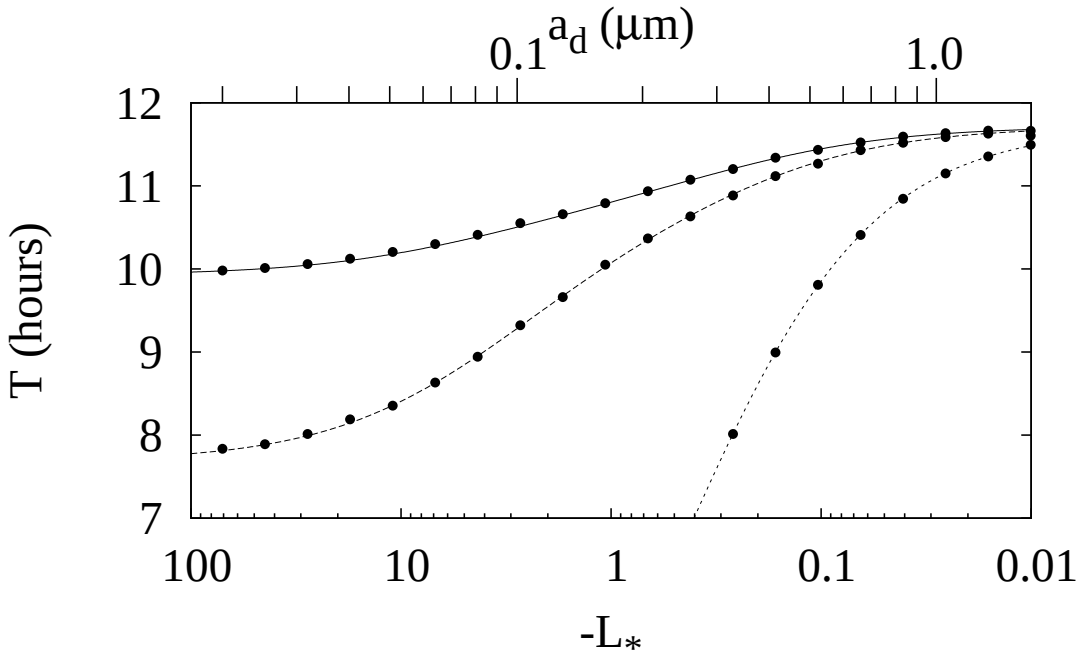

Figure 3.11: The radial, vertical and azimuthal periods for negatively-charged grains launched at $2.5R_p$ around Jupiter. The three curves constitute the full epicyclic solution for the radial period (top curve; Eq. 3.11), the latitudinal bounce period (middle curve; Eq. 3.29), and the azimuthal orbital period (lower curve, Eq. 3.8). The numerical points from integrated trajectories closely match the analytic curves.

magnetic fields are also dominated by the g_{10} aligned dipolar component. The appearance of the stability map for any planet depends on only the parameters R_{syn} and R_p, and not on the substantially different magnetic field strengths which, due to our use of L_*, only affect the conversion to grain radius a_d. The synchronous orbital distance is somewhat closer to the planetary surface at Saturn ($R_{syn} = 1.86R_p$) than at Jupiter ($R_{syn} = 2.24R_p$), while at Earth ($R_{syn} = 6.61R_p$) it is much further away. This leads to interesting differences between the planets, as we shall see below.

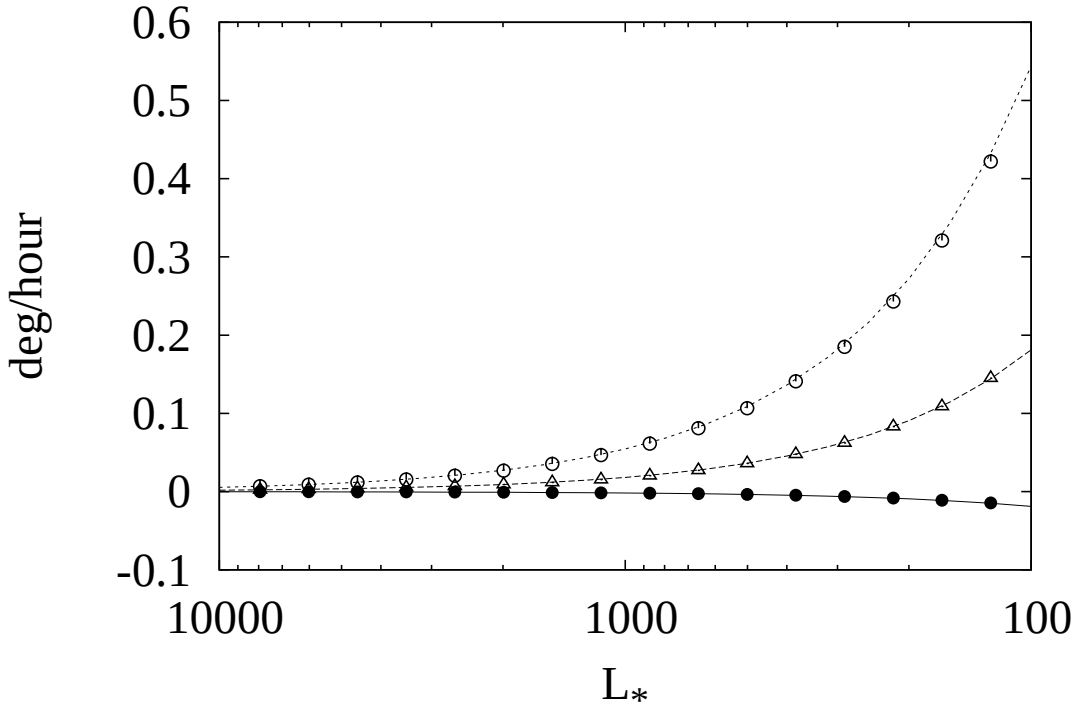

Figure 3.12: Analytical and Numerical Drift rates, in degrees per hour, relative to magnetic field, for highly charged Kepler-launched dust grains in Jupiter's magnetic field. All drift rates are in the frame of the magnetic field lines. The curves are analytical solutions from Eq. 2.22 (upper curve marking the ∇B drift), Eq. 2.18 (middle curve denoting the drift due to the gravitational force perpendicular to the magnetic field lines) and Eq. 3.8 (lower curve), the azimuthal motion of the guiding center with gravity in a rotating magnetic field. In this configuration with grains launched in the magnetic equator, the motion parallel to the magnetic field lines which would cause curvature drift, was negligible. The open circles mark numerical data with Jupiter's gravity and rotation both switched off, so that only ∇B drift remains. The triangles are numerical data with gravity on but the rotation switched off, and the filled circles show numerical data with the Jupiter's gravity and rotation both on.

3.7 Saturn and Earth

A centered and aligned dipole is an excellent approximation for Saturn's magnetic field. We take $g_{10} = 0.2154$ Gauss from Connerney et al. (1984) and plot both our numerical data and analytical stability boundaries in Fig. 3.13. The more recent Cassini measurement of $g_{10} = 0.21162$ Gauss does not vary significantly from the older value that we use (Burton et al. 2009). A lower synchronous orbit at Saturn pushes the local vertical instability inward, as expected from Eq. 3.23. Comparing Fig. 3.13 to Fig. 3.9, we see that the proximity of the surface at Saturn causes all the locally vertically unstable grains to physically collide with the planet. This is true for both negative and positive grains.

Outside synchronous orbit in Fig. 3.13b, the solutions derived for positive escaping grains in section 4 apply at Saturn to very high accuracy, for both the low L_* and high L_* boundaries. As in Fig. 3.9b, grains with $L_* \lesssim \frac{1}{2}$ do not have enough energy to escape despite achieving large radial excursions (light grey region outside R_{syn} in Fig. 3.13b). For these grains, vertical motions are excited over several orbits, as in Fig. 3.5.

Within synchronous orbit, the condition $U(R_p) = U(r_L)$ (solved in Eq. 3.17) bounds most of the unstable grains. As at Jupiter, a small set of large grains near R_{syn} require the semi-analytical analysis of the potential between the launch position and the surface to determine global stability. This analysis yields the curve connecting the filled black circle at ($r_L = 1.568R_p$, $L_* = 0.14$) to the open circle ($r_L = R_{syn}$, $L_* = 2 - \sqrt{3}$) in Fig. 3.13b.

Compared to Jupiter and Saturn, Earth's magnetic field is "inverted" at the current epoch, with magnetic north near the geographic south pole, with $g_{10} = -0.3339$ Gauss Roberts and Soward (1972). Thus at Earth, $L_* > 0$ for negative grains. This causes positive grains to be radially stable, gyrating between the launch position and synchronous orbit, and negatively-charged grains to be radially unstable. The Earth is also far smaller on the scale of its own synchronous orbit than the gas giants, and so serves as an excellent

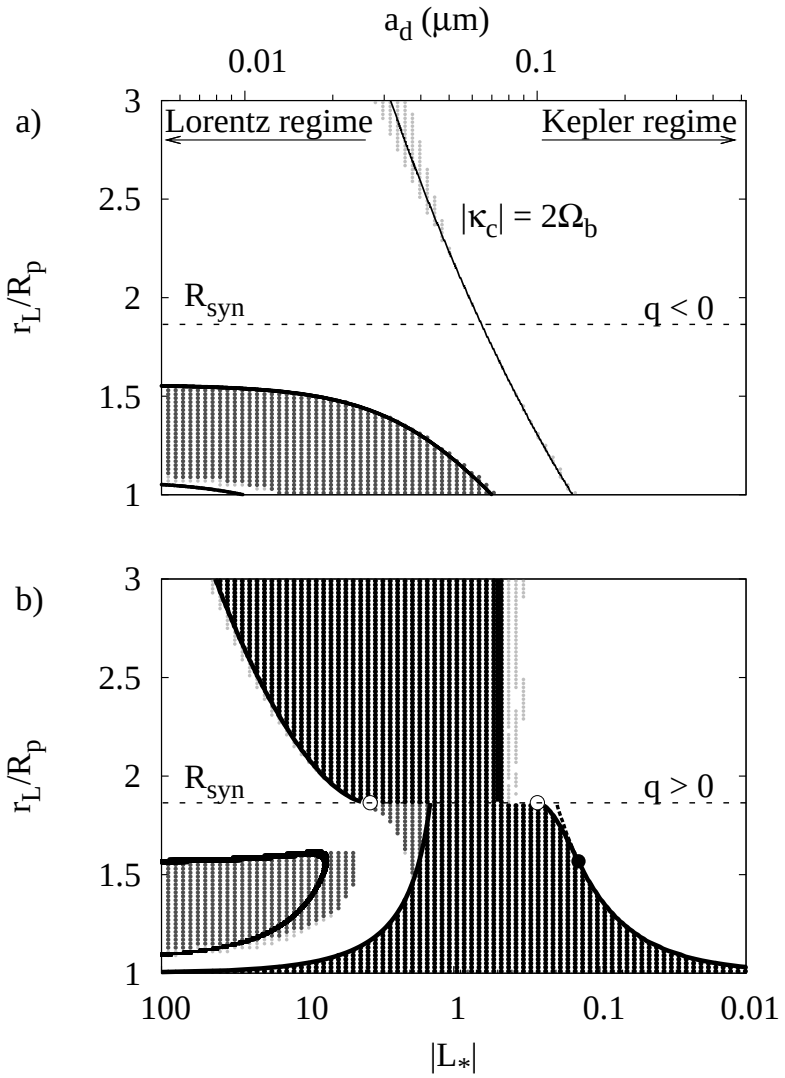

Figure 3.13: Stability of charged grains at Saturn modeled with a centered and aligned dipole field. All initial conditions and theoretical curves are as in Fig. 3.9. Also as in Fig. 3.9, the darkest shade of grey signifies low latitude collision or escape, the middle shade indicates high latitude collisions, and the lightest grey signifies large vertical excursions. For negative charges, **a**) only a tiny stable region exists near ($r_L = R_p$, $L_* = -50$) due to Saturn's smaller R_{syn}. Furthermore, due to the proximity to Saturn, nearly all grains that are locally vertically unstable do in fact hit the planet, unlike their counterparts at Jupiter. For positive charges, too, plotted in **b)**, nearly all the vertically unstable grains hit Saturn. Saturn's radial instability region (darkest grey) looks much like Jupiter's.

test of the accuracy of our analytical solutions far from R_{syn}.

For the Earth, Fig. 3.14a shows the radial global instabilities. Outside R_{syn}, the boundaries are in excellent agreement with our analytical results for large and small grains. Inside R_{syn}, grains are globally radially unstable and all the grains that collide with the planet at low latitudes are launched between our two solutions given by Eq. 3.17. The set of grains for which Eq. 3.17 is an insufficient criterion for collision with the planet, however, is much larger at the Earth than at Jupiter or Saturn. For Earth, just like for the gas giants, the global solution for radial stability inside synchronous orbit perfectly matches the numerical data and meets R_{syn} at the local stability solution ($r_L = R_{syn}, L_* = 2-\sqrt{3}$). Furthermore, the solutions of Eq. 3.17 have shifted to much lower L_* (see Eq. 3.18), reducing, at least near R_{syn}, the total range in L_* for grains which collide with the planet at low latitude.

The local vertical stability boundary matches the numerical data well, although in the Lorentz limit, all grains are globally stable since the high latitude restoring forces become much stronger close to the planet (Howard et al. 2000). Only at $|L_*| \leq 1$ do the positive grains collide with the planet. As in Figs. 3.9 and 3.13 the vertical stability curves match very well for large L_* and deviate from the data for $L_* \approx 1$. The $|\kappa_c| = 2\Omega_b$ resonance also matches the data well.

Earth has a much larger class of grains that experience large radial excursions, which in turn excite vertical motions. Most of these grains, from the medium-grey areas on the stability map of Fig. 3.14a that link the disjoint dark grey regions of global radial instability, collide with the planet at high latitudes. An example of a trajectory in this class is shown in Fig. 3.15.

At Saturn all of the grains in this region collided with the planet, but at the Earth we see three white tracks of orbits that never leave the equatorial plane, and hence are energetically prevented from striking the planet. We plot an example in Fig. 3.16. A

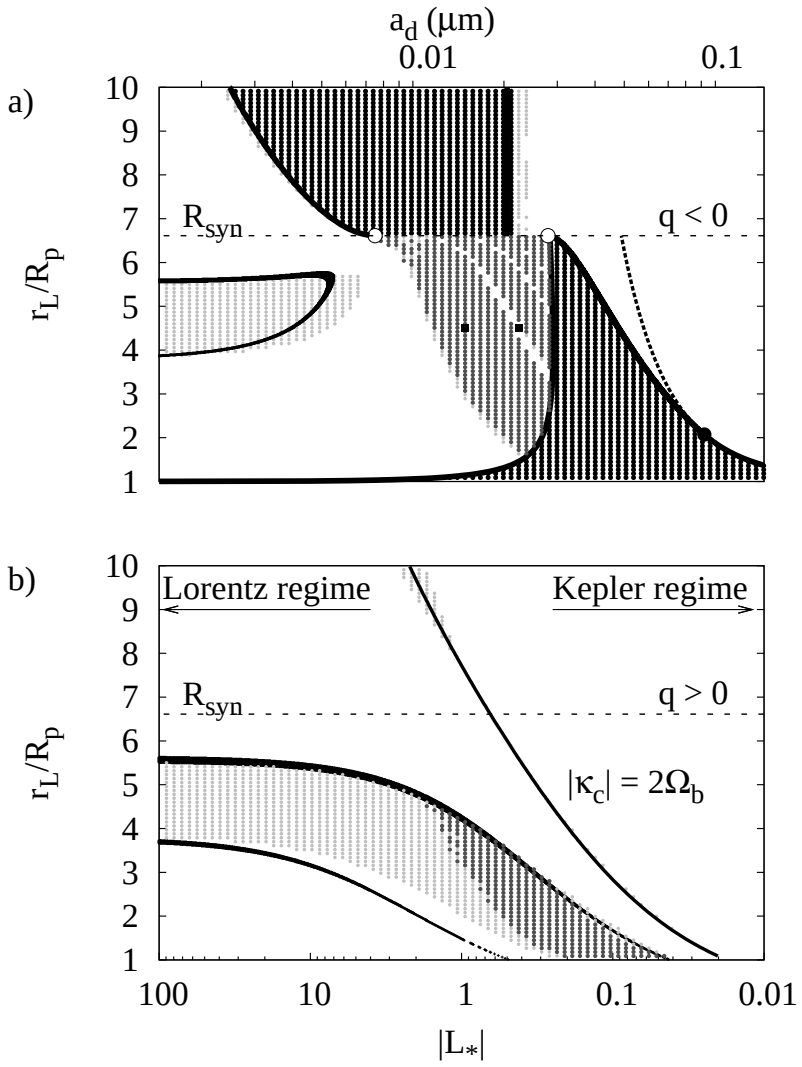

Figure 3.14: Stability of charged grains at Earth, modelled with a centered and anti-aligned dipole field. Theoretical curves and initial conditions are the same as in Figs. 3.9 and 3.13. Since R_{syn} is much larger than for Jupiter and Saturn, we extend the radial range of the integrations to $r_L = 10R_p$ and the distant threshold signifying escape to $r_{esc} = 100R_p$. The open circles at ($r_L = R_{syn}$, $L_* = 2+\sqrt{3}$) and ($r_L = R_{syn}$, $L_* = 2-\sqrt{3}$) are as in Fig. 3.9, and the solid circle, marking the transition from the analytical to semi-analytical boundary for the larger grains is at $L_* = 0.0248, r_L = 2.074R_p$. The two solid squares in **a)** are individual grain trajectories illustrated in Figs. 3.15 and 3.16.

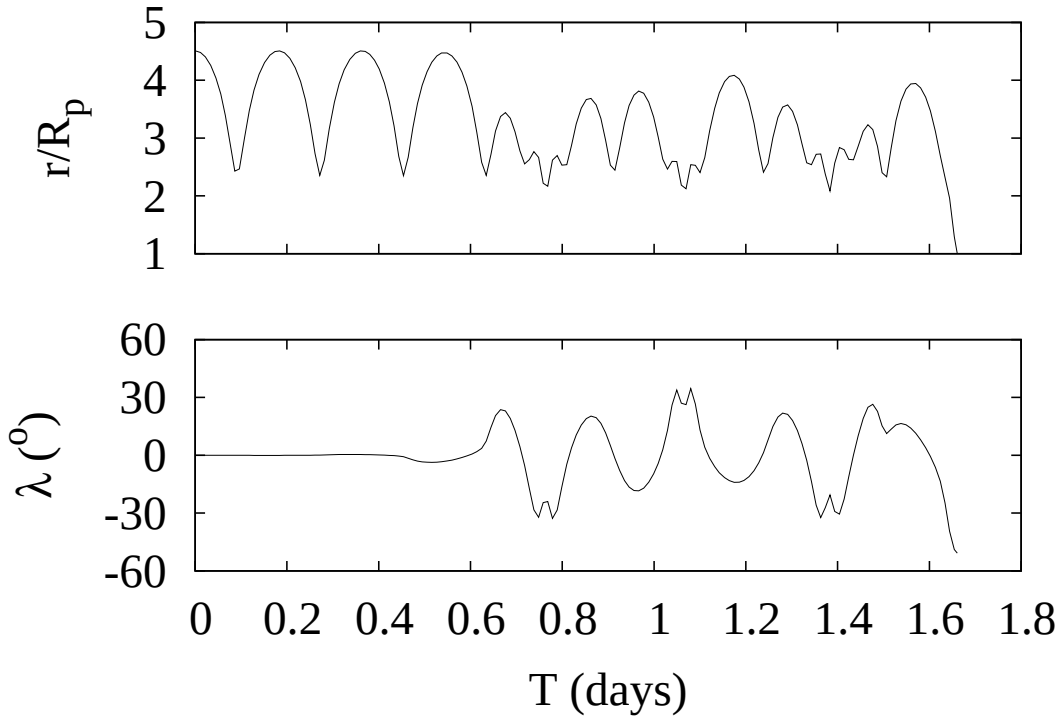

Figure 3.15: A grain with large radial excursions that gradually excite substantial vertical oscillations at the Earth, ($r_L = 4.51R_p$, $L_* = 0.948$, $a_d = 0.0149$ μm).

few of these trajectories are also apparent for Jupiter (small white spots in Figs. 3.1b and 3.9b.) We suspect, based on the similarity of the white stable tracks in Fig. 3.14a and the $|\kappa_c| = 2\Omega_b$ line in Fig. 3.14b, that these are resonant phenomena.

3.8 Conclusion

For Kepler-launched grains in centered and aligned dipole planetary fields, we have employed both local and global stability analyses to provide solutions for stability boundaries that match numerical simulations for Jupiter, Saturn and the Earth. Figure 3.17 provides a summary of the various analytical results discussed in this work for positive grains at Jupiter.

We find that local radial stability is very useful in the immediate vicinity of syn-

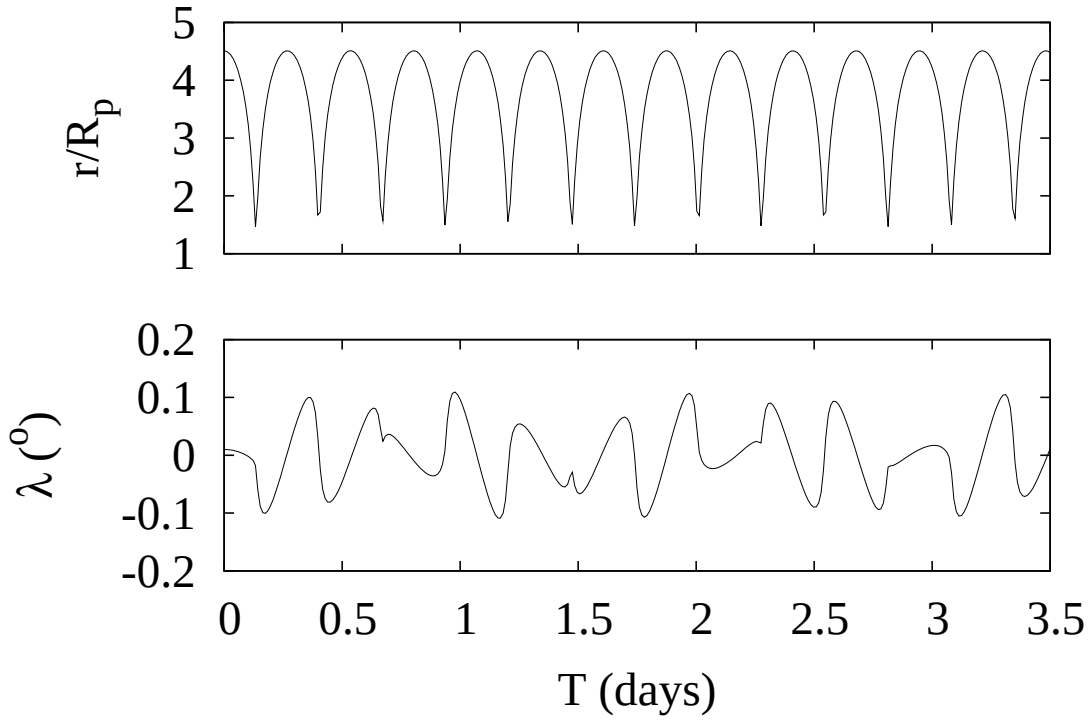

Figure 3.16: A grain with large radial motions like that depicted in Fig. 3.15 that nevertheless always remains near the equatorial plane ($r_L = 4.51R_p$, $L_* = 0.419$, $a_d = 0.0224$ μm).

chronous orbit, since $r_g \to 0$ there (Eq. 3.13). More importantly, our restriction of the global radial analysis to equatorial orbits is justified by the excellent agreement between analytics and numerics. Radial instability has important implications for depleting particles near the surface of a planet but beyond the reach of atmospheric drag forces. At Earth, for example, the radial instability eliminates negatively-charged particles with $r_g \lesssim 0.2$ μm from low Earth orbit, and $\lesssim 0.1$ μm from within 2000 km. For Jupiter, this instability sweeps positive grains with $r_g < 1$ μm from the region within 10,000 km from Jupiter's cloud-tops.

Our local vertical analysis of grains launched on Kepler circles in the equatorial plane adds the effect of the magnetic mirror force and is a major improvement to the equilibrium model of Northrop and Hill (1982). We do not undertake a fully global analysis which

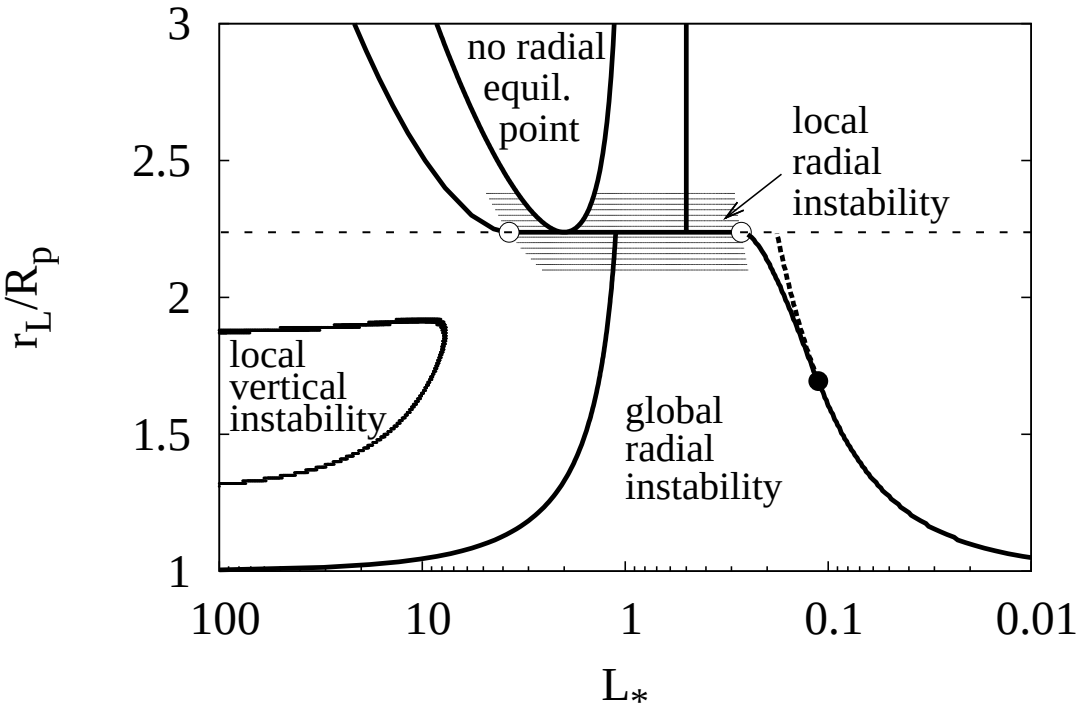

Figure 3.17: Local and global stability boundaries for positive grains at Jupiter. The dashed line is R_{syn}, and the shaded region highlights local radial instability near R_{syn}. The white circles bounding this region on R_{syn} ($L_* = 2 \pm \sqrt{3}$ for all planets) also show where our semi-analytical curves for grains that escape or collide with the planet meet R_{syn}. The solid circle is where the potential at the planet's surface is a local maximum and equals to the launch potential. Outside R_{syn}, entirely within the global instability boundaries, lies the region in which local radial instability is precluded, following Eq. 3.9.

would seek to distinguish grains that strike the planet from those that simply sustain large amplitude oscillations in latitude.

Although the magnetospheres of Jupiter, Saturn and the Earth are all nearly dipolar, each planet has additional components that make the field more complicated. Saturn has the simplest field and is well represented by a dipole offset northward by a few thousand km. Jupiter and the Earth have non-zero dipole tilts that cause the magnetic field seen by an orbiting grain to fluctuate periodically. Nevertheless, since tilts and offsets are generally small, we expect that the radial forces will be only slightly affected, and that the radial instability region will remain nearly the same. Vertical motions, by contrast, should

be strongly affected since a circular orbit in the equatorial plane is no longer an equilibrium point. The global radial analysis, which included the effects of radial oscillations, led to a much larger instability region than the simple local analysis (top of Fig. 3.17); in exactly the same way, we expect the region of vertical instability to expand substantially when dipole tilts or offsets are included. We will take up the study of more complicated magnetic field configurations and more general launch conditions in Chapter 4.

Chapter 4

The Dynamics of Dust in Multipolar Magnetic Fields

4.1 Introduction

[1] When Voyager 1 encountered Jupiter in 1979, the discovery of the tenuous dusty ring system came as a complete surprise. Although the earlier Pioneer missions found some hints of a ring system, many thought that dust close to Jupiter would rapidly spiral in by gas drag (Owen et al. 1979). Voyager 2 confirmed the existence of the ring, as well as the tiny satellites Metis and Adrastea that orbit inside the classical Roche limit, and are the most likely source of the ring material.

High speed impacts with small moons, as well as unseen large parent bodies replenish the dusty rings with debris of all sizes. Similar sources of material for Saturn's tenuous inner D ring have not been found, though massive particles in narrow ringlets with enhanced local densities could serve as these sources (Hedman et al. 2007; Showalter 1996). In both environments, dust ejected by impacts from parent bodies have essentially colli-

[1] This chapter is largely based on Jontof-Hutter and Hamilton (2012b), in press.

sionless trajectories. As debris particles acquire electric charges through interactions with the plasma environment and solar radiation, the smallest reach significant charge-to-mass ratios and, as a consequence, experience strong electromagnetic (EM) forces as they orbit through the magnetic field of their host planet.

For grains smaller than $\sim 1\mu$m in radius, the EM force exceeds perturbations from large satellites, the planetary oblateness and solar radiation pressure (Horányi et al. 1992). Even smaller dust grains may have orbits that are immediately unstable to either radial motion if the grains are positively-charged (Hamilton and Burns 1993a; Horányi et al. 1993a), or vertical motion (both positively- and negatively-charged: Northrop and Hill 1982). Many authors have studied various aspects of charged-particle dynamics. For a recent review, see Jontof-Hutter and Hamilton (2012a), who derived analytic stability boundaries for the idealized case of grains with constant charge, launched at the Kepler speed in an aligned dipolar planetary magnetic field. As in that study, (Chapter 3), the boundaries between stable and unstable orbits are of particular interest to us here. These depend on the launch distance from the planet, and the charge-to-mass ratio of an individual dust grain.

The aim of this chapter is to explore the sensitivity of these stability boundaries to more realistic situations. We relax our idealized assumptions above by considering i) non-zero ejecta speeds from the parent body, and ii) higher-order magnetic field components. In Chapter 5, we study a third effect, namely, variable electric potentials on dust grains.

We use Jupiter as our model planet in these investigations since it has both a complex multipolar magnetic field and a well-studied dusty ring system (Brooks et al. 2004; Burns et al. 1999; de Pater et al. 1999; Ockert-Bell et al. 1999; Showalter et al. 2008; Throop et al. 2004). In this chapter, after a detailed study of Jupiter, and the effects of its offset and tilted dipole magnetic field components, we present stability maps for motion in the complex magnetic fields of Earth, Saturn, Uranus and Neptune. We begin by recapping

Planet	Volts μm$^{-2} \rightarrow L_*$	Coulomb kg$^{-1} \rightarrow L_*$
Jupiter	$5660 \times 10^{-6} V/a_d^2 \rho_d$	$0.21381 \times Q/m$
Saturn	$538 \times 10^{-6} V/a_d^2 \rho_d$	$0.020321 \times Q/m$
Uranus	$92 \times 10^{-6} V/a_d^2 \rho_d$	$0.0034676 \times Q/m$
Neptune	$62 \times 10^{-6} V/a_d^2 \rho_d$	$0.0023415 \times Q/m$
Earth	$-42 \times 10^{-6} V/a_d^2 \rho_d$	$-0.0015839 \times Q/m$

Table 4.1: L_* calculator for the planets. The middle column converts a given potential V (in Volts), grain radius a_d (in μm), and density ρ_d (g cm^{-3}) to L_*. The right column converts a charge-to-mass ratio in C kg^{-1} into L_* for each planet.

the relevant stability results for a simple dipolar planetary magnetic field from Jontof-Hutter and Hamilton (2012a).

4.2 Motion in an Aligned Dipolar Magnetic Field

The charge-to-mass ratio for Kepler-launched grains can be conveniently described by the ratio of the force induced by the corotational electric field of the planet with gravity, given by

$$L_* = \frac{q g_{10} R_p^3 \Omega_p}{G M_p m c} \tag{4.1}$$

(Hamilton 1993a,Hamilton 1993b,Jontof-Hutter and Hamilton 2012a). Here, q and m are the electric charge and mass of a dust grain, g_{10} is the aligned dipolar magnetic field strength at the equator, R_p and M_p are the planetary radius and mass respectively, Ω_p is the spin frequency of the planet, and G and c are the gravitational constant and speed of light. As a dimensionless independent variable, L_* accounts for all the relevant planetary parameters and avoids undue focus on the grain's size, shape, density and electric potential, which are all poorly constrained. The sign of L_* depends on the product qg_{10}, and its value can easily be converted to a grain radius a_d for specified grain properties.

Table 4.2 provides a simple calculator between dust grain radius and L_*, for a given electric potential, material density, and grain radius.

For large grains in the Kepler limit orbiting with semi-major axis a, azimuthal, radial, and vertical motions have the same frequency

$$n_c = \left(\frac{GM_p}{a^3}\right)^{\frac{1}{2}}, \tag{4.2}$$

but for higher charge-to-mass ratios, these frequencies differ. As the charge-to-mass ratio is raised, these frequencies slowly diverge from one another (Hamilton 1993a), and for an aligned dipolar magnetic field, explicit expressions valid for all charge-to-mass ratios are available (Jontof-Hutter and Hamilton 2012a), as illustrated in Fig. 3.11. Since these expressions will prove useful in this chapter, we reproduce them here.

General motions in this problem can be conveniently separated into epicycles about a guiding center which circles the planet at an azimuthal angular speed ω_c. Where radial epicycles are small on the scale of the grain's orbit, balancing the forces of gravity, EM force and the centrifugal force yields an expression for ω_c:

$$0 = \omega_c^2 + \frac{GM_pL_*}{r_c^3}\left(1 - \frac{\omega_c}{\Omega_p}\right) - \frac{GM_p}{r_c^3}. \tag{4.3}$$

(Jontof-Hutter and Hamilton 2012a; Mitchell et al. 2003; Northrop and Hill 1982). Here and throughout, the subscript c refers to the guiding center of motion. The distance to the guiding center of motion, r_c, is the semi-major axis a in the Kepler limit. Note that for gravity-dominated grains ($L_* \to 0$), we have $\omega_c^2 = \frac{GM_p}{r_c^3} = n_c^2$ in agreement with Eq. 4.2. In the strong EM limit, $\omega_c \to \Omega_p$ and the grains are nearly locked to the magnetic field lines.

The radial or epicyclic frequency κ_c satisfies

$$\kappa_c^2 = \omega_c^2 - 4\omega_c\Omega_{gc} + \Omega_{gc}^2, \tag{4.4}$$

(Jontof-Hutter and Hamilton 2012a; Mendis et al. 1982; Mitchell et al. 2003) at the guiding center, where $\Omega_{gc} = \frac{qB}{mc} = \frac{n_c^2L_*}{\Omega_p}$ is the frequency of gyromotion. In the EM-dominated,

Lorentz regime, $\kappa_c = \Omega_{gc}$. In the gravity-dominated, Kepler regime, $\Omega_{gc} \to 0$ and $\kappa_c \to n_c$, the Kepler orbital frequency, as expected.

Most grains are radially confined, suffering excursions of

$$r_g = \frac{r_L(\Omega_p - n_L)\Omega_{gL}}{\Omega_{gL}^2 - \Omega_{gL}(3\Omega_p + n_L) + n_L^2} \tag{4.5}$$

where r_g, the gyroradius, is much smaller than r_L, the launch distance. Here $n_L = \sqrt{\frac{GM_p}{r_L^3}}$ and $\Omega_{gL} = \frac{n_L^2 L_*}{\Omega_p}$ are the Kepler frequency and the gyrofrequency as determined at the launch distance (Jontof-Hutter and Hamilton 2012a; Schaffer and Burns 1994). The epicyclic model fails only for positively-charged grains with $L_* \sim 1$, where the denominator in Eq. 4.5 becomes very small (see Fig. 3.6b).

Finally, the vertical motion of grains with stable epicycles in the equatorial plane has frequency Ω_b, where

$$\Omega_b^2 = 3\omega_c^2 - 2n_c^2 + \frac{r_g^2}{\rho_c^2}\left(\frac{9}{2}\Omega_{gc}^2 - \frac{9}{2}\Omega_{gc}\dot{\phi}_c - \frac{3}{2}n_c^2\right) \tag{4.6}$$

(Jontof-Hutter and Hamilton 2012a). Here, $\dot{\phi}_c = \omega_c - \Omega_p$ is the azimuthal motion of the guiding center in the frame rotating with the planet. Equation 4.6 is valid as long as $r_g/r_L << 1$ which holds in both the Kepler ($L_* \to 0$) and Lorentz ($L_* \to \pm\infty$) limits. In the Kepler limit, all three terms in brackets are negligible, $\omega_c \to n_c$, and hence $\Omega_b \to n_c$. In the Lorentz limit, only the last two terms can be ignored and $\Omega_b^2 \to \frac{15}{2}\Omega_p^2 - 9\Omega_p n_c + \frac{5}{2}n_c^2$.

Where Ω_b tends to zero, grains become locally vertically unstable in the equatorial plane. Equation 4.6 provides good agreement with numerical data on the location and charge-to-mass ratio of boundaries between vertically stable and unstable grains, with two important caveats.

Firstly, in applying the epicyclic approximation, Eq. 4.6 assumes that radial motions are very small on the scale of the orbit ($r_g << r_L$). In addition, Eq. 4.6 is averaged over one gyrocycle, so the epicyclic motion must be on a much shorter timescale than any

stable vertical oscillations ($\kappa_c >> \Omega_b$). Both of these assumptions are met in the Lorentz limit, but both lose accuracy as L_* decreases, particularly for the positively charged grains which become radially unstable as $L_* \rightarrow 1$.

Secondly, setting $\Omega_b = 0$ determines local vertical stability in the equatorial plane of the spinning planet and its aligned magnetic field. Local instability is a necessary condition for global instability (whereby grains collide with the planet at high latitude), but it is not always sufficient. High latitude forces lead to high latitude oscillations (HLOs), which are globally but not locally stable. This class of orbits is more important for slow rotators like the Earth where ($R_{syn} >> R_p$), than it is at Jupiter or Saturn, but they do occur for the smallest grains inside $1.5R_p$ at Jupiter.

With these two caveats in mind, we include the local and global stability boundaries found from numerical integrations in Chapter 3 for Jupiter with an aligned dipolar magnetic field model. In Fig. 4.1, we highlight these regions for a range of charge-to-mass ratios spanning four orders of magnitude and a suite of launch distances from Jupiter's surface to beyond its synchronous orbital distance, with grains all launched at the local circular speed of the large parent bodies.

4.3 Jupiter

We focus most of our attention on Jupiter as its magnetic field has been well studied, and is known out to octupole order (we adopt the O4 model of Acuna and Ness 1976; Dessler 1983). The planet's magnetic field is dominated by the dipolar terms: g_{10}, g_{11} and h_{11} Gauss; these can be combined to determine the dipole tilt angle: $\arctan\left(\frac{(g_{11}^2+h_{11}^2)^{\frac{1}{2}}}{g_{10}}\right) =$ 9.6°. The g_{20} = -0.203 Gauss component can be interpreted as a southward vertical offset to the dipole field. Four additional quadrupolar and seven octupolar terms are known, and the upcoming Juno mission will measure higher-order magnetic field coefficients for

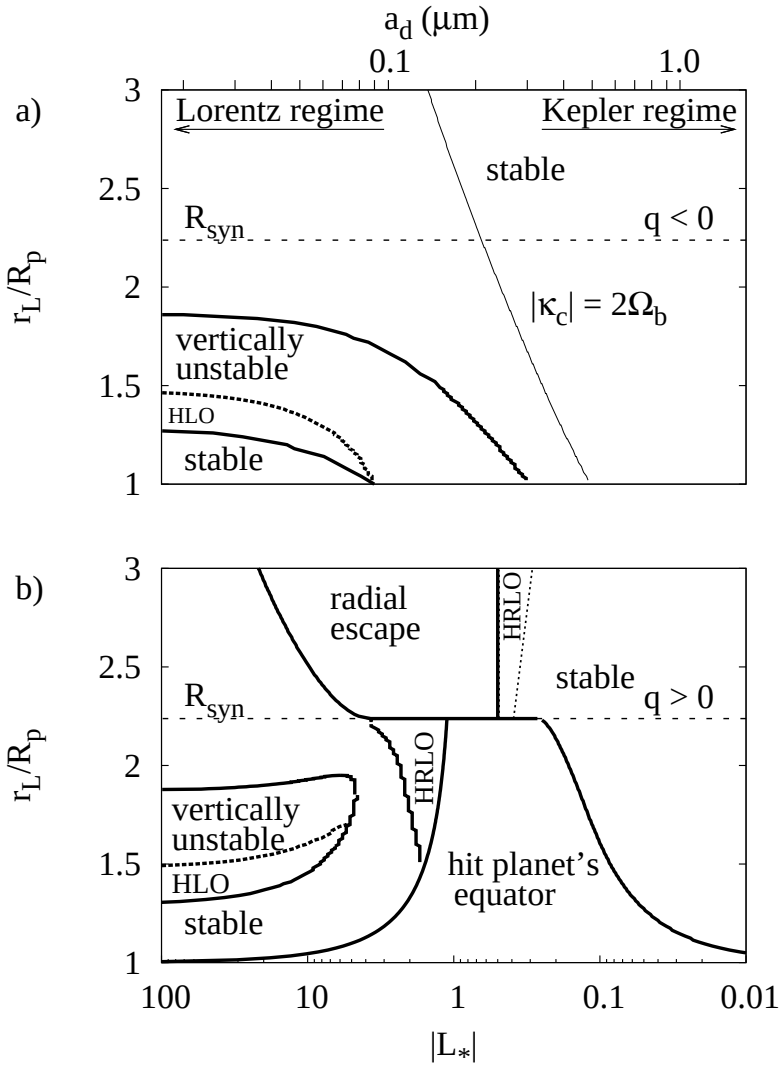

Figure 4.1: Stability boundaries for a) negative ($L_* < 0$) and b) positive ($L_* > 0$) grains in an aligned dipole magnetic field for Jupiter. This figure summarizes numerical data from Jontof-Hutter and Hamilton (2012a), explored in detail in Chapter 3. Here, the top axis shows characteristic grain radii corresponding to a $-5V$ or $+5V$ potential on a spherical grain of material density 1 g cm^{-3}. The vertically unstable grains depart from the equatorial plane and climb to high latitudes immediately after launch, ultimately colliding with the planet. Directly below this unstable region are grain trajectories with high latitude oscillations (HLOs). The radially unstable grains ($L_* > 0$) escape if launched outside synchronous orbit (R_{syn}), or hit the planet if launched from within R_{syn}. Two regions of high radial and latitudinal oscillation zones (HRLOs) abut the radial instability region. Within R_{syn}, large inward radial excursions lead to vertical oscillations (roughly along magnetic field lines) which increase in amplitude until the grains strike the planet at high latitude. Outside R_{syn}, near $L_* = \frac{1}{2}$, some grains experience HRLOs indefinitely. For $L_* < 0$, a curve traces grains that experience HRLOs following the 2:1 resonance between the epicyclic (κ_c) and vertical (Ω_b) frequencies.

the first time. In this section, we add various effects to a simple aligned dipole model to elucidate their importance. We begin with non-zero launch speeds in the frame of the parent particle, as likely occurs with impact ejecta.

4.3.1 Varied Launch Speed

Typical ejecta velocities from an impact are tens to hundreds of meters per second in the rest frame of the parent body, in a cone centered on the impact velocity vector (de Pater and Lissauer 2010). Do these non-circular speeds significantly affect the stability of charged dust grains?

To highlight the effect, we consider large initial velocities of 0.5 km s^{-1} in the prograde azimuthal (Fig. 4.2a) and radial (Fig. 4.2b) directions. Even with these large speeds, we note that EM-dominated grains on the left side of the plots are hardly affected. The Kepler speed at $r_c = 2.0R_p$ is v_k =29.8 km s^{-1}, while the local magnetic field lines rotate at $\Omega_p r_L$= 25.1 km s^{-1}. The azimuthal impulse that we add, therefore, is only $\sim$10% of the $\Omega_{gc} r_g$ = 4.7 km s^{-1} gyrospeed and decreases the gyroradius r_g by a corresponding 10%. Although important, this effect is not noticeable in Fig. 4.2. On the other hand, grains in the Kepler regime experience large radial excursions following a launch impulse. For an azimuthal boost, we can solve for the semi-major axis a and eccentricity e from $r_L = a(1-e)$, and

$$v^2 = GM_p \left(\frac{2}{r} - \frac{1}{a} \right). \tag{4.7}$$

For a small azimuthal impulse, $\frac{\Delta v_\phi}{v_k} << 1$, the radial motions extend outward from the launch position by $2ae \approx 4 r_L \frac{\Delta v_\phi}{v_k} \approx 0.134 R_p$ for the parameters of Fig. 4.2a. Although the intermediate-sized grains have the largest radial excursions in Fig. 4.2a, the grains in the Kepler limit are most strongly affected by a Δv_ϕ kick.

Figure 4.2b shows that a radial impulse produces a more modest radial range of motion than an azimuthal boost. In this case, the impulse is perpendicular to the velocity of the

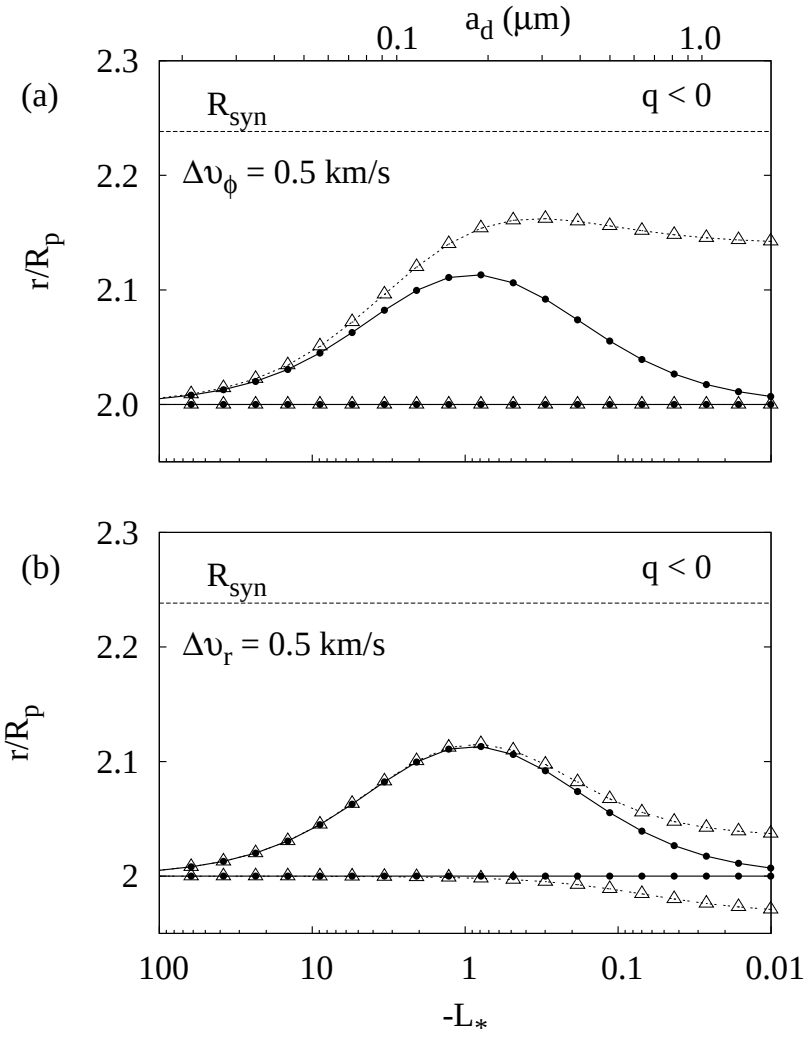

Figure 4.2: Radial range of motion for negatively-charged grains on initially circular orbits subject to an a) azimuthal (Δv_ϕ) and b) a radial (Δv_r) velocity impulse. The small filled circles indicate particles launched on circular orbits with $\Delta v = 0$, while the large open triangles denote those launched with $\Delta v = 0.5$ km s^{-1}.

parent body. For the smallest grains, in the Lorentz limit, this has almost no effect on the motion perpendicular to the field lines, and is akin to altering the initial phase but not the size of the gyrocycle. As with the azimuthal kick, a radial impulse has the largest effect for the largest grains. To first order in $\frac{\Delta v_r}{v_k}$, the orbital energy and semimajor axis are unchanged. The range of motion is therefore centered on the launch distance and has magnitude $2ae = 2r_L\frac{\Delta v_r}{v_k} \approx 0.067R_p$ for the parameters in Fig. 4.2b.

Figure 4.3 highlights the effect of velocity impulses on the stability boundaries of Fig. 4.1 for positively-charged grains in three orthogonal directions: a prograde azimuthal impulse ($\Delta v_\phi = +0.5$ km s^{-1}); a radial boost ($\Delta v_r = +0.5$ km s^{-1}); and the vertical direction ($\Delta v_z = +0.5$ km s^{-1}). In each case, the orbital stability boundaries are only moderately affected by variable launch speeds; circular orbits are thus an excellent approximation when considering stability. Only the azimuthal impulse appreciably affects the orbital energy, and hence shifts the stability boundary (larger grains on the right in Fig. 4.3a). In this case, the positive Δv_ϕ increases the Kepler orbital energy significantly, thereby preventing grains near the right-most radial stability boundary from falling into Jupiter. A negative Δv_ϕ would destabilize grains near this boundary, permitting additional grains to fall into the planet. The left side boundary of the radially unstable zone is basically unaffected by all impulses, in agreement with Fig. 4.2.

The vertical stability boundaries are moderately affected by the Δv_ϕ (Fig. 4.3a) and Δv_z (Fig. 4.3c) initial impulses, but a radial impulse (Fig. 4.3b) has almost no discernable effect. Note that although in the Lorentz limit, the radial range of motion is too small to be significantly altered with a Δv_ϕ launch impulse, the change in the area of a gyroloop still noticeably affects the high L_* stability boundary in Fig. 4.3a. Since $\Delta v_\phi > 0$ in Fig. 4.3a, the increased gyrospeed expands the gyroloop, leading to a stronger mirror force and hence a reduced region of vertical instability. Enhanced instability results for $\Delta v_\phi < 0$. A vertical impulse Δv_z of either sign also leads to additional instability (Fig. 4.3c). For

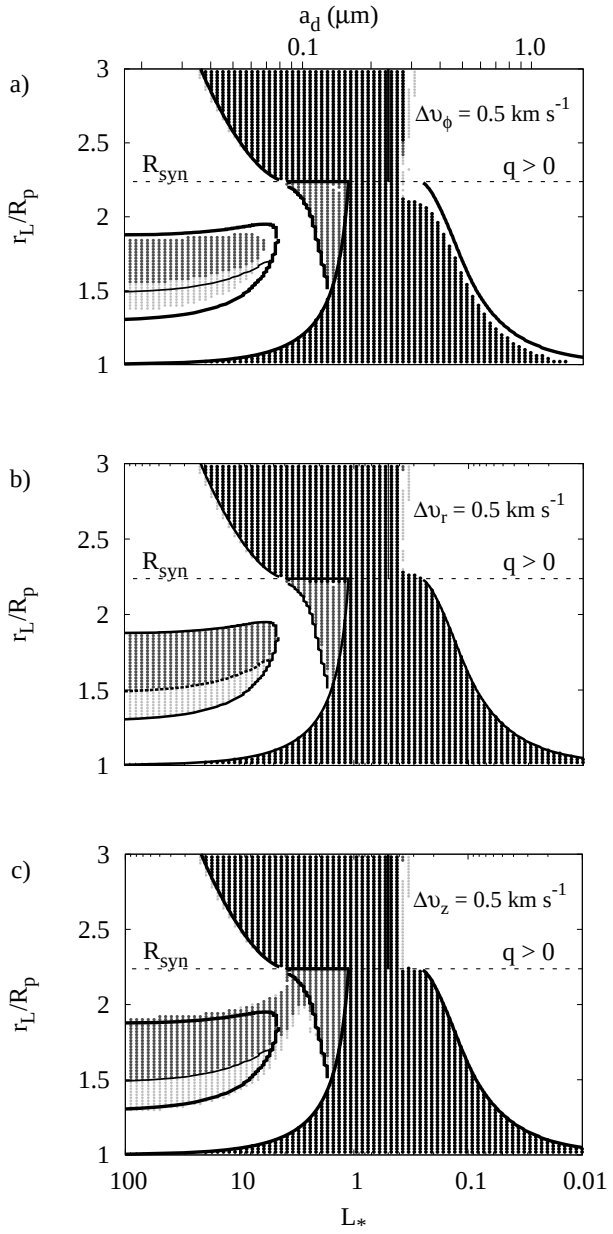

Figure 4.3: Stability of positively-charged grains launched with a) an azimuthal launch speed $\Delta v_\phi = 0.5$ km s^{-1} faster than the local Kepler speed, b) $\Delta v_r = 0.5$ km s^{-1}, and c) $\Delta v_z = 0.5$ km s^{-1}, integrated over 0.1 years. The solid curves are the stability boundaries of Fig. 4.1 where grains are launched at the local circular Kepler speed. The greyscale matches Fig. 3.1b with the darkest points denoting grains that escape or collide with Jupiter near the equator plane, the moderate grey marks collisions at high latitudes ($\lambda > 5°$), the light grey shows HLO grains that were locally unstable and achieved large vertical oscillations, but were otherwise bound globally. The white regions denote trajectories that were locally stable. With these launch impulses, the radial stability is only significantly affected by Δv_ϕ while the vertical stability is affected by both Δv_ϕ and Δv_z. A radial perturbation, Δv_r, has discernable effects.

moderate values of L_* in particular, the Δv_z impulse causes the vertical instability region to dramatically expand near $L_* = 3, r_L = 2R_p$, and merge with the HRLO region of large radial and vertical oscillations. Negatively-charged grains (cf. Fig. 4.1) are similarly affected by 0.5 km s^{-1} impulses.

Overall, since the majority of real debris particles have much smaller speeds relative to their parent satellites, we conclude here that the stability boundaries are fairly insensitive to grain launch conditions. We note that new stability boundaries appropriate for non-circular initial orbits could be derived analytically using Hamiltonian methods (Jontof-Hutter and Hamilton 2012a; Mitchell et al. 2003; Northrop and Hill 1982; Schaffer and Burns 1994), but as the effect is unimportant for our purposes, we turn instead to more complicated magnetic field geometries.

4.3.2 Vertically Offset Dipole

In this section we isolate the effect of Jupiter's dipole offset, modelled by the g_{10} and g_{20} magnetic field terms, on orbital stability. The maps in Fig. 4.4 show that the offset field exacerbates the vertical instability for both negative and positive grains but has little effect on the radial stability boundaries. For the positive grains, the vertically unstable and HRLO zones overlap as in Fig. 4.3c.

In the equator plane, the g_{20} magnetic is radial, and the corresponding $\vec{v} \times \vec{B}$ force is vertical. Thus the g_{20} magnetic field term primarily adds a vertical force, thereby expanding the vertical instability. In fact, the stability map in Fig. 4.4b resembles Fig. 4.3c, which modelled a vertical impulse on the grains at launch in a centered and aligned dipole; comparison of the two figures shows that g_{20} is a far more important effect. Note also that, unlike the effect of a Δv_z impulse, the offset dipole is effective at destabilizing grains near the planet, causing an initial vertical bounce oscillation and expanding the vertical instability.

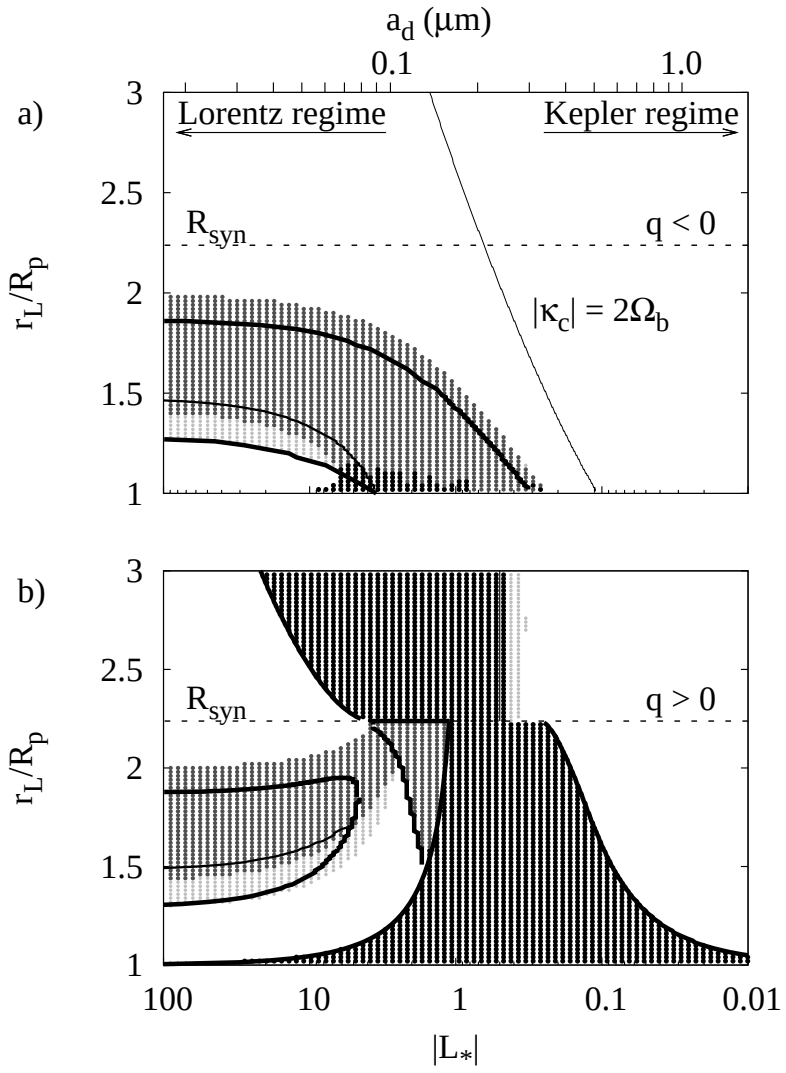

Figure 4.4: Stability of Kepler-launched negative grains (a) and positive grains (b) in a **vertically offset dipole field** for Jupiter, modelled with just the g_{10} and g_{20} magnetic field terms, and integrated over 0.1 years. The curves indicate the stability boundaries for the centered and aligned dipole configurations from Fig. 4.1. In this map, the dark areas are radially unstable grains that either hit the planet or escape at low latitude ($|\lambda| < \lambda_m = 5^\circ$). The moderately grey regions are vertically unstable grains that collide with the planet at high latitude ($|\lambda| > \lambda_m$), and the light grey regions show HLO stable grains that exceed λ_m in latitude; the same criteria we have adopted for the aligned dipole magnetic fields of Fig. 4.3.

Coefficients				Strength (Gauss)			
	g_{10}	g_{11}	h_{11}	4.218	-0.664	0.264	
	g_{20}	g_{21}	g_{22}	-0.203	-0.735	0.513	
		h_{21}	h_{22}		-0.469	0.088	
g_{30}	g_{31}	g_{32}	g_{33}	-0.233	-0.076	0.168	-0.231
	h_{31}	h_{32}	h_{33}		-0.588	0.487	-0.294

Table 4.2: Jupiter's Magnetic Field.

4.3.3 Tilted Dipole

In testing the effect of a tilted dipole field, we include the g_{10}, g_{11} and h_{11} terms in our numerical models, setting g_{20} and all higher-order terms, (reproduced here in Table 4.2) to zero. Both g_{11} and h_{11} are dipolar magnetic field components, orthogonal to the aligned g_{10} field, as well as to each other. The sum of all three is a simple tilted dipole.

Since the magnetic and gravitational equators do not coincide, we consider two separate equatorial launch phases: (i) $\phi_0 = 0^\circ$, the ascending node of the magnetic equator on the geographic equator and (ii) $\phi_0 = 90^\circ$, where the magnetic equator reaches its highest northern latitude of 9.6°. At this launch phase, grains can reach latitudes $\approx 20^\circ$ north and south of the equator, even if their trajectories are stable. Our stability results for negatively-charged grains are plotted in Fig. 4.5.

Although slight differences with launch phase are apparent, Figs. 4.5a and 4.5b are quite similar. Jupiter's tilt is a stronger effect than its offset (see Fig. 4.4a), extending the vertical instability boundary significantly outwards and close to R_{syn}. The dramatic outward expansion of the vertical instability can be understood as follows. For an aligned dipole, as synchronous orbit is approached, both the velocity relative to the magnetic field and the electromagnetic forces tend toward zero. For a tilted dipole, however, the magnetic field lines cross the equator plane with a radial component, causing a substantial $\vec{v} \times \vec{B}$ vertical force as with the offset dipole. These forces push particles out of the plane

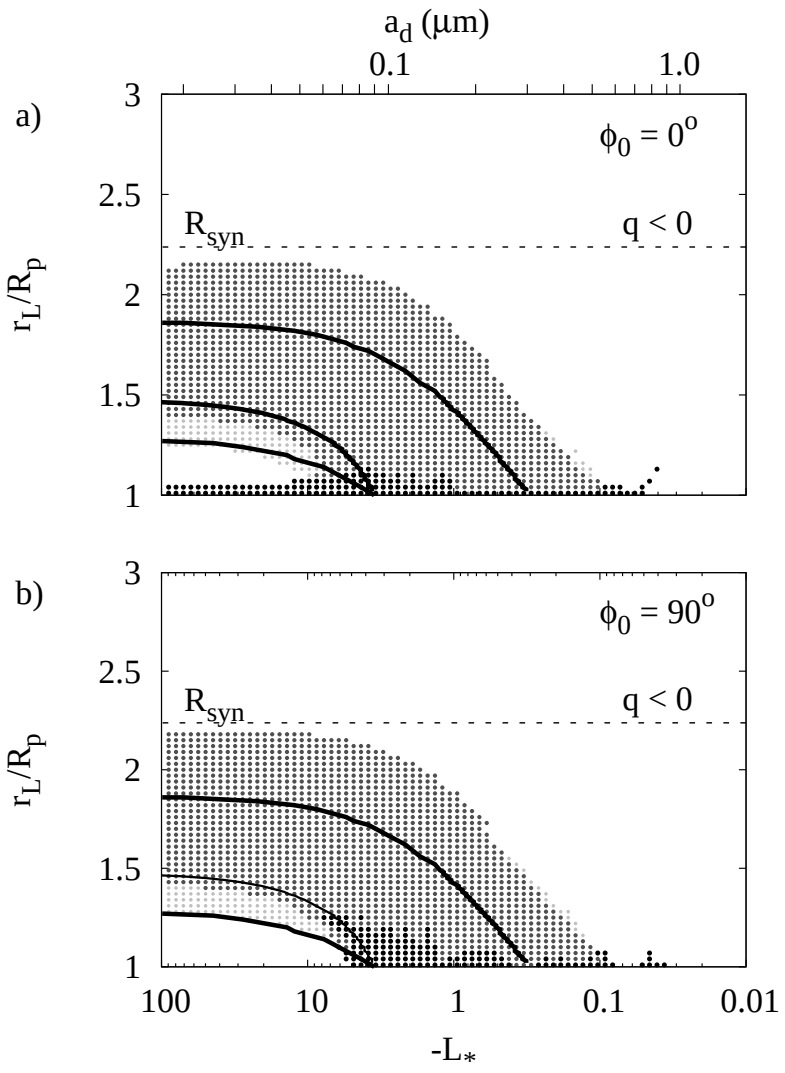

Figure 4.5: Stability of **negative** grains integrated over 0.1 years in a **tilted dipole field** for Jupiter, with the launch longitude at two locations; a) where the magnetic equator crosses the planetary equator plane ($\phi_0 = 0°$), and b) where the magnetic equator reaches its highest geographic latitude ($\phi_0 = 90°$). As before, the curves are the numerically determined stability boundaries for the aligned dipole case from Fig. 4.1a. The grey scale is similar to Figs. 4.3 and 4.4: dark points are grains that collide with the planet at low latitudes, the moderate grey region denotes grains that were vertically unstable to collide with the planet at latitudes higher than $\lambda_m = 20°$, the lightest grey marks trajectories that were excited to higher latitudes but remained bound, and the white areas represent grains that were locally stable. The only difference from Fig. 4.3 and 4.4 is that here we define the low latitude to be $|\lambda_m| < 20°$ rather than 5°.

along field lines, leading to enhanced instability. Interestingly, the inner boundary at ($L_* = -50$, $r_L/R_p = 1.4$) is far less affected.

One key difference in the two panels of Fig. 4.5 occurs for high L_* along $r_L/R_p = 1$; launching at the node ($\phi_0 = 0^\circ$) leads to collisions while launching at $\phi_0 = 90^\circ$ does not. This difference is due to the curvature of the field lines in a dipole. In an aligned dipole magnetic field, stable mirror motion causes EM-dominated grains to oscillate about the magnetic equator, whereby the turning points or mirror points confine the latitudinal range of the grain. Launching from $\phi_0 = 90^\circ$ in the tilted magnetic field ensures that the launch point is at one of the mirror points, and this vertical turning point is relatively close to Jupiter. Thus grains launched near $1R_p$ initially move radially outward and do not collide with the planet. By contrast, for grains launched at the node where $\phi_0 = 0^\circ$, the mirror points are necessarily closer to the planet than the launch distance and, accordingly, we see that grains launched within $1.06R_p$ are forced to collide with Jupiter.

Another, more subtle difference between Figs. 4.5a and 4.5b, is that in the Lorentz limit, grains launched at the node ($\phi_0 = 0^\circ$) are slightly more stable close to R_{syn} than those launched at $\phi_0 = 90^\circ$ e.g. at ($L_* = -100$, $r_L/R_p = 2.21$). In fact, both the inner and outer vertical stability boundaries in the Lorentz limit are shifted slightly outwards for $\phi_0 = 90^\circ$ compared to launches at $\phi_0 = 0^\circ$. Positively-charged dust grains are similarly affected by the addition of the dipole tilt. As with negative grains, we present two launch phases in Fig. 4.6, and find differences in orbital stability similar to those already discussed for Fig. 4.5. In particular, the azimuthal dependencies for highly-charged dust grains ($|L_*| >> 1$) are almost identical for both negative and positive charges (Fig. 4.6). For all launch longitudes, the vertical instability expands greatly outwards nearly to synchronous orbit. For both phases of ϕ_0, the vertical instability expands very little towards the planet. As in Fig. 4.5a trajectories are unstable for $\phi_0 = 0^\circ$ immediately above the planet (Fig. 4.6a).

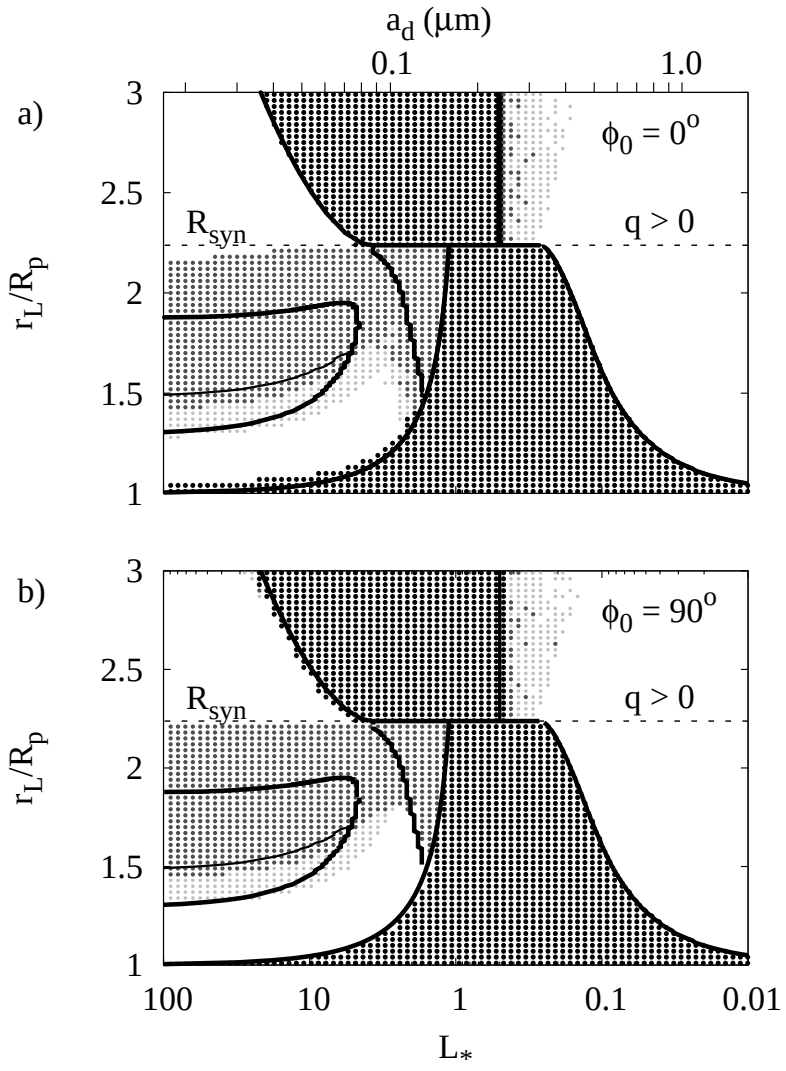

Figure 4.6: Stability of **positive** grains integrated over 0.1 years in a **tilted dipole field** for Jupiter, with two different launch longitudes: $\phi_0 = 0°$, where the magnetic equator crosses the planetary equator plane, and $\phi_0 = 90°$, where the magnetic equator reaches its highest geographic latitude. The solid black curves mark the stability boundaries for the aligned dipole case from Fig. 4.1b. As in Fig. 4.5, the darkest points denote grains that strike the planet at low latitude ($|\lambda_m| < 20°$, within twice the tilt angle), the moderate grey marks grains that strike the planet at high latitudes, the lightest grey marks grains that remain bound between high latitude mirror points, and the white area represents grains that are vertically stable.

As in Fig. 4.5, both the inner and outer vertical stability boundaries in the Lorentz limit are shifted slightly outwards for the $\phi_0 = 90^\circ$ launches of Fig. 4.6b compared to the $\phi_0 = 0^\circ$ launches of Fig. 4.6a. The two boundaries have slightly different explanations. For the outer boundary near R_{syn}, launching at $\phi_0 = 90^\circ$ allows the initially larger vertical electromagnetic forces to drive the grain to higher latitudes where the gravity of the planet can overwhelm the centrifugal force and cause instability (Jontof-Hutter and Hamilton 2012a). Near the inner vertical boundary, grains launched at the node $\phi_0 = 0^\circ$ have a higher latitudinal range and are slightly less stable.

The radial stability boundaries are largely unaffected by the tilt in the magnetic field, although some slight differences are evident to the left of the radial instability region. Note the subtle difference along the left-most radial stability boundaries between Fig. 4.6a and Fig. 4.6b, where grains launched at $\phi_0 = 90^\circ$ inside R_{syn}, are slightly more stable than those with $\phi_0 = 0^\circ$. Outside synchronous orbit, however, the reverse holds true. This is most easily understood as an overall outward shift of the instability region from $\phi_0 = 90^\circ$ to $\phi_0 = 0^\circ$. Thus $\phi_0 = 90^\circ$ grains behave almost exactly like $\phi_0 = 0^\circ$ grains that have been launched a bit further from the planet. Note that this difference with launch phase was seen for the negative grains near the planet as well (Fig. 4.5), and the explanation is the same.

Until now we have only considered instabilities that remove a grain typically within hours. However, the tilted dipolar field causes further instabilities acting over weeks to months, and over a greater range of launch distances than the aligned dipolar case. These longer-term effects are explored below.

4.3.4 Resonant Effects in a Tilted Dipole Field

In an aligned dipole field, it can be shown that negative grains launched from outside R_{syn} at the Kepler speed are permanently confined between their launch distance and R_{syn}; they are energetically unable to escape (Jontof-Hutter and Hamilton 2012a). The tilted dipole field however, permits radial motion away from R_{syn}, and actually enables some negative grains to depart the planet, as was first seen by Hamilton (1996).

In Fig. 4.7, we show the stability maps for Jupiter modelled with the g_{10} and g_{11} magnetic field components for dust grains with both negative and positive charges whose trajectories were integrated for one Earth year. We seek to highlight the motion away from synchronous orbit for the negative grains, and towards R_{syn} for the positive grains, motions precluded by a simple aligned dipolar magnetic field.

Within synchronous orbit, the negatively-charged grains of Fig. 4.7a shows the same short term instabilities seen in Fig. 4.5b. Notice in Fig. 4.7a, however, the large finger of instability outside synchronous orbit. This feature traces grains that suffer significant and unusual motions away from R_{syn}, and it points towards $r_L/R_p = 3.55$ which happens to be the location of the outer 1:2 resonance (Hamilton 1994; Hamilton and Burns 1993b; Schaffer and Burns 1987, 1992; Showalter et al. 2008). Furthermore, the highly detailed dark grey structures near $|L_*| = 1$ outside R_{syn} (Fig. 4.7a) indicate significant numbers of negative grains that escape within one year.

These results are important for escape from the Io plasma torus, the most likely source of the Jovian high-speed dust streams (Graps et al. 2000; Horányi et al. 1993b). Dust streams are comprised of radially-accelerated positively-charged dust grains, although in the plasma torus itself, dust grain electric potentials are likely to be negative, even in sunlight (Bagenal 1994; Krüger et al. 2003a). Lorentz resonances can provide a rapid escape mechanism for negatively-charged grains launched in the plasma torus. Once dust

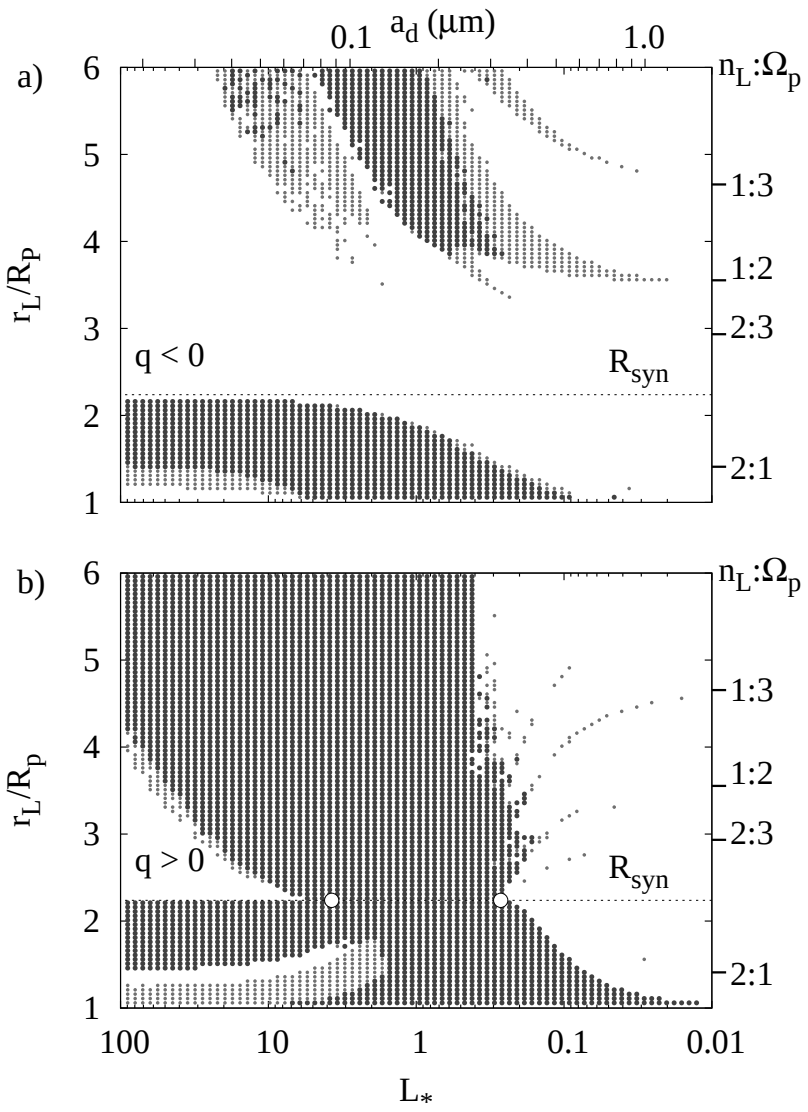

Figure 4.7: Destabilizing effects of a **tilted dipole** magnetic field for Jupiter, with launch at $\phi_0 = 90^\circ$. Integrations are for one Earth year, and we show a greater radial range than in Figs. 4.5 and 4.6. Note that the greyscale that we use here is different from the earlier figures. Here, the darkest region denotes grains that either escape or crash into Jupiter within 1 year of launch. For the negative grains, the light grey marks grains with radial motions *away* from R_{syn} (in the direction opposite that expected for gyromotion), by at least $0.04 r_L$, revealing the destabilizing effect of the tilted magnetic field. For positive grains, the light grey indicates trajectories with radial motions towards R_{syn} of at least $0.02 r_L$. As always, the white indicates stability.

grains is free of the torus, charging currents become positive and the grains are accelerated to escape. We shall discuss this in detail in Chapter 5.

For the positive grains, Fig. 4.7b shows an increased number of grains that are unstable, compared to Fig. 4.6b. The most striking difference is that in Fig. 4.7b, there are rough patches of additional radial instability just outside R_{syn} near ($L_* \approx 0.2$, $r_L/R_p = 3$). These unstable patches transition smoothly to become thin tracks of bound grains with excited radial ranges in the Kepler regime which, like the negative grains in Fig. 4.7a, point towards discrete integer ratios of the planetary spin and Kepler orbital frequencies.

Accordingly, we look to extend the concept of Lorentz resonances, (much studied in the Kepler limit by authors including Burns et al. 1985; Hamilton 1994; Hamilton and Burns 1993b; Schaffer and Burns 1987, 1992), to cover the entire range of charge-to-mass ratios. To determine the location of these Lorentz resonances, we start with the resonant equation

$$\dot{\Psi} = A\omega_c + B\Omega_p + C\dot{\Omega}_{node} + D\dot{\varpi}_{peri}, \tag{4.8}$$

where the coefficients A, B, C and D are integers that must sum to zero (Hamilton 1994). Here ω_c is the orbital frequency of the guiding center, Ω_p is the planetary spin rate, $\dot{\Omega}_{node}$ is the precession rate of the ascending node, $\dot{\varpi}_{peri}$ is the precession rate of the pericenter, and Ψ is the resonant argument; $\dot{\Psi}$ equals zero at a Lorentz resonance.

Next, we rewrite $\dot{\varpi}_{peri}$ and $\dot{\Omega}_{node}$ in terms of our general frequencies from Eqs. 4.3-4.6 which cover all charge-to-mass ratios. The precession rates are simply

$$\dot{\varpi}_{peri} = \omega_c - |\kappa_c| \tag{4.9}$$

and

$$\dot{\Omega}_{node} = \omega_c - \Omega_b \tag{4.10}$$

where κ_c, the epicyclic frequency of motion, is negative by convention for retrograde epicycles. Recall that in the gravity limit, $\omega_c = |\kappa_c| = \Omega_b = n_c$ and hence $\dot{\varpi}_{peri} =$

$\vec{B}$-field terms	Res. name	r_L ($L_* \to 0$)	Res. frequency $\dot{\Psi}$	Corotating form
g_{11}	1:4	$5.64R_p$	$4\omega_c - \Omega_p - 2\dot{\varpi}_{peri} - \dot{\Omega}_{node}$	$\dot{\phi}_c + 2\lvert\kappa_c\rvert + \Omega_b$
g_{11}	1:3	$4.66R_p$	$3\omega_c - \Omega_p - \dot{\varpi}_{peri} - \dot{\Omega}_{node}$	$\dot{\phi}_c + \lvert\kappa_c\rvert + \Omega_b$
g_{11}	1:2	$3.55R_p$	$2\omega_c - \Omega_p - \dot{\Omega}_{node}$	$\dot{\phi}_c + \Omega_b$
g_{21}	1:3	$4.66R_p$	$3\omega_c - \Omega_p - 2\dot{\varpi}_{peri}$	$\dot{\phi}_c + 2\lvert\kappa_c\rvert$
g_{21}	1:3	$4.66R_p$	$3\omega_c - \Omega_p - 2\dot{\Omega}_{node}$	$\dot{\phi}_c + 2\Omega_b$
g_{21}	1:2	$3.55R_p$	$2\omega_c - \Omega_p - \dot{\varpi}_{peri}$	$\dot{\phi}_c + \lvert\kappa_c\rvert$
g_{22}	2:4	$3.55R_p$	$4\omega_c - 2\Omega_p - \dot{\varpi}_{peri} - \dot{\Omega}_{node}$	$2\dot{\phi}_c + \lvert\kappa_c\rvert + \Omega_b$
g_{22}	2:3	$2.93R_p$	$3\omega_c - 2\Omega_p - \dot{\Omega}_{node}$	$2\dot{\phi}_c + \Omega_b$
g_{22}	2:1	$1.41R_p$	$\omega_c - 2\Omega_p + \dot{\Omega}_{node}$	$2\dot{\phi}_c - \Omega_b$

Table 4.3: Selected Lorentz resonances at Jupiter (column 2), driven by the magnetic field coefficient in column 1, appear, for small charge-to-mass ratios, at the locations given in column 3. The resonance frequency is given in its most general form (column 5) and in a second form most useful when gravity dominates (column 4) .

$\dot{\Omega}_{node} = 0$, as expected. As an illustration, we focus on radial resonances for which $C = 0$.

Setting Eq. 4.8 to zero and using Eq. 4.9, we find:

$$-B\omega_c + B\Omega_p - D|\kappa_c| = 0 \tag{4.11}$$

or

$$B\dot{\phi}_c + D|\kappa_c| = 0, \tag{4.12}$$

since in the frame corotating with the magnetic field, the azimuthal frequency of the guiding center is given by $\dot{\phi}_c = \omega_c - \Omega_p$.

Equation 4.12 shows that a Lorentz resonance affecting radial oscillations reduces to a simple ratio between the epicyclic frequency $|\kappa_c|$, and the motion of the guiding center relative to the rotating magnetic field ($\dot{\phi}_c$). Our approach thus shows how to extend classical Lorentz resonances to remain valid at arbitrary charge-to-mass ratios.

In Table 4.3, we show select Lorentz resonances for all charge-to-mass ratios and their driving magnetic field terms, taken from Hamilton (1994). In the Kepler limit, these

Lorentz resonances act to slowly increase eccentricities and/or inclinations, destabilizing trajectories over many orbits. The resonances that include multiple instances of $\dot{\varpi}_{peri}$ or $\dot{\Omega}_{node}$ such as the three 1:3 resonance in Table 4.3, are weaker since their strengths in the Kepler regime depend on higher powers of the small quantities e (eccentricity) and i (inclination). At higher charge-to-mass ratios, however, all of these resonances increase in strength, and their effects on grain orbits occur on much shorter timescales than in the Kepler regime. Some negative grains at $6.0R_p$ in Fig. 4.7a escape in as little as a few days.

Figure 4.8 overlays the g_{11} Lorentz resonances of Table 4.3 on the stability map for a tilted dipolar field (the data from Fig. 4.7)a. For negative grains outside synchronous orbit, the Lorentz resonances curve upwards directly into the region of escape for increasing L_*. This occurs because the epicyclic frequency $|\kappa_c|$ increases rapidly with L_* (Eq. 4.4), hence $\dot{\phi}_c$ must also increase to maintain the same resonance (Eq. 4.12). Since $\dot{\phi}_c$ increases away from R_{syn}, remaining in resonance as $|\kappa_c|$ increases necessitates a greater launch distance from synchronous orbit. Although these curves are determined from frequencies that are valid strictly for an aligned dipole field, they nevertheless show an impressive match to our data, despite the more complex magnetic field.

For the positive grains, the resonant tracks in Fig. 4.8b begin at the same locations in the Kepler limit, but curve towards synchronous orbit as L_* increases. The resonant instabilities are all on the right side of the short-term radial instability of Fig. 4.1, and all resonant solutions converge to a single point at ($L_* = 2-\sqrt{3}$, $r_L = R_{syn}$). This is the point at synchronous orbit where $|\kappa_c| = \dot{\phi}_c = 0$, and grain orbits are locally unstable in even a simple aligned dipolar field (Jontof-Hutter and Hamilton 2012a). The convergence to synchronous orbit as L_* increases occurs because for positive grains with $L_* << 1$, $|\kappa_c|$ decreases as L_* increases (Eq. 4.4), and in the resonance $\dot{\phi}_c$ must also decrease (Eq. 4.12), driving distances towards R_{syn}.

The Lorentz resonances destabilize the motion of grains, and hint that a non-axisymmetric

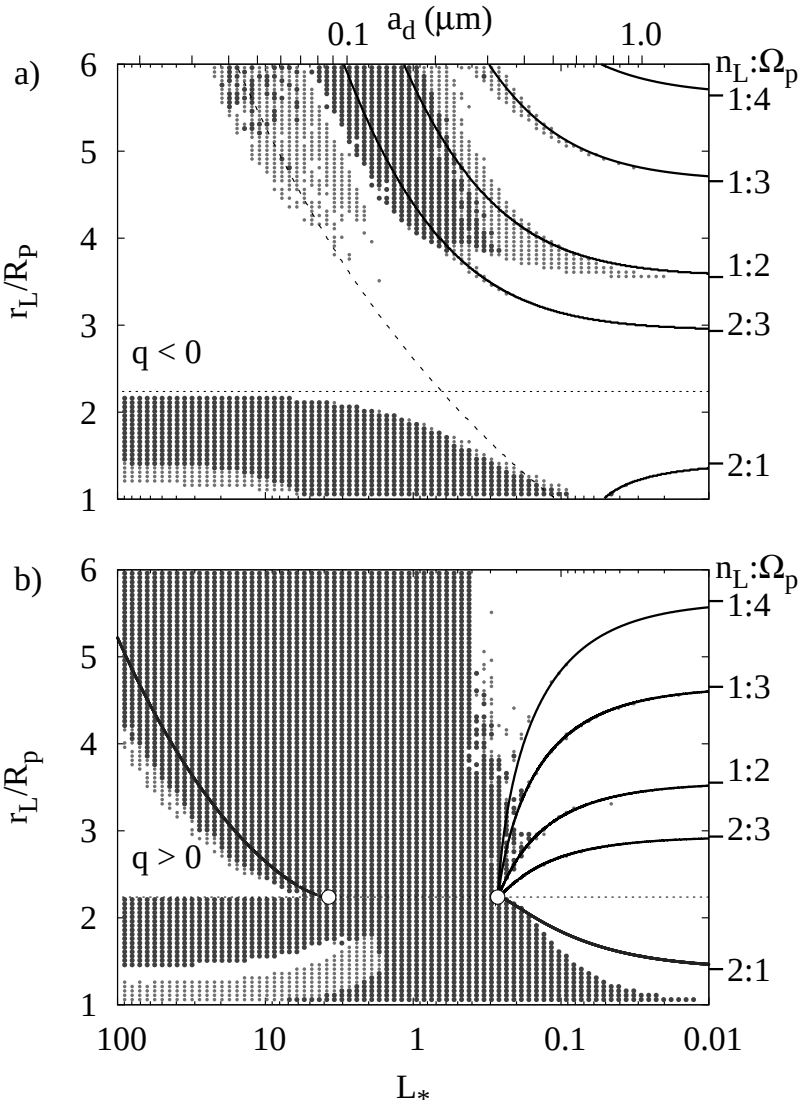

Figure 4.8: The **tilted dipole** stability map of Fig. 4.7 with theoretical curves $\Psi = 0$ from Table 1 superimposed as solid curves. The theoretical curves fall atop the instability "fingers" seen in Fig. 4.7, attesting to the accuracy of the theory. The 2:1 resonance between epicyclic frequency $|\kappa_c|$ and vertical Ω_b motions is also shown in the upper panel, as a dotted curve. In the lower panel, the open circles mark the point ($L_* = 2 \pm \sqrt{3}$, $r_L/R_{syn} = 1$), where all the resonant tracks for positive grains converge. For large L_*, all radial resonances lie nearly atop one another in panel b).

field allows the negative grains to tap into the planetary rotation, making escape energetically favorable. The detailed structure in the stability map of Fig. 4.8, including the escaping negatively-charged grains, is due only to the effects of g_{10} and g_{11}. The theory, however, can only explain the 1:N resonances (Table 4.3) and not the instability of the 2:3 and 2:1 resonances, which nevertheless are definitely present in Figs. 4.7 and 4.8. We will return to explain this discrepancy shortly.

In addition to Lorentz resonances of the type shown in Eq. 4.8, there are also resonances between the dust grain's radial and vertical motions, analogous to the Kozai resonance experienced by highly-inclined orbits. The dominant resonance of this type satisfies: $\omega_c - 2\dot{\Omega}_{node} + \dot{\varpi}_{peri} = 0$, such that $|\kappa_c| = 2\Omega_b$. This 2:1 resonance between radial and bounce motions is the strongest of its type since during one bounce period, north-south symmetry ensures that the dust grain experiences two cycles in magnetic field strength (Jontof-Hutter and Hamilton 2012a). The resonance track also passes close to the high charge-to-mass boundary of the resonant structure in Fig. 4.8a. We turn now to investigate the effects of the individual asymmetric quadrupolar magnetic field terms, which should also power resonances (Table 4.3).

4.3.5 Quadrupole Terms

In this and the following sections, we focus on the escaping negative grains outside synchronous orbit, because these escapes are the most fundamental new effect added by a non-axisymmetric magnetic field. In the stability maps of Fig 4.9, we isolate the effects g_{21} and g_{22} to highlight their respective Lorentz resonances, as compared to the stability boundaries of the tilted dipole from Fig. 4.7a (solid curves). For stable negatively-charged grains in an aligned dipole field, radial motion is always confined between the launch distance and synchronous orbit. Thus, as in Fig. 4.7a, the light grey data in Fig. 4.9 trace where grain trajectories show motions away from R_{syn} that are significant on the scale of

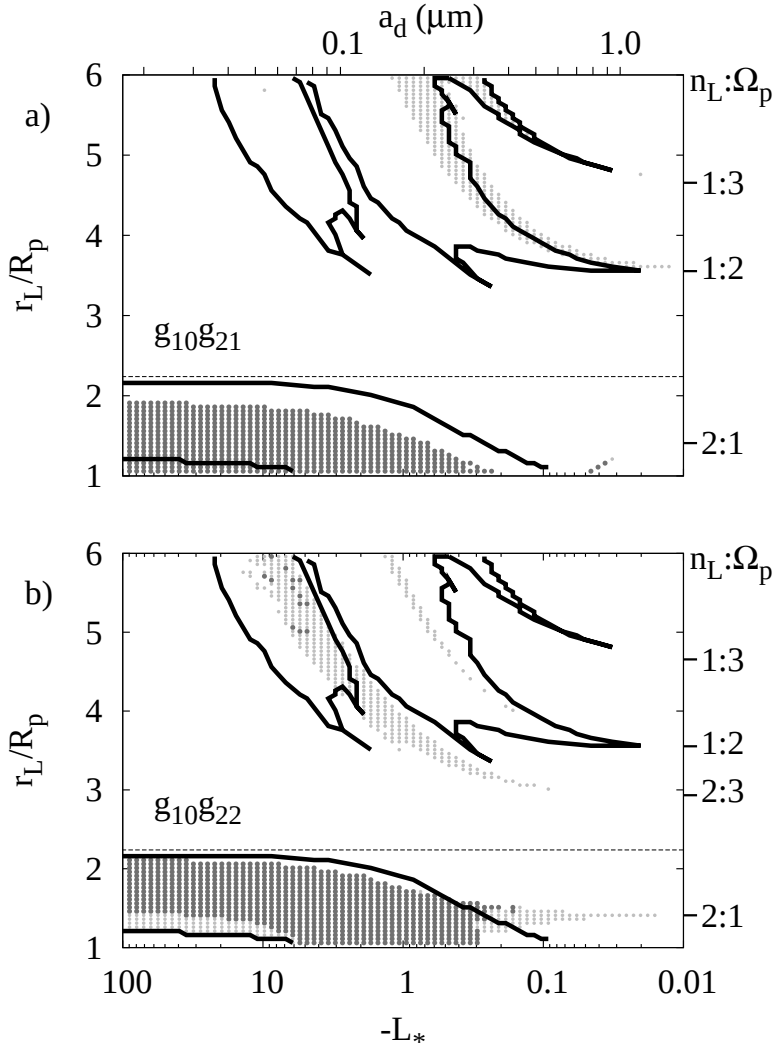

Figure 4.9: **Quadrupole-order terms** isolated in stability maps for negatively-charged dust: To g_{10} we add just g_{21} in panel a) and just g_{22} in panel b), with a 1-year simulation for each dust grain. The light grey marks stable grains whose radial excursions *away* from R_{syn} exceeded 4% of the launch distance, while dark grey indicates collision just as in Fig. 4.7a and 4.8a. The dark curves mark the envelope of instability when just the g_{10} and g_{11} coefficients are included, from the numerical data of Fig. 4.7a.

the launch distance.

The g_{21} and g_{22} terms studied in Figs. 4.9a and 4.9b clearly cause less overall instability than g_{11} in Fig. 4.7a. Consider first, motion within synchronous orbit. The g_{21} term (Fig. 4.9a) is nearly as effective as g_{11} in inducing vertical instability, and in fact is

better able to clear out the region just above the planet's cloudtops. The effect of the g_{22} term (Fig. 4.9b) is similar to, but typically weaker than, g_{11} with one important exception. Note the long, horizontal feature extending towards the 2:1 inner Lorentz resonance in the Kepler regime (small L_*). These stable grains are strongly stirred by the 2:1 vertical Lorentz resonance excited by g_{22}. A similar effect can be seen on the right-hand side of Fig. 4.9a; a small trail of points near ($r_L/R_p \approx 1.05$, $L_* \approx -0.03$) hints that g_{21} causes a weak 2:1 inner Lorentz resonance. However, the first-order theory of Hamilton (1994) predicts that g_{32} rather than g_{21} should excite this resonance!

Outside R_{syn}, the situation is more straightforward. Figure 4.9a shows that the g_{21} term strongly excites the 1:3 and 1:2 Lorentz resonances, as expected from Table 4.3. Notice that the 1:2 resonance is significantly stronger than the 1:3 resonance because, in the Kepler limit, the former has a strength proportional to the small orbital inclination i while the latter's strength depends on the product of two small quantities e and i, where e is the orbital eccentricity (Hamilton 1994). Interestingly, in one way the g_{21} term has a stronger effect on radial motion than the g_{11} term, extending the 1:2 and 1:3 resonances further into the Kepler limit. This can be understood from Table 4.3 and Hamilton (1994), which show that the g_{21} term should strongly excite both of these resonances.

Figure 4.9b shows two main features from the g_{22} term outside R_{syn}, which tend towards 1:2 and 2:3 in the Kepler limit. The g_{22} term excites vertical motions (Hamilton 1994), which are not traced directly in Fig. 4.9, but which clearly couple to radial motions. This causes the outer 1:2 and 2:3 resonances seen in Fig. 4.9b, as well the strong inner 2:1 resonance that reaches far into the Kepler regime. A glance at Table 4.3 shows that g_{22} excites a first-order 2:3 inclination resonance and a second-order mixed 2:4 resonance, accounting for the differing responses of grains near these resonances visible in Fig. 4.9b.

We are left with a few paradoxes. First, how does the g_{11} magnetic field term excite the 2:3 and 2:1 Lorentz resonance? And how does the g_{21} term excite the 2:1 resonance? To

answer these questions, we require a second-order expansion of the Gaussian perturbation equations (Danby 1988), for the electromagnetic force. The first-order Fourier series expansion in the small parameter L_* was obtained by Hamilton (1994) for each magnetic field coefficient by treating the orbital elements as constants. To extend this to second order, we take the Fourier series first-order solution for each orbital element and insert it on the right-hand side of the Gaussian perturbation equations. Simplifying requires identities for the product of two trigonometric functions and we end up with second-order L_*^2 corrections to the time rates of change of the orbital elements. Thus the power in each resonant frequency in Table II of Hamilton (1994) is augmented by a second-order correction. Calculating the strength of these corrections is a straight-forward but unenlightening exercise which we do not undertake here, as the calculation is clearly invalid for $L_* > 1$ when the third- and higher-order terms cannot be ignored. Indeed, the very concept of orbital elements also breaks down for $L_* > 1$ when electromagnetism is no longer a small perturbation to gravity.

Instead, we explore the form of the corrections and show how magnetic field coefficients can excite resonant terms other than those shown in our Table 4.3 and in Table II of Hamilton (1994). Consider first the $g_{10}g_{11}$ simulation of Figs. 4.7 and 4.8. To second order, this combination of coefficients excites two relevant 2:3 resonances: $\dot{\Psi} = 3\omega_c - 2\Omega_p - \dot{\varpi}_{peri}$ and $\dot{\Psi} = 3\omega_c - 2\Omega_p + \dot{\varpi}_{peri} - 2\dot{\Omega}_{node}$, both with amplitude proportional to $L_*^2(R_p/r)^6 g_{11}^2 ei^2$. In addition, a 1:2 resonance, $\dot{\Psi} = \omega_c - 2\Omega_p + \dot{\varpi}_{peri}$ is also excited, with amplitude also proportional to $L_*^2(R_p/r)^6 g_{11}^2 ei^2$. These resonances show up in Figs. 4.7 and 4.8 near the planet where the radial term is relatively large, near instability boundaries where e and/or i are large, and for particles where L_* itself is relatively large. Comparison of Figs. 4.7b and 4.8b shows that these resonances are weaker than the already-discussed first-order resonances, as expected.

In a similar manner, the second-order theory shows that g_{21} drives the 2:1 resonance

with frequency $\dot{\Psi} = \omega_c - 2\Omega_p + \dot{\varpi}_{peri}$ and amplitude $L_*^2 g_{21}^2 (R_p/r)^8 e^3$ (Fig. 4.9a). The rest of Figs. 4.9a and 4.9b appear to be well explained by the linear theory of Hamilton (1994), which predicts both pairs of instability outside R_{syn}.

The second-order corrections, however, should excite the resonant frequency $\dot{\Psi} = 5\omega_c - 4\Omega_p + \dot{\varpi}_{peri} - 2\dot{\Omega}_{node}$ with amplitude proportional to $L_*^2 (R_p/r)^8 g_{22}^2 e i^2$; the very weak feature just below the 2:3 track and near the center of Fig. 4.9b may be due to this resonance. Furthermore, the frequency $\dot{\Psi} = 3\omega_c - 2\Omega_p - \dot{\varpi}_{peri}$ with amplitude proportional to $L_*^2 (R_p/r)^8 g_{21}^2 e^3$, should excite particle motions in Fig. 4.9a, but no evidence for these motions is seen. This may be due to the fact that horizontal resonances driven by g_{21} are intrinsically weaker than the vertical resonances driven by g_{22} (Hamilton 1994). In any case, given the strong drop in the strength of second-order corrections with distance, their effects outside R_{syn} are minimal.

4.3.6 Realistic Full Magnetic Field Models

Figure 4.10a combines the effects of all dipolar and quadrupole terms for negative grains. Within synchronous orbit, all grains in the Lorentz limit are now unstable, as are all grains within the g_{11} envelope. Furthermore, g_{22} powers a 2:1 vertical resonance with frequency $\dot{\Psi} = \omega_c - 2\Omega_p + \dot{\Omega}_{node}$, seen as the dominant horizontal feature extending from the instability region. Adding the octupole term g_{32} strengthens this feature by exciting a 2:1 radial resonance $\dot{\Psi} = \omega_c - 2\Omega_p + \dot{\varpi}_{peri}$. These resonances have the most dramatic effect on large dust grains due to the strength of the magnetic field near the planet. The g_{33} octupole term adds a spike of instability at the 3:2 resonance as well ($\dot{\Psi} = 2\omega_c - 3\Omega_p + \dot{\Omega}_{node}$).

Outside R_{syn}, a large region of escaping negative grains exceeds the sum of the effects of g_{11} (Fig. 4.7a), g_{21} (Fig. 4.9a) and g_{22} (Fig. 4.9b), although the main resonant tracks are easily identified. In particular, a huge swath of grains centered on $L_* = 5$ at $r_L/R_p = 5$

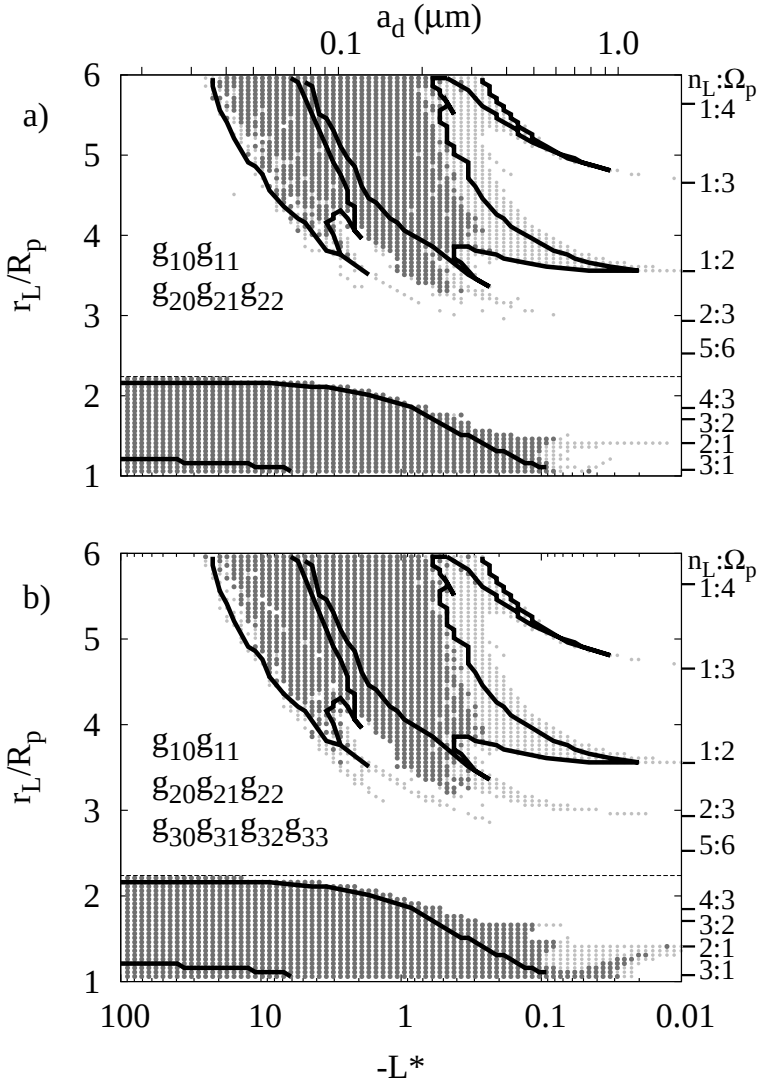

Figure 4.10: Resonant **quadrupolar and octupolar effects** in stability maps for negative dust grains: To the tilted dipole model of Fig. 4.7a, shown here as the solid curves, we add all quadrupole terms (panel a), and all terms out to octupole order (panel b). The darkest regions mark grains that collide with the planet or escape during a 1-year integration. The lighter grey indicates stable grains whose radial excursions *away* from R_{syn} exceeded 4% of the launch distance, as in Figs. 4.7a, 4.8a and 4.9.

escapes here, but is bound for the simpler field geometries of Figs. 4.7a, 4.9a, and 4.9b.

Adding the octupole magnetic field coefficients (Fig. 4.10b) presents only subtle differences from the quadrupole mode of Fig. 4.10a outside R_{syn}. In particular, the locations of the resonant tracks appear to be unchanged. The three narrow fingers in the center of

Fig. 4.10b, however, are noticeably more prominent than the corresponding structures in Fig. 4.10a. The outer 2:3 resonance is driven by the g_{22} term ($\dot{\Psi} = 3\omega_c - 2\Omega_p - \dot{\Omega}_{node}$), but the other resonances cannot be excited by quadrupole terms in the linear theory. The 3:4 resonance is driven by the g_{33} coefficient, but also by a second-order term proportional to $g_{11}g_{22}$. Both are active in the lower plot, while only the latter affects the upper plot. Similarly, the 5:4 resonance is excited by the non-linear g_{22}^2 term (both plots) and by the $g_{11}g_{33}$ term (bottom plot only). As always, when multiple resonances are active, chaos ensues and escape becomes more likely. Note that these differences between Figs. 4.10a and 4.10b are confined within $\sim 4R_p$, due to the rapid radial weakening of the high-order magnetic field terms.

In general, we see that Lorentz resonances widen in launch distance and charge-to-mass ratio as L_* increases. This causes the resonances to overlap and destabilize most of the grains near $L_* = -1$ if grains are launched beyond the immediate vicinity of synchronous orbit. As $|L_*|$ increases, higher-order dependencies on the charge-to-mass ratio permit even more resonances to emerge and vie for control of dust grain dynamics. In Fig. 4.11, the vertical and radial Lorentz resonances for negative and positive grains are plotted atop the stability map for Jupiter's full magnetic field modeled out to octupole order. For the negative grains of Fig. 4.11a, as L_* increases going from right to left, all the radial resonances diverge rapidly from R_{syn}. Most of the vertical resonances however, diverge from synchronous orbit more slowly as $|L_*|$ increases, and in the Lorentz regime these pile up on the vertical stability boundary inside R_{syn} (Fig. 4.1a), where $\Omega_b \rightarrow 0$ and hence, by the resonant condition, $\dot{\phi}_c \rightarrow 0$. The combined effects of many vertical resonances near this boundary destabilizes all grains in the Lorentz regime out to synchronous orbit in Fig. 4.11a.

For the positive grains of Fig. 4.11b, all radial resonances converge on the two locally unstable points along R_{syn}. In the Lorentz regime, the curve outside synchronous orbit

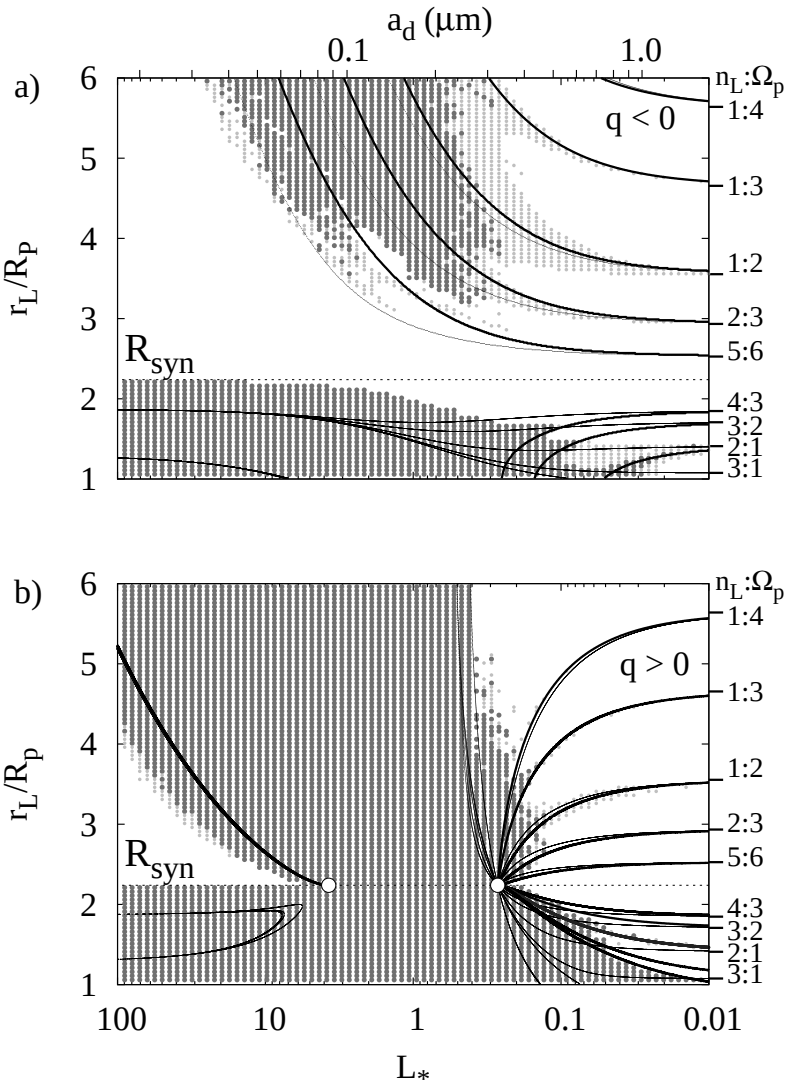

Figure 4.11: Theoretical resonance curves over all charge-to-mass ratios superimposed on a stability map of Jupiter's full magnetic field for a) negative grains (from Fig. 4.10b) and b) positive grains. The dark grey marks dust grains that escaped or crashed into Jupiter during the 1-year integration. The faint grey points denote grains that experience radial motions away from synchronous that exceeded 4% of the launch distance for the negative grains, and towards R_{syn} by at least 2% of r_L for the positive grains. The thick bold curves mark radial Lorentz resonances, and the thin curves track the vertical Lorentz resonances. At synchronous orbit $\dot{\phi}_c = 0$, and the white circles mark the local stability threshold from Jontof-Hutter and Hamilton (2012a) where $\kappa_c \to 0$.

satisfies $\kappa_c \rightarrow 0$. This is further to the left of the stability boundary for an aligned dipole (Fig. 4.1b), ensuring that resonances pile up and further destabilize grains with the additional magnetic field terms in the Lorentz regime. Physically, it means that smaller grains are likely to be expelled for a particular positive electric potential than calculated using the aligned dipolar approximation. For the larger grains, in the Kepler regime, the vertical Lorentz resonances asymptote near the $L_* = 1/2$ boundary where the guiding center distance rapidly increases and the bounce frequency $\Omega_b \rightarrow 0$.

For both positive and negative grains where $L_* << 1$, the outer 1:3 radial and vertical resonances coincide implying $\dot{\varpi}_{peri} = \dot{\Omega}_{node}$. This is indeed the case to first order in L_* as was first deduced by Hamilton (1993a). The result can also be obtained from our Eqs. 4.3, 3.11 and 4.6.

In the Kepler regime, N:N+1 resonances pile up at synchronous orbit (like the 5:6 resonance marked in Fig. 4.11a); for higher N, these are driven by g_{NN} magnetic field terms beyond the octupole that we have considered here. Our model of Jupiter's magnetic field out to octupole order is incomplete; inclusion of higher-order terms would lead to additional escapes. Given the strong radial dependence of higher-order magnetic field components, we expect changes to be limited to regions close to the planet and at high L_*, just like the differences between Figs. 4.10a and 4.10b. Nevertheless, we eagerly await the improved magnetic field model that the Juno spacecraft will soon provide.

4.4 Other planets

After our detailed investigation of Jupiter, we are now in a position to map and interpret stability results for each of the planets in the Solar System. We begin with the planet with the simplest magnetic field, Saturn.

Coefficients	Strength (Gauss)
g_{10}	0.21535
g_{20}	0.01642
g_{30}	0.02743

Table 4.4: Saturn's Magnetic Field.

4.4.1 Saturn

Saturn's full magnetic field can be described by an aligned dipole with a slight vertical offset; the magnetic field coefficients from Connerney et al. (1984) are given in Table 4.4.

Figure 4.12a shows the stability map for negatively-charged grains in Saturn's full magnetic field, with the numerically determined stability boundaries for an aligned and centered dipole included for comparison, as in Fig. 4.4.

As at Jupiter, (see Fig. 4.4) Saturn's dipole offset increases the instability of grains to vertical perturbations. This eliminates the stable zone close to the planet that we saw for the aligned dipole case, and moves the outer vertical stability boundary significantly further from the planet. The effect is stronger at Saturn due to its relative large g_{20} term and to the larger R_p/R_{syn} at Saturn, making the planet a bigger target. By contrast, at Jupiter (see Fig. 4.4), a locally stable region in the Lorentz limit close to the surface survives the inclusion of g_{20}.

For positively-charged grains, in Fig. 4.12b, the offset dipolar field causes the vertical instability to join the radial instability, as in Fig. 4.4b. However, a small island of globally stable grains survives near ($L_* = 3$, $r_L/R_p = 1.3$). The radial stability boundaries for an aligned dipole field for Saturn (solid curves in Fig. 4.12b), match Saturn's full magnetic field remarkably well.

At Saturn we also see a slightly wider range of charge-to-mass ratios excited by the 2:1 resonance between epicyclic and vertical motions, when compared to Jupiter (Fig. 4.4a).

This is due to the range of launch distances extending further out in units of R_{syn} in Fig. 4.12a.

The transition from grains that are lost to the vertical instability to those that remain bound in the B ring is at $1.70R_p$ or $\approx 102,000$ km in the Lorentz limit (Fig. 4.12). This is close to the increase in optical depth in the B ring that begins around $1.65R_p$, and losses to erosion may play a role in ring evolution across this boundary. Northrop and Connerney (1987) argued for a link between the inner edge of B ring and the vertical stability boundary. Their model for vertical motion predicted all highly-charged grains to be unstable within $1.54R_p$ at Saturn, close to the sharp inner edge of the B ring. However, their model did not provide a detailed mechanism and also invoked poorly understood electrostatic effects (Northrop and Connerney 1987; Northrop and Hill 1983b). Voyager 2 data revealed the transition in optical depth between $1.63R_p$ and $1.65R_p$ (98,000 - 99,000 km), a few thousand kilometers inside the vertical stability boundary at Saturn with its full magnetic field configuration. While the proximity of this transition to the vertical stability boundary is intriguing, a detailed model to explain this congruency remains elusive.

Vertical Equilibrium in an Offset Dipole Field

We have seen that even in the Lorentz limit, gravity and the planetary rotation are of crucial importance in the vertical motion of Kepler-launched dust. Here, whilst studying orbital stability in Saturn's full magnetic field, we make a brief digression to consider the location of the vertical equilibrium point for dust grains in an offset dipolar field. In an aligned dipolar magnetic field, grains launched in the equator plane are at equilibrium initially, even if that equilibrium is unstable at certain distances. The additional magnetic field terms g_{20} and g_{30} cause the equator to shift to a vertically-offset position. The g_{20} magnetic field term shifts the magnetic equator to:

$$\frac{z}{R_p} = \frac{g_{20}}{2g_{10}}. \tag{4.13}$$

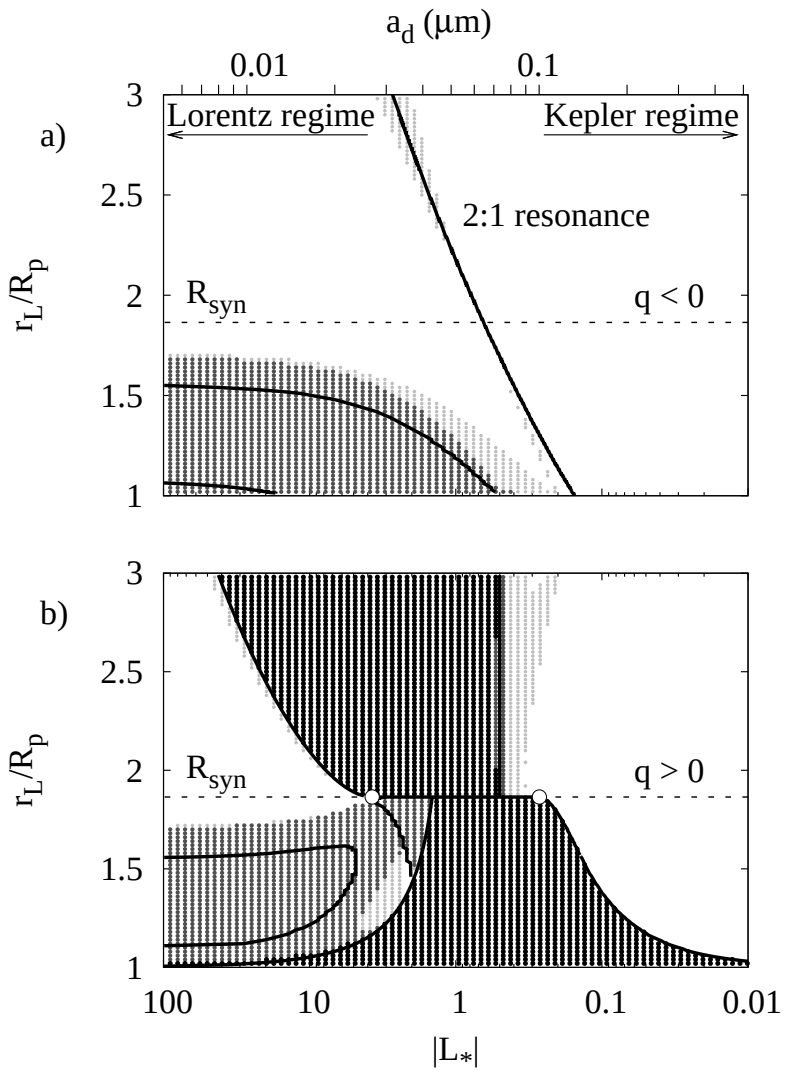

Figure 4.12: Stability of a) negative and b) positive Kepler-launched grains, followed for 0.1 years in Saturn's full magnetic field. The greyscale matches that of Figs. 4.3 and 4.4. The darkest region denotes grains that are radially unstable to escape or strike the planet (positive charges only), the moderate grey scale marks trajectories that were vertically unstable to climb out of the ring plane and strike the planet at high latitude, the light grey scale marks grains that are vertically unstable in the equatorial plane but remain globally bound with mirror points further than $|\lambda_m| = 5^\circ$ from the equator, and the white area marks locally stable orbits. Superimposed on the data are the numerically determined stability boundaries for an aligned and centered dipolar magnetic field model for Saturn (Jontof-Hutter and Hamilton 2012a), as well as the curve marking the analytical 2:1 resonance between epicyclic and vertical motion, which closely tracks band of grains that reach high latitudes but remain bound. The white circles mark the local stability threshold at R_{syn}, where $L_* = 2 \pm \sqrt{3}$.

We obtain this result analytically, by finding the location where $\vec{B}$ is entirely in the $\hat{z}$ direction. Adding g_{30} complicates the analytics substantially. Using numerical data with both the planetary gravity and rotation switched off, however, we find the following empirical expression for the offset magnetic equator:

$$\frac{z}{R_p} = \frac{3g_{20}}{6g_{10} - g_{30}\left(\frac{R_p}{r}\right)^2}. \tag{4.14}$$

This reduces to Eq. 4.13 if g_{30} is neglected, as well as in the distant limit, since the effect of g_{30} declines rapidly with distance. At the planetary surface, the extra g_{30} term at Saturn increases the vertical shift by only $\approx 2\%$, and at Jupiter the effect of g_{30} is even weaker. Vertical oscillations are centered on the offset equator in the distant limit, which at Saturn is $0.038R_p$ northwards. At Jupiter, $g_{20} < 0$, hence the dipolar field is shifted southwards, by $0.024R_p$.

Including the effects of gravity and planetary rotation, we seek vertical equilibrium point for grains launched in the dusty rings. Our launch condition makes synchronous orbit a unique location where the Lorentz force disappears, independent of the magnetic field configuration. Thus at this location, vertical equilibrium remains in the ring-plane. In Fig. 4.13, we determine the vertical equilibrium location in the EM regime, comparing Saturn's full magnetic field to a comparable $g_{10}g_{20}g_{30}$ model for Jupiter, and simple $g_{10}g_{20}$ magnetic field models for both planets. In each case, the equilibrium point is in the ring-plane at R_{syn}, and asymptotes to the offset magnetic equator in the distant limit. As suggested by Eq. 4.14, the addition of g_{30} in the numerical simulations of Fig. 4.13 have only a modest influence.

Inside synchronous orbit, the vertical equilibrium points switch to the opposite hemisphere of the magnetic equator. This change in the direction of the vertical force across synchronous orbit is due to the added Lorentz force from the g_{20} magnetic field on a dust grain launched in the ring-plane, drifting azimuthally in the rotating frame. The direc-

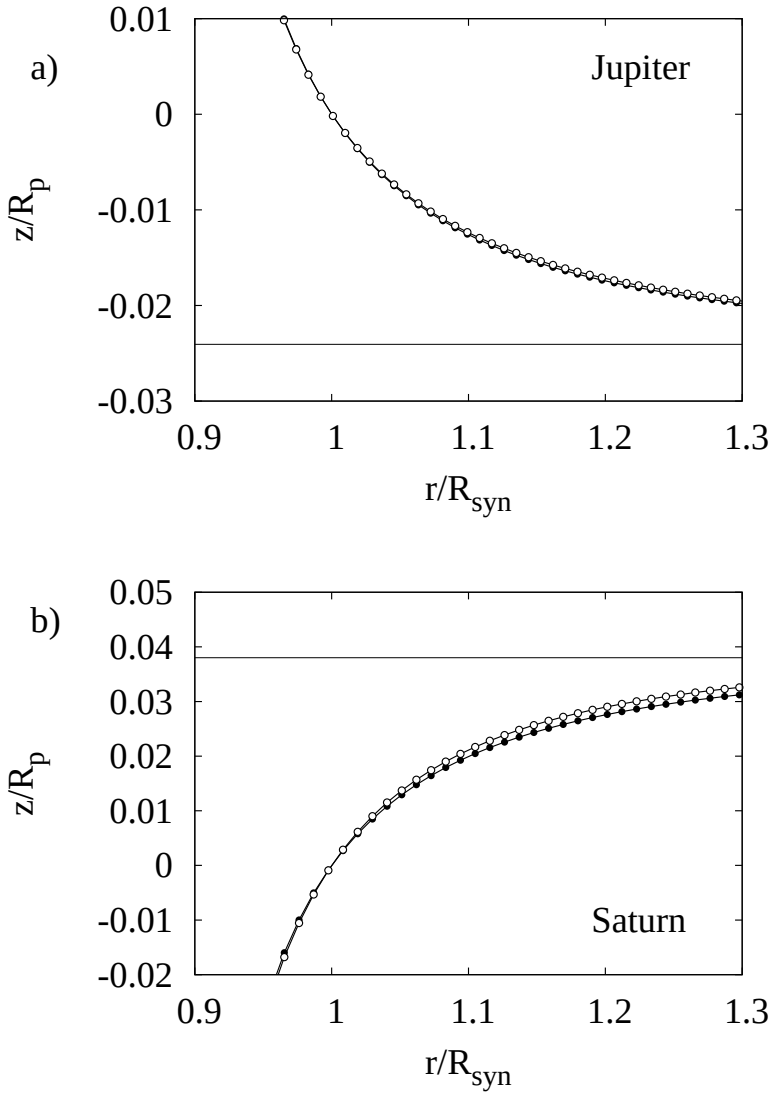

Figure 4.13: Numerically-determined vertical equilibrium points in the EM regime at a) Jupiter and b) Saturn comparing $g_{10}g_{20}$ (filled circles) and $g_{10}g_{20}g_{30}$ (open circles) magnetic field models. For all trajectories, $|L_*| = 10^5$. The horizontal line in each plot is the offset magnetic equator due to g_{20}, in the absence of rotation and gravity. The points mark the midpoints between vertical extrema for Kepler-launched dust grains from $\lambda_L = 0^\circ$, and asymptote towards the magnetic equator with increasing distance. The horizontal axis marks radial distances in units of R_{syn}, while the vertical axis represents vertical distances in units of planetary radii R_p.

Coefficients				Strength (Gauss)			
	g_{10}	g_{11}	h_{11}		-0.30339	-0.02123	0.05758
	g_{20}	g_{21}	g_{22}		-0.01654	0.02994	0.01567
		h_{21}	h_{22}			-0.02006	0.00130
g_{30}	g_{31}	g_{32}	g_{33}	0.01297	-0.02036	0.01289	0.00843
	h_{31}	h_{32}	h_{33}		-0.04093	0.00242	-0.00176

Table 4.5: Earth's Magnetic Field.

tion of the additional force (Eq. 3.1) depends on the sign of product $qV_{drift}g_{20}$. Following Eq. 3.8, inside R_{syn} if $L_* < 0$, the azimuthal drift in the Lorentz regime is prograde. In Saturn's ring-plane, the magnetic field lines due to g_{20} are directed radially inwards. Hence the vertical Lorentz force is directed southwards, and the equilibrium points in Fig. 4.13b are offset in that direction. Furthermore, all vertically unstable grains at Saturn crash in the southern hemisphere. By contrast at Jupiter, $g_{20} < 0$, and (ignoring its other magnetic field terms), vertically unstable grains crash in the northern hemisphere. Note that the azimuthal drift rate changes sign if the grain charge changes sign, hence the vertical force is in the same direction for both negative and positive grains. The drift speed, V_{drift}, also changes sign across synchronous orbit. Hence the vertical equilibrium location switches hemispheres at R_{syn}.

4.4.2 Earth

The Earth's magnetic field is dominated by a dipole tilted by a moderate 11.4° from the axis of rotation. For our full field models, we use the magnetic field coefficients out to octupole order (Table 4.5) taken from Roberts and Soward (1972). For the Earth, $g_{10} < 0$ and the magnetic field is inverted compared to all of the giant planets. Thus for the Earth, $L_* > 0$ for negatively-charged grains, and it is these negative grains that suffer the radial instability (Jontof-Hutter and Hamilton 2012a).

Figure 4.14 compares the stability of grains in Earth's full magnetic field to an aligned dipolar model. With an aligned dipolar field, the vertical instability at Earth in the Lorentz limit is local, leading to a region of high-latitude globally-stable oscillations. For the positive grains ($L_* < 0$, Fig. 4.14b) this locally vertically unstable region curves towards the planet as $|L_*|$ decreases, and only from within a small range of launches near the surface between $L_* \approx -0.1$ and -1.0 do grains actually collide with the planet. This changes very little with the inclusion of Earth's higher-order magnetic field terms, as Fig. 4.14 indicates. More dramatically, the higher-order terms (primarily g_{11}) expand the vertical instability in the Lorentz limit to further distances, almost to R_{syn}. In this region, grains do in fact collide with the planet. The feature is very similar to what we saw at Jupiter in Figs. 4.5 and 4.6, except that the transition from high-latitude oscillations to globally unstable is further from the planet (relative to R_{syn}) in the case of the Earth. Just as at Jupiter, tilting the magnetic field does not move the inner vertical stability boundary significantly. For the negative grains, Fig. 4.14a shows that the vertical instability is also displaced towards R_{syn} and curves slightly upwards to merge with the region of radial instability. The expansion of the vertical instability for both positive and negative charges nearly to synchronous orbit has a unique benefit in assisting the removal of dusty space debris from this crowded region of Earth orbit (Horányi et al. 1988; Juhász and Horányi 1997; Valk and Lemaître 2008).

The radial instability however, is very different at Earth than at Jupiter. Outside synchronous orbit, the higher-order magnetic field terms have little effect and the radial stability boundaries of Jontof-Hutter and Hamilton (2012a) match the data remarkably well. Inside synchronous orbit, Earth has a larger area of HLROs that abut the disjoint regions of equatorially-confined radial instability. Thus Earth's full magnetic field barely alters the radial instabilities expected for an aligned dipole: The few unstable grains that exceed the radial stability boundary on the right side of Fig. 4.14a may be associated with Lorentz

resonances. In particular, the small cluster of points near ($L_* = 0.01$, $r_L/R_p = 2.0$) closely corresponds to the inner 6:1 Lorentz resonance. All else being equal, the Lorentz resonances are more important close to the planet where the magnetic field irregularities are strongest.

As an exercise, we compared the results displayed in Fig. 4.14 with a simpler tilted-dipole model, including just the g_{10} and g_{11} terms (figure not shown). The only noticeable difference that arises is that the positive and negative grains that are excited to high latitudes, near ($|L_*| = 10$, $r_L/R_p = 1.3$) are not excited in the tilted dipole model. A more subtle difference is the extra set of collisions to the right of the radial instability boundary on the right-hand side of Fig. 4.14a marking grains that were lost because of Lorentz resonances. These grains survive in the simple tilted dipole model. Deviations at greater distances are not expected due to the steep radial dependence of the quadrupole and octupole terms, and indeed, they are not seen. All in all, a tilted magnetic dipole is a robust model for the motion of charged dust grains at the Earth.

4.4.3 Uranus

Uranus' complex magnetic field destabilizes grains for a much wider range of charge-to-mass ratios than Jupiter, Saturn or Earth. Figure 4.15 shows the stability of grains launched at Uranus, with magnetic field coefficients out to octupole order (Table 4.6) taken from Ness et al. (1991). This figure highlights the significant dependence of launch azimuth on grain lifetimes. Grain orbit stability was modeled for 12 equally-spaced azimuthal launch positions, and trajectories were followed for 1 year.

Beyond R_{syn}, Uranus's full magnetic field causes a large class of grains to escape rapidly, for both negatively- and positively-charged dust. In general the stability maps for negative and positive grains are very similar, especially inside synchronous orbit. Within R_{syn} all trajectories in the Lorentz limit appear unstable for both negative and positive

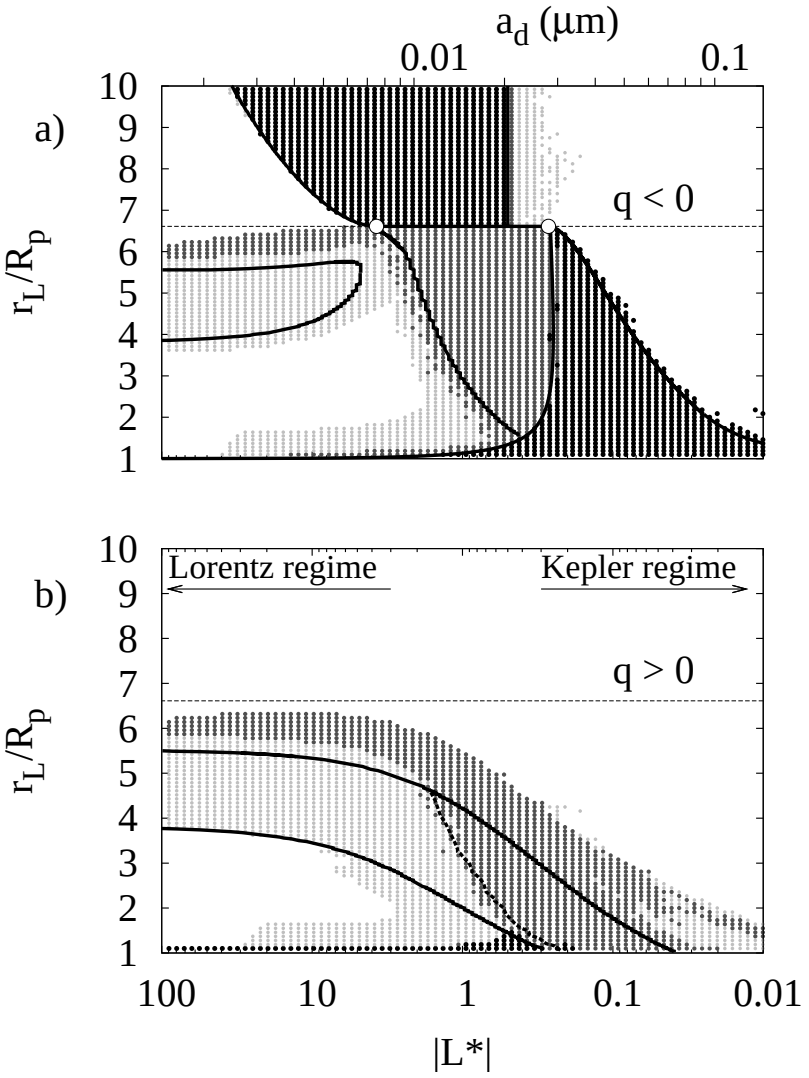

Figure 4.14: Stability of Kepler launched negative (a) and positive (b) grains in Earth's magnetic field complete to octupole order, integrated over 1 year, with launch at $\phi_0 = 0$. The solid curves mark the numerical stability boundaries for the Earth with its anti-aligned g_{10} component alone (Fig. 12 from Jontof-Hutter and Hamilton 2012a). Grains in the darkest region, (negative charges only) crashed into the planet or escaped at a latitude less than twice Earth's 11.4° tilt angle. The moderate grey region marks grains that struck the planet at latitudes higher than twice the tilt angle, the light grey marks grains with stable vertical oscillations with mirror points exceeding twice the tilt angle in latitude, and white regions are the remaining stable orbits. The white circles mark the points $L_* = 2 \pm \sqrt{3}$, at $r_L = R_{syn}$, where grains are on the threshold of radial instability.

Coefficients				Strength (Gauss)			
	g_{10}	g_{11}	h_{11}		0.11893	0.11579	-0.15684
	g_{20}	g_{21}	g_{22}		-0.06030	-0.12587	0.00196
		h_{21}	h_{22}			0.06116	0.04759
g_{30}	g_{31}	g_{32}	g_{33}	0.02705	-0.01188	-0.04808	-0.02412
	h_{31}	h_{32}	h_{33}		-0.07095	-0.01616	-0.02608

Table 4.6: Uranus' Magnetic Field.

charges, which significantly constrains the low-energy plasma environment in the Uranian inner ring system. Furthermore, both Figs. 4.15a and 4.15b show far more dependence on launch phase at high charge-to-mass ratio, on the left side of the stability maps, than on the right, consistent with our results for Jupiter (Fig. 4.6).

Uranus's magnetic tilt as well as its quadrupole and octupole magnetic field coefficients are far more important when compared to its g_{10} term than at Jupiter or Saturn, causing strong Lorentz resonances, and hence a dramatic expansion of escaping negative grains over that seen at Jupiter in Fig. 4.10b. Furthermore, at Uranus, grains as close as R_{syn} can escape, unlike at Jupiter. In Fig. 4.15a, a spike at $(L_* = -0.03, r_L/R_p = 2)$ appears to be associated with the 2:1 inner Lorentz resonance that approaches the Kepler limit at $2.04R_p$. Oddly, this resonance appears stronger for negative grains than for positive ones. At Jupiter, two spikes in Fig. 4.10b distinguish the inner 2:1 vertical and radial resonances. At Uranus, Fig. 4.15a hints at a similar pairing of destabilizing resonances, one curving downward towards the planet as $|L_*|$ increases, arcing slightly upward.

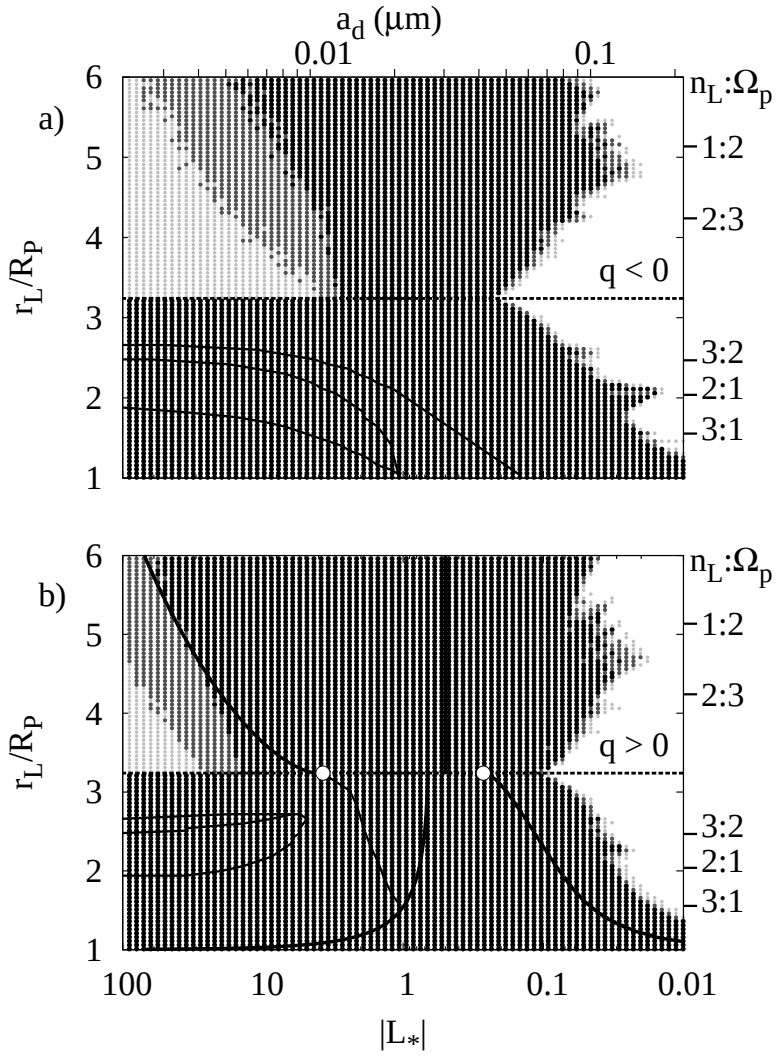

Figure 4.15: Stability of Kepler-launched grains in Uranus' full field over one year. There are three shades of grey, plus white to highlight the effect of azimuthal launch position on grain orbit stability. The darkest grey marks grains that were unstable for all of 12 equally-spaced launch longitudes. The intermediate grey denotes unstable trajectories for 6 to 11 launch positions, the lighter grey 1 to 5 launches, and the white regions were stable for all launch positions. The embedded curves mark the Uranian equivalent of those in Fig. 4.1, the stability boundaries for an aligned dipole magnetic field model. The white circles mark the local radial stability at R_{syn}, where $L_* = 2 \pm \sqrt{3}$.

Coefficients				Strength (Gauss)			
	g_{10}	g_{11}	h_{11}		0.09732	0.03220	−0.09889
	g_{20}	g_{21}	g_{22}		−0.07448	−0.00664	0.04499
		h_{21}	h_{22}			0.11230	−0.00070
g_{30}	g_{31}	g_{32}	g_{33}	−0.06592	0.04098	−0.03581	−0.00484
	h_{31}	h_{32}	h_{33}		−0.03669	0.01791	−0.00770

Table 4.7: Neptune's Magnetic Field.

4.4.4 Neptune

We model Neptune's magnetic field configuration (Table 4.7) with data taken from Connerney et al. (1991). As for Uranus, above, the stability map includes the effect of launch longitude on grain-orbit stability. As with Fig. 4.15, Fig. 4.16 indicates the number of 12 equally-spaced launch azimuths that survive a 1-year integration.

Figure 4.16a maps the stability of negatively-charged dust at Neptune, and includes a large region of escaping negative grains, though this range is slightly smaller at Neptune than at Uranus (Fig. 4.15a). However, the escape region is still much more significant at Neptune than at Jupiter (see Fig. 4.10b), and it too reaches R_{syn}. As at Uranus, grain orbit stability on the Lorentz-dominated side of Figs. 4.16a and 4.16b is strongly dependent on the launch phase. Inside synchronous orbit, much of the Lorentz limit is unstable but in a small region, around $r_L/R_p = 2.2$ for both positive and negative grains, stability varies significantly with launch phase. This contrasts with Uranus, where all grains inside R_{syn} in the Lorentz regime were unstable. Again, however, the instability at Neptune vastly exceeds that of Jupiter.

In the Kepler-dominated regime of Fig. 4.16a, two spikes most likely associated with the inner 2:1 Lorentz resonance feature prominently. Just as we saw at Uranus for positive grains, in Fig. 4.16b, this inner 2:1 resonance appears to be weaker. For negative grains, the stable zone on the gravity-dominated side of Fig. 4.16a reaches to higher L_* values

than we saw for Uranus (Fig. 4.15a). For both planets, the dependence on azimuthal launch position for stability is only important for $|L_*| > 1$. In the Kepler regime, grains move rapidly across magnetic field lines, and instabilities are effectively averaged over all launch phases. All evidence points to greater instability at Uranus than at Neptune. This is consistent with the Uranian dipole tilt of 59° exceeding Neptune's 47°.

4.5 Discussion

In this chapter, we have studied two main effects on charged particle motion: i) non-zero launch velocities from orbiting parent bodies and ii) complex magnetic fields. We shall address one remaining major effect, time-variable electric charges, in Chapter 5.

Non-zero launch impulses relative to the Kepler flow, whether radial, vertical or azimuthal, have very little effect on charged-grain dynamics. Only an azimuthal kick can cause a noticeable effect on the radial stability boundaries. Vertical instability, by contrast, is affected by both azimuthal and vertical impulses. Finally, a radial kick barely affects dust grain motions at all.

When considering the stability of grains in the wide variety of planetary magnetic fields in the Solar System, we have shown in that an aligned and centered dipolar magnetic field provides the maximum stability possible at each planet. The simplest full magnetic field that we have considered, that of Saturn, is well-described as a moderately-offset dipole. With its northward dipole offset, Saturn's magnetic field noticeably expands the vertical instability but has little discernable effect on radial motions.

Jupiter's magnetic field is substantially more complex than Saturn's with a moderate tilt, a southward offset, and sizeable higher-order field coefficients. The tilted dipole strongly affects vertical stability boundaries, and the loss of axisymmetry powers Lorentz resonances. These act to destabilize dust grains, allowing even negative grains at Jupiter

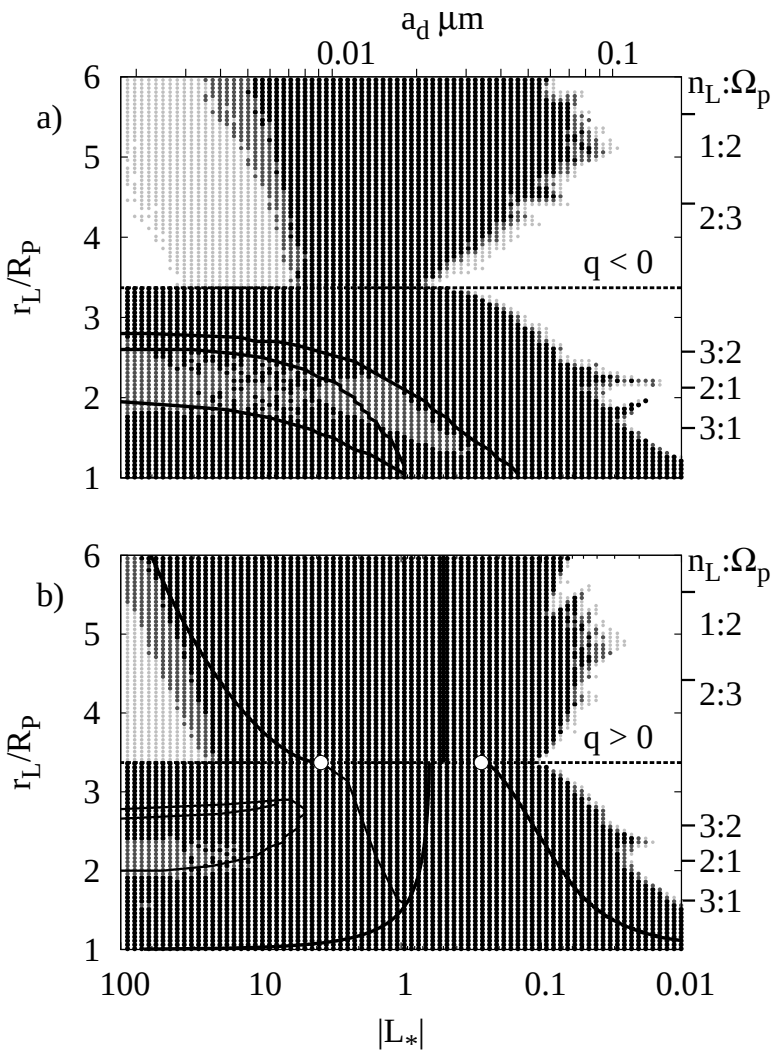

Figure 4.16: Stability of Kepler-launched grains in Neptune's full magnetic field, for twelve equally-spaced azimuthal launch positions, and integrated over one year. The greyscale is as in Fig. 4.15 with the darkest grey unstable for all launch longitudes and grains in the white areas surviving for all launch positions. As in previous figures, we superpose numerically-determined stability results for an aligned dipole as solid curves, and mark the local radial stability threshold at R_{syn}, where $L_* = 2 \pm \sqrt{3}$ with white circles.

to escape. Extending the concept of Lorentz resonances from the Kepler regime to cover all charge-to-mass ratios, we have derived analytical solutions for their locations under the epicyclic model for radial, vertical and azimuthal orbital frequencies.

Like Jupiter, the Earth also has a magnetic field that is dominated by a moderately-tilted dipole. Two important differences, however, distinguish charged-particle motion at Earth from that at Jupiter. Firstly, due to its inverted magnetic dipole, the radial instability at Earth affects negative not positive charges. Secondly, the Earth is very small compared to the size of its synchronous orbital distance, making a local stability criteria poor at predicting global stability boundaries. Because of its small relative size and the rapid decay with distance of higher-order magnetic field terms, Earth's full magnetic field differs little from a simple tilted dipole in destabilizing dust grain trajectories.

Uranus and Neptune both have complex magnetic field configurations which render aligned or even simple tilted dipolar models inapplicable. Both of these planets have substantial quadrupolar and octupolar components, which act to destabilize both negative and positive grains across the synchronous orbital distance, and over a far greater range of charge-to-mass ratios than at the other planets that we have studied. These planets highlight how increases in magnetic field complexity dramatically exacerbate dynamical instabilities. Although future spacecraft missions may provide more detailed planetary magnetic field configurations than we have adopted, any changes to the stability maps we provide here for constant-charge dust grains are likely to be negligible.

Chapter 5

Time Variable Grain Charging

5.1 Introduction

[1] In Chapter 3 we considered the motion of charged grains for the idealized case of an aligned dipolar magnetic field, with a simple Kepler launch origin. In Chapter 4 we tested the robustness of these results against non-zero launch impulses, and studied the wide variety of actual magnetic field configurations that exist in the Solar System. We now relax the assumption of a constant charge-to-mass ratio on a dust grain. We begin by introducing the charging currents that determine the electric potential of a dust grain, and then apply this charging model to determine new stability maps at Jupiter. Charging effects are quite complicated and model dependent— our goal here is to elucidate the important physical processes rather than to have the last word on stability at Jupiter.

There are two applications of interest to us here. Firstly, we shall consider the effect of charge variation due to transit through Jupiter's shadow. This has been shown to sculpt the Thebe ring just beyond synchronous orbit (Hamilton and Krüger 2008), and here, we shall study the effect of the shadow resonance on dust in the main ring inside synchronous

[1] This chapter is partially based on results from (Jontof-Hutter and Hamilton 2012b), in press.

orbit. In this tenuous plasma environment, the equilibrium electric potential on a dust grain in the planetary shadow differs substantially from that in sunlight. This can cause the charge to switch between positive and negative sign and back again with each transit of the shadow. Below we shall explore the stability of grains in the main ring and the gossamer rings covering distances from 1-3R_p.

Our second application is to the Jovian dust streams, whose likely source is the Io plasma torus covering 5-7R_p. The relatively dense plasma of the Io torus keeps dust grain charges strongly negative even in sunlight; and we shall explore the effect of the planetary shadow on these dust grains.

5.2 Spherical Dust Grain Model

Grains orbiting in space acquire electric charges from a variety of sources. These equations are implemented in our numerical simulations, where we allow the grain charge to vary with time. We assume throughout that grains act as spherical capacitors in free space, such that

$$C = 4\pi\varepsilon_0\varepsilon_r a_d = q/V, \tag{5.1}$$

where a_d is the grain radius, q is the charge and V is the electric potential of the grain. Here, ε_0 is the permittivity of free space, and ε_r, the dielectric constant of the medium equals unity in a vacuum. This is a good approximation for the sparse plasmas that we are concerned with, and we shall maintain the assumption that $\varepsilon_r \approx 1$ throughout.

An important caveat to note here is that for the smallest grains, at nanometer scales, the total charge corresponds to a small excess or lack of electrons, and hence the charging currents are quantized and stochastic. Furthermore, real dust grains have complex shapes and inhomogeneities. Nevertheless, the simple spherical capacitor model will serve the purpose of enabling detailed dynamical studies.

Unfortunately, there is no standard set of units amongst authors of papers on charged grains in planetary magnetic fields. We have found the parameter L_* (Hamilton 1993a,Hamilton 1993b) particularly useful, however, other authors frequently refer to grain size and electric potential. Schaffer and Burns (1994), for example, express V in volts, and a_d in μm which gives

$$q(\mathrm{statC}) = 3.218 \times 10^{-6} \left(\frac{\mathrm{a_d}}{\mu\mathrm{m}}\right) \left(\frac{\mathrm{V}}{\mathrm{volts}}\right) \tag{5.2}$$

The mass of a grain equals its volume multiplied by its density ρ_d; for simplicity, we adopt $\rho_d = 1$ g cm^{-3} throughout.

5.3 Plasma Effects

5.3.1 Direct Capture of Electrons and Ions

We begin by assuming a conducting sphere immersed in a plasma that has a Maxwellian velocity distribution. Now this assumption is almost certainly false in a strong magnetic field, where the motion of ions and electrons perpendicular to the magnetic field lines involves tightly bound gyrations, whilst the motion parallel to magnetic field lines is unencumbered. Nevertheless, with a brief reminder that all model-dependent results should be treated with caution, we continue to describe such models.

A Grain at Rest

For a grain at rest in a Maxwellian plasma, the current density from the surrounding plasma is

$$J_e = n_e q_e \frac{< c_s >}{4} f(\varphi) \tag{5.3}$$

where n_e is the number density of electrons, q_e and m_e are the charge and mass of an electron, φ is the electric potential of the dust grain, and the mean speed $< c_s >= \sqrt{\frac{8kT_e}{\pi m_e}}$,

is a measure of the sound speed through the plasma. Here, T_e is the electron temperature, and the Boltzmann constant $k = 1.38 \times 10^{-16}$ erg K^{-1} relates temperature to thermal energy. The dimensions of J_e are current per area, since a grain at rest can intercept electrons from all directions. A negatively-charged grain will repel electrons from being captured, preventing some of them from being captured, hence the function

$$f(\varphi) = \exp\left[-\frac{q\varphi}{kT_e}\right] \tag{5.4}$$

which reduces the current as the charge increases. The argument of the exponential in Eq. 5.4 is a ratio of two energies, the potential of the dust grain, and the thermal energy of the electrons in the plasma. Whilst a higher negative potential on the dust will act to reduce the current, at high temperatures some electrons will overcome this barrier.

A positively-charged dust grain on the other hand will attract more plasma electrons; thus if the charge $\varphi > 0$, then

$$f(\varphi) = 1 - \frac{q\varphi}{kT_e}. \tag{5.5}$$

For an initially neutral grain $\varphi = 0$ and $f(\varphi) = 1$.

Note that Eqs. 5.3, 5.4 and 5.5 are easily adapted to calculate the capture of ions J_i from the plasma, for a given ion density n_i, charge q_i, mass m_i, and temperature T_i. In all of our numerical models, we shall assume that the plasma is in full thermal equilibrium with $T_i = T_e$.

In general, since the ions are much more massive than the electrons and move more slowly, ion capture currents for a neutral grain at rest in a plasma composed purely of electrons and protons are a small fraction of the electron currents. Since the mass ratio of an electron to a proton is ~ 1800, the ratio of sound speeds for each species is ~ 43, and hence, for an initially neutral dust grain, the most that ions can reduce the net current by charge capture is $\sim 2.3\%$. For heavier ions, the positive currents are reduced even more.

The net current on the dust grain of size a_d due to electron and ion capture is simply:

$$I_{net} = 4\pi a_d^2 (J_e + J_i). \tag{5.6}$$

Since the negative currents dominate I_{net}, the dust grain approaches an equilibrium potential that is negative. This causes a region of positive charge to build up near the grain, known as the positive-ion sheath, or more generally, the Debye sheath. The Debye length is defined as the distance to the outer boundary of the sheath

$$\lambda_D = \left(\frac{\varepsilon_0 kT}{n_e e^2} \right)^{1/2} \tag{5.7}$$

(Nicholson 1983), where the net electric field from the charged grain is cancelled by intervening opposite charges. The diffusion of currents into the Debye sphere from the external plasma would favor electrons since they move faster, hence a weak electric field is invoked to balance this bias, attracting ions and repelling electrons (Kanal 1962).

A Grain in Motion

The currents to a grain are complicated by the grain's motion through the plasma. We assume that despite this motion, the Debye sheath remains spherical. Kanal (1962) derived a formula for the charging current on a grain with repulsive potential $q_e \varphi < 0$ moving with respect to plasma at speed v_{rel}, sweeping up electrons:

$$I_{mov} = \frac{1}{2} \pi a_d^2 n_e q_e v_{rel} \left[a_1 \left(\mathrm{erf}(a_2) + \mathrm{erf}(a_3) \right) + \frac{c_s}{\sqrt{\pi} v_{rel}} \left(a_4 e^{-a_3^2} - a_5 e^{-a_2^2} \right) \right] \tag{5.8}$$

(Kanal 1962, Whipple 1981, Graps et al. 2008), where $c_s = \sqrt{\frac{2kT_e}{m_e}} = \sqrt{\frac{\pi}{4}} < c_s >$, another measure of the sound speed, is the most probable velocity of the incoming electrons, at the peak of the Maxwell-Boltzmann distribution.

Here, the dimensionless coefficients are:

$$a_1 = 1 + \frac{c_s^2}{2v_{rel}^2} - \frac{U_q^2}{v_{rel}^2}$$

$$
\begin{aligned}
a_2 &= \frac{v_{rel}+U_q}{c_s} \\
a_3 &= \frac{v_{rel}-U_q}{c_s} \\
a_4 &= \frac{U_q}{v_{rel}}+1 \\
a_5 &= \frac{U_q}{v_{rel}}-1
\end{aligned}
$$

where $U_q = (2q_e\varphi/m_e)^{1/2}$. Note that equation 5.8 is easily adapted to the capture of ions with mass m_i, and temperature T_i. For negatively-charged grains, the quantity U_q is a measure of the minimum radial velocity required by an electron to overcome the potential of the dust grain and reach the surface, that is, to climb up the potential gradient in the Debye sheath. If $c_s << U_q$, the plasma is too cold for the electrons to reach U_q in large numbers. Since an electric field is conservative, the electron current is independent of the Debye sheath radius.

In Eq. 5.8, the error function erf(), is related the cumulative sum of a Gaussian distribution, except that the summation begins at zero, not at $-\infty$:

$$\mathrm{erf}(x) = \frac{2}{\sqrt{\pi}}\int_0^x \exp(-y^2)dy. \tag{5.9}$$

Many of the terms in Eq. 5.8 depend on the ratio v_{rel}/c_s (the Mach number), a measure of the importance of the grain's motion through the plasma. Note that in the limit that the grain is not moving relative to the plasma, $v_{rel} << c_s$, and $I_{mov} \rightarrow I_e$.

For a grain that is electrically neutral, $\varphi = U_q = 0$ Eq. 5.8 simplifies substantially:

$$I_{mov,0} = \pi a_d^2 n_e q_e v_{rel}\left[\left(1+\frac{c_s^2}{2v_{rel}^2}\right)\mathrm{erf}\left(\frac{v_{rel}}{c_s}\right)+\frac{c_s}{\sqrt{\pi}}v_{rel}\exp\left(-\frac{v_{rel}^2}{c_s^2}\right)\right] \tag{5.10}$$

If $v_{rel} << c_s$, the exponential approaches unity, and $\mathrm{erf}\left(\frac{v_{rel}}{c_s}\right) \rightarrow \frac{2v_{rel}}{\sqrt{\pi}c_s}$. In this limit, Eq. 5.10 reduces to Eq. 5.6. For dust grains in planetary magnetospheres, this approximation is reasonable over a broad range of plasma temperatures. For example, suppose

a Kepler-launched dust grain orbits through a rotating magnetic field at $v_{rel} \sim 10$ km s^{-1}. For the electron sound speed to exceed 10 km s^{-1} requires $T_e \gtrsim 2$ K, and for ions $T_i \gtrsim 6000$ K, whereas even in the cold plasma torus just inside of Io's orbit, measured energies exceed ~ 5 eV corresponding to $T_e \approx 5 \times 10^4$ K.

Nevertheless, for completeness, we include the limit of a grain traveling much faster than the sound speed. In this case, $v_{rel} >> c_s$, all the error function terms in Eq. 5.8 approach unity and the exponentials tend to zero, leaving:

$$I_{mov}(v_{rel} >> c_s) = \pi a_d^2 n_e q_e v_{rel}. \tag{5.11}$$

This is exactly what is expected for stationary plasma particles. Given charge neutrality, Eq. 5.6 predicts that $\varphi \rightarrow 0$ in this limit.

And finally, with an attractive potential on the dust, considering ion currents to a negative grain,

$$I_{mov,i} = \pi a_d^2 n_i q_i v_{rel} \left(\left(1 + \frac{c_s^2}{2v_{rel}^2} \right) \mathrm{erf}\left(\frac{c_s}{v_{rel}} \right) + \frac{c_s}{\sqrt{\pi}} v_{rel} \exp\left[- \left(\frac{v_{rel}}{c_s} \right)^2 \right] \right) \tag{5.12}$$

(Kanal 1962). This is much simpler than Eq. 5.8 because the minimum speed requirement for ions to reach the negatively-charged grain is zero; for them, the grain is not repulsive. If the Debye sheath is thin compared to the size of the dust grain ($\frac{a_d}{\lambda_D} \approx 1$), essentially all ions that enter the sheath are captured by the grain. If the Debye length is much greater than the grain radius ($\lambda_D >> a_d$), however, then the capture probability depends on λ_D, the incident angle of the incoming ion, and its speed. Equations 5.8 and 5.12 are the result of integrating incoming ions over all velocities (in a Maxwellian) and all incident directions for each area element at the Debye surface. We assume here and throughout that the Debye sphere is much larger than the dust grain. This assumption is fairly simple to justify for the problem that motivated Kanal (1962), namely, large spherical probes in Earth's very high temperature inner Van Allen belt, but its applicability for sub-micron dust grains with small numbers of individual charges is unknown. Thus once more, we

caution the reader. As we shall soon see, other charging currents also have significant uncertainties.

5.3.2 Secondary Electron Emission

The next charging process we shall include is the effect of secondary electron emission, whereby incident electrons excite secondaries within the dust grain. Some of the secondary electrons escape causing a net positive current to the dust grain. This becomes important in warm plasma where the thermal energy of electrons is enough to eject electrons from the surface of a grain.

Secondary electron emission depends on a number of factors. Firstly, the energy of the incoming electron determines the yield δ, or the number of secondary electrons created for each incident primary. Low energy incoming electrons have a yield $\delta < 1$, and hence produce no secondaries. At the other extreme, high energy electrons have a greater penetration depth and can even pass through the grain without losing much energy. There is thus a characteristic primary electron energy, E_m, between these extremes which results in a maximum yield δ_m (Dionne 1975). The most widely used expression for secondary electron yields assumes incoming electrons interact with a planar slab of material.

$$\delta(E) = 7.4 \left(\frac{E}{E_m} \right) \exp \left[-2\sqrt{\frac{E}{E_m}} \right] \tag{5.13}$$

(Sternglass 1954, Meyer-Vernet 1982, Goertz 1989, Graps et al. 2008). Nevertheless, secondary electron emission models are not settled in the literature. More recent models for secondary electron emission attempt to account for the finite depth of small dust grains (Chow et al. 1993). If the stopping distance of an electron within a dust grain is small compared to its overall size, the number of secondaries that reach the surface and escape declines exponentially with depth, and surface yields using the expression of Sternglass (1954) should suffice. However, in small grains, secondary electrons may escape the far

end of a grain from the primary electron incidence location. Chow et al. (1993) found that this increases yields substantially for grains smaller than 0.1 μm.

To apply either model for secondary electron yields to orbiting dust grains, we rely on experimentalists to measure E_m and δ_m for each type of material. Nevertheless, since the details of experimental yields are still disputed, we adopt a far simpler secondary electron emission model in our numerical simulations. Whipple (1981) lists typical values for δ_m near or just above unity for a diverse range of materials, thus we adopt $\delta_m = 1$ throughout. Typical incident energies that provide the maximum yield are ~ 0.3 keV (Whipple 1981), which we adopt throughout. Integrating Eq. 5.13 over a Maxwellian primary electron distribution, the current is

$$I_{sec} = 3.7\delta_m f_5 \left(\frac{E_m}{4kT_e}\right) I_e, \tag{5.14}$$

(Meyer-Vernet 1982). Here we assume that the electron capture current I_e (Eqs. 5.3 and 5.6) is in the slow-moving regime, and that the charge on the dust grain is negative. In Eq. 5.14, the function,

$$f_5(x) = x^2 \int_0^\infty u^5 \exp[-(xu^2 + u)]du. \tag{5.15}$$

has a simple iterative solution (Meyer-Vernet 1982):

$$f_{n+1}(x) = \frac{n f_{n-1}(x) - f_n(x)}{2x} \tag{5.16}$$

given the initial solutions:

$$f_1(x) = \frac{x^2 - f_0(x)}{2x} \tag{5.17}$$

and

$$f_0(x) = \frac{1}{2}x^2\sqrt{\frac{\pi}{x}}\exp\left[\frac{1}{4x}\right]\left(1 - \mathrm{erf}\left[\frac{1}{2\sqrt{x}}\right]\right) \tag{5.18}$$

For positively-charged dust grains, the secondary electron current becomes

$$I_{sec} = 3.7\delta_m f_{5\varphi} \left(\frac{E_m}{4kT_e}\right) I_e, \tag{5.19}$$

where

$$f_{5\varphi}(x) = x^2 \int_B^\infty u^5 \exp[-(xu^2+u)]du. \tag{5.20}$$

Here, the definite integral begins at $B = \frac{q_e\varphi}{kT_e}$, because positively-charged grains attract electrons, thus preventing low energy secondaries from escaping. For an initially neutral grain, $\varphi = 0$ and Eqs. 5.15 and 5.20 are equal.

We shall compare the competing effects of electron capture and secondary electron emission after introducing our final source of current, the photoelectric effect.

5.4 Insolation

The ultraviolet radiation in sunlight ejects photoelectrons from the surface of a grain, causing a positive current. For a grain with a negative potential, currents are limited only by the flux of UV photons and the work function of the material. Hence,

$$I_\nu = -\pi a_d^2 q_e \chi \frac{f_{1AU}}{d_{AU}^2}, \tag{5.21}$$

where πa_d^2 is the cross-sectional area of the grain, χ, the yield, is related to the work functions, and d_{AU} is the distance from the Sun in astronomical units. Here $f_{1AU} = 2.5 \times 10^{10}$ is the flux of UV photons at 1 AU from the Sun.

A positively-charged dust grain, on the other hand, reduces the number of escaping electrons, and thus the current depends on the electric potential of the grain:

$$I_\nu = -\pi a_d^2 q_e \chi \frac{f_{1AU}}{d_{AU}^2} \exp\left(-\frac{q_e\varphi}{kT}\right). \tag{5.22}$$

Note that a high yield to incoming electrons has no bearing on a material's yield to incoming photons. Typical yield values for solar UV are 0.1 for dielectrics and 1.0 for conductors, under the rather simple assumption that in conductors, loose charges congregating at the surface are more readily freed (hence $\chi = 1$), whereas in insulators, charges

are spread uniformly throughout the grain and the estimate for χ is reduced by one order of magnitude. Here and throughout, we adopt the value $\chi = 1$.

5.4.1 Charging Timescale

All of the charging currents discussed above depend on the surface area of the dust grain ($I = dq/dt \propto a_d^2$). Hence smaller grains charge up more slowly. Given that the time constant for a capacitor $\tau = RC$, then, following Ohm's law, the resistance $R = V/I$, and recalling Eq. 5.1, $\tau \propto V/a_d$. We therefore find that time for a dust grain to charge to equilibrium is inversely proportional to its size (Horányi and Juhász 2010).

We now have the tools to model variable grain charge in two very different charging environments. First, we shall consider dynamics in an environment where tenuous plasma currents compete with sunlight in determining the equilibrium charge on a dust grain. This regime applies directly in the main and gossamer rings at Jupiter, inside and immediately exterior to the synchronous orbital distance. Secondly, we shall consider variable grain charging effects in a relatively dense plasma environment, like in the Io plasma torus.

5.5 The Shadow Resonance in the Main and Gossamer Rings

We have seen that the plasma environment, the flux of solar radiation and the physical properties of a dust grain all play a role in its electric charging. Since the nature of the grains in the dusty rings of the outer planets, and the plasma environment in which they reside are poorly constrained, the motion of any particular grain with varying charge is highly model dependent. Our goal in this section is not to pick the best model for Jupiter's dusty rings, but rather to elucidate the physics of orbital changes driven by charge variations. Possibly the simplest non-trivial model which, nevertheless, must occur in

circumplanetary applications, is the shutoff of the photoelectric current during planetary shadow passages (Horányi and Burns 1991). This effect will be present even if all other model-dependent charging effects are absent. The azimuthal asymmetries that the shadow induces have a profound effect on dust grain motions, as we shall soon see.

Returning to our aligned dipolar magnetic field model, and assuming that the plasma distribution is perfectly axisymmetric, the effect of the planetary shadow transit is to introduce a strong azimuthal asymmetry in the charging environment for a dust grain. In the shadow, the photoelectric effect of sunlight is absent, and interactions with the plasma cause a net negative charge on the grains (Schaffer and Burns 1987). In the sunlight, by contrast, equilibrium typically favors a slight positive electric potential.

In Fig. 5.1, we plot the contribution by the different charging mechanisms on an initially neutral grain in tenuous plasma over a range of plasma temperatures. The secondary electron emission I_{sec} is the least important source of charge in this plasma, and it only becomes important at high temperatures where $T_e \gtrsim 100$ eV $\approx 10^6$ K. The capture of electrons and ions by a moving dust grain, I_{mov}, would cause a net negative current on the dust grain. It is superseded at typical temperatures, however, by the positive current of the photoelectric effect in sunlight ($I_{\rm v}$). The result is that the equilibrium charge on this grain in sunlight would be positive, but each transit through the planetary shadow halts the photoelectric charging, and the currents become negative. This constant switching between positive and negative charge has important dynamical consequences.

Fig. 5.2 highlights the differing effect of charge variation with grain size, given the same launch distance. Here, we have chosen two example grains launched inside synchronous orbit at a location that avoids the short term vertical instability in an aligned dipole model for Jupiter (Fig. 4.1).

Firstly, we note from Fig. 5.2 that the equilibrium charge on a sunlit dust grain is 2.75 Volts, whereas in the shadow, the equilibrium electric potential is -27 Volts. The large

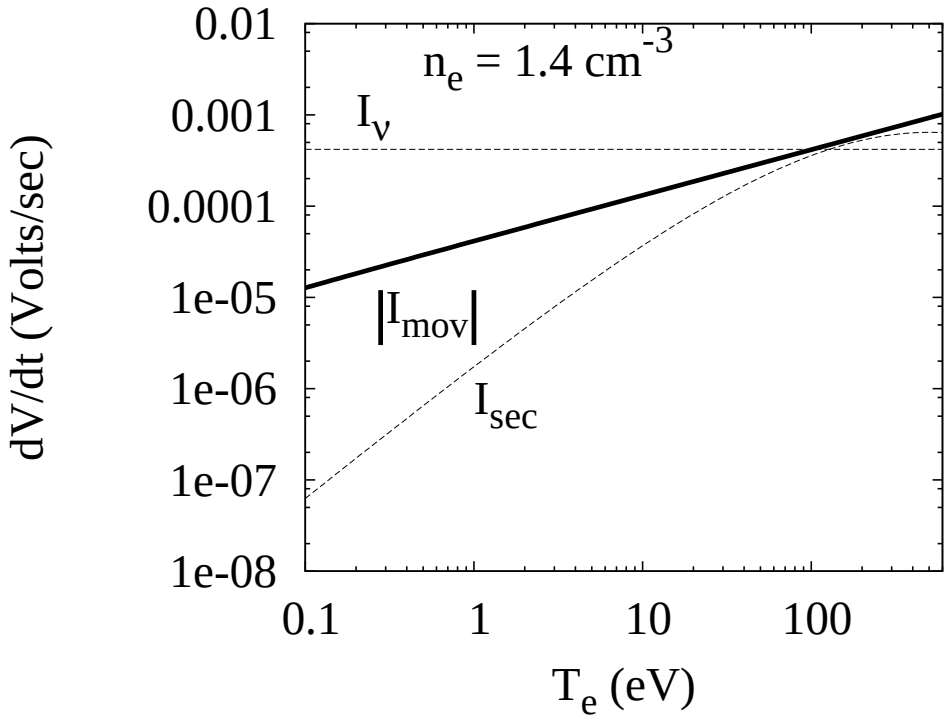

Figure 5.1: The charging contribution, in Volts/sec, on an initially-neutral 10 nm dust grain launched in Jupiter's main ring at $1.70R_p$. We have adopted a tenuous plasma density ($n_e = 1.4$ cm^{-3}), and plot the various charging currents over a range of temperatures, expressed in electron-volts (eV). The electron capture by a moving dust grain, I_{mov}, is marked with a solid curve, the photoelectric effect I_ν is shown as the dashed line, and the secondary electron emission I_{sec} is marked as the dotted curve.

grains reach equilibrium potential far more rapidly than the smaller grains. Indeed, the charge response is typically inversely proportional to the size of the dust grain (Horányi and Juhász 2010). For the larger grain in Fig. 5.2a, the increasing amplitude of the radial oscillations is caused by the fact that charge variation repeats each dust grain orbit, thereby resonating with the epicyclic frequency for grains in the Kepler regime. This is the destabilizing shadow resonance (Horányi and Burns 1991; Hamilton and Krüger 2008) which we will find strongly affects our stability map.

In Fig. 5.2b, the smaller dust grain does not have enough time to reach charge equilibrium during the shadow transit. This dust grain experiences stochastic kicks both inwards

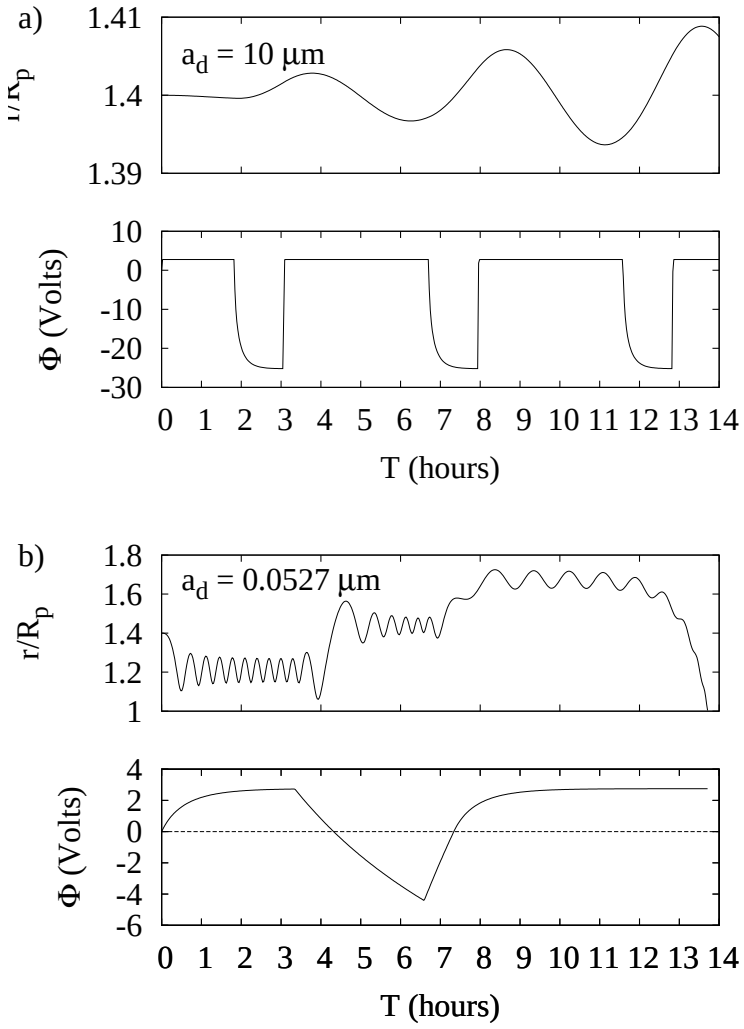

Figure 5.2: The charge response of a dust grain in plasma and sunlight depends on grain size: a) 10 μm and b) 0.0527 μm grains, launched at $1.4R_p$ at local noon, with an aligned dipole magnetic field for Jupiter, in a uniform plasma with density $n_e = 1.4$ cm^{-3} and temperature $T_e = 10$ eV. The grains initially carry no charge. Each panel shows that grain's radial trajectory and instantaneous electric potential in Volts. The large grain experiences three 1-hour long shadow passages during which the charge decreases, while the smaller grain has a single 3-hour eclipse.

and outwards from its launch distance and eventually becomes vertically unstable and crashes into the planet at high latitude after 14 hours. Each kick in the guiding center distance r_c occurs when the electric potential on the dust grain is $\sim$1 Volt, when the instantaneous value L_* places the grain near the left-most radial stability boundary of Fig. 4.1b ($L_* \approx 2$). When the potential is higher than 2 Volts or negative, the grain experiences stable radial oscillations with a slow decline in radial range. This decreasing amplitude is due to the grain reaching higher charge-to-mass ratios ($|L_*|$), and hence experiencing tighter gyrations. After several random steps in r_c due to the grain's periodic encounters with the radial instability, it moves into the vertical instability zone, spirals up the magnetic field and is lost to Jupiter.

In Fig. 5.3 we present stability maps for a large range of grains sizes from 0.001μm to 10μm, over a broad range of launch distances, to test the effect of charge variations on orbital stability. In these models, dust grains are free to vary their charge as the environment allows, both with the shadow present (Fig. 5.3b), and explicitly ignored (Fig. 5.3a).

Without the planetary shadow, grain charges quickly converge to equilibrium values, and the stability map in Fig. 5.3a looks very similar to one for a constant (positive) charge (Fig. 4.1b). In Fig. 5.3a, the superimposed boundaries, corresponding to a +2.75 Volt constant potential, match the data very closely on the right-hand side of the radial instabilities. Since the large grains rapidly converge on their electric potential, the Kepler-regime side of the radial instability closely conforms to the analytical boundaries developed in Chapter 3. The smaller grains, however, take significant amounts of time to reach charge equilibrium. The grains on the left side of the left-most radial stability boundary in Fig. 5.3a either escape (outside R_{syn}) or fall into the planet (inside R_{syn}), before they have enough time to reach their equilibrium charge. During the time that these tiny dust grains experience modest electric charges, a different set of stability curves shifted to the left of those in Fig. 5.3a applies. Within $1.2R_p$, 0.01-μm sized grains collide with Jupiter within a few

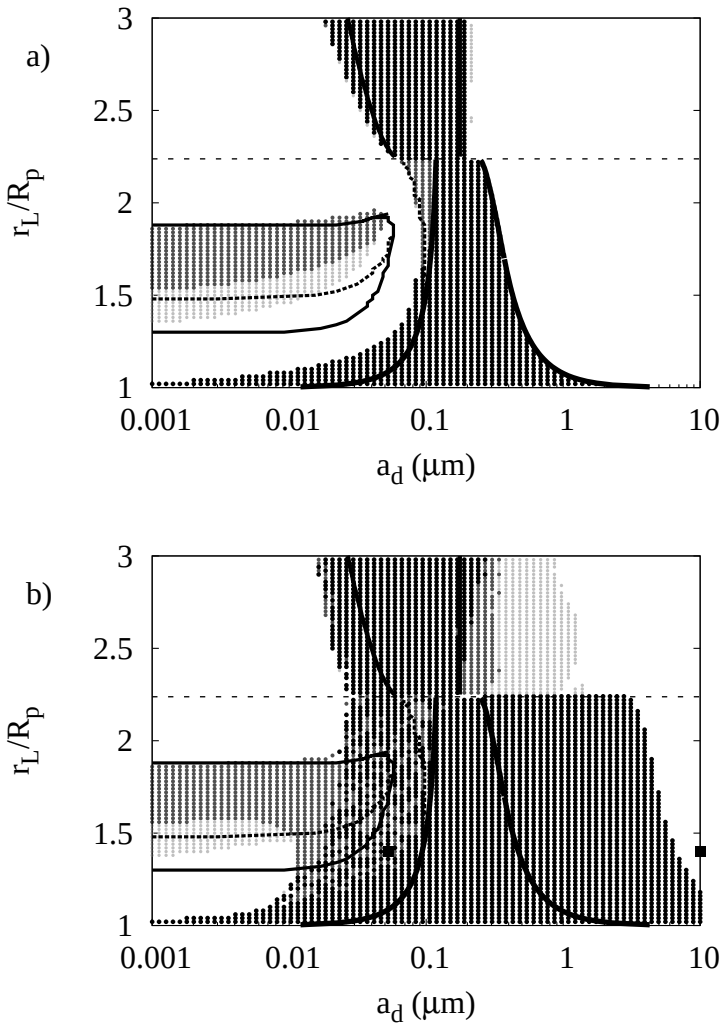

Figure 5.3: Stability of grains with variable charge response to plasma for two grain charging models: a) constant photoelectron emission, and b) a more realistic photoelectric response which is interrupted during shadow transit. We adopt an aligned dipole for Jupiter's magnetic field, and neglect its 3.12° obliquity. Grains, all launched at local noon, begin with zero electric potential and are integrated over 1 year, a timescale long enough to cover the orbital precession in the Kepler regime due to J_2, which is included in our model of the gravity field. Consistent with the greyscale in Figs. 4.3 and 4.4, the darkest region denotes radial instability— either collision with the planet or escape within $\lambda_m = 5^\circ$ of the equator plane, the moderate grey represents high-latitude collisions with Jupiter, and the lightest grey marks surviving grains with high-latitude oscillations. The two filled squares correspond to the trajectories illustrated in Fig. 5.2. Note that the horizontal axis, now marking increasing grain radius, spans twice the range as in previous figures. In both a) and b), the numerical boundaries are included for an assumed electric potential of Φ =+2.75 Volts.

hours while the characteristic charging time is a day. Similarly, outside synchronous orbit, 0.01-μm sized grains just to the left of the radially unstable zone for constant +2.75 Volt grains escape the planet. These grains, initially neutral, charge up slowly in the sunlight. Hence, even if their equilibrium charge would permit stable motion, the time spent in the radially unstable regime causes them to collide with Jupiter or escape before reaching charge equilibrium. Some tiny grains near the inner boundary of the vertical instability are saved by a shift closer to Jupiter whilst charging up immediately after launch.

With the planetary shadow turned on, the shadow resonance acts to increase eccentricities, destabilizing grains over a far broader range of sizes than those that remain at their equilibrium potential (Fig. 5.3b). For the largest of these grains ($a_d \gtrsim 1$ μm), the change in electric potential induced by the shadow causes a radial impulse at the same phase in each orbit. This shadow resonance destabilizes grains more than an order of magnitude larger than those unstable without the shadow. The shadow resonance increases eccentricities on gravity-dominated grains that move outwards during the shadow transit. This continues until either the grain collides with Jupiter, or until the precession of the orbit causes grains to approach Jupiter during the shadow transit, thereby damping the eccentricity (Horányi and Burns 1991; Hamilton and Krüger 2008). Since the dominant component of orbital precession for larger grains is due to the planetary oblateness, we include the J_2 term in our models for Fig. 5.3, and adjust our initial conditions to ensure launch from a circular orbit.

The smallest grains in Fig. 5.3b respond to changes in the charging environment over a longer timescale. Thus, grains that survive the initial charging process (the stable grains of Fig. 5.3a) reach an electric potential that deviates little from its mean over the orbital period, and hence the shadow has little effect on grains smaller than 0.01 μm in size. This region of Fig. 5.3b essentially matches Fig. 4.1b in the Lorentz limit, with either vertical instability or stable high latitude oscillations between $1.29R_p$ and $1.70R_p$.

Grains between 0.01 μm and 0.1 μm launched outside $1.2R_p$, but within R_{syn}, experience charge variations that cause them to spend brief moments during each orbit entering a radially-unstable regime. Eventually they strike the planet, although the timing for this is unpredictable. As we saw in Fig. 5.2b, such grains experience random walks in radial location but do not cross synchronous orbit. Roughly half the grains in this region of Fig. 5.3b collided with the planet at high latitudes.

Grains larger than 0.5 μm launched outside R_{syn} in Fig. 5.3b experience excited radial motions and vertical motion close to the radial stability boundary of Fig. 5.3a ($L_* = \frac{1}{2}$, Hamilton 1993a; Jontof-Hutter and Hamilton 2012a), which extends the Thebe ring away from Jupiter (Hamilton and Krüger 2008). Inside R_{syn}, Fig. 5.3b shows that the shadow resonance destabilizes grains more than 10 times as large as those than the largest grains destabilized with the shadow switched off. The boundary between stable and unstable here is determined not by the time of the integration but by the precession timescale. This has several components, including one due to the Lorentz perturbations on the dust, but for the largest grains the timescale is dominated by the higher-order gravity field components at Jupiter, specifically, J_2. The precession time due to J_2 is approximately 0.25 years in the main ring, and longer further out. For our particular choice of grain charging parameters, grains larger than roughly 5 μm in the main ring are saved from colliding with Jupiter by orbital precession.

We emphasize that resonant charge variation on dust grains due to the photoelectric current clearly has an important effect on grain dynamics, although the shadow resonance is by no means the only destabilizing process that may be important in the main ring. Epicyclic motion also provokes resonant charge variations due to both radial gradients in the plasma properties and the varying collision speed between dust and plasma with gyrophase. Of the effects studied so far in the previous chapter and here: launch speeds, realistic magnetic fields and the shadow resonance, the latter appears to be the

most important. Non-zero launch impulses, by contrast, are a minor effect on grain-orbit stability. The relative importance of the different effects, however, will vary dramatically with plasma properties. The charging environment that we have adopted here, namely a fairly sparse plasma, is appropriate for the dusty main ring and gossamer rings at Jupiter. Our primary result is that the removal of dust is dominated by the basic dipolar radial instability for positive grains, substantially extended to both larger and smaller particles by variable charging.

We now turn our attention to the dense plasma environment of the Io torus, the likely source of the high-speed dust streams.

5.6 The Io Plasma Torus and Jovian Dust Stream

Prior to its Jupiter flyby in 1992, and from as far as 1 AU in distance from the giant planet, the Ulysses spacecraft detected dust grains streaming from the Jupiter system at high speed. Grün et al. (1993) estimated the characteristic size of the dust grains at 0.1 μm, though this value was based on an under-estimate of the sensitivity of Ulysses dust detector. The effect of Jupiter's corotational electric field acting on positively-charged dust grains was soon invoked as a mechanism to accelerate the dust grains (Hamilton and Burns 1993a; Horányi et al. 1993b, see Section 3.4.1). This eliminated potential sources of the dust inside the synchronous orbital distance, including the main ring, which is fully contained within R_{syn}, but did not initially distinguish between production models based in the Gossamer ring, (Hamilton and Burns 1993a), and Io's volcanic plumes (Horányi et al. 1993b). Zook et al. (1996) reviewed the Ulysses data, and taking into account the modulating effect of the interplanetary magnetic field on dust streams, concluded that the grains were far smaller than previously thought, with sizes ranging between just 5 and 15nm. This size implies high charge-to-mass ratios, that permits grains to accelerate to

$\sim$200 km s^{-1}.

The rate of dust detections during Ulysses' Jupiter encounter was highly variable, with peaks three orders of magnitude above the nominal impact rate. Hamilton and Burns (1993a) identified the periodicity to be due to the solar wind, which varies periodically with the Sun's rotation. They found that the interplanetary magnetic field, modulated by the solar rotation period, strongly accelerates the dust streams explaining the 28$\pm$3 day period in dust stream detection rates. Further periodicities were resolved in the Galileo data during its six-year sojourn deep inside the Jovian magnetosphere. Galileo detected variations in dust impact rates of up to five orders of magnitude, strongly correlated with Jupiter's rotation period (Krüger et al. 2003a). Graps et al. (2001) produced a periodogram of Galileo dust detection data from the first two years of the mission: 1996 to 1997. They found that the strongest signal had a period between 9.6 and 10.4 hours, consistent with Jupiter's rotation period of 9^h55^m, and a weaker signal with a period of 4.8-5.0 hours, or half of Jupiter's rotation period. They also found strong periodicities at: 27-48 hours (consistent with Io's 42 hour orbital and rotational period), as well as a peak at 12.6-16 hours, most likely modulated by Io's motion relative to Jupiter's rotating magnetic field (13 hours), with sidelobes repeating at 7.5-8.0 hours, and 5.6-6.5 hours. Hence, Graps et al. (2001) interpreted the clear signal with Io's orbital period and motion in the frame co-rotating with Jupiter as dynamical evidence for Io as the source of the dust.

The Cassini flyby of Jupiter en route to Saturn, in 2000, provided an opportunity for Cassini's Cosmic Dust Analyzer to record mass spectra of impacting dust grains. Postberg et al. (2006) found that the detections of sodium chloride and sulfur in the dust implicated Io's volcanic plumes as the source. Furthermore, the tiny size of the dust grains already favors Io as a potential source. This is because the radial instability that expels positively-charged dust grains at high speed extends to smaller grain sizes farther

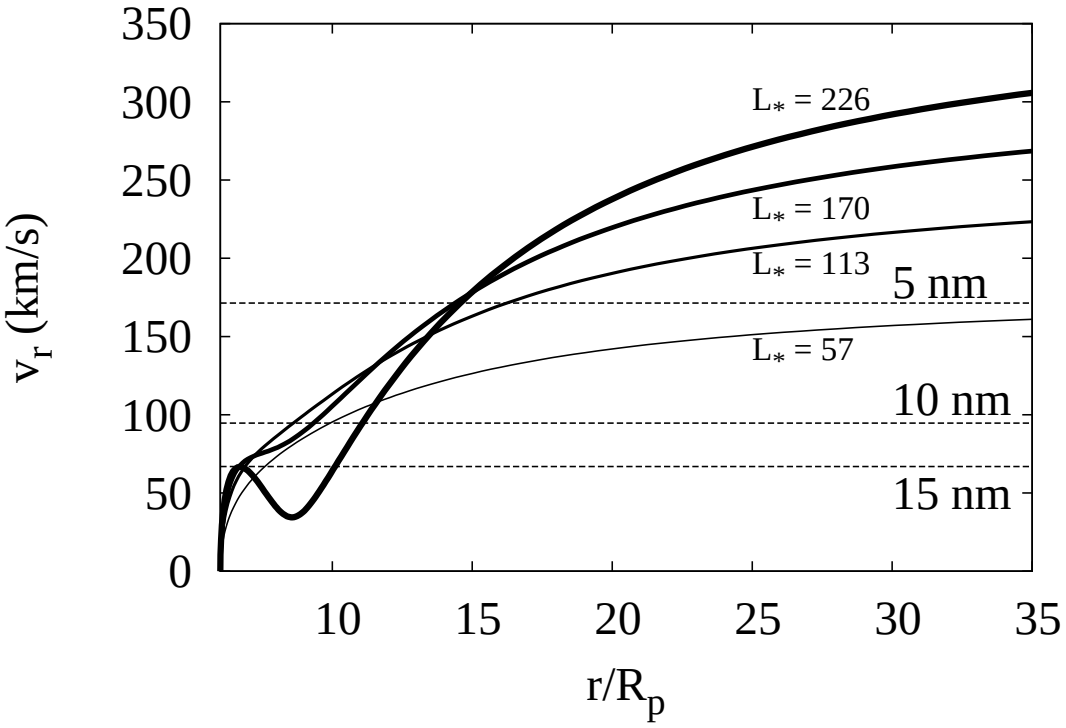

Figure 5.4: Radial speeds of expelled 10nm dust grains launched near Io at $6.0R_p$, with charge-to-mass ratios L_* ranging from 57 (thin solid curve), to 226 (thick solid curve), equivalent to a range in potential from 1 to 4 Volts on a 10-nm sized grain. A 5 Volt potential is enough to keep a 10-nm grain ($L_* = 283$) bound to Jupiter. Although escaping grain speeds plateau beyond $\sim 30R_p$, the accelerations from $10R_p$ to $30R_p$ can have an important effect on the speed of detected grains, and even more significantly affect their energies. The dotted lines are the minimum speeds for detection by the Galileo Dust Detector, for 5nm grains (171 km s^{-1}), 10 nm (95 km s^{-1}), and 15 nm (67 km s^{-1}), assuming spheres of material density 2 g cm^{-3}. Only beyond $12R_p$ are all 10-nm grains detectable.

out from synchronous orbit, (Hamilton and Burns 1993a, see Fig. 3.1b).

In Fig. 5.4, we model the acceleration of radially unstable constant-charge grains launched at Io's distance from Jupiter, and compare the results to the Galileo dust detector threshold (Grün et al. 1994). The detection threshold for the smallest grains, 5 nm in radius, is 170 km s^{-1}, and for the larger 15-nm grains, the minimum speed for detection is 70 km s^{-1}. Fig. 5.4 shows that accelerating grains cover large radial distances before reaching Galileo's detection threshold. For the modeled trajectories, we assumed a

single grain size of 10nm and varied the electric potential from 1 to 4 Volts (or following Table 4.1, L_* varied from 57 to 226) to see the effect of charge-to-mass ratio on the speed of an escaping grain. At 5 Volts, 10nm-sized dust grains are trapped ($L_* = 283$). There is thus some sorting of grains by detectability: beyond $16R_p$ most grains larger than 5nm can be detected, but within $8R_p$, no grains 10nm or smaller can be detected. Note that the grain with the highest charge-to-mass ratio ($L_* = 226$ or a 10-nm grain with a 4V potential), slows down shortly after launch before accelerating beyond $8R_p$, only superseding the other grains in speed beyond $15R_p$. This complex trajectory is due to the shape of the potential well near the radial stability boundary, illustrated in Fig. 3.7. The required distance covered by escaping grains to achieve high speeds is consistent with the low rates of dust detection by Galileo at perijove (Krüger et al. 2003b). Note that this interpretation is not without controversy. Krüger et al. (2003b) hypothesize that the dust stream rate is modulated by local solar time in the plasma torus. The observed dawn-dusk asymmetry in the plasma torus (Schneider and Trauger 1995) in turn causes charging conditions in the plasma to vary with longitude. In the Krüger et al. (2003b) model, dust grains achieve positive electric potentials around 6:00 and 18:00 due to secondary electron emission, which they invoke to explain the observed dust stream rates detected by Galileo during its six-year mission orbiting Jupiter. In their study, however, Krüger et al. (2003b) did not account for the radial distance of Galileo and the detectability of dust. We shall return to discuss charging models in the plasma torus shortly. The problem arises because dust grains must be positively charged to escape. Here therefore, we digress briefly to summarize the charging environment near Io.

Dust from Io's volcanoes soon encounters the environment of the Io plasma torus, which is roughly 2 Jupiter radii thick, and ranges from 5-7R_p. Although the structure of the plasma torus varies with longitude and local solar time, our aim here is to estimate an average charging potential for a grain embedded in the plasma near Io.

The gas near Io has various components. Herbert et al. (2008) describe the inner "cold torus" as washer-shaped, with a large radial extent from 5.0 to $5.6R_p$, and a vertical thickness roughly $0.25R_p$ that has little azimuthal variation. Between this cold plasma and Io's orbital distance is a gap of low density plasma, first observed by Voyager I (Bagenal and Sullivan 1981). Beyond the gap lies a narrow ribbon of warm plasma at Io's orbital distance ($5.9R_p$). A diffuse warm plasma extends both vertically and outwards radially from the ribbon, filling a torus roughly $2R_p$ thick vertically, and extending out to $7R_p$ radially. The electron temperature in the ribbon ($T_e \approx 5$ eV) is significantly lower than the ion temperature ($T_i \approx 20-50$ eV). Herbert et al. (2008) invoke inelastic collisions between electrons and ions with orbiting electrons to explain the absence of thermal equilibrium. The ions with orbiting electrons absorb energy in collisions and relax by radiating photons. The observed difference in temperature between ions and electrons complicates charging models. Furthermore, the temperatures parallel to the magnetic field lines differ significantly from the perpendicular temperatures. Voyager 1 also measured the number density of electrons in the plasma torus, finding a peak of roughly 3000 cm^{-3} at $5.7R_p$ declining slightly to 1500 cm^{-3} at $6.4R_p$ (Bagenal 1994; Gurnett et al. 1996; Smyth et al. 2011). This high density makes even tiny dust grains of order 10nm in size reach charge equilibrium within minutes. In our charging models below, we adopt an average electron density of 2000 cm^{-3}, and a uniform temperature of $T_e = T_i = 5$ eV.

Fig. 5.5 compares the charging currents on a 10-nm sized dust grain in Io's warm plasma torus. With densities up by a factor of ~ 1400, I_{mov} and I_{sec} are correspondingly higher than in Fig. 5.1. With electron capture being the dominant charging term, dust grains are likely to be strongly negatively charged. Note that although the net current is negative for temperatures near 5 eV, secondary electron emission is far more important than the photoelectric effect in the warm torus. Nevertheless, the grain is drenched in electrons, and will remain so both in sunlight and in shadow, in stark contrast to the

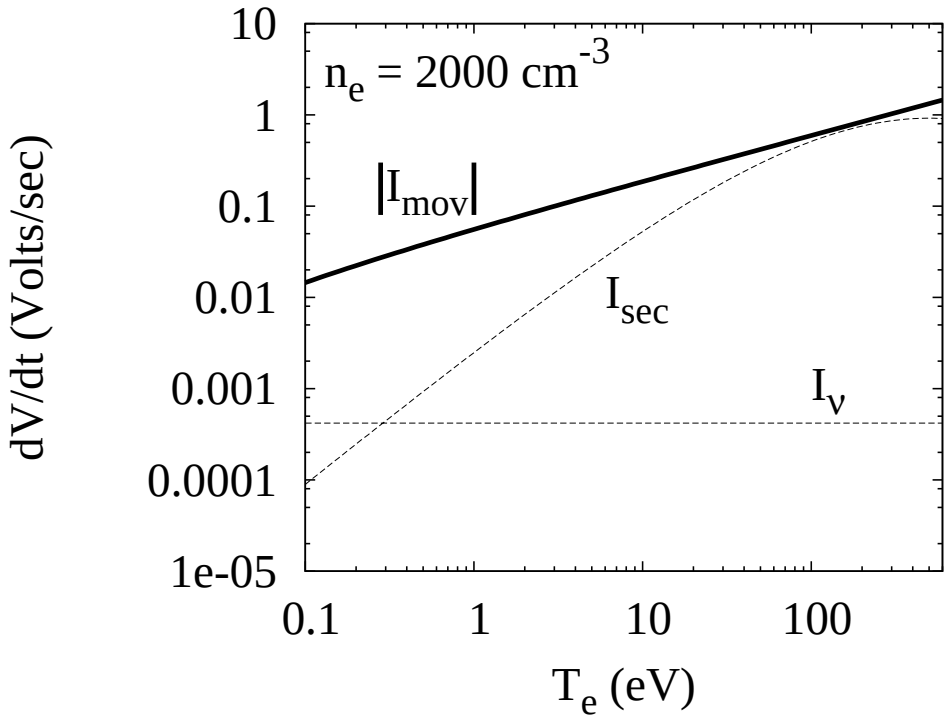

Figure 5.5: The rate of change in electric potential, in Volts per second, for an initially neutral 10nm sized dust grain in Io's plasma torus, as a function of electron temperature, (T_e). The dashed line labelled I_ν marks the photoelectric emission in sunlight, and the dotted curve, labelled I_{sec}, denotes the secondary electron emission. These are both positive currents. The solid curve is the negative electron capture current for a grain moving through plasma (I_{mov}) which dominates the charging. Thus grains launched in the warm plasma torus, where $T_e \approx 5$ eV, are likely to be strongly negatively charged.

tenuous plasma model shown in Fig. 5.1. The net negative charge here makes dust grain orbits, in the short term, radially stable (see Fig. 3.6a). To join a high speed dust stream, however, dust grains must escape from the high density plasma torus, where, beyond $7R_p$, the photoelectric effect in sunlight may become the dominant charging current.

In Fig. 5.6, we present the stability map for grains from the surface of Jupiter out to Io, in a uniform plasma environment consistent with the dense warm plasma that is observed near Io. The grains in Fig. 5.6, initially neutral, all rapidly charge to equilibrium: $\Phi = -14.3$ V in sunlight and $\Phi = -14.6$ V in Jupiter's shadow. The tiny difference between the potential equilibria from sunlight to shadow dramatically weakens the destabilizing

effect of the shadow that dominates the dynamics in a tenuous plasma. Thus, in dense plasma, grains essentially behave as if their charges remain constant, even with periodic transits through the planetary shadow. Accordingly, the stability map Fig. 5.6a strongly resembles the constant charge stability map of Jupiter with its magnetic field configured out to octupole order (Fig. 4.10b). There, we saw that constant charge negative dust grains are primarily destabilized by Lorentz resonances.

Note that Krüger et al. (2003b) posit that dust grains reach positive potentials in the plasma torus. This difference highlights just how model-dependent variable charge dynamics can be. In their study, Krüger et al. (2003b) employ a plasma torus model with detailed radial and azimuthal structure. Nevertheless, the escape of negative dust grains under the destabilizing effects of Jupiter's full magnetic field, that we invoke here, provides a simple and robust escape mechanism without the need for additional physics. Once negative grains have escaped the plasma torus, the photoelectric effect is strong enough to cause a net positive charge on the grains, and they can accelerate radially to high speeds.

In Fig. 5.6b, our numerical simulations include the additional effect of radiation pressure. Note that in our numerical models we neglect Jupiter's contribution to the radiation experienced by the dust grain. This factor depends on the solid angle of Jupiter in the dust grain's frame, which decreases rapidly with distance even as the relative strength of solar radiation pressure compared to Jupiter's gravity increases. Reflected Jovian radiation is also a function of local time, peaking for grains at the subsolar longitude, where Jupiter appears as a full disk. Finally, reflected light from Jupiter is reduced by the geometric albedo of 0.52 (de Pater and Lissauer 2010). Thus Jupiter reduces solar radiation pressure by $\sim 18\%$ at local noon in the main ring, down to just $\sim 1.4\%$ near Io.

Solar radiation pressure causes the eccentricities to increase for grains in the Kepler regime, on the right side of Fig. 5.6b. For smaller dust grains, as the influence of the

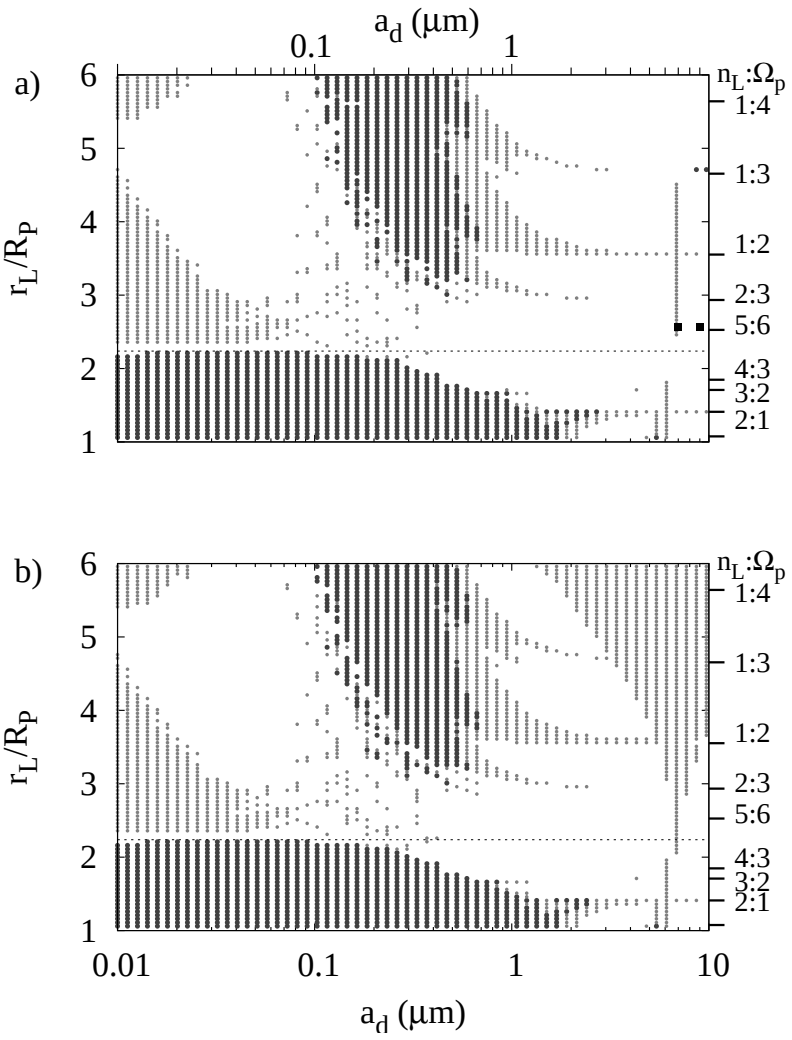

Figure 5.6: The stability of initially neutral grains launched in a uniform plasma of electrons and O^+ ions, with a density of $n_e = n_i = 2000$ cm^{-3}, at temperature $T_e = T_i = 5$ eV, consistent with Voyager 1 data of the Io plasma torus. In the top panel, a), we include charging currents from electron and ion capture, the photoelectric effect and secondary electron emission. The small black squares mark two trajectories that are illustrated in detail in Fig. 5.7. In the bottom panel, b), we include all of these and include the additional effect of radiation pressure acting on dust grains. Jupiter's magnetic field is modelled out to octupole order, and the gravitational field includes J_2 and other higher-order terms. All the grains rapidly charge up to strong negative potentials, hence we have adopted a greyscale matches that of Fig. 4.10, with excursions away from synchronous orbit by more than $0.02r_L$ depicted in light grey, and grains that escape or collide with Jupiter marked in dark grey. Along the vertical axis on the right-hand side, Lorentz Resonance locations in the Kepler limit are shown.

electromagnetic force increases, radiation pressure becomes far less important. The effect of radiation pressure on the right side of Fig. 5.6b clearly increases in scope to include smaller grains with increasing distance from Jupiter. This is due to the decline in Jupiter's gravitational influence with distance compared to the essentially constant force of solar radiation pressure.

Even without the additional physics of radiation pressure, there are important differences between Figs. 4.10 (constant charges) and Fig. 5.6a. On the right of Fig. 5.6a, we see a near vertical strip of unstable trajectories. This feature disappears at R_{syn} and curves to encompass smaller grains, or higher charge-to-mass ratios, closer to the planet. These grains are unstable due to the shadow resonance. Two grain trajectories, one just inside this feature and one just outside it are depicted in Fig. 5.7. For the 7 μm grain, the precessions due to Lorentz perturbations (retrograde) and the gravitational effect of Jupiter's oblateness (prograde) are almost in balance, enabling the shadow resonance to steadily increase the dust grain's radial range over four years. A slightly larger dust grain in Fig. 5.7 has a slower EM precession rate, and the destabilizing effect of the shadow resonance is limited primarily by the J_2 precession timescale.

Another important difference between the stability maps of Fig. 5.6 and the constant charge model of Fig. 4.10 is the region of instability in the Lorentz regime for the smallest dust grain on the left side of both Figs. 5.6a and b. An example is plotted in Fig. 5.8. This tiny grain remains stable, confined between its launch location and R_{syn} for over three years, as its latitudinal range slowly increases. Eventually however, the grain becomes unstable. There are various dynamical effects that we have not addressed here, that may cause this long term instability. Northrop et al. (1989) identified the slow "gyrophase drifts" in EM-dominated dust grains, due to changes in the charging currents with epicyclic phase. These can be due to gradients in the plasma temperature or density, but even in a uniform plasma will be present since the speed of the dust grain moving through

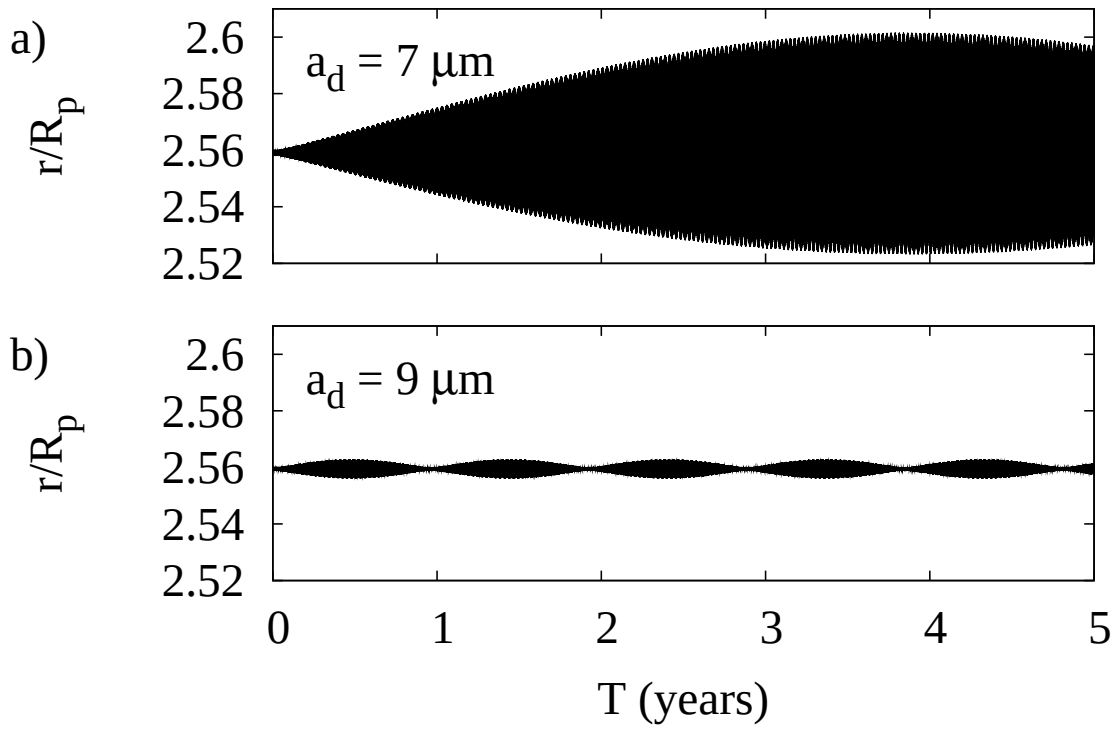

Figure 5.7: Two dust grains precessing due to Lorentz perturbations and the gravitational effect of Jupiter's oblateness, with charge varying due to the planetary shadow. Following launch at $1.56R_p$, we plot the radial range of a 7 μm dust grain (a) and a marginally larger 9 μm dust grain (b).

plasma varies around the epicycle. Northrop et al. (1989) found that highly-charged dust grains migrate slowly toward R_{syn}, consistent with the initial evolution of the trajectory seen in Fig. 5.8. However, the gradual and concurrent increase in latitudinal range ultimately brings the grain orbit to a regime that is chaotic but still globally bound. This phenomenon certainly merits more attention, but for our purposes, the extreme delay in the onset of this instability and its probable cause puts the effect beyond the scope of this thesis. Many other physical effects that we have neglected, including plasma density or temperature gradients, as well as drag forces, will likely have an effect on a ever shorter timescales.

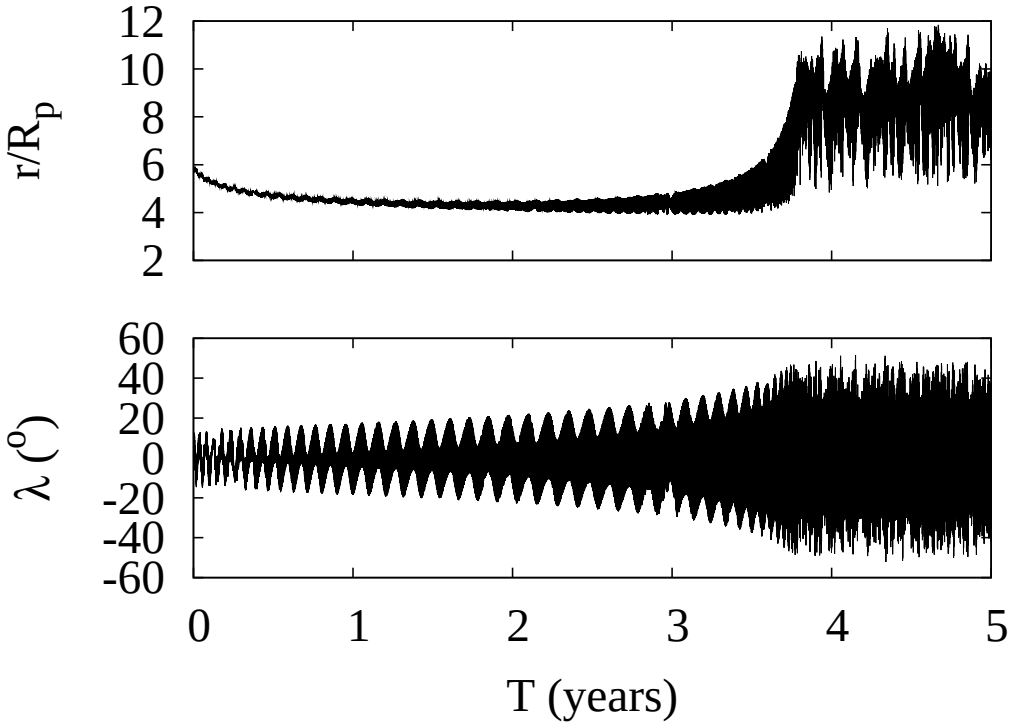

Figure 5.8: A 10-nm dust grain launched in a uniform plasma with $n_e = 2000$ cm^{-3}, and $T_e = T_i = 5$ eV.

5.7 Discussion

Relaxing the assumption of constant charge-to-mass ratios leads to a substantial increase in the range of dust-grain sizes that are destabilized in tenuous plasma. Results are highly model dependent, and for simplicity we adopted a sparse plasma with constant spatial density and photoelectric charging. The time-variable charging currents on a dust grain due to passage through the planetary shadow significantly expands the range of grain sizes that are globally unstable, particularly inside synchronous orbit. Larger dust grains respond rapidly to changes in the charging environment and hence stability is determined by comparing the destabilizing timescale of variable Lorentz forces with the orbital precession time (Horányi and Burns 1991; Hamilton and Krüger 2008). For our nominal model, this increases the threshold radius for destabilized grains by more than an order

of magnitude. For smaller grains, by contrast, charging is slow with the result that different stability curves apply at different times, expanding the zone of instability by an order of magnitude over that expected for a constant charge. The sparse plasma that we have adopted here is appropriate for the dusty main ring and gossamer rings at Jupiter. We find that the removal of dust at Jupiter is dominated by the basic dipolar radial instability for positive grains, substantially extended to both larger and smaller particles by the effects of variable charging.

In the far denser plasma environment in the Io plasma torus, dust grains rapidly reach strongly negative electric potentials and behave much as constant charge, negative dust grains. This permits the destabilizing effects of Jupiter's non-axisymmetric magnetic field to determine grain orbit stability, and thus Lorentz resonances emerge as the destabilizing effect that acts on the shortest timescale. With the parameters chosen here, this leads to the escape of particles nominally larger than those found in the high-speed dust streams. It remains to be seen whether this discrepancy is due to inaccuracies in our assumed grain parameters or if this truly means that Lorentz resonances do not populate dust streams.

Chapter 6

Saturn's Spokes

6.1 Introduction

Four hundred years have passed since Galileo first struggled to understand Saturn's majestic ring system, and while the quality of our observations and our understanding of the rings have improved immeasurably, phenomena that are surprising, unsought and novel have been discovered in our time too.

As Voyager 1 approached Saturn in November 1980, the first high resolution images of the optically-thick B ring revealed dark radial features against the lighter B ring background. Named "spokes", the features had not been seen by the earlier Pioneer 11 encounter with Saturn, due to the poorer quality of the Pioneer cameras. By maintaining a long, well-defined radial profile for hours, the spokes clearly resisted the rapid Keplerian shear that should separate ring particles within tens of minutes (Hill and Mendis 1981). As Voyager 1 moved behind Saturn, the spokes seen in forward scattered light appeared as bright features on a dark background, indicating a characteristic dust grain size of $\sim$1 μm. Because the radial edge of the features corotated with Saturn, the intrinsic magnetic field of the planet was implicated as having a crucial role in spoke formation (Terrile et al.

1981). This premise gained further support when Porco and Danielson (1982) found a strong correlation between periodic spoke activity and Saturn's 10^h39^m rotation period as measured in kilometric wavelength radiation (the so-called Saturn Kilometric Radiation, or SKR, Desch and Kaiser 1981). Porco and Danielson (1982) proposed that the spoke activity is likely associated with the magnetic field sector that gives rise to the SKR.

Despite the observational constraints on spokes, a detailed working model proved elusive. Less than a year later, Voyager 2 arrived at Saturn ready to scrutinize the B ring, taking far more images of the spokes than its predecessor. These new data permitted detailed studies of spoke formation and evolution, challenging theorists and constraining their models. Many theories to explain the spokes have been proposed. The biggest challenge to theorists, then and now, is the fact that micron-sized dust grains are massive enough to make rapid radial excursions covering large distances extremely unlikely, (see Fig. 3.6a). The Goertz and Morfill (1983) model, for two decades, was the most detailed and became the most widely accepted. In their model, a plasma cloud initially triggered by an impacting meteoroid induces the electrostatic levitation of dust above the ring plane. The radial progression of the plasma cloud explained the active edge of the spokes, and the Keplerian shear of the dust explained the wedge-shaped spoke morphology. Farmer and Goldreich (2005), however, found that the radial progression of the released plasma in the Goertz and Morfill (1983) model could not be rapid enough to match certain observations. We shall address the Goertz and Morfill (1983) model in more detail below.

After the Voyager probes left Saturn, there were no instruments capable of seeing Saturn's spokes until the Hubble Space Telescope was serviced in 1993. The HST monitored Saturn and observed spokes from 1996 until 1998 when they disappeared completely (McGhee et al. 2005). The lack of spokes was confirmed when the Cassini orbiter arrived at Saturn in 2004. One year after Cassini's arrival, the mysterious spokes returned (Mitchell et al. 2006), and have been observed extensively since then. It appears that the

spoke phenomenon is seasonal, with peak activity near Saturn's solar ring-plane crossing.

Despite thirty years of work, there are no models for spoke formation that fully satisfy all of the observations. In this chapter, we will summarize the observations of the spokes phenomenon and review some of the theories that have been proposed to explain the data. The fundamental dynamics that we have explored in previous chapters will serve as a foundation for both evaluating the theoretical basis of the various proposed hypotheses for the spokes and for building a robust alternative. We evaluate all models for the spokes phenomenon critically, considering both observational and dynamical constraints.

6.2 The Radial Spokes in Saturn's B-ring

6.2.1 Spoke Particles are Dust

In backscattered light, the spokes appear as dark features on the lighter B-ring background. In forward-scattered light, the spokes appear as bright features (Smith et al. 1982). This was the first hint that the spoke particles are distinct from those in the main rings, and that the characteristic size of spoke particles is commensurate with optical wavelengths.

Thomsen et al. (1982) considered the constraints on spoke particles imposed by their azimuthal progression between images taken by Voyager 1. They found that a small deviation from the Kepler orbital frequency seen in the spoke patterns implied a charge-to-mass ratio of $q/m = -7$ C kg^{-1} or $L_* = -0.14$ (see Table 4.1). Thomsen et al. (1982) identified this as requiring very high electric potentials ($\sim$ 1 kV) if the grains indeed are 1 μm in size, as indicated by the light scattering properties. More recently, Mitchell et al. (2011) found that spoke growth, if due to the motions of individual micron-sized dust grains, would require a potential ~ -1 kV, equivalent to a charge-to-mass ratio of $L_* \approx -0.5$.

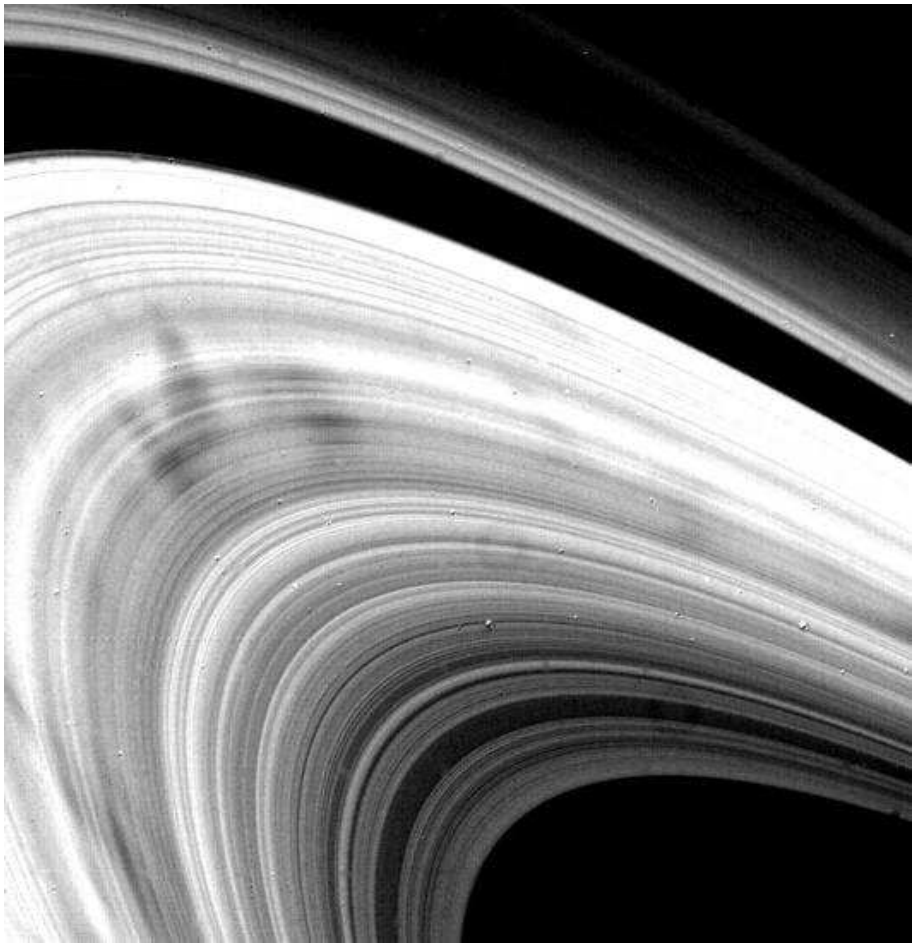

Figure 6.1: First seen by the two Voyager spacecraft, the spokes have peculiar properties— their morphology, formation times and locations, as well as their seasonality are all well-constrained but poorly understood.

Eplee and Smith (1987) argued that the timescale for radial growth in a spoke was determined by the charge decay timescale on a dust grain, and on this basis argued for a characteristic grain size of 0.1 μm for the spoke particles. A detailed analysis of the Voyager color data by Doyle and Grün (1990) constrained the grain size to 0.6 ± 0.2 μm. This slightly lower estimate for the grain size was supported by HST observations of the spokes in the 1990s (McGhee et al. 2005). They also found a rather narrow size distribution, with an effective grain size of 0.57 ± 0.05 μm. Cassini IR spectra of spokes, however, indicate a larger model grain size, at 1.9 μm (D'Aversa et al. 2010). Notwithstanding this discrepancy, the spoke particles are clearly large enough to be in the gravitational regime

whereby their charge-to-mass ratios are small ($|L_*| < 0.1$).

6.2.2 Morphology and Formation

Spokes have a radial edge corotating with Saturn, and a leading edge rotating at the Kepler orbital frequency. Terrile et al. (1981) interpreted this morphology as indicative of an active radial edge corotating with Saturn's magnetic field as the source of the spoke particles, with the tilted edge marking the azimuthal extent of Kepler shear. This also explained why both edges reach a vertex at the synchronous orbit, where the two periods are equal. The width of the Keplerian shear reveals the age of an extended spoke, which range from 16 minutes to 4 hours, with an average age of $\sim$1 hour. Most of the spokes form on the morning ansa of the ring, with the oldest ones originating in shadow. Note that even the widest spokes never appear to reach half a rotation period (i.e. half of 10.7 hours) in age.

Grün et al. (1983) describe three types of spokes. As the most prominent and well-defined, the extended spokes are wedge-shaped features within the synchronous orbit at $R_{syn} = 1.86R_p$. These are typically older than 1 hour, and exhibit optical depths $\tau \sim 0.1$. Narrow spokes with sharply defined edges are just 500 km wide and typically 5000 km long, and many were observed straddling the corotation distance, keeping the same width all along their length. They remain active for between 16 and 67 mins, and continue to undergo Keplerian shear, tilting from a purely radial attitude over time. In total, they contribute roughly 10% of the spoke particles by number compared to the extended spokes. Filamentary spokes are the narrowest type. They are only seen outside the corotation distance, and have active ages of less than 16 mins. They are usually connected to narrow or extended spokes further in, and occasionally merge with wider spokes. Their contrast and hence optical depth is much lower than for extended or narrow spokes; $\tau \sim 0.05$, and the total number of particles in one is $\sim 0.5\%$ of that seen in an extended spoke.

In a movie of consecutive images taken by Voyager 2, Smith et al. (1982) identified the rapid appearance of a narrow spoke that could not be seen in previous frames. The spoke was ~ 6000 km in length, and in subsequent frames, its length appeared unchanged although its contrast (and its width) increased. The frame rate of the Voyager 2 movie thus had constrained the formation timescale of this spoke to just 5 minutes, which implies a minimum radial progression of 20 km s^{-1}. Although one might argue that an isolated spoke may appear spontaneously due to changing viewing effects as both the spacecraft and the ring are in constant motion, the rapid appearance of the narrow spoke within a pattern of neighboring spokes made the Smith et al. (1982) discovery more compelling. Grün et al. (1983) identified another example of a new spoke forming between older spokes, with a total length of 8000 km. It must be stressed that these isolated observations are somewhat controversial. If valid, they place an important dynamical constraint on spoke formation models, which we shall explore in the next section. More importantly, Mitchell et al. (2011) have not found evidence for such rapid spoke formation in the Cassini data. They limit the radial growth rate of spokes to be ~ 1 km s^{-1}. Eplee and Smith (1985) conducted a detailed investigation of the radial progression of a single spoke in the Voyager 2 low-resolution movie. They estimate speeds of up to 0.7 km s^{-1} over a 50-minute period, with a charge-to-mass ratio of -60 C kg^{-1} ($L_* \approx -1.2$).

Smith et al. (1982) noted that some spokes can be traced as they rotate through 360°. It is unknown if this indicates that an individual spoke can survive a rotation period, or if there was rather an active corotating region that happened to be fertile ground for spoke formation, but at least one recurring spoke was seen in two frames at the same location $10^h37.6^m$ apart. The angle between the radial edge and the Kepler shear on the later observation implied a spoke age of 3.3 hours. We shall return to this apparent age limit of spoke shear despite extended periods of spoke activity later.

Spokes appear most prominently on the dawn ansa of the ring, with roughly four

times as much spoke activity seen by Voyager 2 on the morning ansa than the evening ansa (Grün et al. 1992), and a peak in spoke activity between 03:00 and 07:00 local time, with a few spokes having formed in the shadow. For both the morning and evening ansae, spoke activity peaked near two corotating longitudes, at 120° and 300° SLS (the Saturn Longitude System). The peaks in activity at the morning ansa are 2.2σ and 1.3σ above the mean at these longitudes (Grün et al. 1992). Given the near-perfect axisymmetry of Saturn's intrinsic magnetic field, both the longitudinal dependence of spoke activity, and indeed the SKR, are poorly understood.

Radially, there seems to be a strong correlation between spoke activity and the optical depth of the B ring (Grün et al. 1992), with almost all of the spoke activity occurring beyond $1.72R_p$, where the B ring is thicker. Within this distance, spoke activity covers $\sim 1\%$ of the ring area from $1.62R_p$ and the increase to $\sim 12\%$ at $1.72R_p$ is immediate. Hill and Mendis (1982) attributed the inner boundary of spokes to the Northrop instability at $1.63R_p$ (see Chapter 3). Note that our revised location for this boundary, including the effects of the stabilizing mirror force and Saturn's g_{20} and g_{30} magnetic field terms, is at $1.70R_p$, very close to the observed spoke boundary (Fig. 4.12). Further out in the B ring, spoke activity smoothly declines to zero towards the outer edge of the B ring at $1.95R_p$. Interestingly, this smooth decline seems unaffected by the synchronous orbital distance at $1.86R_p$.

6.3 Spoke Formation Theories

The spoke phenomenon has proven to be a rich source for speculation and theory since the Voyager encounters. Thirty years on, after more observation and analysis, the spokes continue to inspire creativity and create puzzlement. A full understanding of spokes must explain 1) the morphology and rapid spoke formation timescale, 2) the longitudinal de-

pendence of spoke activity, and 3) the seasonal variation in spoke activity. Even before the Voyager 2 encounter with Saturn, theories about spokes formation began appearing in the literature. In summarizing these theories below, we will concentrate on two broad themes which have been developed by spoke theorists. The first involves the radial alignment of prolate dust grains due to magnetic or electric field effects, while the second involves the levitation of dust above the ring plane along the radial active edge of a spoke, due to plasma processes.

6.3.1 Grain Orientation Models

Bastin (1981) proposed that albedo changes on orbiting dust grains passing through local magnetic field anomalies cause spokes. In their model, there was no need for bulk motions of dust relative to the larger ring particles. Forming spokes simply required a fraction of dust grains to be reoriented by the local magnetic field lines. As an alternative to the magnetic field, Bastin (1981) suggested electrostatic forces on clustering dust grains to change their albedos. Their model did little to address the wedge-shaped morphology of the spokes, with the apex near synchronous orbit, or even why the spokes had long radial active edges. Bastin (1981), however, correctly identified what has proved to be the major challenge in all spoke models. Although EM effects are somehow causing the spokes, the spoke particles are too large to be moved in bulk by the Lorentz force. Bastin (1981) realized that the growth of spokes is due to the emergence of high contrast between the dust and the B ring background, rather than the motion of the dust itself. In other words, it is not the dust but rather the optical properties of the dust that propagates radially.

Bastin (1981) provided little detail about their idea that electric fields could polarize the orientation of dust grains. The suggestion of electric fields, however, was picked up and developed in more detail by Carbary et al. (1982). They dismissed the corotational electric field as a cause for the spokes since such fields would be uniform, would not

be time variable, and would not be confined to the B ring. However, they proposed that viscous drag from zonal winds in Saturn's atmosphere causes super-rotation in the ionosphere, resulting in south-to-north electric fields in the ionosphere. For currents flowing down the magnetic field lines to the ring-plane, this translates to a radial potential difference across the B ring. As orbiting 1 to 10-μm sized dust grains pass through this electric field, their orientations are polarized radially, altering their light scattering properties.

In the Carbary et al. (1982) model, the spokes dissipate whilst undergoing Keplerian shear as radiation pressure from sunlight randomizes the dust grain orientations. They proposed that spokes are the visible manifestation of Saturn's electrostatic discharges (SEDs). These have a typical episodic period of 610 minutes (Warwick et al. 1981) and were originally thought to originate in the rings, but eventually equatorial storms in Saturn's atmosphere became the favored model (Fischer et al. 2006). In any event, the link between spokes and SEDs was at odds with the findings of Porco and Danielson (1982); namely that spoke activity peaked at the same longitude as the SKR, with its 639 minute periodicity. However, since the spoke activity itself from the Voyager data showed a periodicity of 621 ± 22 min, neither the SED nor the SKR period could be ruled out as the determinative timescale for spokes. Nevertheless, Cassini observations have laid at least this particular aspect of the spokes phenomenon to rest. Cassini revealed two characteristic SKR periodicities, one in each Saturnian hemisphere. Mitchell et al. (2011) have significantly reduced the uncertainty of spoke periodicity which favors the northern SKR on the north side of the rings, and may vary with both the northern and southern SKR on the south side of the rings.

Weinheimer and Few (1982) identified more fundamental problems with the Carbary et al. (1982) electric field model. Firstly, the torques expected from the electric field on prolate spheroidal dust-particles are small compared to the rotational kinetic energies typical in cold grains, even if we ignore collisions. Although ferroelectric materials exist

which could react to the proposed electric field with enough torque to polarize dust grains, the pure water ice of the B ring is not such a material. Furthermore, the poor electrical conductivity of ice grains would make the polarization timescale too long to form spokes.

In response to this challenge, Handel and James (1983) proposed a "polarization catastrophe" model to align dust grains in a weak electric field. They found that contrary to the assumptions of Weinheimer and Few (1982), ice at $T \lesssim 70 - 100$ K is indeed a ferroelectric material. Close to this temperature threshold is the temperature of the B ring itself (68K, Hanel et al. 1982). Handel and James (1983) proposed that in Saturn's shadow, a portion of the crystalline ice grains make the transition to a ferroelectric state and are spontaneously polarized. The electric dipole moment of the ice crystals aligning with the electric field increases the local electric field strength, making the polarization of other dust grains more likely, and therefore leading to the polarization catastrophe. Upon leaving the shadow, the crystallites experience an increase in temperature and the polarization disappears. Handel and James (1983) posited that a small initial polarization due to the corotational electric field is enough to ensure that the polarization catastrophe proceeds radially, but one consequence of this is that the spokes would only be able to grow outwards from their trigger point, since the corotational electric field is directed radially outwards (Eq. 2.20, Chap. 2). Handel and James (1983) freely admit that in their model, grains have far lower charge-to-mass ratios than calculated by Thomsen et al. (1982). They also proposed that a tilted dipole model for Saturn's magnetic field should cause two maxima in SED and spoke activity 180° apart in the B ring. Although the Voyager data permitted an upper limit of 1° for a magnetic dipole tilt (Smith et al. 1981), the more recent Cassini data has reduced this upper limit substantially (Cao et al. 2011). Furthermore, the Cassini spoke observations do not find strong evidence for two maxima in spoke activity (D'Aversa et al. 2011).

Despite these disagreements, it appears that the critique from Weinheimer and Few

(1982) had convinced most authors that the grain alignment model could not work. Moreover, the "polarization catastrophe" attempted to link spoke activity with the electrostatic discharges that we now know originate in Saturn's atmosphere and not the rings. Ultimately, the grain alignment models faded from the literature.

6.3.2 Grain Levitation Models

Hill and Mendis (1981) also published a theory on spoke formation even before the Voyager 2 flyby of Saturn, and their model, too, invoked magnetic field effects on charged dust grains. In their theory, currents from Saturn's magnetosphere charge up ring particles with loosely-bound fine dust on their surfaces. As the boulder-sized ring particles become electrically charged by this electron stream, a small fraction of the dust on the particles also acquire negative potentials, until they are levitated out of the ring plane. Reaching even higher charge-to-mass ratios in the free space outside the ring plane, the dust grains are quickly brought to corotation with Saturn's magnetic field. In their model, Hill and Mendis (1981) attempted to address the increased spoke activity at the morning ansa. They proposed that in sunlight, dust grains discharge to a low charge-to-mass ratio and the spoke dust begins to move at the Kepler speed. Their model required the electron currents to follow field-aligned filaments, otherwise, the levitated grains would appear in broad sectors instead of in discrete spokes. The Hill and Mendis (1981) theory is distinct from the Carbary et al. (1982) model in its proposed source of charging currents to the B ring. The former proposed currents originating in the solar wind flowing from the magnetotail into the auroral regions, while the latter assumed Saturn's ionosphere as the source.

One critique of the Hill and Mendis (1981) model was that the source current to make a radial spoke would have to be highly extended in latitude and confined in longitude, which is difficult to explain (Tagger et al. 1991). Moreover, the low conductivity of ice

grains identified by Weinheimer and Few (1982), initially invoked as a critique of the Carbary et al. (1982) grain alignment model, is a challenge to the Hill and Mendis (1981) model too, since the grains can only levitate from the B ring after they have charged up sufficiently from contact with a ring particle.

Another problem with the Hill and Mendis (1981) theory is that it involves large dust grains sustaining corotational motion along the radial active edge, requiring unreasonably high electrostatic potentials on dust grains. Nevertheless, the authors developed their model further in Hill and Mendis (1982). They hypothesized that the wedge-shaped morphology of spokes was due to the dynamical sorting of dust by grain size. They assumed that each grain size forms its own "rib" radiating out from the apex of the spoke at R_{syn}. Following Eq. 3.8 (Chap. 3, Northrop and Hill 1982), the guiding centers of positively-charged dust grains inside R_{syn} for $L_* < 1$ move slower than the rotating magnetic field, while the negative grains orbit faster than the magnetic field inside corotation. In the Hill and Mendis (1982) interpretation, the spokes are fan-shaped populations of negatively-charged dust, with a whole range of charge-to-mass ratios at the radial active edge, but only larger grains $|L_*| << 1$ at the Kepler leading edge as the spoke ages. Their model argued against the possibility of positively-charged dust in spokes, since while negative grains could explain the observed leading spoke edges, positively-charged grains would succumb to the radial instability (Fig. 3.6b). The Hill and Mendis (1982) model posits that the radial spreading of the spokes is strongly dependent on grain size, and it predicts multi-modal size distributions of dust in spokes at different radial distances.

A concurrent theory involving the levitation of dust grains from B ring particles was proposed by Goertz and Morfill (1983). This model ultimately became the most successful in the Voyager era, although, as we shall see, it has been challenged more recently. In the Goertz and Morfill (1983) model, a meteor impact on the B ring generates a dense plasma cloud above the ring plane. Although most of the plasma is reabsorbed by the

ring, some escapes out of the ring plane and can survive a half-bounce period as the plasma particles climb magnetic field lines to mirror points before returning to the ring plane. Under ordinary conditions, fine dust on ring particles do not readily reach electric potentials high enough to escape from the surfaces of ring particles and the gravity of the ring plane. However, under the influence of much denser, localized plasma, dust grains become charged enough to levitate against the gravity of the ring. Those that escape the ring plane rapidly increase their charges in the plasma cloud and attain heights above the ring plane well beyond the Debye length. (This is the distance over which the electric field of a charged grain can act before being shielded by intervening charges in the plasma that cancel the electrostatic potential.) Goertz and Morfill (1983) calculate that the dust grains reach several kilometers out of the ring plane, enabling them to charge up to an equilibrium potential. In their model, the positively-charged plasma cloud begins to move radially due to the corotational electric field, lifting negatively-charged dust grains out of the ring plane in its wake. In sunlight, the negatively-charged grains produce a cloud of electrons which, after one bounce period, interact with ring particles, charging the surfaces to elevate more fine dust (Morfill et al. 1983).

In the Goertz and Morfill (1983) model, the motion of the plasma determines the radial active edge of the spoke. They posit that the plasma cloud moves inwards if it is created inside synchronous orbit, and outwards from beyond R_{syn}. Plasma clouds that initially straddle this location can create spokes that grow in both directions. The spoke formation ceases when the plasma density becomes too low to elevate dust grains. Goertz and Morfill (1983) noted that the plasma cloud they invoke in their model would not survive long enough to form a long radial spoke if the plasma were on the south side of the rings. Since the magnetic equator at Saturn is north of the ringplane, plasma south of the ring plane would be reabsorbed within a bounce period.

Morfill et al. (1983) note that since the process they invoke is initiated by insolation,

spokes can only begin to evolve radially at the morning ansa, explaining the strong variation in spoke activity with local solar time. The meteor-impact model was bolstered by Cuzzi and Durisen (1990) on the basis of a solar-time bias in ring bombardment by meteoroids. They found impact speeds in the B ring should peak around local midnight, with a concurrent increase in dust generation.

Both the Hill and Mendis (1981) and Goertz and Morfill (1983) theories involved the levitation of dust grains resting on ring particles with charging processes; the former with external currents in the magnetosphere guided to the ring plane, and the latter with dense plasma clouds induced by meteor impacts. Meyer-Vernet (1984) found that centrifugal disruption of spinning grains 1 mm to 10 cm in size would eject loosely bound 0.1 to 1 μm particles, making the electrostatic expulsion of dust from the surfaces of boulder-sized ring particles arguably unnecessary.

One of the reasons that the Goertz and Morfill (1983) model was preferred by authors including Eplee and Smith (1984) was that the spokes were seen to form primarily on the morning ansa but also, to a lesser extent, in the afternoon, whereas in the Hill and Mendis (1981) scenario, spoke formation is suppressed in sunlight as the photoelectric effect rapidly discharges the negatively-charged spoke grains. More importantly, the Weinheimer and Few (1982) critique examining the torques in the Carbary et al. (1982) scenario had convinced most authors that the grain alignment hypothesis was unworkable (Horányi et al. 2004). This was how things stood as Cassini approached Saturn, when interest in the spokes was rekindled.

Farmer and Goldreich (2005) offered a strong critique of Goertz and Morfill (1983). They showed that the plasma motion invoked in the Goertz and Morfill (1983) model would be limited to the difference in Kepler and corotation speeds, (a few kilometers per second), whereas Goertz and Morfill (1983) invoked speeds of 23 km s^{-1} at $1.9R_p$ to explain the apparent rapid spoke formation time. In answer to Farmer and Goldreich

(2005), Morfill and Thomas (2005) defended the original model. They conceded that the science of dusty plasmas had evolved substantially since the early 1980s, and they adapted their original idea by invoking a multi-layered structured plasma cloud with differential radial plasma speeds.

Recently, Jones et al. (2006) revived the Carbary et al. (1982) theme of ionospheric currents affecting the B ring with a new theory invoking spoke production by lightning from Saturn's atmosphere. In this model, grains are levitated from B-ring particles by electrostatic forces, but instead of invoking magnetospheric currents (Hill and Mendis 1981) or micrometeoroid induced plasma clouds (Goertz and Morfill 1983), Jones et al. (2006) invoke currents from Saturn's atmosphere flowing down magnetic field lines to the ring plane. In this theory, a cosmic ray triggers an upward electron avalanche above a thunderstorm. The planetary magnetic field guides electron beams from the storm to the B ring, inducing a negative charge on ring particles. Large ring particles then shed the dust grains, which are electrostatically levitated out the ring plane. In this model, the electron beam footprint would be the active edge of the spoke. Jones et al. (2006) point out that a circular storm feature in Saturn's atmosphere would have an elliptical footprint on the B ring with an aspect ratio of $\approx 1:2.8$, and the apparent linearity of spoke edges is the result of a low-inclination view of this ellipse. In their model, the apparently sharp active edge is an illusion accentuated by Kepler shear. Jones et al. (2006) attribute the abundance of spokes near the morning ansa to the minimum density of Saturn's ionosphere at dawn, which favors the electron avalanche.

6.3.3 Other Theories for Spoke Formation

There are a few other theories about spoke formation. Tagger et al. (1991) suggested magnetosonic compression waves in the B ring. In their model, a standing wave in the dusty plasma forms a bar that straddles synchronous orbit between the inner and outer Lindblad resonances. They ignore electrostatic effects since their mechanism has no need for spoke particles to leave the ring plane. One problem with their model is that it assumes Keplerian shear in the standing wave. This explains the tilt of narrow spokes, but cannot explain the persistent radial active edge of an extended spoke without extremely high charge-to-mass ratios in the dust.

Finally, in a one-sentence abstract, Perov (2012) invokes the unstable points of libration in the ten-body problem, with the planet Saturn, 8 satellites and spoke-dust. We anticipate more details from him in the future.

6.3.4 Comments on Spoke Seasonality

The disappearance and reappearance of spokes over time has been a source of much speculation in the literature. The phenomenon is clearly seasonal, with spoke activity at its peak near years of solar ringplane crossing, which occurs twice per Saturn's 29 year orbital period, most recently in 1980, 1995, and 2009. McGhee et al. (2005) proposed that the viewing geometry favors spoke observations when the ring opening angle is small. This contrasts with the model of Farrell et al. (2006) that attributes the seasonality of the spokes to the plasma condition in the B ring and its effect on how easily grains can be levitated from the ring plane. Farrell et al. (2006) examined Cassini data on the electron density in rings and modeled the effect of opening angle on the charge of the ring. They found that a low solar elevation angle favors a net negative charge on the ring, modeled as a sheet, supporting the electrostatic levitation of negatively-charged dust.

On the other hand, a high solar elevation angle positively charges the ring on the sunlit side, strongly attracting negatively-charged dust back to the ring-plane, and therefore, suppressing the Goertz and Morfill (1983) mechanism. Farrell et al. (2006) found that a solar opening angle of 11° or more would prevent spoke formation, although the accuracy of this number is clearly dependent on many poorly-constrained parameters. However, their result was broadly consistent with the results of McGhee et al. (2005), who found that the spokes disappeared when the ring opening angle reached $\sim 15^\circ$. Jones et al. (2006) also proposed a hypothesis on spoke seasonality that did not involve viewing geometry. They attribute the presence or absence of spokes to seasonal changes in storm latitudes on Saturn, as well as solar activity.

The Cassini observations appear to rule out the possibility of viewing geometry influencing apparent spoke activity. Mitchell et al. (2006) found that spoke activity occurs independently of viewing angle and concluded that varying plasma effects are the most likely cause of spoke seasonality.

6.4 Collisional Cascade Model

None of the spoke models that have been proposed comply fully with all observational constraints. Here we present an alternative, relying on the dynamics that we have explored in this thesis, and then assess its viability. This project is ongoing.

We propose that a collisional cascade of charged dust grains in the B ring causes the spokes. An initial trigger, which we assume is a meteor collision, creates dust grains covering a broad spectrum of grain sizes in the B ring, and hence a wide range of charge-to-mass ratios. Most grains are launched out of the ring plane, reach their mirror point at high latitude, and return after half a bounce period. There is a high probability of colliding with a ring particle when the grain returns, because of the high optical depth of the B ring.

If these grains experience an integer number of epicycles during the bounce period, the collision speed of the grain with the ring will be moderate. However, for other gyrophases at the moment the grain re-enters the ring plane, collisional impact speeds of up to $\sim$5 kilometers per second can result, with enough impact energy to release more charged grains over a range of grain sizes. Figure 3.6 shows that depending on L_*, the radial excursions of such grains can be thousands of kilometers, away from synchronous orbit if the grains are positively charged, and towards that location if negatively charged. The grains with the highest impact speeds are much smaller than the visible spoke-particles that follow Keplerian motion. We hypothesize that spoke particles are the visible evidence of a cascade of hypervelocity impacts involving smaller, unseen dust grains. The high charge-to-mass ratios of these unseen grains keeps the cascade confined azimuthally as the gyrating grains drift slowly in longitude. However, the radial ranges vary immensely, with grains of $|L_*| \sim 1$ potentially landing at any radial location within epicyclic range after a half bounce period, and grains with $|L_*| >> 1$ landing close to their launch location. This might explain the long and narrow radial active edge of a spoke. In our model, the potentially rapid formation timescale for spokes is not due to the radial motion of the observed spoke particles, but rather is due to the phase speed at which the particles become visible, after generations of collisions in a confined longitudinal range, but over a broad radial range in the B ring. While alternative theories in the literature have struggled extensively with the problem of sustaining dense plasma in the B ring to charge up grains resting on larger ring particles, a collisional cascade model has no need for grain levitation.

6.5 Strategy

In this section we map out a strategy to evaluate the collisional cascade model. A direct simulation of a collisional cascade with all the relevant physics discussed in Chapters 3, 4 and 5 would be prohibitively expensive. Even if the size distribution of ejected dust from hypervelocity impacts were known, and all parameters to determine grain charging currents were known, simulating the trajectories of the released grains as their numbers increase exponentially is unfeasible.

Instead, we shall develop and verify the numerical tools required to follow a simple cascade model in controlled numerical experiments. Firstly, we shall introduce the equations, using the epicyclic model, that predict the impact locations and kinetic energies of grains launched in the B ring. We shall use these results to verify our numerical scripts that trace the creation of dust at an impact location. Then we can use these scripts on the simple cascade models involving variable-charge dust grains. Finally, we can test simple cascade models to test the effects of plasma conditions and the planetary shadow on a chain of collisions in the B ring. We assume that spokes are driven by the impacts with the highest kinetic energies. As we shall see below, the impact energy is a trade-off between mass (favoring large grains), and impact speeds which tend to zero in the Kepler limit.

6.5.1 Measuring Impact Energies Numerically

For negatively-charged grains with a constant charge-to-mass ratio, the epicyclic model accurately predicts the radial, vertical, and azimuthal motions (see Fig. 3.11). Our aims in this section are: i) to elucidate the relevant dynamics in our spokes model, and ii) to critically test our scripts that measure the impact location and kinetic energy for grain trajectories simulated numerically.

We begin by introducing new equations that we shall use to determine impact locations. Firstly, we assume that the impact occurs half a bounce period after launch, at a time

$$T_{impact} = \frac{\pi}{\Omega_b}. \tag{6.1}$$

Note that at Saturn, the critical distance for the vertical instability is in the B ring, and hence is of crucial importance to our spoke model. As $|L_*| \to \infty$, this crucial distance is at $1.70R_p$ using Saturn's full magnetic field configuration. This is very close to the observed distance within synchronous orbit where spoke activity sharply declines (Grün et al. 1992). Note however, that impacts in a collisional cascade can still occur within this distance. Following Fig. 4.12a, the vertical stability boundary moves closer to the planet for larger grains, suggesting that the cascade may continue for a narrower range of grain sizes.

The gyrophase at impact

$$\theta_{impact} = \kappa_c T_{impact}, \tag{6.2}$$

determines the relative speeds at the impact location, where the epicyclic frequency κ_c (Eq. 3.11) is evaluated at the guiding center distance, $\rho_c = r_L + r_g$. The radial position of the impact is simply

$$R_{impact} = \rho_c - r_g \cos\theta_{impact}, \tag{6.3}$$

noting that r_g is a signed quantity (Eq. 3.13). Given a longitudinal launch location ϕ_L, the impact longitude depends on the azimuthal drift rate $\dot{\phi}$, and the gyrophase, such that

$$\phi_{impact} = \phi_L + (\dot{\phi} + \Omega_p)T_{impact} - \frac{r_g}{\rho_c}\sin\theta_{impact}. \tag{6.4}$$

To determine the kinetic energy of the impacting grain, we measure its impact speed in the frame of the ring particle, which we assume is on a zero-eccentricity Kepler ellipse. The radial impact velocity is given by:

$$v_{r,impact} = \kappa_c r_g \sin\theta_{impact}. \tag{6.5}$$

For the azimuthal impact velocity, we assume the grain is launched at $v_L = \sqrt{\frac{GM_p}{r_L}}$, and that gyromotion is uniform and circular. This approximation is valid in the Lorentz limit, but since the epicycles are not circular at low $|L_*|$, it loses accuracy for larger grains. Nevertheless, to first order:

$$v_{\phi,impact} = v_c + \kappa_c r_g \cos\theta_{impact} - \sqrt{\frac{GM_p}{r_{impact}}}, \tag{6.6}$$

where the first term is the speed of the guiding center (Eq. 3.8), the next term has $\kappa_c r_g = \sqrt{\frac{GM_p}{r_L}} - v_c$, the speed of gyration, and the final term is the Kepler speed of the target ring particle. All of these equations can be tested using L_* as an independent variable, without making any assumptions about the model-dependent electric potential on a dust grain in equilibrium. Thus we plot these equations against numerical data, for grains launched at $1.8R_p$, comparing impact parameters measured from dI output with these analytical predictions.

Figure 6.2 traces the impact locations of negatively-charged grains with a constant charge-to-mass ratio both azimuthally and radially. Each grain is confined radially between the launch location and R_{syn}. The minima in radial range correspond to grains that land in the ring plane after a half-bounce period with an integer number of epicycles and hence an epicyclic phase matching the launch phase. For the larger grains, the epicyclic timescale matches the bounce period and the exact impact phase can be accurately calculated. For the small grains, where $\kappa >> \Omega_b$, the impact phase is essentially random. Near $L_* = -1$, the last term in Eq. 6.4, a first order approximation, causes small periodic deviations between the numerics and the analytical impact longitude, as seen in the top panel of Fig. 6.2. Nevertheless, the close agreement between the data points and the curves verifies the accuracy our numerical tools to measure impact locations for trajectories that cannot be solved analytically. In addition to impact location, we seek the impact kinetic

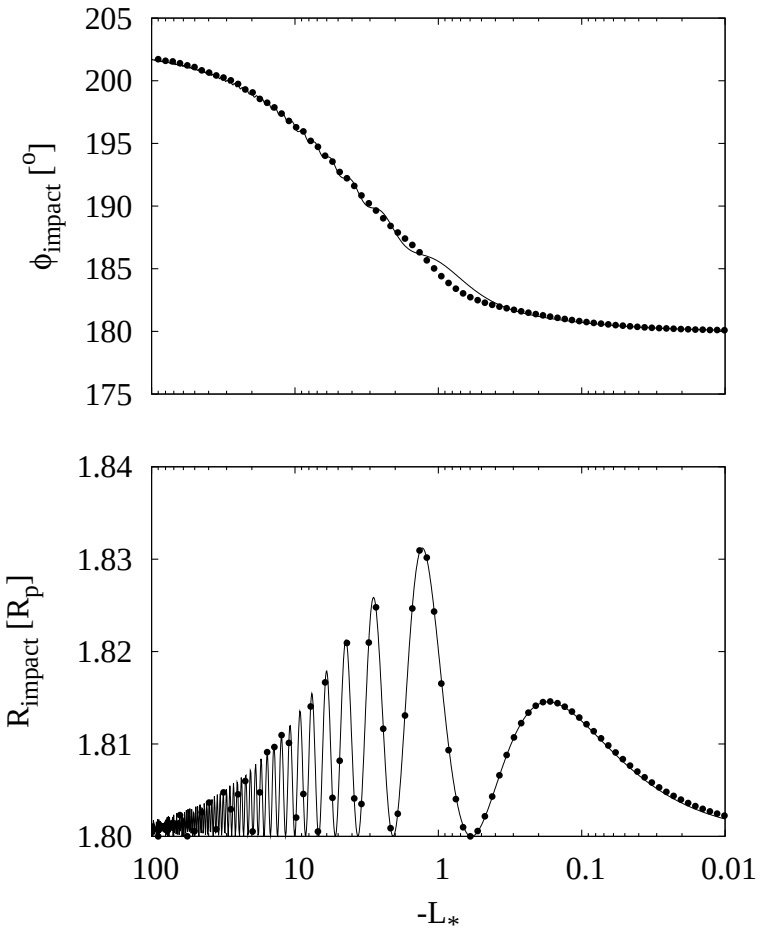

Figure 6.2: Impact longitudes (top) and radial locations (bottom) for dust grains with constant negative charges, launched at $r_L = 1.8R_p$, $\phi_L = 0^\circ$, in the B ring and within R_{syn}. The points are data read from outputs to dI, and the curves are the analytically-calculated impact locations (Eqs. 6.4 and 6.3). While the impact longitude varies smoothly with L_*, the radial impact location has periodic dips due to the epicyclic phase.

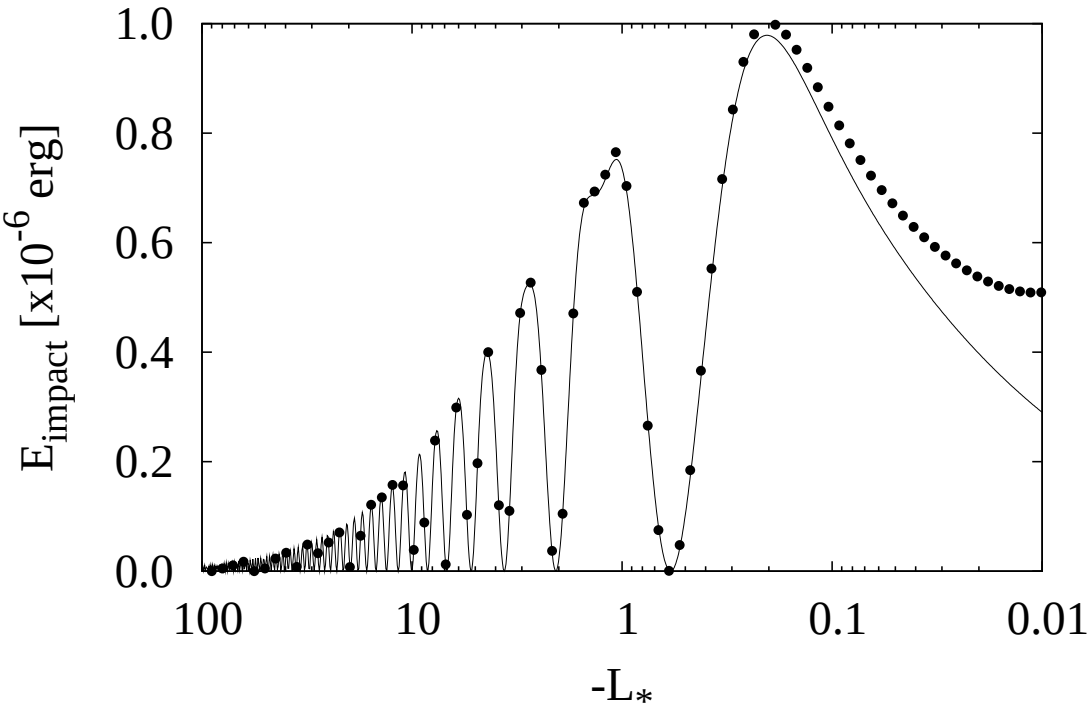

Figure 6.3: Impact energies for dust grains with constant negative charges, launched at $1.8R_p$ over a range of charge-to-mass ratios. We calculate the impact energies (curves, following Eqs. 6.5 and 6.6) and compare them to numerical data (points). The non-circular epicycles in the Kepler regime leads to an underestimate of impact energies.

energy of a dust grain of mass m:

$$E_{impact} = \frac{m}{2}\left(v_{r,impact}^2 + v_{\phi,impact}^2\right). \tag{6.7}$$

Figure 6.3 shows the impact energies for negatively-charged grains of constant L_*. In both the Kepler and Lorentz regimes, impact energies are low due to small speeds and masses respectively. Between these two regimes, where $L_* \sim -1$, if the gyrophase $\theta \approx \pi$, high impact energies occur.

The epicyclic model accurately predicts impact energies in the Lorentz limit and in the transition near $L_* \sim -1$. The agreement, which closely follows the change in impact energy with gyrophase, verifies our accuracy in measuring impact energies numerically. The disagreement between the numerical data and the epicyclic model in the Kepler limit is

due to the approximation of circular epicycles which loses accuracy in the Kepler regime. For the largest grains, the epicycles are ellipses with a 2:1 aspect ratio, and in the guiding center frame, the azimuthal speed at phase $\theta = \pi$ is non-zero, unlike the predictions of Eq. 6.6.

6.6 A Simple Cascade

For our numerical models, we now permit grain charges to vary in a tenuous plasma model with plasma density $n_e = 1$ cm^{-3}, temperature $T_e = 10$ eV, and with solar UV light interrupted during shadow transit. Note that since no plasma detector has ever been placed in the B ring, this choice is little more than a starting point for testing the collisional cascade hypothesis. Our aim here is to examine one possible cascade model and understand its properties in detail. Thus, we construct the simplest cascade possible in this plasma, whereby an impacting grain creates just one new, initially electrically neutral grain of identical size at the time and place of the impact. We follow the orbit of the grain, as its charge-to-mass ratio varies, until it collides with the ring plane after a half-bounce period, launching an identical grain. We shall assume that wherever the cascade proceeds, larger tracers of these collisions would be released as observable spoke particles.

We have done this numerical experiment for a range of grain sizes and present some preliminary results using Saturn's full magnetic field below. We begin with a choice of grain size that illustrates the possibility of a cascade traversing the radial width of the B ring within just a few collisions. Later, we shall consider an alternative cascade, one with many short steps in radial progression.

6.6.1 Leaping Across the B Ring

The presence of Saturn's shadow introduces azimuthal asymmetry to the grain dynamics, hence in Fig. 6.4 below, we show separate cascade chains for 12 equally-spaced initial launch longitudes. This causes the time taken for a cascade chain to traverse the B ring to vary substantially, from 20 to 30 hours depending on launch longitude. We see that all of the cascade chains accelerate away from R_{syn}. The cascades all progress radially inwards from R_{syn} because the equilibrium charge in sunlight is positive. Nevertheless, some grains move outwards if launched soon after sunset; they spend a few hours in the shadow collecting negative charges, and discharge after emerging on the morning ansa. These grains spend their entire short lifetimes negatively charged and hence move outwards, towards R_{syn}. All of the cascade chains that last at least 15 hours have one or more grains that are negative most of the time.

Note that some grains launched inside $1.7R_p$ land inside the inner edge of the B ring, ending the cascade chain. Most, however, do not. This is surprising since in the Lorentz limit, grains launched from within $1.7R_p$ are vertically unstable. The grains in Fig. 6.4, however, charge up to just $L_* \sim 10$ and remain vertically stable. For the grains that move outwards, the vertical stability boundary for negative grains applies (Fig. 4.12a), and for moderately-charged grains, this boundary curves downwards to distances inside the inner edge of the B ring, and hence these dust grains can keep the cascade going for at least one extra leap.

The energetics of these collisions is plotted in Fig. 6.5 below. Firstly, we see that impact energies can span two orders of magnitude at any particular radial location, and four orders of magnitude overall. The impact energy is likely to have a crucial bearing on the amount of dust produced in any particular collision, something that our simple model neglects. We also see that impact energies increase substantially with distance from R_{syn}.

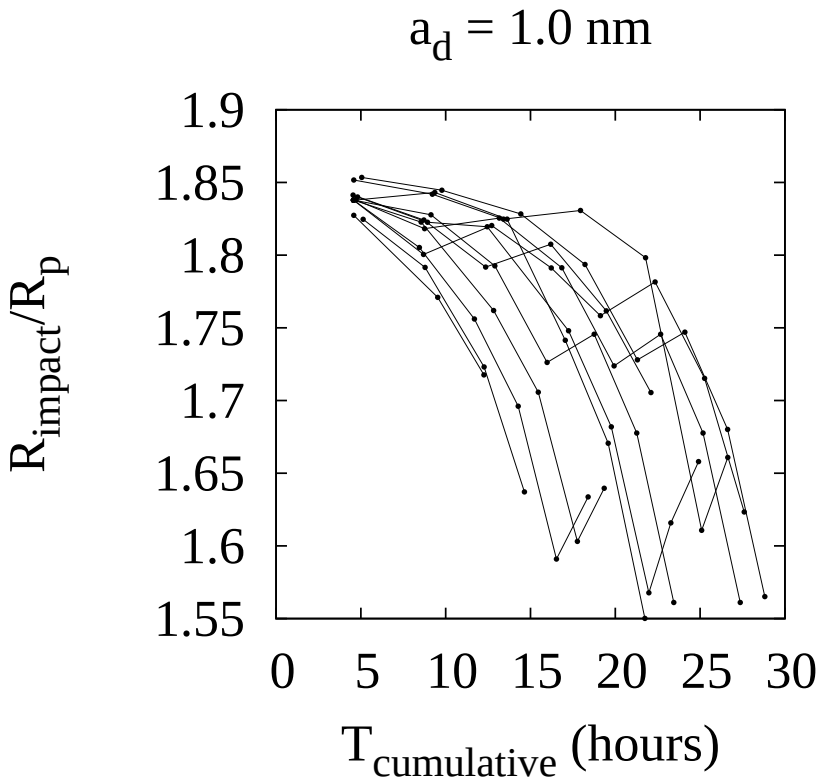

Figure 6.4: The progression of a simple model cascade, in which each grain of size $a_d = 0.001$ μm produces an identical grain at impact. We initiate the cascade at 12 equally-spaced azimuthal positions, plotting the radial position of impact after cumulative time given in hours. The radial distance of the initial trigger in each case is $1.85R_p$, just interior to the synchronous orbital distance at Saturn ($R_{syn} = 1.865R_p$).

Coupled with the slow progression of the cascade near R_{syn}, these two plots hint at an interesting trade-off in the cascade chain between the time for multiple collisions to build up near R_{syn}, and the strength of the collisions far from R_{syn}. The latter probably produce more dust per collision, but much less of the resulting dust lands in the B ring.

The data in these models also provide useful information on the longitudinal progression of a cascade chain. We plot the azimuthal spread of the same simple cascade chains in Fig. 6.6. The total azimuthal spread is a measure of how narrow a spoke formed by a cascade can be. Here, most of the collisions take place within 2 degrees of the trigger in the rotating frame, although, amongst the grains that are generated within $1.7R_p$, the

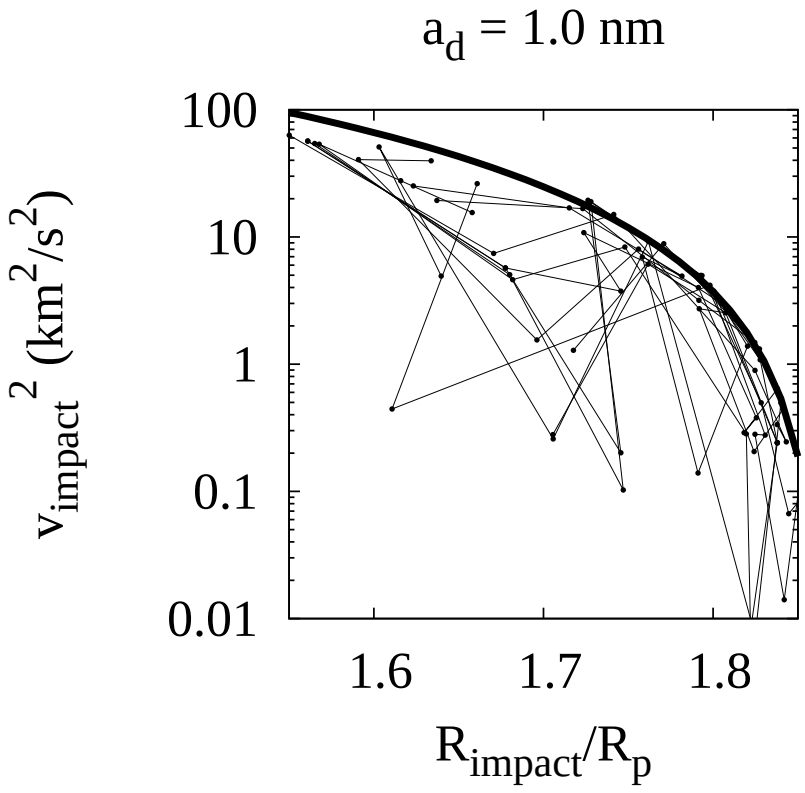

Figure 6.5: Following the same 12 cascade chains of Fig. 6.4, here we plot v^2_{impact} as a measure of specific impact energy at the end of each dust grain's trajectory. The curved envelope to the upper right marks the theoretical maximum for v^2_{impact}, for small epicycles using Eq. 6.7.

large epicycles cause some grains to stray more than 5° in the rotating frame. Note that an azimuthal spread of just 5° would be difficult to reconcile with spoke observations, for the following reason. At a distance of $\sim 1.8R_p$ from Saturn, this angle translates to an azimuthal distance of $\approx 0.15R_p$, resulting in a spoke with roughly the same width its radial length. Thus, if a cascade is to produce a narrow spoke with a suitably high length-to-width ratio, the total azimuthal range of the cascade should be, say, $\Delta\phi_{rot} \lesssim 1°$.

We follow the individual trajectories of the dust grains in one of the cascades from Fig. 6.6 in Fig. 6.7, below. In this sequence, each grain's epicycle slowly winds into a tighter spiral over the course of its half-bounce lifetime, as the charge-to-mass ratio

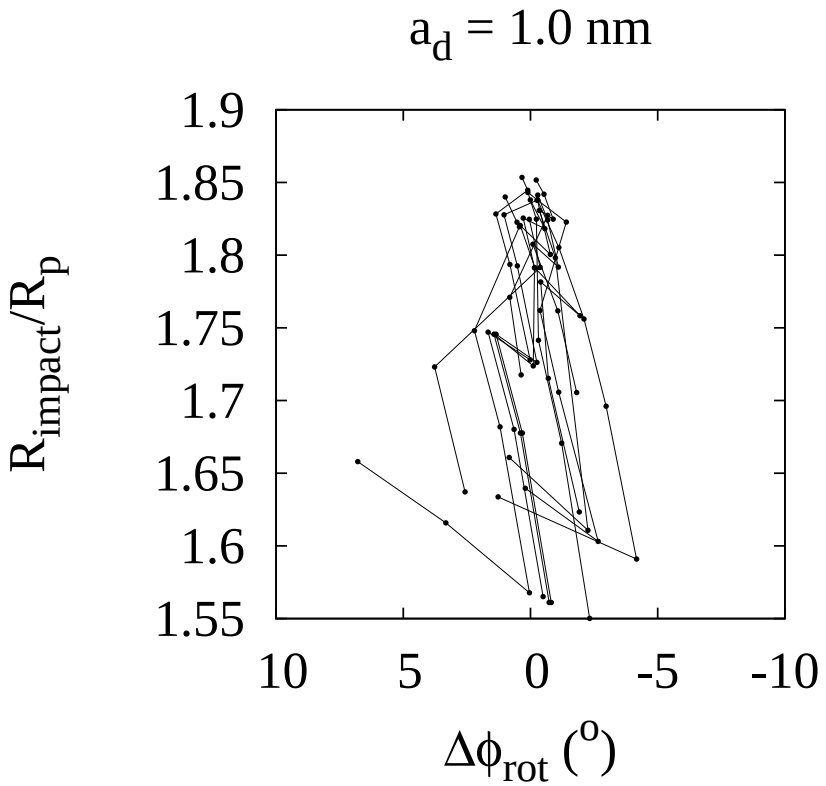

Figure 6.6: The azimuthal spread in the same simple model cascade, for 12 equally-spaced initial longitude positions. The horizontal axis marks the total azimuthal range $\Delta\phi_{rot}$, in degrees, in a frame rotating with Saturn, with prograde motion to the left.

increases, reaching a maximum value of $L_* \sim 10$ after a few hours. Each individual dust grain trajectory ends on a tight epicycle, and a new grain, initially neutral, begins with a wide gyrocycle that moves it to a new radial location.

At the top of Fig. 6.7, the first few grains have very tight epicycles because of their proximity to R_{syn} (Eq. 3.13). One of the grains enters Saturn's shadow and switches from spiralling prograde to retrograde as it becomes negatively charged. Nevertheless, for most of the time during this cascade, grains are positively charged and have enormous epicycles which give them both the radial depth to cover the B ring in a few steps, and the azimuthal range that makes this particular cascade a poor analog for a spoke.

We turn now to an alternative grain size for our simple model, one that will have much

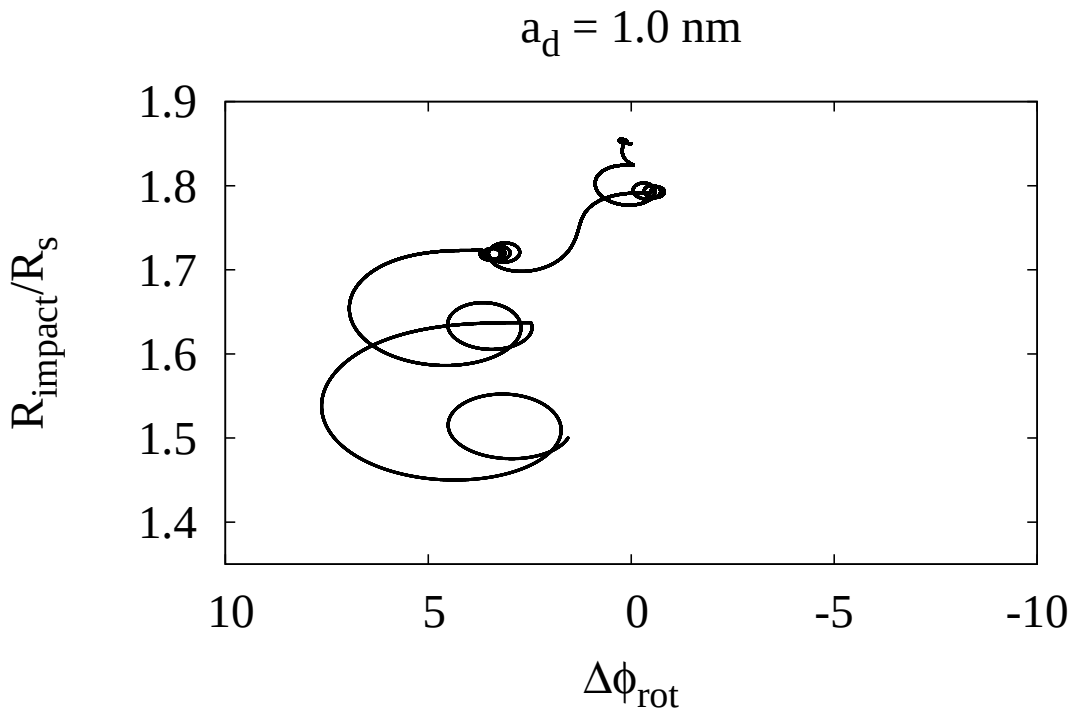

Figure 6.7: Tracing the path of a cascade chain leaping across the B ring. Plotted here are the azimuthal and radial positions of grains in a cascade chain. This particular cascade is triggered at $1.85R_p$ at local noon, in sunlight. The trajectory of each grain in the cascade is followed in the rotating frame (with prograde motion to the left), until the last grain lands beyond the inner edge of the B ring.

shorter radial steps for each half-bounce period.

6.6.2 Tip-toeing Across the B Ring

In the following set of cascade chains, we adopt a smaller grain size, 0.4 nm. Although this is probably too small to dominate a real cascade chain that leaves micron-sized debris, the actual choice of grain-size here is determined by our plasma model. A different set of plasma parameters could produce similar dynamics for a larger characteristic grain size.

In Fig. 6.8, we plot the radial progression of a cascade chain. Here, far more collisions take place before the cascade chain reaches the inner edge of the B ring. Most launches trigger a cascade that lasts between 20 and 40 hours, although one cascade chain takes

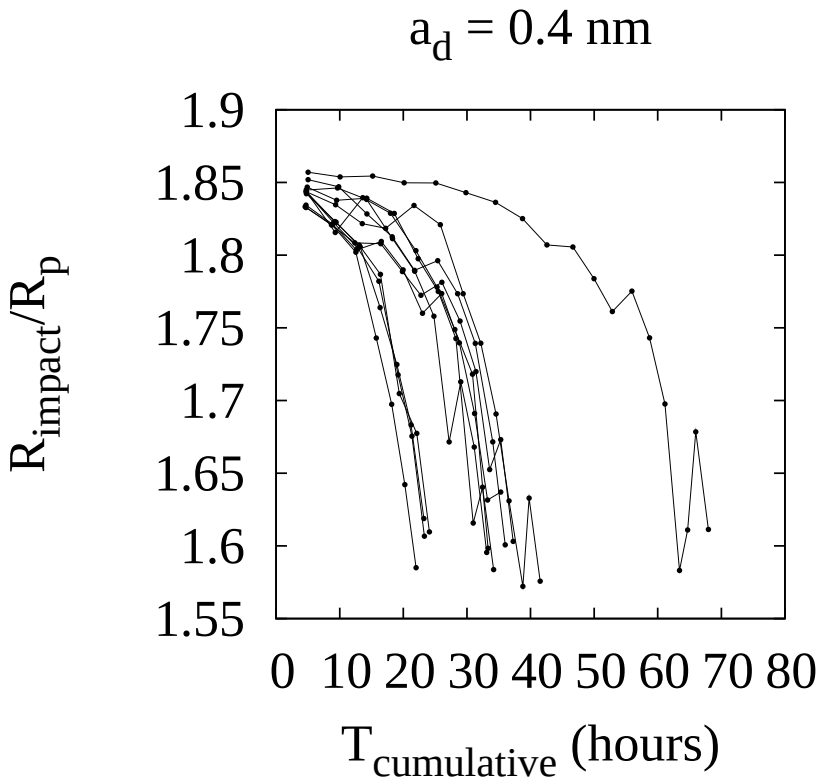

Figure 6.8: The progression of a simple model cascade, in which each grain of size $a_d = 0.4$ nm produces an identical grain at impact. We initiate the cascade at 12 equally-spaced azimuthal positions, plotting the radial position of impact after cumulative time given in hours. The radial distance of the initial trigger in each case is $1.85R_p$, just interior to the synchronous orbital distance at Saturn ($R_{syn} = 1.865R_p$).

much longer. This is in contrast to the larger grain size of Fig. 6.4, where the cascade progressed far more rapidly.

The azimuthal range of the cascade chains illustrated in Fig. 6.9 initially appear more confined, at least for all the collisions outside $1.7R_p$. Inside this location, the epicycles are large both in radial and azimuthal extent, and the collisional cascade broadens substantially in longitude. One of the cascade chains in this dataset is traced in Fig. 6.10, highlighting the effect of compact epicycles in keeping the collisions closely confined in azimuth. Being smaller, these grains charge up more slowly, but they still reach higher charge-to-mass ratios. In Fig. 6.10, each grain reaches $L_* \approx 70$, after a half bounce period,

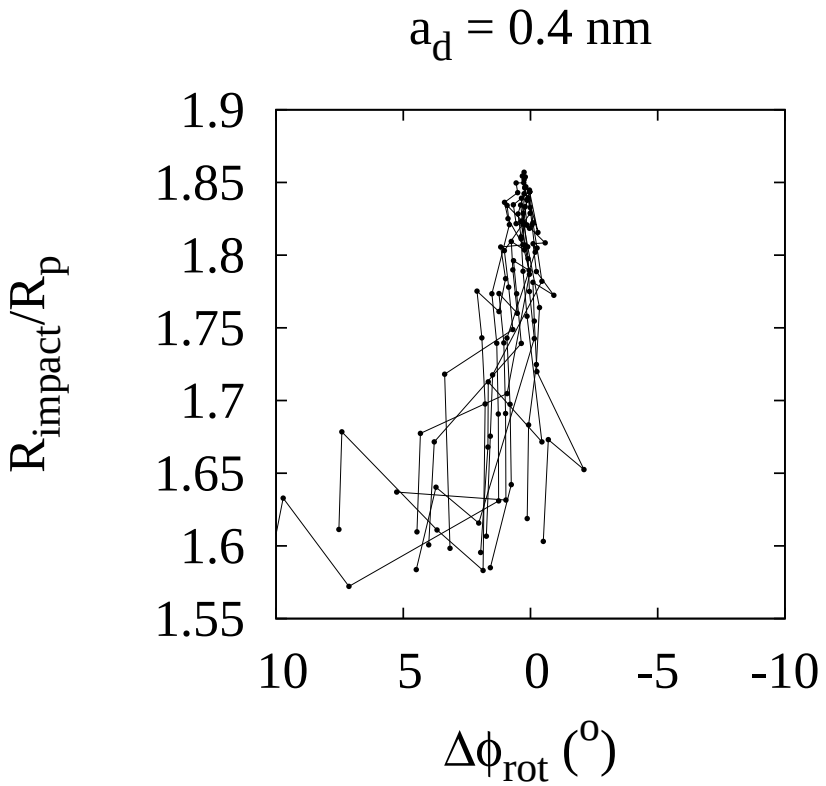

Figure 6.9: The azimuthal spread in the same simple model cascade, for 12 equally-spaced initial longitude positions. The horizontal axis marks the total azimuthal range $\Delta\phi_{rot}$, in degrees, in a frame rotating with Saturn, with prograde motion to the left.

($L_* \approx -44$ in the shadow).

6.7 Discussion and Prospects

We have considered two possible models for a collisional cascade to create the radial active edge of a spoke. The tip-toeing model, involving the slow radial progression of small grains with compact epicycles appears to be more narrowly confined in azimuthal range than the leaping model which spans the ring with just a few collisions (Figs. 6.7 and 6.10).

The tip-toeing model has the additional advantage of naturally confining the spokes

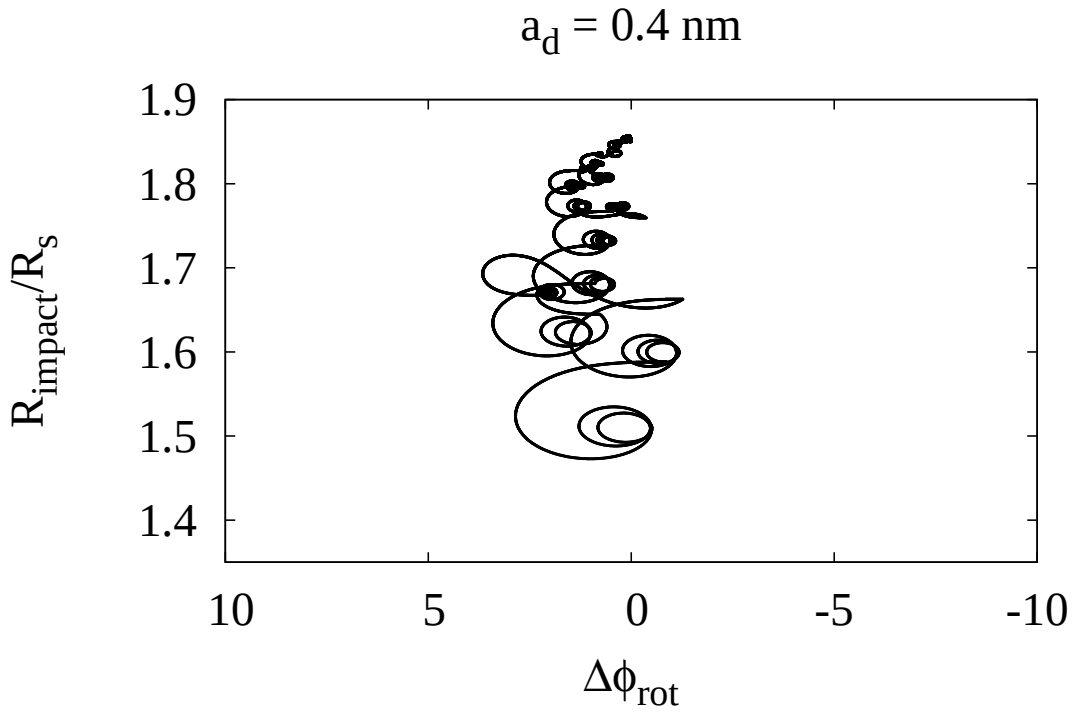

Figure 6.10: Tracing the path of a cascade chain tiptoeing across the B ring. Here we plot the azimuthal and radial positions of grains in a cascade chain. The initial trigger for this is at $1.85R_p$ at local noon, in sunlight. The trajectories of each grain are followed in the rotating frame (with prograde motion to the left), until the last grain lands beyond the inner edge of the B ring.

to the B ring. If dust grains with large radial ranges dominate the collisional cascade, we would expect to see spokes crossing the Cassini Division into the A ring. On the other hand, if collisional cascades are responsible for the spokes, then the size of the Cassini Division hints at the maximum size for epicycles in the trajectories of the dust grains that dominate the cascade. One problem with the tip-toeing model is that, for the choice of plasma parameters that we have adopted, it requires sub-nanometer-sized grains, which would make the production of micron-sized spoke particles difficult to explain. Nevertheless, the plasma model that we have adopted here is an initial estimate only.

Increasing the plasma density reduces the time for small dust grains to reach charge equilibrium in the shadow, but may also lead to a negative equilibrium charge in sunlight

(compare Figs. 5.1 and 5.5). This would make a collisional cascade converge on synchronous orbit from an initial trigger far from that location, in contrast to the models in Figs. 6.4 and 6.8. Negatively-charged dust would be consistent, however, with investigation by Eplee and Smith (1985) who found the radial progression of a spoke was in accordance with a charge-to-mass ratio of $L_* \approx -1.2$, as well as the findings of Mitchell et al. (2011). The latter found radial growth rates in Cassini data consistent with charge-to-mass ratios around $L_* = -0.5$.

Although this work is still in progress, there is nevertheless much that we can glean about prospects for the collisional cascade model. In both the leaping and tip-toeing cascade models that we have introduced here, (see Figs. 6.7 and 6.10) most of the azimuthal spread occurs in the first epicycle, as each grain charges up from its initially-neutral electric potential. This is because the charging timescale and the epicyclic period are comparable. We also see that as each grain charges up in sunlight, its charge-to-mass ratio increases from $L_* = 0$ to $L_* \approx 10$ in the leaping model and $L_* \approx 30$ in the tiptoeing model. Thus each grain spends several hours in the instantaneously radially unstable regime during its half-bounce lifetime. This causes a large radial shift in the guiding center or mean distance of the dust grain, very much like the grain trajectory illustrated in Fig. 5.2b, where we saw a tiny grain experience chaotic kicks in radial distance due to Jupiter's shadow. This radial shift is large on the scale of an epicycle, and is the main contribution to both the radial and azimuthal range of the grain.

To further evaluate our collisional cascade hypothesis, our strategy is twofold. Firstly, we shall perform numerical simulations of the cascade over a range of plasma densities. The main outcome that we anticipate from this is that denser plasma will lead to faster charging times and a smaller azimuthal and radial range for each grain in the cascade chain. The equilibrium potential on grains in these models may be negative, which would cause the cascade to converge towards R_{syn} from an initial trigger, although this is

consistent with observations. Nevertheless, if grains are strongly negatively charged, the azimuthal asymmetry caused by the shadow will be damped (Fig. 5.5).

Secondly, we shall enhance the treatment of grain creation in our simulated collisions. In the simple cascade model that we have performed here, each grain creates an identical daughter following a collision in the B ring. This neglects that fact that collisions have higher impact energies at gyrophase $\theta = \pi$, where the azimuthal range is a minimum and the radial range is a maximum. This would naturally increase the aspect ratio of the cascade footprint. One way to implement this numerically is to create multiple grains in each collision with the total proportional to v^2_{impact}.

Besides the large radial-to-azimuthal aspect ratio of the spokes, many other observational constraints demand explanation. For example, the observed maximum wedge-angle in the spokes, corresponding to an age of ~ 5 hours is seemingly at odds with the observation that some spokes remain active for an entire rotation period of 11 hours (Smith et al. 1982). In the collisional cascade model, this is likely due to the reabsorption of grains in the B ring after a half bounce period, even as collisions sustain the radial active edge of a spoke. This contrasts with the grain levitation models including Goertz and Morfill (1983), who posit that spoke particles are suspended above the ring plane by electrostatic forces. Their model provides little detail about how the additional force alters the expected lifetime of a dust grain. In our model, electromagnetism and gravity are the only forces acting on dust and hence grains have no need to be levitated; they all live for a half-bounce period irrespective of whether or not they contribute to future dust production.

The increase in spoke activity at the morning ansa suggests that a strong azimuthal asymmetry exists in the spoke formation mechanism. Saturn's shadow, and its effect on grain charging, is an obvious source of asymmetry, however, as we have seen in Chapter 5, the influence of the shadow strongly depends on the plasma density. We look forward

to garnering more insights into the potential for azimuthal asymmetry in the collisional cascade model over a range of plasma properties.

One outstanding uncertainty in spoke observations is the spoke formation timescale. Smith et al. (1982) found one spoke appear between successive Voyager 2 images which required radial motions of at least 20 km s^{-1} which, as Farmer and Goldreich (2005) pointed out, cannot be achieved by the plasma invoked in the Goertz and Morfill (1983) model. Nevertheless, Mitchell et al. (2011) see no evidence for such rapid spoke formation in the Cassini dataset. In the collisional cascade hypothesis, dust grains in the leaping model are created along the entire length of the active radial edge after just a few generations of collisions. Here the possible rapid formation time for spokes would be due to the time it takes for the collisions over a long radial distance to build up enough debris to make spokes visible. Thus the emergence of visible spoke dust could appear at the same time over a distance of thousands of kilometers. On the other hand, in the tiptoeing model, the collisional cascade would progress radially at roughly the radial speed of individual dust grains, without the need to invoke potentials of order 10^3 Volts.

Finally, we consider the seasonality of the spokes phenomenon in light of the collisional cascade theory. This too is an area in which there is no consensus in the literature. It may be the spoke visibility is an artifact of viewing geometry (McGhee et al. 2005), although Cassini has found no preferred viewing angle for spoke observations. Alternatively, the spoke formation process itself may be seasonal (Farrell et al. 2006; Mitchell et al. 2006). Since the plasma conditions are crucial in determining the trajectories of grains in the collisional cascade model, seasonal variation in the charging environment may have a dramatic effect on the progression of a cascade chain.

6.8 Conclusion

The collisional cascade hypothesis for the spokes is a promising work in progress. We know that collisions in the B ring must produce debris of all sizes, and that some of the dusty debris will re-enter the B ring at a different radial location and collide at high speed with a ring particle. Much of the physics that we have explored in this thesis plays a role in how dust grains in such a cascade move. Beyond the spokes phenomenon, the dynamics that we have explored in this dissertation will certainly further enlighten the curious on the motion of dust in the dusty rings of the giant planets, and perhaps in contexts as diverse as circumstellar dust and white dwarf debris disks. Nobody can anticipate where the study of dust grain dynamics will take us next, but we eagerly await the voyage.

Bibliography

Acuna, M. H. and Ness, N. F. (1976). The main magnetic field of Jupiter. *J. Geophys. Res.*, 81:2917–2922.

Bagenal, F. (1994). Empirical model of the Io plasma torus: Voyager measurements. *J. Geophys. Res.*, 991:11043–11062.

Bagenal, F. and Sullivan, J. D. (1981). Direct plasma measurements in the Io torus and inner magnetosphere of Jupiter. *J. Geophys. Res.*, 86:8447–8466.

Bastin, J. A. (1981). Note on the Rings of Saturn. *Moon and Planets*, 24:467–467.

Brooks, S. M., Esposito, L. W., Showalter, M. R., and Throop, H. B. (2004). The size distribution of Jupiter's main ring from Galileo imaging and spectroscopy. *Icarus*, 170:35–57.

Burns, J. A. and Schaffer, L. (1989). Orbital evolution of circumplanetary dust by resonant charge variations. *Nature*, 337:340–343.

Burns, J. A., Schaffer, L. E., Greenberg, R. J., and Showalter, M. R. (1985). Lorentz resonances and the structure of the Jovian ring. *Nature*, 316:115–119.

Burns, J. A., Showalter, M. R., Hamilton, D. P., Nicholson, P. D., de Pater, I., Ockert-Bell, M. E., and Thomas, P. C. (1999). The Formation of Jupiter's Faint Rings. *Science*, 284:1146–1150.

Burton, M. E., Dougherty, M. K., and Russell, C. T. (2009). Model of Saturn's internal planetary magnetic field based on Cassini observations. *Planet. Space Sci.*, 57:1706–

1713.

Canup, R. M. (2010). Origin of Saturn's rings and inner moons by mass removal from a lost Titan-sized satellite. *Nature*, 468:943–926.

Cao, H., Russell, C. T., Christensen, U. R., Dougherty, M. K., and Burton, M. E. (2011). Saturn's very axisymmetric magnetic field: No detectable secular variation or tilt. *Earth and Planetary Science Letters*, 304:22–28.

Carbary, J. F., Bythrow, P. F., and Mitchell, D. G. (1982). The spokes in Saturn's rings - A new approach. *Geophys. Res. Lett.*, 9:420–422.

Chow, V. W., Mendis, D. A., and Rosenberg, M. (1993). Role of grain size and particle velocity distribution in secondary electron emission in space plasmas. *J. Geophys. Res.*, 98:19065–19076.

Connerney, J. E. P., Acuna, M. H., and Ness, N. F. (1991). The magnetic field of Neptune. *J. Geophys. Res.*, 96:19023–19042.

Connerney, J. E. P., Davis, Jr., L., and Chenette, D. L. (1984). *Magnetic field models*, pages 354–377. University of Arizona Press.

Cuzzi, J. N. and Durisen, R. H. (1990). Bombardment of planetary rings by meteoroids - General formulation and effects of Oort Cloud projectiles. *Icarus*, 84:467–501.

Danby, J. M. A. (1988). Fundamentals of celestial mechanics. In Danby, J. M. A., editor, *Richmond, Va., U.S.A. : Willmann-Bell, 1988. 2nd ed., rev. enl.*

D'Aversa, E., Bellucci, G., Nicholson, P. D., Brown, R. H., Altieri, F., and Carrozzo, F. G. (2011). Spokes in the Saturn's B Ring: Distributions observed by Cassini-VIMS. In *EPSC-DPS Joint Meeting 2011*, page 1805.

D'Aversa, E., Bellucci, G., Nicholson, P. D., Hedman, M. M., Brown, R. H., Showalter, M. R., Altieri, F., Carrozzo, F. G., Filacchione, G., and Tosi, F. (2010). The spectrum of a Saturn ring spoke from Cassini/VIMS. *Geophys. Res. Lett.*, 37:1203–1207.

de Pater, I. and Lissauer, J. (2010). *Planetary Sciences*. Cambridge University Press.

de Pater, I., Showalter, M. R., Burns, J. A., Nicholson, P. D., Liu, M. C., Hamilton, D. P., and Graham, J. R. (1999). Keck Infrared Observations of Jupiter's Ring System near Earth's 1997 Ring Plane Crossing. *Icarus*, 138:214–223.

Desch, M. D. and Kaiser, M. L. (1981). Voyager measurement of the rotation period of Saturn's magnetic field. *Geophys. Res. Lett.*, 8:253–256.

Dessler, A. J. (1983). *Physics of the Jovian magnetosphere*. Cambridge University Press.

Dionne, G. (1975). Origin of Secondary Electron Emission Yield Curve Parameters. *Journal of Applied Physics*, 46:3347–3351.

Doyle, L. R. and Grün, E. (1990). Radiative transfer modeling constraints on the size of the spoke particles in Saturn's rings. *Icarus*, 85:168–190.

Eplee, R. E. and Smith, B. A. (1984). Spokes in Saturn's rings - Dynamical and reflectance properties. *Icarus*, 59:188–198.

Eplee, R. E. and Smith, B. A. (1985). Radial growth of an extended spoke in Saturn's B ring. *Icarus*, 63:304–311.

Eplee, R. E. and Smith, B. A. (1987). A dynamical constraint on particulate sizes for Saturn's B ring spokes. *Icarus*, 69:575–577.

Farmer, A. J. and Goldreich, P. (2005). Spoke formation under moving plasma clouds. *Icarus*, 179:535–538.

Farrell, W. M., Desch, M. D., Kaiser, M. L., Kurth, W. S., and Gurnett, D. A. (2006). Changing electrical nature of Saturn's rings: Implications for spoke formation. *Geophys. Res. Lett.*, 33:7203–7206.

Fischer, G., Desch, M. D., Zarka, P., Kaiser, M. L., Gurnett, D. A., Kurth, W. S., Macher, W., Rucker, H. O., Lecacheux, A., Farrell, W. M., and Cecconi, B. (2006). Saturn lightning recorded by Cassini/RPWS in 2004. *Icarus*, 183:135–152.

Goertz, C. K. (1989). Dusty plasmas in the solar system. *Reviews of Geophysics*, 27:271–292.

Goertz, C. K. and Morfill, G. (1983). A model for the formation of spokes in Saturn's rings. *Icarus*, 53:219–229.

Graps, A., Grün, E., Krüger, H., Horányi, M., and Svedhem, H. (2001). Io revealed in the Jovian dust streams. In B. Warmbein, editor, *Meteoroids 2001 Conference*, volume 495 of *ESA Special Publication*, pages 601–608.

Graps, A. L., Grün, E., Svedhem, H., Krüger, H., Horányi, M., Heck, A., and Lammers, S. (2000). Io as a source of the jovian dust streams. *Nature*, 405:48–50.

Graps, A. L., Jones, G. H., Juhász, A., Horányi, M., and Havnes, O. (2008). The Charging of Planetary Rings. *Space Science Reviews*, 137:435–453.

Grün, E., Baguhl, M., Hamilton, D., Kissel, J., Linkert, D., Linkert, G., and Riemann, R. (1994). Reduction of Galileo and Ulysses Dust Data. In *Galileo and Ulysses Dust Measurements*, Max-Planck-Institut für Kernphysik, page 30.

Grün, E., Goertz, C. K., Morfill, G. E., and Havnes, O. (1992). Statistics of Saturn's spokes. *Icarus*, 99:191–201.

Grün, E., Krüger, H., Graps, A. L., Hamilton, D. P., Heck, A., Linkert, G., Zook, H. A., Dermott, S., Fechtig, H., Gustafson, B. A., Hanner, M. S., Horányi, M., Kissel, J., Lindblad, B. A., Linkert, D., Mann, I., McDonnell, J. A. M., Morfill, G. E., Polanskey, C., Schwehm, G., and Srama, R. (1998). Galileo observes electromagnetically coupled dust in the Jovian magnetosphere. *J. Geophys. Res.*, 103:20011–20022.

Grün, E., Morfill, G. E., Terrile, R. J., Johnson, T. V., and Schwehm, G. (1983). The evolution of spokes in Saturn's B ring. *Icarus*, 54:227–252.

Grün, E., Zook, H. A., Baguhl, M., Balogh, A., Bame, S. J., Fechtig, H., Forsyth, R., Hanner, M. S., Horänyi, M., Kissel, J., Lindblad, B., Linkert, D., Linkert, G., Mann, I., McDonnell, J. A. M., Morfill, G. E., Phillips, J. L., Polanskey, C., Schwehm, G., Siddique, N., Staubach, P., Svestka, J., and Taylor, A. (1993). Discovery of Jovian dust streams and interstellar grains by the ULYSSES spacecraft. *Nature*, 362:428–430.

Gurnett, D. A., Kurth, W. S., Roux, A., Bolton, S. J., and Kennel, C. F. (1996). Galileo Plasma Wave Observations in the lo Plasma Torus and Near lo. *Science*, 274:391–392.

Hamilton, D. P. (1993a). Motion of dust in a planetary magnetosphere - Orbit-averaged equations for oblateness, electromagnetic, and radiation forces with application to Saturn's E ring. *Icarus*, 101:244–264.

Hamilton, D. P. (1993b). Erratum: "motion of Dust in a Planetary Magnetosphere: Orbit-Averaged Equations for Oblateness, Electromagnetic, and Radiation Forces with Application to Saturn's E-Ring. *Icarus*, 103:161.

Hamilton, D. P. (1994). A comparison of Lorentz, planetary gravitational, and satellite gravitational resonances. *Icarus*, 109:221–240.

Hamilton, D. P. (1996). Dust from Jupiter's Gossamer Ring and the Galilean Satellites. In *Bulletin of the American Astronomical Society*, volume 28 of *Bulletin of the American Astronomical Society*, page 1123.

Hamilton, D. P. and Burns, J. A. (1993a). Ejection of dust from Jupiter's gossamer ring. *Nature*, 364:695–699.

Hamilton, D. P. and Burns, J. A. (1993b). Lorentz and gravitational resonances on circumplanetary particles. *Advances in Space Research*, 13:241–248.

Hamilton, D. P. and Krüger, H. (2008). The sculpting of Jupiter's gossamer rings by its shadow. *Nature*, 453:72–75.

Handel, P. H. and James, P. B. (1983). Polarization catastrophe model of static electrification and spokes in the B-ring of Saturn. *Geophys. Res. Lett.*, 10:1–4.

Hanel, R., Conrath, B., Flasar, F. M., Kunde, V., Maguire, W., Pearl, J. C., Pirraglia, J., Samuelson, R., Cruikshank, D. P., Gautier, D., Gierasch, P. J., Horn, L., and Ponnamperuma, C. (1982). Infrared observations of the Saturnian system from Voyager 2. *Science*, 215:544–548.

Hedman, M. M., Burns, J. A., Showalter, M. R., Porco, C. C., Nicholson, P. D., Bosh,

A. S., Tiscareno, M. S., Brown, R. H., Buratti, B. J., Baines, K. H., and Clark, R. (2007). Saturn's dynamic D ring. *Icarus*, 188:89–107.

Herbert, F., Schneider, N. M., and Dessler, A. J. (2008). New description of Io's cold plasma torus. *Journal of Geophysical Research (Space Physics)*, 113:A01208.

Hill, J. R. and Mendis, D. A. (1981). On the braids and spokes in Saturn's ring system. *Moon and Planets*, 24:431–436.

Hill, J. R. and Mendis, D. A. (1982). The dynamical evolution of the Saturnian ring spokes. *J. Geophys. Res.*, 87:7413–7420.

Horányi, M. and Burns, J. A. (1991). Charged dust dynamics - Orbital resonance due to planetary shadows. *J. Geophys. Res.*, 96:19283–19289.

Horányi, M., Burns, J. A., and Hamilton, D. P. (1992). The dynamics of Saturn's E ring particles. *Icarus*, 97:248–259.

Horányi, M., Hartquist, T. W., Havnes, O., Mendis, D. A., and Morfill, G. E. (2004). Dusty plasma effects in Saturn's magnetosphere. *Reviews of Geophysics*, 42:4002.

Horányi, M., Houpis, H. L. F., and Mendis, D. A. (1988). Charged dust in the earth's magnetosphere. I - Physical and dynamical processes. *Ap&SS*, 144:215–229.

Horányi, M. and Juhász, A. (2010). Plasma conditions and the structure of the Jovian ring. *Journal of Geophysical Research (Space Physics)*, 115:A09202 1–12.

Horányi, M., Morfill, G., and Grün, E. (1993a). Mechanism for the acceleration and ejection of dust grains from Jupiter's magnetosphere. *Nature*, 363:144–146.

Horányi, M., Morfill, G., and Grün, E. (1993b). The dusty ballerina skirt of Jupiter. *J. Geophys. Res.*, 98:21245–21251.

Howard, J. E., Dullin, H. R., and Horányi, M. (2000). Stability of Halo Orbits. *Physical Review Letters*, 84:3244–3247.

Howard, J. E. and Horányi, M. (2001). Nonkeplerian dust dynamics at Saturn. *Geophys. Res. Lett.*, 28:1907–1910.

Howard, J. E., Horányi, M., and Stewart, G. R. (1999). Global Dynamics of Charged Dust Particles in Planetary Magnetospheres. *Physical Review Letters*, 83:3993–3996.

Jones, G. H., Krupp, N., Krüger, H., Roussos, E., Ip, W., Mitchell, D. G., Krimigis, S. M., Woch, J., Lagg, A., Fränz, M., Dougherty, M. K., Arridge, C. S., and McAndrews, H. J. (2006). Formation of Saturn's ring spokes by lightning-induced electron beams. *Geophys. Res. Lett.*, 33:21202–21207.

Jontof-Hutter, D. and Hamilton, D. P. (2012a). The fate of sub-micron circumplanetary dust grains I: Aligned dipolar magnetic fields. *Icarus*, 218:420–432.

Jontof-Hutter, D. and Hamilton, D. P. (2012b). The Fate of Sub-Micron Circumplanetary Dust Grains II: Multipolar Magnetic Fields. *Icarus*, in press.

Juhász, A. and Horányi, M. (1997). Dynamics of charged space debris in the Earth's plasma environment. *J. Geophys. Res.*, 102:7237–7246.

Juhász, A. and Horányi, M. (2004). Seasonal variations in Saturn's E-ring. *Geophys. Res. Lett.*, 31:19703–19706.

Kanal, M. (1962). *Theory of Current Collection of Moving Spherical Probes*. University of Michigan, College of Engineering, Space Physics Research Laboratory, Scientific Report No. JS-5.

Kempf, S., Srama, R., Horányi, M., Burton, M., Helfert, S., Moragas-Klostermeyer, G., Roy, M., and Grün, E. (2005). High-velocity streams of dust originating from Saturn. *Nature*, 433:289–291.

Krüger, H., Geissler, P., Horányi, M., Graps, A. L., Kempf, S., Srama, R., Moragas-Klostermeyer, G., Moissl, R., Johnson, T. V., and Grün, E. (2003a). Jovian dust streams: A monitor of Io's volcanic plume activity. *Geophys. Res. Lett.*, 30(21):2101.

Krüger, H., Hamilton, D. P., Moissl, R., and Grün, E. (2009). Galileo in-situ dust measurements in Jupiter's gossamer rings. *Icarus*, 203:198–213.

Krüger, H., Horányi, M., and Grün, E. (2003b). Jovian dust streams: Probes of the Io

plasma torus. *Geophys. Res. Lett.*, 30(2):1058.

Lenchek, A. M., Singer, S. F., and Wentworth, R. C. (1961). Geomagnetically Trapped Electrons from Cosmic-Ray Albedo Neutrons. *J. Geophys. Res.*, 66:4027–4046.

Lew, J. S. (1961). Drift Rate in a Dipole Field. *J. Geophys. Res.*, 66:2681–2685.

McGhee, C. A., French, R. G., Dones, L., Cuzzi, J. N., Salo, H. J., and Danos, R. (2005). HST observations of spokes in Saturn's B ring. *Icarus*, 173:508–521.

Mendis, D. A., Houpis, H. L. F., and Hill, J. R. (1982). The gravito-electrodynamics of charged dust in planetary magnetospheres. *J. Geophys. Res.*, 87:3449–3455.

Meyer-Vernet, N. (1982). Flip-flop of electric potential of dust grains in space. *A&A*, 105:98–106.

Meyer-Vernet, N. (1984). Some constraints on particles in Saturn's spokes. *Icarus*, 57:422–431.

Mitchell, C., Porco, C., Dones, L., and Spitale, J. (2011). The Behavior of Spokes in Saturn's B Ring. In *AAS/Division of Dynamical Astronomy Meeting #42*, page 807.

Mitchell, C. J., Horányi, M., Havnes, O., and Porco, C. C. (2006). Saturn's Spokes: Lost and Found. *Science*, 311:1587–1589.

Mitchell, C. J., Horányi, M., and Howard, J. E. (2003). Accuracy of epicyclic description of dust grain orbits about Saturn. *Journal of Geophysical Research (Space Physics)*, 108:1179–1188.

Morfill, G. E., Grün, E., Goertz, C. K., and Johnson, T. V. (1983). On the evolution of Saturn's 'Spokes' - Theory. *Icarus*, 53:230–235.

Morfill, G. E. and Thomas, H. M. (2005). Spoke formation under moving plasma clouds—The Goertz Morfill model revisited. *Icarus*, 179:539–542.

Ness, N. F., Connerney, J. E. P., Lepping, R. P., Schulz, M., and Voigt, G.-H. (1991). The magnetic field and magnetospheric configuration of Uranus. In Bergstralh, J. T., Miner, E. D., and Matthews, M. S., editors, *Uranus*, pages 739–779. University of

Arizona Press.

Nicholson, D. (1983). *Introduction to Plasma Physics*. Wiley.

Northrop, T. G. and Connerney, J. E. P. (1987). A micrometeorite erosion model and the age of Saturn's rings. *Icarus*, 70:124–137.

Northrop, T. G. and Hill, J. R. (1982). Stability of negatively charged dust grains in Saturn's ring plane. *J. Geophys. Res.*, 87:6045–6051.

Northrop, T. G. and Hill, J. R. (1983a). The adiabatic motion of charged dust grains in rotating magnetospheres. *J. Geophys. Res.*, 88:1–11.

Northrop, T. G. and Hill, J. R. (1983b). The inner edge of Saturn's B ring. *J. Geophys. Res.*, 88:6102–6108.

Northrop, T. G., Mendis, D. A., and Schaffer, L. (1989). Gyrophase drifts and the orbital evolution of dust at Jupiter's Gossamer Ring. *Icarus*, 79:101–115.

Ockert-Bell, M. E., Burns, J. A., Daubar, I. J., Thomas, P. C., Veverka, J., Belton, M. J. S., and Klaasen, K. P. (1999). The Structure of Jupiter's Ring System as Revealed by the Galileo Imaging Experiment. *Icarus*, 138:188–213.

Owen, T., Danielson, G. E., Cook, A. F., Hansen, C., Hall, V. L., and Duxbury, T. C. (1979). Jupiter's rings. *Nature*, 281:442–446.

Perov, N. I. (2012). On a Model of Spokes Origin in the Celestial Mechanical Systems. In *Lunar and Planetary Institute Science Conference Abstracts*, volume 43 of *Lunar and Planetary Institute Science Conference Abstracts*, page 1002.

Porco, C. A. and Danielson, G. E. (1982). The periodic variation of spokes in Saturn's rings. *AJ*, 87:826–833.

Postberg, F., Kempf, S., Srama, R., Green, S. F., Hillier, J. K., McBride, N., and Grün, E. (2006). Composition of jovian dust stream particles. *Icarus*, 183:122–134.

Roberts, P. H. and Soward, A. M. (1972). Magnetohydrodynamics of the Earth's Core. *Annual Review of Fluid Mechanics*, 4:117–154.

Schaffer, L. and Burns, J. A. (1987). The dynamics of weakly charged dust - Motion through Jupiter's gravitational and magnetic fields. *J. Geophys. Res.*, 92:2264–2280.

Schaffer, L. and Burns, J. A. (1992). Lorentz resonances and the vertical structure of dusty rings - Analytical and numerical results. *Icarus*, 96:65–84.

Schaffer, L. and Burns, J. A. (1994). Charged dust in planetary magnetospheres: Hamiltonian dynamics and numerical simulations for highly charged grains. *J. Geophys. Res.*, 99:17211–17223.

Schaffer, L. and Burns, J. A. (1995). Stochastic charging of dust grains in planetary rings: Diffusion rates and their effects on Lorentz resonances. *J. Geophys. Res.*, 100:213–234.

Schneider, N. M. and Trauger, J. T. (1995). The Structure of the Io Torus. *ApJ*, 450:450–462.

Showalter, M. R. (1996). Saturn's D Ring in the Voyager Images. *Icarus*, 124:677–689.

Showalter, M. R., de Pater, I., Verbanac, G., Hamilton, D. P., and Burns, J. A. (2008). Properties and dynamics of Jupiter's gossamer rings from Galileo, Voyager, Hubble and Keck images. *Icarus*, 195:361–377.

Smith, B. A., Soderblom, L., Batson, R., Bridges, P., Inge, J., Masursky, H., Shoemaker, E., Beebe, R., Boyce, J., Briggs, G., Bunker, A., Collins, S. A., Hansen, C. J., Johnson, T. V., Mitchell, J. L., Terrile, R. J., Cook, A. F., Cuzzi, J., Pollack, J. B., Danielson, G. E., Ingersoll, A., Davies, M. E., Hunt, G. E., Morrison, D., Owen, T., Sagan, C., Veverka, J., Strom, R., and Suomi, V. E. (1982). A new look at the Saturn system: The Voyager 2 images. *Science*, 215:505–537.

Smith, B. A., Soderblom, L., Beebe, R. F., Boyce, J. M., Briggs, G., Bunker, A., Collins, S. A., Hansen, C., Johnson, T. V., Mitchell, J. L., Terrile, R. J., Carr, M. H., Cook, A. F., Cuzzi, J. N., Pollack, J. B., Danielson, G. E., Ingersoll, A. P., Davies, M. E., Hunt, G. E., Masursky, H., Shoemaker, E. M., Morrison, D., Owen, T., Sagan, C., Veverka, J., Strom, R., and Suomi, V. E. (1981). Encounter with Saturn - Voyager 1

imaging science results. *Science*, 212:163–191.

Smyth, W. H., Peterson, C. A., and Marconi, M. L. (2011). A consistent understanding of the ribbon structure for the Io plasma torus at the Voyager 1, 1991 ground-based, and Galileo J0 epochs. *Journal of Geophysical Research (Space Physics)*, 116:A07205.

Sternglass, E. J. (1954). *The Thoeory of Secondary Electron Emission*. Sci. Pap. 1772, Westinghouse Res. Lab., Pittsburgh, Pa.

Störmer, C. (1955). *The Polar Aurora*. Oxford University Press.

Tagger, M., Henriksen, R. N., and Pellat, R. (1991). On the nature of the spokes in Saturn's rings. *Icarus*, 91:297–314.

Terrile, R. J., Yagi, G., Cook, A. F., and Porco, C. C. (1981). A Morphological Model for Spoke Formation in Saturn's Rings. In *Bulletin of the American Astronomical Society*, volume 13 of *Bulletin of the American Astronomical Society*, page 728.

Thomsen, M. F., Goertz, C. K., Northrop, T. G., and Hill, J. R. (1982). On the nature of particles in Saturn's spokes. *Geophys. Res. Lett.*, 9:423–426.

Thomsen, M. F. and van Allen, J. A. (1980). Motion of trapped electrons and protons in Saturn's inner magnetosphere. *J. Geophys. Res.*, 85:5831–5834.

Throop, H. B., Porco, C. C., West, R. A., Burns, J. A., Showalter, M. R., and Nicholson, P. D. (2004). The jovian rings: new results derived from Cassini, Galileo, Voyager, and Earth-based observations. *Icarus*, 172:59–77.

Valk, S. and Lemaître, A. (2008). Semi-analytical investigations of high area-to-mass ratio geosynchronous space debris including Earth's shadowing effects. *Advances in Space Research*, 42:1429–1443.

Warwick, J. W., Pearce, J. B., Evans, D. R., Carr, T. D., Schauble, J. J., Alexander, J. K., Kaiser, M. L., Desch, M. D., Pedersen, M., Lecacheux, A., Daigne, G., Boischot, A., and Barrow, C. H. (1981). Planetary radio astronomy observations from Voyager 1 near Saturn. *Science*, 212:239–243.

Weinheimer, A. J. and Few, Jr., A. A. (1982). The spokes in Saturn's rings - A critical evaluation of possible electrical processes. *Geophys. Res. Lett.*, 9:1139–1142.

Whipple, E. C. (1981). Potentials of surfaces in space. *Reports on Progress in Physics*, 44:1197–1250.

Zook, H. A., Grun, E., Baguhl, M., Hamilton, D. P., Linkert, G., Liou, J., Forsyth, R., and Phillips, J. L. (1996). Solar Wind Magnetic Field Bending of Jovian Dust Trajectories. *Science*, 274:1501–1503.